

Investigation of Localized Corrosion of Carbon Steel in H₂S Environments

A dissertation presented to
the faculty of
the Russ College of Engineering and Technology of Ohio University

In partial fulfillment
of the requirement for the degree
Doctor of Philosophy

Haitao Fang

March 2012

© 2012 Haitao Fang. All Rights Reserved

This dissertation entitled
Investigation of Localized Corrosion of Carbon Steel in H₂S Environments

by

HAITAO FANG

has been approved for
the Department of Chemical and Biomolecular Engineering
and the Russ College of Engineering and Technology by

Srdjan Nesic

Russ Professor of Chemical and Biomolecular Engineering

Dennis Irwin

Dean, Russ College of Engineering and Technology

ABSTRACT

FANG, HAITAO, Ph.D., March 2012, Chemical Engineering

Investigation of Localized Corrosion of Carbon Steel in H₂S Environments

Director of Thesis: Srdjan Nesic

Corrosion, especially the localized corrosion of carbon steel, in sour systems (H₂S dominant) has progressively become a greater concern to the oil and gas industry as a result of production from increasingly sour environments. In this study, the effects of chloride ion concentration on the localized H₂S corrosion were initially investigated, followed by the investigation of the corrosion of carbon steel in the presence of elemental sulfur, which is often present in sour systems. Attempts were also made to determine if classic galvanic theory can be applied to explain the propagation of localized corrosion in sour systems.

A series of experiments were performed to study high chloride concentration effects on the initiation and propagation of localized H₂S corrosion. Localized corrosion events were detected in both chloride-free and high chloride concentration conditions. The results suggest that chloride ion may not be the direct cause of initiation of localized H₂S corrosion. Instead, high concentrations of chloride ions significantly decreased overall general H₂S corrosion.

The corrosion of carbon steel in the presence of elemental sulfur was also studied. Elemental sulfur was shown to cause catastrophic corrosion of carbon steel when water is present. The addition of salts significantly accelerates the corrosion. From the experimental results, it has been concluded that an electrochemical process is the

dominant corrosion mechanism of elemental sulfur corrosion, and that solution conductivity plays a very important role. Based on the experimental data, an electrochemical model is proposed for elemental sulfur corrosion.

Propagation of localized corrosion in an H₂S system was also studied using an artificial pit technique. From the experimental results, it was determined that standard galvanic theory cannot be used to explain the propagation of localized corrosion in H₂S systems.

Approved: _____

Srdjan Nestic

Russ Professor of Chemical and Biomolecular Engineering

DEDICATION

To

Suocheng Fang, and Fanai Qu (my parents)

Lei Huang (my wife)

Ella Fang (my little princess)

Haiyan Fang and Haifeng Fang (my sister and brother)

ACKNOWLEDGEMENTS

I would like to express my great gratitude to my advisor, Professor Srdjan Nestic for his continuous support in both my research and my personal life. He always guided me through the problems encountered in my study with unimaginable patience. I feel so lucky to have him as an academic adviser and a life mentor for seven years during the MS and Ph.D. studies in Ohio University.

Great thanks go to Dr. David Young who was directly involved in this project. The project benefited greatly from his expertise.

I would like to acknowledge my indebtedness to Mr. Bruce Brown, my research group leader for his invaluable advice. He was always there when I needed help.

Many thanks go to my committee members, Professor Daniel Gulino, Professor Michael Prudich, Professor Howard Dewald and Professor Lauren McMills for their instructions, time and patience during my Ph.D. studies.

I would also like to acknowledge the contribution of the consortium of companies whose continuous financial support and technical guidance made this research possible.

Great thanks go to Dr. Guy Riefler for his assistance on the analysis of Ion Chromatography data.

Part of the XRD analysis on the corrosion products was performed by Dr. Srebri Petrov from Department of Chemistry in University of Toronto and Dr. Scott Oliver from University of California in Santa Barbara. This help is sincerely appreciated.

TABLE OF CONTENTS

	Page
ABSTRACT	3
DEDICATION.....	5
ACKNOWLEDGEMENTS.....	6
LIST OF TABLES.....	9
LIST OF FIGURES.....	10
CHAPTER 1 INTRODUCTION.....	17
CHAPTER 2 INSTRUMENTATION.....	20
2.1 Scanning electron microscopy (SEM).....	20
2.2 Energy-dispersive X-ray spectroscopy (EDX).....	22
2.3 X-ray diffraction (XRD).....	24
2.4 Infinite focus light microscopy (IFM).....	25
CHAPTER 3 HIGH CHLORIDE CONCENTRATION EFFECTS ON LOCALIZED H ₂ S CORROSION	27
3.1 Literature review.....	27
3.1.1 Hydrogen sulfide	27
3.1.2 H ₂ S corrosion.....	29
3.1.2.1 Mackinawite	32
3.1.2.2 Pyrrhotite	33
3.1.2.3 Smythite.....	33
3.1.2.4 Greigite	34
3.1.2.5 Marcasite	34
3.1.2.6 Pyrite.....	34
3.2 Research objectives and test matrices.....	36
3.2.1 Research objectives	36
3.2.2 Test matrices.....	36
3.3 Experimental setup and test procedure.....	38
3.3.1 Specimen preparation	38
3.3.2 Experimental setup	38
3.4 Experimental results and discussion.....	43
3.4.1 25°C, 50 ppm H ₂ S (0.05 mbar H ₂ S at P _{total} 1 bar), 0 wt.% NaCl.....	43
3.4.1.1 1st day.....	44
3.4.1.2 4th day	47
3.4.1.3 6th day	50
3.4.1.4 12th day	55
3.4.2 25°C, 50 ppm H ₂ S (0.05 mbar H ₂ S at P _{total} 1 bar), 10 wt.% NaCl.....	60
3.4.2.1 1st day.....	61
3.4.2.2 3 days.....	63
3.4.2.3 7 days.....	65
3.4.2.4 15 days.....	69
3.4.2.5 26 days.....	72

3.4.3	Why Did Pitting Attack Initiate but Not Propagate?	74
3.4.4	80°C, 5000 ppm H ₂ S (0.01 bar H ₂ S at P _{total} 2 bar), 10 wt.% NaCl	78
3.4.5	80°C, 50000 ppm H ₂ S (0.1 bar H ₂ S at P _{total} 2 bar), 10 wt.% NaCl	84
3.4.6	80°C, 50 % H ₂ S (1 bar H ₂ S at P _{total} 2 bar), 10 wt.% NaCl	88
3.5	Summary	95
CHAPTER 4 INVESTIGATION OF GALVANIC EFFECTS ON THE PROPOGATION OF LOCALIZED CORROSION IN H ₂ S SYSTEMS		96
4.1	Introduction	96
4.2	Objectives and test Matrix	97
4.3	Experimental set-up	97
4.4	Experimental results and discussion	99
4.4.1	Experimental results	99
4.4.2	Discussion	107
CHAPTER 5 INVESTIGATION OF THE ROLE OF ELEMENTAL SULFUR IN LOCALIZED CORROSION OF CARBON STEEL		112
5.1	Introduction	112
5.2	Literature review	113
5.3	Objectives and test matrices	120
5.4	Experimental setup	121
5.5	Experimental results and discussion	125
5.5.1	Oxidation of iron sulfide	125
5.5.1.1	100 ppm H ₂ S (0.1 mbar H ₂ S at P _{total} 1 bar)	125
5.5.1.2	10000 ppm H ₂ S (0.01 bar H ₂ S at P _{total} 1 bar)	137
5.5.1.3	Summary	153
5.5.2	Elemental sulfur corrosion mechanism	155
5.5.2.1	Sulfur hydrolysis reaction	155
5.5.2.2	Direct sulfur/iron reaction mechanism	162
5.5.3	Proposed mechanism of elemental sulfur corrosion of mild steel	249
5.5.4	Electrochemical modeling	252
5.5.4.1	Foundation of the electrochemical transport model	252
5.5.4.2	Mathematic model	255
CHAPTER 6 CONCLUSIONS AND FUTURE WORK		270
6.1	Conclusions	270
6.2	Future work	271
REFERENCES		272

LIST OF TABLES

	Page
Table 1. Test conditions for chloride effects on H ₂ S corrosion.....	37
Table 2. Chemical composition of C1018 carbon steel (wt.%)	38
Table 3. Parameters of gas mixing.....	43
Table 4. Test conditions	97
Table 5. Test conditions	121

LIST OF FIGURES

	Page
Figure 1. SEM image of iron carbonate.....	21
Figure 2. EDX spectrum of the mineral crust of <i>Rimicaris exoculata</i>	23
Figure 3. Standard XRD data for Mackinawite.....	25
Figure 4. A 3D image of steel surface with iron sulfide by IFM.....	26
Figure 5. Crystal structure of mackinawite (generated with Crystalmaker™ software).....	33
Figure 6. Experimental set up for low pressure H ₂ S concentration condition.....	40
Figure 7. Experimental setup for high partial pressure of H ₂ S.....	41
Figure 8. Autoclave schematic.....	42
Figure 9. Image of bare steel surface polished by sand paper.....	45
Figure 10. Corrosion specimen exposed to H ₂ S for 1 day at 0 wt% NaCl, 25°C, with corrosion product layer.....	46
Figure 11. Corrosion specimen exposed to H ₂ S for 4 days at 0 wt% NaCl, 25°C, with corrosion product layer.....	48
Figure 12. Corrosion specimen exposed to H ₂ S for 4 days at 0 wt% NaCl, 25°C, without corrosion product layer.....	49
Figure 13. Corrosion specimen exposed to H ₂ S for 6 days at 0 wt% NaCl, 25°C, with corrosion product layer.....	51
Figure 14. Corrosion specimen exposed to H ₂ S for 6 days at 0 wt% NaCl, 25°C, without corrosion product layer.....	53
Figure 15. 3D view of corrosion specimen exposed to H ₂ S for 6 days at 0 wt% NaCl, 25°C, without corrosion product layer.....	55
Figure 16. Corrosion specimen exposed to H ₂ S for 12 days at 0 wt% NaCl, 25°C, with corrosion product layer.....	57
Figure 17. Corrosion specimen exposed to H ₂ S for 12 days at 0 wt% NaCl, 25°C, without corrosion product layer.....	59
Figure 18. 3D view of corrosion specimen exposed to H ₂ S for 12 days at 0 wt% NaCl, 25°C, without corrosion product layer.....	60
Figure 19. Corrosion specimen exposed to H ₂ S for 1 days at 10 wt% NaCl, 25°C, with corrosion product layer.....	62
Figure 20. Uniform corrosion rates versus time at 25°C, 50 ppm H ₂ S, 0 wt% and 10 wt. % NaCl.....	63
Figure 21. Corrosion specimen exposed to H ₂ S for 3 days at 10 wt% NaCl, 25°C, with corrosion product layer.....	64
Figure 22. Corrosion specimen exposed to H ₂ S for 7 days at 10 wt% NaCl, 25°C, with corrosion product layer.....	67
Figure 23. Corrosion specimen exposed to H ₂ S for 7 days at 10 wt% NaCl, 25°C, without corrosion product layer.....	68
Figure 24. Corrosion specimen exposed to H ₂ S for 15 days at 10 wt% NaCl, 25°C, with corrosion product layer.....	70

Figure 25. Corrosion specimen exposed to H ₂ S for 15 days at 10 wt% NaCl, 25°C, without corrosion product layer.	71
Figure 26. 3D view of corrosion specimen exposed to hydrogen sulfide for 12 days at 0 wt% NaCl, 25°C, without corrosion product layer.	72
Figure 27. Corrosion specimen exposed to H ₂ S for 26 days at 10 wt% NaCl, 25°C, with corrosion product layer.	73
Figure 28. Corrosion specimen exposed to H ₂ S for 6 days at 0 wt% NaCl, 25°C, without corrosion product layer.	75
Figure 29. Freshly prepared bare corrosion specimen surface polished to 600 grit sand paper.	76
Figure 30. Analysis of gold sputter-coated sand paper.	77
Figure 31. Corrosion specimen exposed to 0.01 bar H ₂ S for 7 days at 10 wt% NaCl, 80°C, with corrosion product layer.	80
Figure 32. Corrosion specimen exposed to 0.01 bar H ₂ S for 7 days at 10 wt% NaCl, 80°C, without corrosion product layer.	81
Figure 33. Cross-section of a corrosion specimen exposed to 0.01 bar H ₂ S for 7 days at 10 wt.% NaCl, 80°C, with corrosion product layer.	83
Figure 34. Corrosion specimen exposed to 0.1 bar H ₂ S for 7 days at 10 wt.% NaCl, 80°C, with corrosion product layer.	85
Figure 35. Corrosion specimen exposed to 0.1 bar H ₂ S for 7 days at 10 wt.% NaCl, 80°C, without corrosion product layer.	87
Figure 36. Corrosion specimen exposed to 1 bar H ₂ S for 7 days at 10 wt.% NaCl, 80°C, with corrosion product layer.	89
Figure 37. Corrosion specimen exposed to 1 bar H ₂ S for 7 days at 10 wt.% NaCl, 80°C, without corrosion product layer.	91
Figure 38. Cross-section of a corrosion specimen exposed to 1 bar H ₂ S for 7days at 10 wt.% NaCl, 80°C, with corrosion product layer.	93
Figure 39. Comparisons of general corrosion rates for different H ₂ S partial pressures tested.	94
Figure 40. Experimental setup.	98
Figure 41. Schematic of an artificial pit.	99
Figure 42. Uniform corrosion rates vs. time at 25°C, 50 ppm H ₂ S, 0 wt.% NaCl.	100
Figure 43. Galvanic current between cathode and anode, pit depth 0 mm.	101
Figure 44. Galvanic current between cathode and anode, pit depth 4 mm.	102
Figure 45. Galvanic current between cathode and anode, pit depth 6 mm.	102
Figure 46. Corrosion rate and potential of cathode vs. time.	104
Figure 47. Comparison of potential change during iron sulfide layer forming process between cathode and anode. (pit depth 0 mm)	104
Figure 48. Galvanic current between cathode and anode, pit depth 0 mm.	105
Figure 49. Comparison of potential change during iron sulfide layer forming process between cathode and anode. (pit depth 6 mm)	106
Figure 50. Galvanic current between cathode and anode, pit depth 6 mm.	107

Figure 51. Simplified sketch of corrosion mechanisms in a sweet system showing the change in corrosion potential and corrosion current when a passive layer forms on the steel surface.....	108
Figure 52. Simplified sketch of corrosion mechanisms in a sour system showing the change in corrosion potential and corrosion current for an iron sulfide layer building process in a pure H ₂ S system.....	109
Figure 53. Simulation of three possible potential difference scenarios during pit growth.....	110
Figure 54. X-ray diffraction data from S.Boursiquot (S: sulfur [S ₈]; M: mackinawite [FeS]; G: greigite [Fe ₃ S ₄].....	118
Figure 55. X-ray diffraction data for mackinawite oxidation in aqueous solution (S: sulfur [S ₈]; M: mackinawite [FeS]; G: greigite [Fe ₃ S ₄]; P: pyrite [FeS ₂].....	120
Figure 56. Experimental setup.....	122
Figure 57. Sulfur in a glass Petri dish and the autoclave used in the sulfur hydrolysis experiments.....	124
Figure 58. LPR corrosion rate vs. time at 100 ppm H ₂ S (layer formation).....	126
Figure 59. SEM image and EDX spectrum of a specimen surface after a 1 day exposure to 100 ppm H ₂ S.....	128
Figure 60. SEM image and EDX spectrum of a specimen surface after a 1 day exposure to air (H ₂ S was stopped purging).....	130
Figure 61. SEM image and EDX spectrum of a specimen surface after a 5 days exposure to Certified Breathing Air (H ₂ S was stopped purging).....	132
Figure 62. SEM image and EDX spectrum of a specimen surface after a 10 days exposure to Certified Breathing Air (H ₂ S was stopped purging).....	133
Figure 63. SEM image and EDX spectrum of a specimen surface after a 16 days exposure to Certified Breathing Air (H ₂ S was stopped purging).....	134
Figure 64. X-ray diffraction data of corrosion and oxidation products (4 days exposure to H ₂ S, 1 day and 5 days exposure to air).....	136
Figure 65. X-ray diffraction data of corrosion and oxidation products (10 days exposure to air).....	137
Figure 66. LPR corrosion rate vs. time at 10000 ppm H ₂ S (corrosion product layer formation).....	139
Figure 67. SEM image and EDX spectrum of a specimen surface after a 2 days exposure to 10,000 ppm H ₂ S.....	140
Figure 68. SEM image and EDX spectrum of a specimen surface after a 1 day exposure to air. (H ₂ S was stopped purging).....	142
Figure 69. SEM image and EDX spectrum of a specimen surface after a 5 days exposure to Certified Breathing Air. (H ₂ S was stopped purging).....	144
Figure 70. SEM image and EDX spectrum of a specimen surface after a 10 days exposure to air (H ₂ S was stopped purging).....	145
Figure 71. Raman data of corrosion products (two days exposure to 10000 ppm H ₂ S). 148	
Figure 72. Raman data of corrosion products (1 day exposure to air).....	151
Figure 73. Raman data of corrosion products (10 days exposure to air).	153
Figure 74. pH at equilibration after mixing water with sulfur at various temperatures..	156

Figure 75. Mesh-capped pH probe ⁸⁷ applied to the sulfur corrosion system.....	157
Figure 76. Surface pH measurements for sulfur hydrolysis on a corroding steel mesh.	158
Figure 77. Ion chromatogram for standard solution with SO_4^{2-}	159
Figure 78. Chromatogram for deionized water after purging of the chromatographic column.....	160
Figure 79. Chromatograms for water/sulfur solutions exposed at different temperatures.	161
Figure 80. pH of the test solution after degassing for the studied temperatures.....	162
Figure 81. Elemental sulfur deposited on the surface of a corrosion specimen before exposure.	163
Figure 82. The overall surface of a corrosion specimen after exposure to elemental sulfur (25°C, 3 days).	163
Figure 83. Corrosion specimen contacted with elemental sulfur for 1 day at 25°C, with corrosion product layer.	165
Figure 84. IFM data for corrosion specimen contacted with sulfur for 1 day at 25°C, without corrosion product layer, appearance of the surface (top images) and a line profile.....	166
Figure 85. Corrosion specimen contacted with elemental sulfur for 4 days at 25°C, with corrosion product layer.	167
Figure 86. IFM data for specimen contacted with sulfur for 4 days at 25°C, without corrosion product layer.	168
Figure 87. Corrosion specimen contacted with elemental sulfur for 5 days at 25°C, with corrosion product layer.	169
Figure 88. IFM data for specimen contacted with sulfur for 5 days at 25°C, without corrosion product layer.	170
Figure 89. Corrosion specimen contacted with elemental sulfur for 1 day at 80°C, with corrosion product layer.	171
Figure 90. IFM data for specimen contacted with sulfur for 1 day at 80°C, without corrosion product layer.	171
Figure 91. Corrosion specimen contacted with elemental sulfur for 4 days at 80°C, with corrosion product layer.	172
Figure 92. IFM data for specimen contacted with sulfur for 4 days at 80°C, without corrosion product layer.	173
Figure 93. Corrosion specimen contacted with elemental sulfur for 5 days at 80°C, with corrosion product layer.	173
Figure 94. XRD data of the corrosion product after 4 days at 80°C.....	174
Figure 95. Comparison of general and localized corrosion rates at 25°C, DI water.	175
Figure 96. Comparison of general and localized corrosion rates at 80°C, DI water.	176
Figure 97. Experimental set-up for solid state reaction.....	177
Figure 98. Specimen surface after 6 hour exposure at 25°C and 60°C.....	178
Figure 99. Specimen surface after 2 days exposure at 80°C.....	178
Figure 100. Specimen surface during and after 6 hours exposure at 125°C.....	179
Figure 101. Materials used for the physical separation of sulfur and iron: a) plastic mesh, b) graphite sheet, c) graphite sheet with 0.043” ID holes, d) X65 steel sample.	181

Figure 102. Sample arrangement for the sulfur/plastic-mesh/steel test, where steel surface is in close proximity to sulfur but electrically insulated from each other.....	182
Figure 103. Steel sample surface after exposure in the sulfur/plastic-mesh/steel test where it was in close proximity to sulfur but electrically insulated from each other.....	183
Figure 104. SEM/EDX data for the typical corroded steel surface after exposure in the sulfur/plastic-mesh/steel test where it was in close proximity to sulfur but electrically insulated from each other.....	184
Figure 105. Sample arrangement for sulfur/carbon-sheet/steel test where the steel was separated from the sulfur but electrically connected.....	186
Figure 106. Steel sample surface after exposure in the sulfur/carbon-sheet/steel test where the steel was separated from the sulfur but electrically.....	186
Figure 107. SEM/EDX data for the steel sample surface underneath the carbon sheet after exposure in the sulfur/carbon-sheet/steel test where the steel was separated from the sulfur but electrically connected to it.....	187
Figure 108. Sample arrangement for sulfur/carbon-sheet-with-holes/steel test where the steel was in physical proximity to the sulfur and electrically connected.....	189
Figure 109. SEM/EDX data for the sample surface underneath the hole from the experiment where the steel was in physical proximity to the sulfur and electrically connected.....	190
Figure 110. SEM data for the sample surface underneath the hole, from the experiment where the steel was in physical proximity to the sulfur and electrically connected.....	191
Figure 111. SEM image of the sample surface underneath the carbon sheet with holes from the higher temperature experiment where the steel was in physical proximity to the sulfur and electrically connected.....	192
Figure 112. Corrosion specimen before and after 1 day exposure at 25°C.....	193
Figure 113. Corrosion specimen before and after 4 days exposure at 25°C.....	194
Figure 114. Corrosion specimen before and after 5 days exposure at 25°C.....	194
Figure 115. Corrosion specimen contacted with elemental sulfur for 1 day at 25°C, with corrosion product layer.....	196
Figure 116. IFM data for corrosion specimen for 1 day at 25°C, without corrosion product layer, appearance of the surface (top images) and a line profile.....	197
Figure 117. Corrosion specimen contacted with elemental sulfur for 4 days at 25°C, with corrosion product layer.....	198
Figure 118. IFM data for specimen contacted with sulfur for 4 days at 25°C, without corrosion product layer.....	199
Figure 119. Corrosion specimen contacted with elemental sulfur for 5 days at 25°C, with corrosion product layer.....	200
Figure 120. IFM data for specimen contacted with sulfur for 5 days at 25°C, without corrosion product layer.....	201
Figure 121. Corrosion specimen before and after 1 day exposure at 80°C.....	202
Figure 122. Corrosion specimen before and after 4 days exposure at 80°C.....	202
Figure 123. Corrosion specimen before and after 5 days exposure at 80°C.....	203

Figure 124. Corrosion specimen contacted with elemental sulfur for 1 day at 80°C, with corrosion product layer	204
Figure 125. IFM data for specimen contacted with sulfur for 1 day at 80°C, without corrosion product layer.	205
Figure 126. Corrosion specimen contacted with elemental sulfur for 4 days at 80°C, with corrosion product layer.	206
Figure 127. Corrosion specimen contacted with elemental sulfur for 5 days at 80°C, with corrosion product layer.	207
Figure 128. IFM data for specimen contacted with sulfur for 5 days at 80°C, without corrosion product layer.	208
Figure 129. Comparison of general corrosion between salt free and 10 wt.% NaCl conditions at 25°C.	209
Figure 130. Corrosion specimen contacted with elemental sulfur for 4days with and without film at 25°C, salt free condition.....	210
Figure 131. Corrosion specimen before and after 1 day exposure to sulfur at 25°C, salt free condition.	212
Figure 132. SEM image of specimen surface after 1 day exposure to sulfur at 25°C, salt free condition.	212
Figure 133. IFM data for corrosion specimen for 1 day at 25°C, salt free condition, without film, appearance of the surface.....	213
Figure 134. Corrosion specimen before and after 1 day exposure to sulfur at 25°C, 0.175 M NaCl.....	214
Figure 135. SEM image of specimen surface after 1 day exposure to sulfur at 25°C, 0.175 M NaCl.....	215
Figure 136. IFM data for corrosion specimen for 1 day at 25°C, 0.175 M NaCl, without film, appearance of the surface and surface profile.	216
Figure 137. Corrosion specimen before and after 1 day exposure to sulfur at 25°C, 0.175 M NaClO ₄	218
Figure 138. SEM image of specimen surface after 1 day exposure to sulfur at 25°C, 0.175 M NaClO ₄	219
Figure 139. IFM data for corrosion specimen for 1 day at 25°C, 0.175 M NaClO ₄ , without film, appearance of the surface and surface profile.	220
Figure 140. Corrosion specimen before and after 1 day exposure to sulfur at 80°C, salt free condition.	222
Figure 141. SEM image of specimen surface after 1 day exposure to sulfur at 80°C, salt free condition.	223
Figure 142. Corrosion specimen before and after 1 day exposure to sulfur at 80°C, 1.5 M NaCl.....	225
Figure 143. SEM image of specimen surface after 1 day exposure to sulfur at 80°C, 1.5 M NaCl.	226
Figure 144. IFM data for corrosion specimen for 1 day at 25°C, 1.5 M NaCl, without film, appearance of the surface and surface profile.	227
Figure 145. Corrosion specimen before and after 1 day exposure to sulfur at 80°C, 1.5 M NaClO ₄	229

Figure 146. SEM image of specimen surface after 1 day exposure to sulfur at 80°C, 1.5 M NaClO ₄	230
Figure 147. IFM data for corrosion specimen for 1 day at 25°C, 1.5 M NaClO ₄ , without film, appearance of the surface and surface profile.	231
Figure 148. Comparisons of general corrosion rate of two different salt conditions at 25°C and 80°C.....	232
Figure 149. Pictures of specimen surface after corrosion.....	235
Figure 150. SEM images of specimen surface on the sulfur edge.....	236
Figure 151. pH effect on film formation underneath (upper pictures) and outside the sulfur droplet (25°C, N ₂ purged).....	240
Figure 152. pH effect on sulfur/iron reaction rate(25°C, N ₂ purged).	241
Figure 153. Surface morphology underneath the sulfur droplet at different systems (a) pure N ₂ , b) pure CO ₂ , c) N ₂ +100 ppm H ₂ S, d) CO ₂ +100 ppm H ₂ S).	244
Figure 154. Surface morphology outside the sulfur droplet at different systems (pure N ₂ and pure CO ₂).	245
Figure 155. Surface morphology outside the sulfur droplet at different systems (N ₂ +100 ppm H ₂ S, and CO ₂ +100 ppm H ₂ S).	247
Figure 156. Corrosion rate underneath the sulfur droplet at different systems.	248
Figure 157. Simulation of elemental sulfur attack in low conductivity conditions.	249
Figure 158. Simulation of elemental sulfur attack in high conductivity conditions.....	251
Figure 159. Schematic of the modeled electrochemical system in elemental sulfur corrosion	253
Figure 160. Elemental sulfur corrosion system used in the model.	256
Figure 161. Computational domain of the model.	257
Figure 162. Computational domain used in Comsol Multiphysics® software.....	259
Figure 163. 2D Potential and current distribution – simulation 1.....	261
Figure 164. Current distribution along the steel surface – simulation 1	262
Figure 165. 2D Potential and current distribution – simulation 2.....	263
Figure 166. Current distribution along the steel surface – simulation 2.....	264
Figure 167. 2D Potential and current distribution – simulation 3.....	265
Figure 168. Current distribution along the steel surface – simulation 3.....	265
Figure 169. 2D Potential and current distribution – simulation 4.....	267
Figure 170. Current distribution along the steel surface – simulation 4.....	268

CHAPTER 1 INTRODUCTION

Carbon steel is widely used in the fabrication of infrastructure for oil and gas extraction, transmission and processing. Corrosion of carbon steel is a pervasive problem encountered by the oil and gas industry. Depending on the gas composition, the corrosive environment can be classified into two categories: sweet systems and sour systems. Corrosion of mild steel in the sweet systems, also called CO₂ corrosion, is well understood after over 60 years of investigation. The first significant CO₂ corrosion model was established by deWaard and Milliams in 1975¹. In their model, the combined effects of temperature and CO₂ partial pressure were first identified as the most important factors affecting CO₂ corrosion. Other parameters such as the effect of pH, flow velocity, organic acids and corrosion product layer formation were covered in different CO₂ corrosion prediction models²⁻⁷. Localized corrosion in sweet systems was also studied⁸⁻¹⁸. The initiation and propagation processes of localized corrosion in sweet corrosion have been extensively studied and were determined to be due to the local breakdown of a passive-like film and development of a galvanic cell, and hence the current, between the bare metal and passivated surface. Although there is still debate on the composition of the passive film, the abovementioned localized corrosion mechanism is accepted by the research community.⁸⁻¹⁸ However, how localized corrosion occurs in sour systems remains unclear. Determining its mechanism becomes increasingly important as more sour gas fields are developed.

The severity of H₂S corrosion problems in oil and gas production, as well as in the oil refining industry, is increasing as production fields age. Localized/pitting corrosion

along the bottom of the pipeline is the primary corrosion factor leading to failure of sour gas pipelines¹⁹. It is well known that the kinetics of H₂S corrosion are controlled by the nature of the corrosion product layer, FeS, in terms of both phase type and morphology²⁰. Local breakdown of iron sulfide layers is the main factor in the initiation of localized H₂S corrosion. Breakdown of FeS layers may be due to environmental factors, such as the presence of solids, chlorides, elemental sulfur, and high velocity¹⁹, etc.

Severe pitting corrosion has been observed in production field failures of both wells and pipelines when there are very high concentrations of H₂S and chlorides present²¹. Hence, chloride ion has been suspected to be the direct cause of initiation of localized corrosion in H₂S corrosion systems. However, virtually no dedicated systematic laboratory studies of chloride effects on localized H₂S corrosion have been performed. Therefore one can conclude that the role of chloride in localized H₂S corrosion has been insufficiently determined.

Another parameter that is suspected to lead to localized corrosion in sour systems is the presence of elemental sulfur. Typically, elemental sulfur is carried by the sour gas through the pipeline. However, as pressures and temperatures decrease, sulfur will be deposited on the pipeline walls. In aqueous conditions, contact of solid sulfur with mild steel may result in the onset of catastrophic corrosion.

In addition to the previously described environmental effects, microbiologically induced corrosion (MIC) may also cause localized corrosion in sour systems²²⁻²⁶. Microbiologically induced corrosion is a type of corrosion caused by the growth of sessile microorganisms in a biofilm. Generally speaking, MIC is caused by bacteria. MIC

is officially accepted by NACE as the term for this type of corrosion and mostly occurs locally due to specific bacterial behavior. The main type of bacteria related to sour corrosion is sulfate-reducing bacteria (SRB)²⁴⁻²⁶. They can reduce sulfate, sulfite, thiosulfate and even sulfur to sulfide, which is corrosive to steel. Although greater attention has been paid to the problems caused by MIC, and efforts have been made to understand this type of corrosion, the mechanisms of MIC remain unclear.

Based on what has been discussed above, two key reported factors were chosen for the study of localized corrosion in sour systems: the effects of chloride on H₂S corrosion and the role of elemental sulfur corrosion. Experimental results and their discussion are included in the following chapters.

CHAPTER 2 INSTRUMENTATION

Iron sulfide layers are always formed on the steel surface when H₂S corrosion occurs in real systems. Localized corrosion events in H₂S systems have been considered to be related to the morphology and composition of the corrosion product layers²⁷. Therefore, surface analytical tools became very important in the investigation of localized corrosion in the presence of H₂S. Surface analytical tools can also help to quantify the rate of localized corrosion. In this project, four specific surface analytical tools: scanning electron microscopy (SEM), energy-dispersive X-ray spectroscopy (EDX), X-ray diffraction (XRD) and infinite focus microscope (IFM) were adopted to analyze the surface of a corrosion specimen. The function and the theory behind each are summarized in the following paragraphs.

2.1 Scanning electron microscopy (SEM)

Scanning electron microscopy (SEM) was used to examine the morphology of the corrosion products generated on specimen surfaces. It can display a clear view of the morphology and key features of the corrosion products, which can all be considered as factors used to explain the occurrence of localized corrosion.

SEM is a method that enables generation of images of a sample surface after scanning with a high energy beam of electrons. The atoms in the surface features of the samples interact with and scatter the incident electrons, in the form of a beam, generated and focused within the column of the SEM instrument. The scattered electrons are detected and create signals that confer information on surface morphology, as well as qualitative composition and electric conductivity characteristics of the sample. The

signals are converted into a high resolution image after processing. Figure 1 shows an example of a SEM image of iron carbonate²⁸ (FeCO_3).

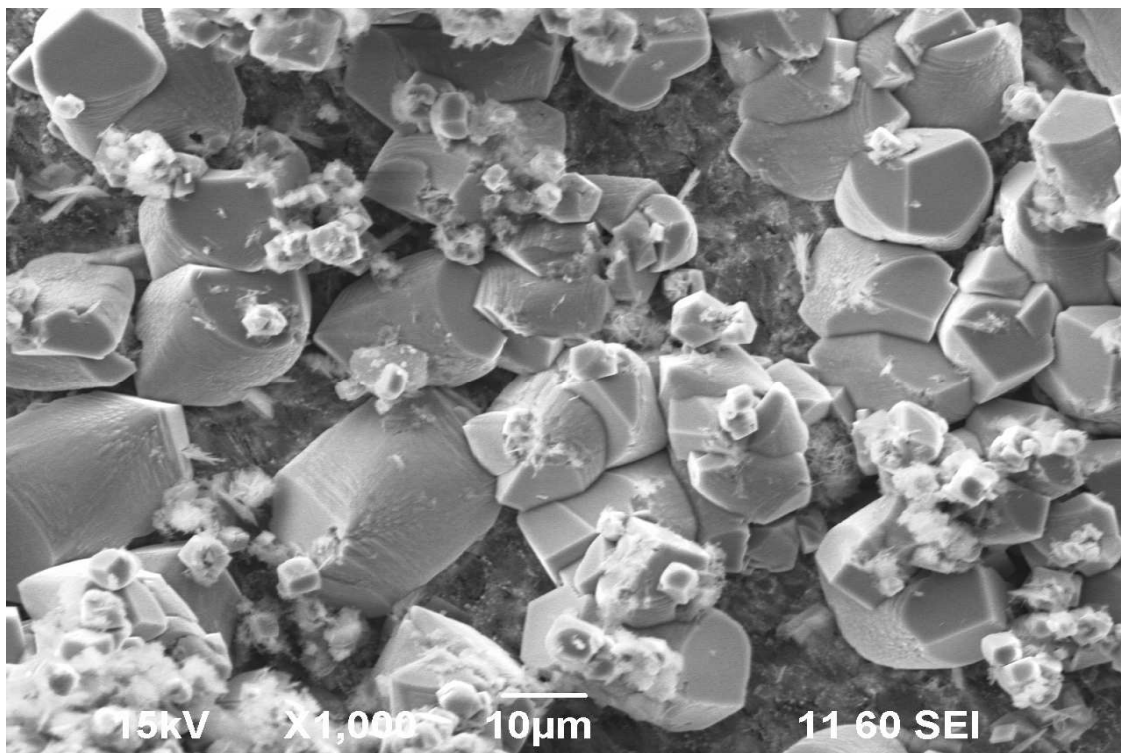


Figure 1. SEM image of iron carbonate²⁸.

Different from the traditional optical microscope, the magnification in SEM does not depend on the power of the objective lens. The objective lens in the SEM is only used to focus the beam to a spot, not to provide an image of the sample. If the electron gun can generate a small enough beam, the objective lens can be eliminated from the SEM. Basically, the magnification in SEM is controlled by the ratio of the dimensions of the raster on the sample and the raster on the display monitor.

To be scanned in a SEM, the sample has to be electrically conductive or at least the scanned surface needs to be conductive. When scanned by the electron beam, non-conductive samples are likely to exhibit “charging” effects. This will result in poor images. Therefore, for nonconductive samples, the surface has to be coated with an electrically conductive material, such as by sputter-coating with gold. Sometimes, even conductive samples need to be gold coated to obtain higher quality images of the surface.

In this study, SEM can help to better understand the morphology of the corrosion products at different test conditions by giving a visual image of the sample surface.

2.2 Energy-dispersive X-ray spectroscopy (EDX)

Energy-dispersive X-ray spectroscopy, usually shortened to EDX or EDS, is an analytical tool used to identify the elements in the test sample. It is commonly used in conjunction with SEM, so that a visual image and an elemental analysis can be compared. This can provide local compositional information unavailable by a bulk chemical analysis method.

During the measurement, a high energy beam of charged particles such as electrons bombard the sample surface. These displace inner shell electrons from around the nuclei of the atoms being analyzed. Outer shell electrons then fall to fill the now vacancy lower energy site, emitting a characteristic X-ray for the transition specific to the element involved. By analyzing the resultant sample emission spectrum, data on the elemental composition of the sample is obtained. Figure 2 shows an example of data from EDX analysis²⁹. This method follows a principle that each element has an exclusive atomic structure corresponding to a unique X-ray emission spectrum, allowing each

element to be identified. In addition to this qualitative analysis, EDS can also perform quantitative analysis by comparing the elemental peak areas of the sample and versus those for calibration standards.

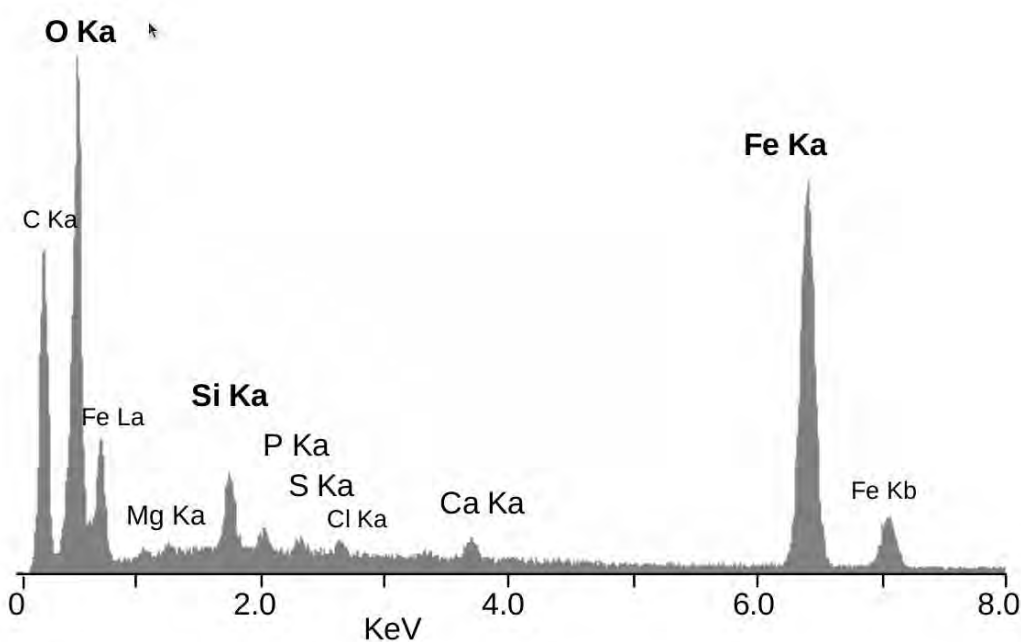


Figure 2. EDX spectrum of the mineral crust of *Rimicaris exoculata*²⁹.

The accuracy of the EDX measurement depends on many factors. EDX detectors cannot detect H, He and Li, elements with atomic number less than 4, and has poor accuracy for elements lighter than Na. Emission spectra from these elements will be at low energy, the windows in front of the detectors can absorb such low energy X-rays³⁰. Many elements (Ti K_{β} and V K_{α} , Mn K_{β} and Fe K_{α}) have overlapped peaks in their emission spectra, which sometimes make it difficult for EDS to differentiate between particular elements, especially when the analyzed sample is compositionally complex.

The elemental analysis provided by EDX can help to determine the composition of the corrosion products, especially if they are amorphous.

2.3 X-ray diffraction (XRD)

X-ray diffraction (XRD) is a non-destructive technique which is able to provide information about chemical composition, physical properties and the crystallographic structure of a test specimen (thin layer or crystalline particles). Different from EDS, the XRD can identify the crystal structure and phase identity of the test sample.

During the measurement, the XRD instrument generates an X-ray beam that is imposed on the sample from different angles. When X-rays pass through the crystalline sample, the X-rays are diffracted by the sample due to the unique crystal structure. Each crystal structure has its own unique X-ray diffraction pattern. Therefore, comparing the XRD results of an unknown compound with the standard XRD database can determine the phase identity, and additional compositional information, of the unknown sample. Figure 3 shows an example of the standard XRD data for mackinawite, which is often seen in the products of H₂S corrosion.

In this research, XRD was used to identify the composition of the corrosion product layers in sour systems, mainly the different types of iron sulfide layers. However, to get reliable XRD data, products have to be crystalline.

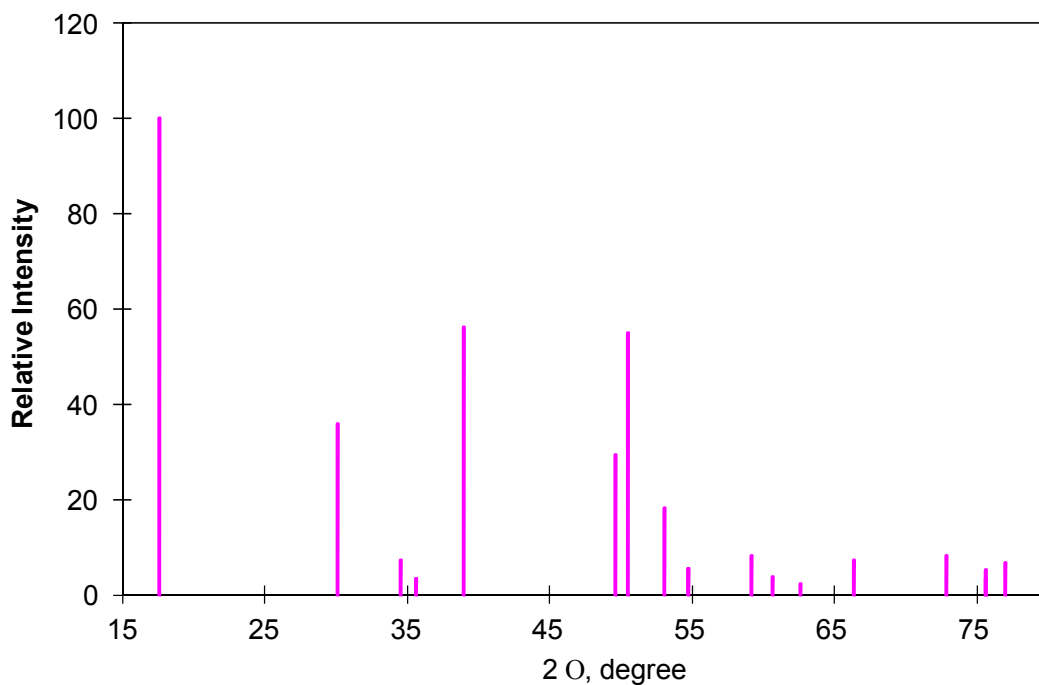


Figure 3. Standard XRD data for Mackinawite.

2.4 Infinite focus light microscopy (IFM)

The infinite focus light microscope (IFM) is a new type of digital optical microscope, which is capable of measuring surface profiles, roughness, depth, *etc.* It can also generate the 3D topographical images for analysis and measurement as shown in Figure 4³¹.

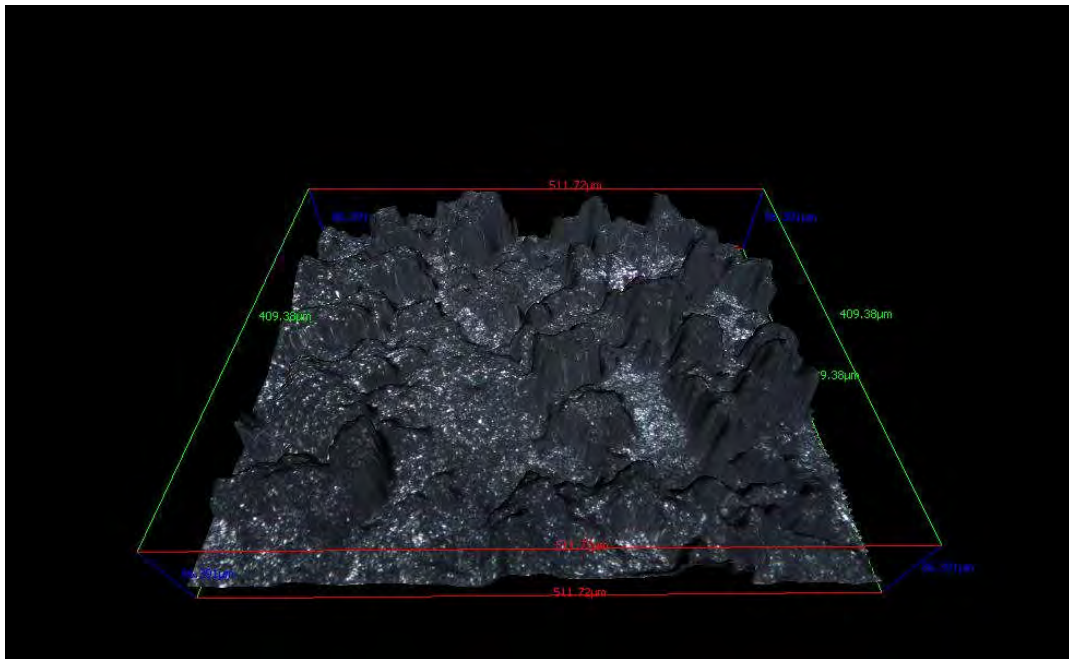


Figure 4. A 3D image of steel surface with iron sulfide by IFM³¹.

Different from the conventional optical microscope, during the measurement, the InfiniteFocus - light Microscope is able to vary the working distance into different in-focus planes on the specimen surface. By doing this, a stack of images are captured. Then the image processing software constructs the image with all the information including the surface profile, roughness, depth, etc. IFM can also control an artificial light source to effectively illuminate the whole sample surface area being scanned.

In this project, IFM was used to measure the depth of localized corrosion attack. The depth was then converted to the localized corrosion rate.

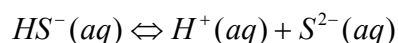
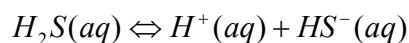
CHAPTER 3 HIGH CHLORIDE CONCENTRATION EFFECTS ON LOCALIZED H₂S CORROSION

3.1 Literature review

3.1.1 Hydrogen sulfide

Hydrogen sulfide is a chemical compound that naturally occurs in the environment, such as in sewers, bogs, volcanic gas, natural gas and some well waters. It often results from thermochemical processes as well as the digestion and metabolism of sulfur-containing materials by bacteria³².

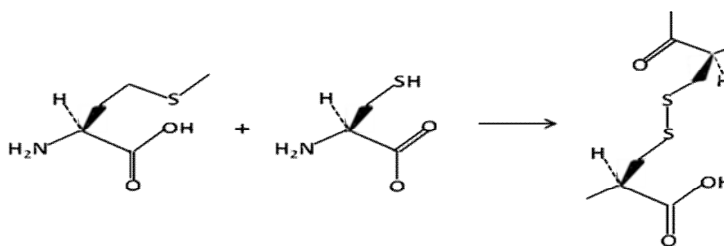
The molecular formula of hydrogen sulfide is H₂S. It is a colorless, flammable and extremely toxic gas. H₂S is soluble in water and forms a weak acid called sulfhydic acid or hydrosulfuric acid, which dissociates to bisulfide and sulfide ions in two steps. Each step generates one hydrogen ion:



H₂S gas issues can be related to the oil and gas industry, because it is a naturally occurring component of crude oil and natural gas. Crude oil and natural gas were produced over long periods of time during the process of the thermal conversion of organic substances, which are called kerogen; it is usually locked in sedimentary rocks. If kerogen contains high sulfur content, it will release H₂S during the process of its decomposition. H₂S is then trapped in the oil and natural gas deposit³³.

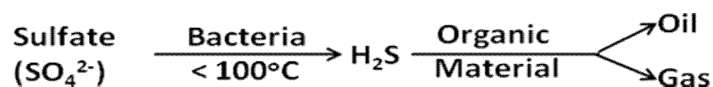
H_2S is released in three different pathways in oil and gas³⁴: sulfur combined in “living precursor material”, microbial reduction of sulfates and thermochemical sulfate reduction. The processes are illustrated in the following equations:

Sulfur combined in “living precursor material”:

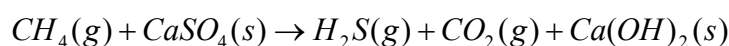


Such organosulfur compounds then decompose to form H_2S .

Microbial reduction of sulfates:



Thermochemical sulfate reduction:



This can occur with higher alkanes as well as methane.

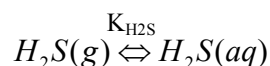
H_2S is a significant impurity of produced oil and natural gas³⁵. According to the Environmental Protection Agency (EPA) standard, if the concentration of H_2S in natural gas exceeds 5.7 milligrams per normal cubic meter, it is considered to be sour³⁶. It has been reported that 15% to 25% of natural gas in the United States may contain H_2S . Worldwide, this number could be as high as 30%. Sour well production may continually increase because new drilling is increasingly focusing on deep gas production which

tends to be sour³⁷. Consequently, H₂S corrosion has become a major issue in the oil and gas industry.

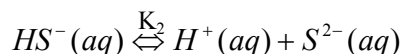
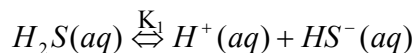
3.1.2 H₂S corrosion

As mentioned above, H₂S corrosion, or “sour corrosion”, of carbon steel has become a major problem encountered in the oil and gas industry since more sour oil and gas wells are now in production. The mechanism of general and localized H₂S corrosion has been debated by the researchers through the past decades, and still remains unclear.

The water chemistry of H₂S is important for understanding the mechanism of H₂S corrosion. When H₂S is dissolved in water, a vapor-liquid equilibrium is established:



The dissolved H₂S partially dissociates into bisulfide and sulfide in two steps:



Many studies³⁸⁻⁴³ have been performed to investigate the thermodynamics of H₂S water chemistry. The expressions of the equilibrium constants of K_{H_2S} proposed by different researchers vary, but all are dependent on temperature. The equation for the H₂S solubility constant K_{H_2S} proposed by Weiss³⁹ is shown below:

$$K_{H_2S} = e^{-41.0563 + 66.4005\left(\frac{100}{T_K}\right) + 15.1060 \ln\left(\frac{T_K}{100}\right)}$$

This successfully fits the extensive experimental data provided by Douabul and Riley⁴⁴ later reported in 1979.

Similar to the H₂S solubility constant K_{H_2S} , the first dissociation constant of K_1 at room temperature also has various values as reported by different researchers⁴⁵⁻⁵⁴. Values lie in a narrow range at the same order of magnitude within $(1.0 \pm 0.1) \times 10^{-7}$. The equation for K_1 at different temperatures proposed by Suleimenov and Seward in 1997⁴³ was widely accepted and used for calculations in H₂S system by other researchers:

$$K_1 = 10^{782.43945 + 0.36126T_K - 1.6722 \times 10^{-4}T_K^2 - \frac{20565.7315}{T_K} - 142.741722 \ln T_K}$$

The second dissociation constant K_2 also has been reported to have different values by different researchers. The scatter is up to seven orders of magnitude.

Unlike carbon dioxide corrosion, H₂S corrosion always involves the formation of corrosion products that are predominantly iron sulfide. The formation of the iron sulfide generally controls the corrosion rate. However, there is still debate on how the initial corrosion product layers form.

It is well known that the corrosion rate of carbon steel immediately decreases after a small concentration of H₂S is introduced into the system. The cause of the decrease of corrosion rate is believed to be due to the fast formation of a mackinawite-type iron sulfide layer. Shoesmith, *et al.*, proposed that the first layer of mackinawite is generated by a direct, solid-state reaction between the steel surface and H₂S^{55,56}. Mackinawite then grows with time. The corrosion product layer growth rate depends upon the corrosion rate as well as the water chemistry with regards to pH, temperature, etc. Sun and Nescic studied the mechanism of general H₂S corrosion in 2007⁵⁷. It has been found that when the thickness of iron sulfide reaches a critical value, this corrosion product layer cracks due to the development of internal stresses. More corrosive species

such as H₂S or hydrogen ion diffuse through the now porous iron sulfide layer and attack the steel surface. More iron sulfide is then formed either by solid-state reaction between steel and H₂S, akin to what happened initially, or precipitation of iron sulfide due to local FeS supersaturation. This direct, solid-state reaction theory is supported by other researchers^{58,59}.

Another possible mechanism for iron sulfide formation is that the iron sulfide layer is formed only by precipitation of iron sulfide when its concentration reaches the solubility limit, analogous to how precipitation equilibrium governs the mechanism of iron carbonate formation. However, if this is to be true, the kinetics of iron sulfide formation must be much faster than that for iron carbonate. In cases where iron sulfide is highly under-saturated in the bulk, it still can be formed on the steel surface. This is suspected to be due to the high surface pH caused by consumption of hydronium ions by corrosion as well as locally high ferrous ion concentration, which results in a supersaturation of iron sulfide on the steel surface. Therefore, iron sulfide forms relatively fast on the steel surface, irrespective of the bulk conditions.

How iron sulfide forms in the first place is important, because it can help to better predict the H₂S corrosion. However, until now research efforts have not achieved agreement on this subject, which is the focus of ongoing work in the Institute for Corrosion and Multiphase Technology (ICMT).

The situation is complicated by the variety of iron sulfide types which can be formed depending on the conditions relating to the corrosion environments: mackinawite,

pyrrhotite, greigite, smythite, marcasite and pyrite are the six naturally occurring iron sulfide minerals²⁷.

3.1.2.1 Mackinawite

Mackinawite has been typically reported to be a sulfur deficient iron sulfide with a formula Fe_{1+x}S , where $x = 0.057$ to 0.064 ²⁷. This reported non-stoichiometry is likely an artifact relating to chemical analysis, with its actual formula being FeS ²⁷. Mackinawite is a two dimensional layer structure consisting of stacked FeS sheets, see Figure 5. Thermodynamically, mackinawite is unstable compared with other iron sulfide minerals, such as pyrrhotite⁶⁰. It has been found that mackinawite is converted to greigite, marcasite and pyrite by reaction with sulfur²⁷. In low H_2S concentration environments, the first iron sulfide corrosion product is usually mackinawite²⁷.

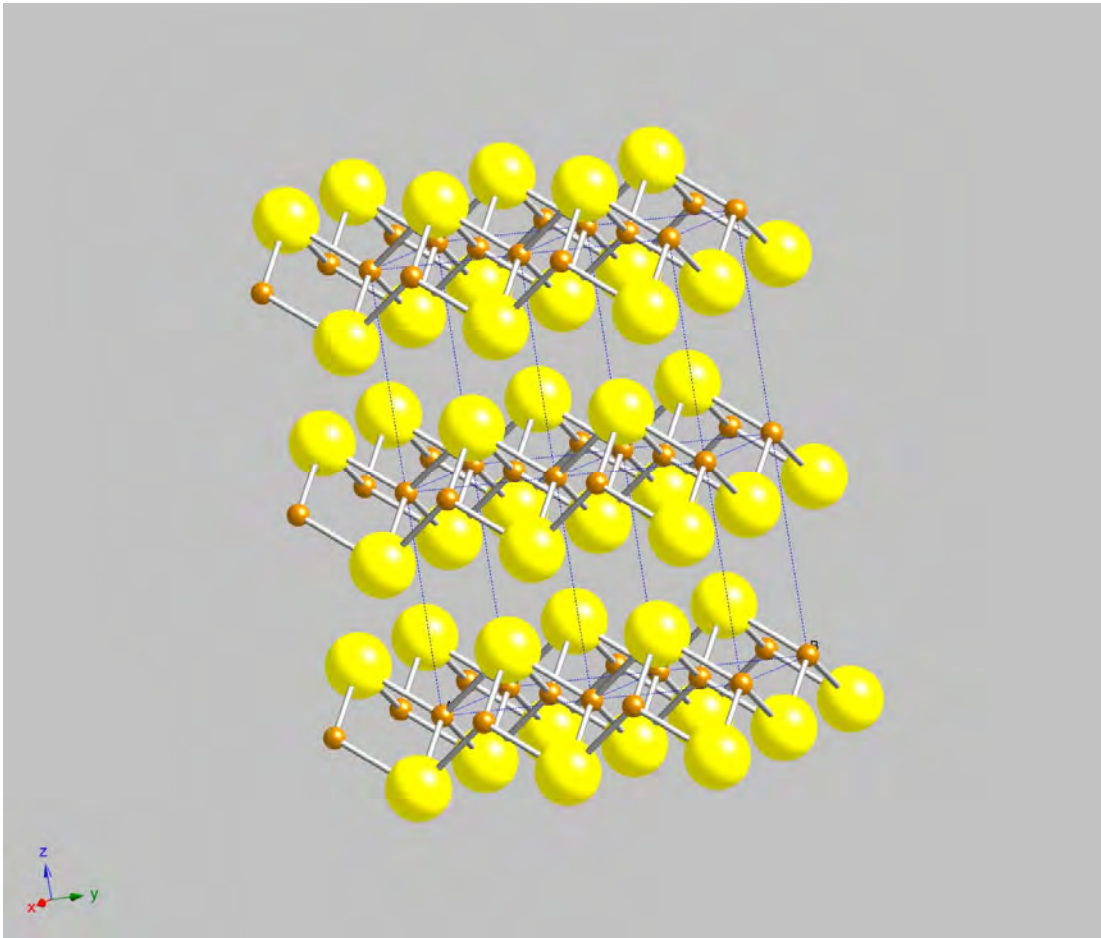


Figure 5. Crystal structure of mackinawite (generated with Crystallmaker™ software).

3.1.2.2 Pyrrhotite

Pyrrhotite is another non-stoichiometric iron sulfide – this time iron deficient, with a composition range from Fe_7S_8 to FeS (which is called troilite)^{61,62}.

3.1.2.3 Smythite

Smythite is an iron sulfide mineral morphologically and structurally similar to pyrrhotite and troilite (hexagonal pyrrhotite²⁷), but more iron deficient. Similar to greigite,

smythite has been reported to be strongly ferromagnetic⁶³. Smythite can be converted to pyrrhotite at high temperatures²⁷.

3.1.2.4 Greigite

Greigite is another type of naturally occurring iron sulfide with the formula Fe_3S_4 . It was named after the mineralogist and physical chemist Joseph W. Greig in 1964. Greigite is ferromagnetic and semiconductive^{60,64,65}. Greigite is isostructural with magnetite (Fe_3O_4). Greigite has been identified as a corrosion product of steel in the presence of H_2S ²⁷.

3.1.2.5 Marcasite

Marcasite is an orthorhombic ferrous disulfide²⁷ with formula FeS_2 . It has also been called “white iron pyrite” due to it having the same formula as pyrite. The crystal structure of marcasite is not stable, so it tends to undergo transformations to other phases.

3.1.2.6 Pyrite

Pyrite has the same formula as marcasite, FeS_2 , but a cubic crystal structure. It is also called “fool’s gold” due to its similar appearance. Pyrite is the most common iron sulfide mineral because of its stable structure. Pyrite can especially be found in corrosion products when sulfur is present.

As mentioned above, due to the formation of the iron sulfide layers, the corrosion rate decreases after H_2S is introduced into the system. Therefore, general corrosion due to H_2S is not a big concern for oil and gas industry. On the contrary, localized corrosion (pitting corrosion) is one of the least understood and thorniest corrosion problems encountered by oil and gas industry^{66,67}.

It has been argued above that localized corrosion in sour systems occur after protective layers are partially removed, which allegedly generates permanent anodic and cathodic sites on the steel surface. A number of laboratory studies and field observations on localized corrosion in sour systems have been reported in the past⁶⁸⁻⁷⁶. According to these studies, the initiation of localized sour corrosion has been contributed to by intense flow, temperature, under deposit effects, chloride ion, elemental sulfur and other chemicals (such as corrosion inhibitors).

Chloride ion was suspected to be the most possible cause of localized corrosion due to its bad reputation in stainless steel corrosion. A great deal of research has been conducted on the effects of the chloride ion on the pitting corrosion of stainless steel⁷⁷⁻⁸². It has been found that the chloride ion can lead to a breakdown of the passive layer by generating a local acid environment on the surface of stainless steel. Lending support to this scenario, localized corrosion of carbon steel in sour systems was found in systems where high concentration of chloride was present²¹. Therefore, the chloride ion was hypothesized to be the direct cause of initiation of localized corrosion of carbon steel in sour systems. However, no systematic laboratory studies of chloride effects on localized H₂S corrosion have been performed. While one can accept that an empirical correlation between the presence of chlorides and localized corrosion in sour systems has been established, in order to clarify if there is a true causative effect, more systematic laboratory studies are necessary. Part of the research work described below has been published in 2011⁸³.

3.2 Research objectives and test matrices

3.2.1 Research objectives

Based on the field experiences and research literature, the effects of high chloride concentration on localized H₂S corrosion is set to be first parameter investigated in this study. The objective of this research direction is to answer the following questions:

1. How does the presence of a high concentration of chloride ions affect the general H₂S corrosion of carbon steel?
2. Will the presence of a high content of chloride ions initiate localized corrosion in sour systems?
3. If the initiation of localized corrosion is detected in the presence of chloride ions, what is the mechanism?
4. How can this effect be modeled?

3.2.2 Test matrices

To address the above questions, the test matrix was defined as shown in Table 1:

Table 1. Test conditions for chloride effects on H₂S corrosion

Parameters	Conditions
Total pressure	1 bar, 2 bar
H₂S concentration/pressure in the gas phase	low: 50 ppm ($P_{\text{H}_2\text{S}} = 0.05 \text{ mbar}$ at $P_{\text{total}} = 1 \text{ bar}$) and high: 50% ($P_{\text{H}_2\text{S}} = 1 \text{ bar}$, $P_{\text{total}} = 2 \text{ bar}$)
Temperature	25°C, 80°C
Solution	NaCl at 0 wt.%, 1 wt.%, 10 wt.%, 20 wt.%
pH	5.0
Material	C1018

It has to be mentioned that the test conditions were determined at the beginning of the study, prior to initial data collection and analysis. The test conditions covered a large range of chloride concentration (from 0 to 20 wt.%), low and high H₂S concentrations, and low and high temperatures. However, not all the permutations in this test matrix were conducted as certain test conditions were deemed redundant after more experimental evidence was revealed during the study.

3.3 Experimental setup and test procedure

3.3.1 Specimen preparation

One type of carbon steel (C1018) was used for weight loss and surface analysis. The chemical composition of the carbon steel used in the experiment is shown in Table 2.

Table 2. Chemical composition of C1018 carbon steel (wt.%)

C	Si	P	S	Mn	Al	Fe
0.21	0.38	0.09	0.05	0.05	0.01	balance

The specimen was polished by silicon carbide sand paper before it was tested, with the grit number in the following order: 240, 400, 600; this was done using a polishing wheel. During the polishing process, water was applied onto the specimen surface to cool the sample. After polishing, the specimen was immersed in isopropyl alcohol in an ultrasonic cleaner for 1 to 2 minutes and then air dried.

3.3.2 Experimental setup

For low concentration of H₂S (50 ppm / 0.05 mbar H₂S at 1 bar total pressure), the experiments were conducted in a glass cell. The whole experimental set up is shown in Figure 6. A cylinder containing mixed nitrogen and approximately 500 ppm H₂S gas was used as the source of the H₂S. A second cylinder containing pure nitrogen was used to dilute the H₂S concentration from the source with a gas mixing rotameter. Before the gas was bubbled into test solutions, the H₂S concentration in the gas phase was measured with a H₂S colorimetric detector tube. The H₂S off-gas was absorbed with a high alkalinity H₂S scrubber that utilized calcium hydroxide.

Experiments were performed in a glass cell filled with 2 liters of deionized water or electrolyte with a NaCl concentration of 10 wt. %. Henceforth, these systems will be referred to as 0 and 10 wt. % NaCl. Initially, the test cell was deoxygenated by purging with nitrogen. After that, H₂S gas of a defined concentration was added. The temperature was controlled by a hot plate with a thermocouple. The pH was adjusted to 5.0 by addition of deoxygenated hydrochloric acid.

Three sets of specimens were placed into the test solutions. A single set is comprised of three specimens. Two specimens were used for weight loss measurement and surface analysis. The third one was used for X-ray diffraction (XRD) analysis. After one set of specimens was removed after a certain period of time, another new set of specimens was put back into the test solution. Corrosion product layers were analyzed by scanning electron microscopy (SEM) and energy dispersive X-ray analysis (EDX).

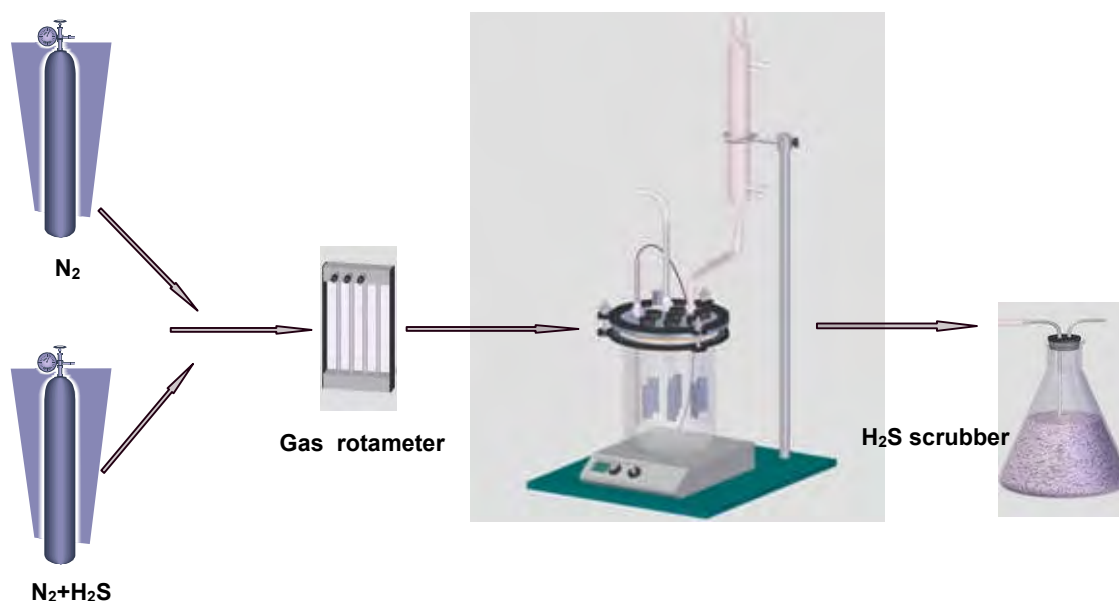


Figure 6. Experimental set up for low pressure H₂S concentration condition.

For the experiments at high partial pressure of H₂S, the tests were conducted in a set of autoclaves. Figure 7 shows the actual picture of the overall view of the experimental setup. The main components of the setup are the three autoclaves with surrounding heating elements. Temperature was controlled by a digital controller. A schematic of the 1 liter autoclave is shown in Figure 8. Stainless steel tubing with a check valve was used to purge the solution. A temperature probe was inserted into the thermal well. Test specimens were hung on the specimen holder and isolated from any galvanic corrosion by heat shrinkable tubing while immersed in the test solution.



Figure 7. Experimental setup for high partial pressure of H₂S.

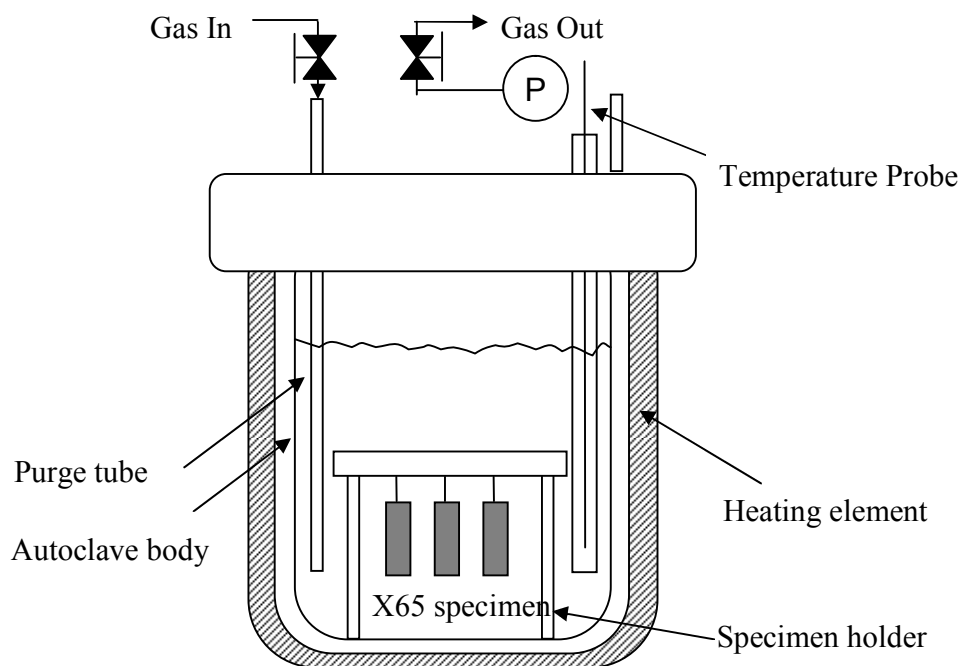


Figure 8. Autoclave schematic

To prepare for this experiment, molar concentrations of each component at operating temperature and pressure were determined with a water chemistry model based on H_2S water chemistry equilibrium in order to prepare a nitrogen purged solution at ambient conditions. The addition of H_2S to an unbuffered solution at 80°C would decrease the pH: pH 4.9 for pH_2S 0.01 bar, pH 4.4 for pH_2S 0.1 bar, and pH 3.9 for pH_2S 1.0 bar. In addition, 800 milliliters of 10 wt.% NaCl solution used in each autoclave was purged overnight with nitrogen. The water chemistry model was used to calculate the amount of deoxygenated sodium hydroxide solution that needed to be added to achieve the desired pH in the autoclave. The test duration was 1 day.

H₂S/N₂ gas mixtures for each autoclave were mixed and stored individually prior to injection separately into each autoclave. The detailed parameters of gas mixing for each H₂S partial pressure are shown in Table 3.

Table 3. Parameters of gas mixing

H ₂ S Partial Pressure	Mixing at ambient temperature		
	P _{total} /psi	P _{N₂} /psi	P _{H₂S} /psi
1 bar	100	35	65
0.1 bar	300	280	19
0.01 bar	300	300	2

Samples were sealed in the autoclaves at ambient conditions and then test conditions were adjusted. After pH adjustment of each autoclave, a set of polished specimens were put into the test autoclaves. Nitrogen was kept purging through the test solution during this process. The temperature controller was set to 80°C. After the temperatures were stabilized at 80°C, the purged gas was changed from nitrogen to the pre-mixed H₂S and N₂ gas mixture. Each autoclave was continuously purged with its H₂S/N₂ gas mixture for three minutes to assure the test solution was saturated by H₂S and then pressurized to 2 bar. Conditions were monitored, but not adjusted during the test. After 7 days, the solutions were purged with nitrogen to remove the H₂S, and the corrosion specimens were taken out.

3.4 Experimental results and discussion

3.4.1 25°C, 50 ppm H₂S (0.05 mbar H₂S at P_{total} 1 bar), 0 wt.% NaCl

Experiments were first conducted at low H₂S concentration (50 ppm) in deionized water, which is referred to as 0 wt.% NaCl (salt free condition). The purpose of this

experimental set was to determine whether the localized corrosion can be initiated in the absence of chloride after carbon steel specimens had been exposed to H₂S environment for an extended period of time. The test duration for the first set of experiment was 12 days. The test specimens were taken out from the test solution at first day, fourth day, sixth day and twelfth day. The results are shown in the following paragraphs.

3.4.1.1 1st day

A fresh polished carbon steel specimen was scanned by SEM before it was exposed to the corrosive environment. A SEM picture of a bare metal surface is shown in Figure 9 for comparison with the surface of corrosion specimens after corrosion. The polishing marks are clearly seen in the SEM image.

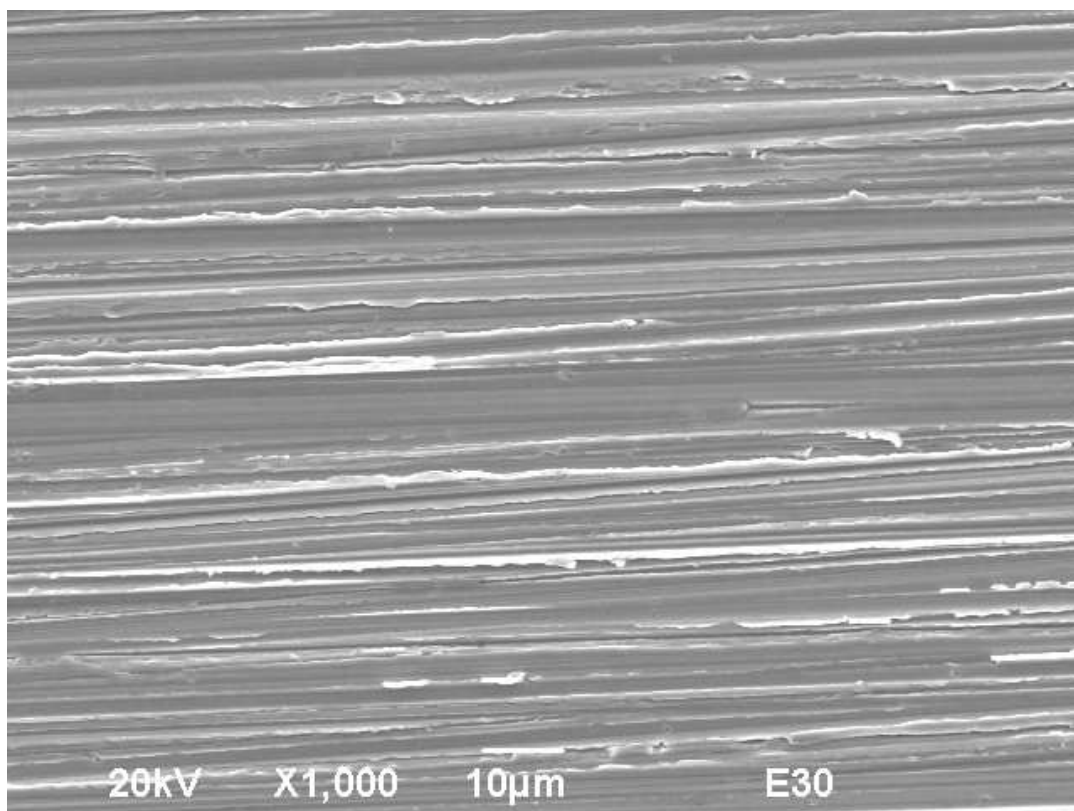


Figure 9. Image of bare steel surface polished by sand paper.

The first set of steel specimens was taken out after 1 day exposure to the test solution. Figure 10 shows the SEM image and EDX spectrum of the specimen surface after a 1 day exposure. It has been observed that a very thin layer of corrosion scale formed on the specimen surface. Polishing marks are still obvious on the surface. This suggests that the corrosion rate is relatively low at this condition. It is also noticed that the scale appears to be fragmented. EDX data show that sulfur and iron are the main components of the scales, consistent with the formation of FeS.



Figure 10. Corrosion specimen exposed to H₂S for 1 day at 0 wt% NaCl, 25°C, with corrosion product layer.

3.4.1.2 4th day

Figure 11 shows the morphology of the iron sulfide scale formed on the specimen surface after 4 days of exposure to H_2S . Compared with the 1 day result, the scale at the 4th day appears to be thicker. However, the layer is still sufficiently thin that the polish marks can be readily observed.

To detect possible localized corrosion on the steel surface, iron sulfide scale was removed by Clarke's solution (2% Sb_2O_3 , 5% $SnCl_2$, in concentrated HCl). The SEM image of the specimen surface after Clarke treatment is shown in Figure 12. The EDX analysis shows that the iron sulfide layer has been removed from the surface. Clearly, the test specimen underwent corrosion attack after four days exposure to H_2S . However the corrosion attack was not significant and appears to be general attack. No initiation of localized corrosion was observed under this condition.

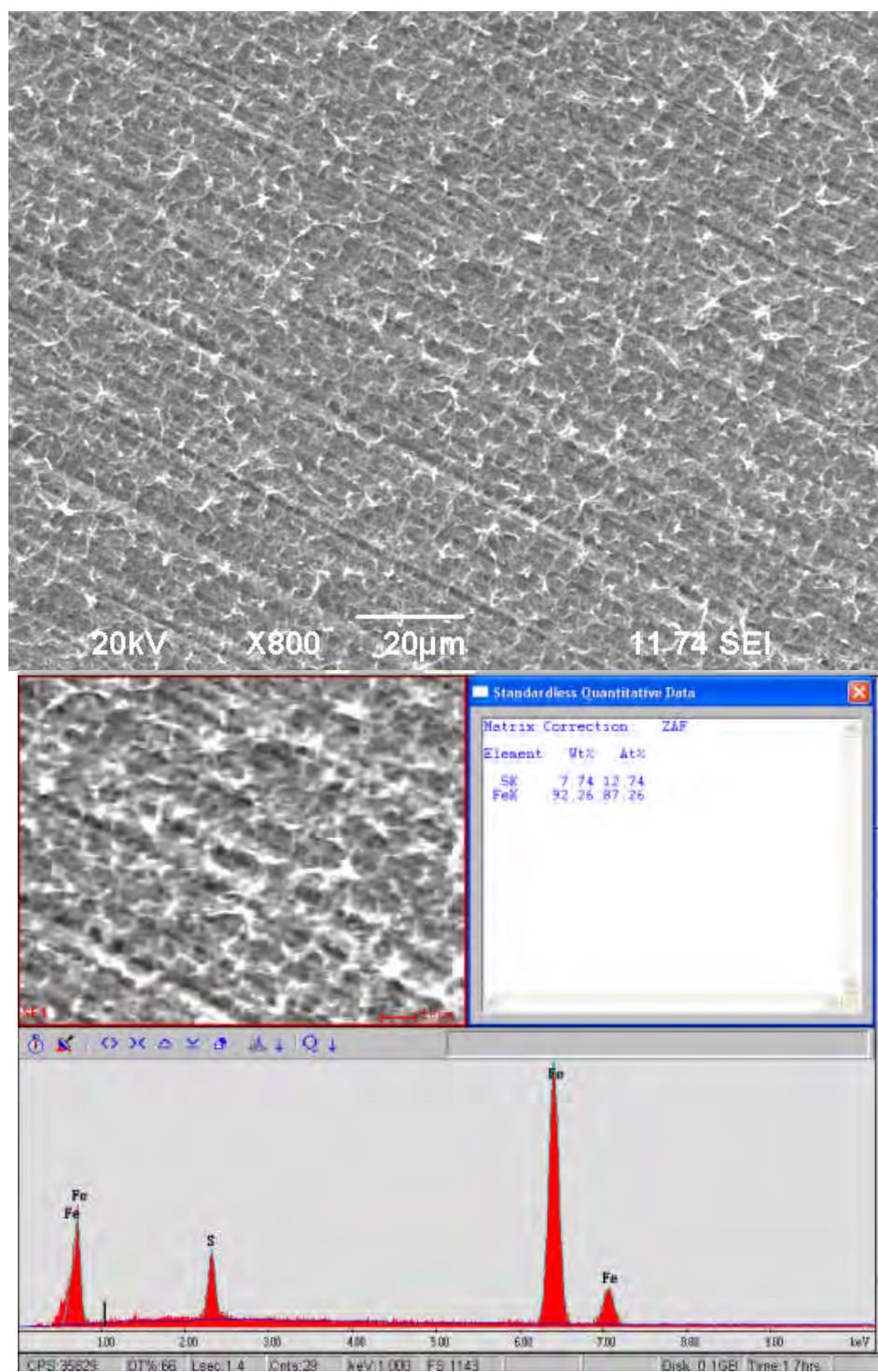


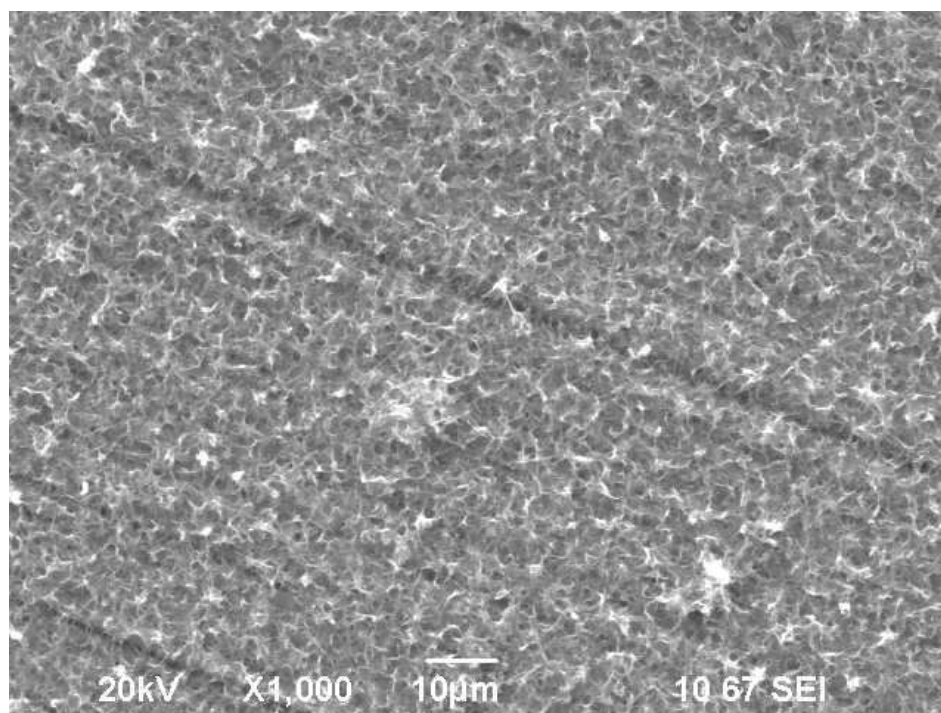
Figure 11. Corrosion specimen exposed to H_2S for 4 days at 0 wt% NaCl, 25°C, with corrosion product layer.



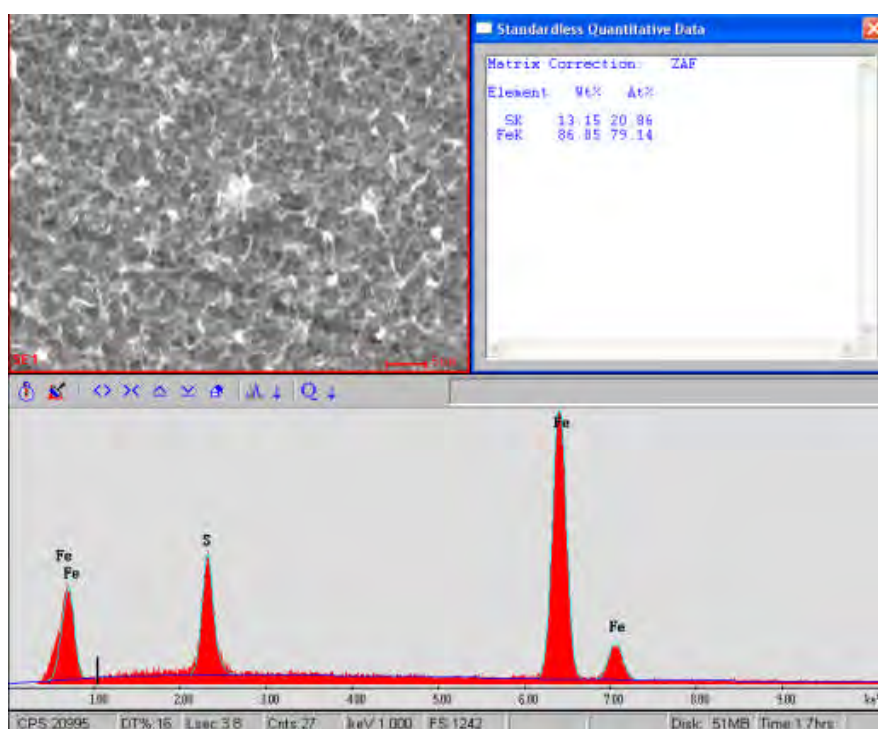
Figure 12. Corrosion specimen exposed to H₂S for 4 days at 0 wt% NaCl, 25°C, without corrosion product layer.

3.4.1.3 6th day

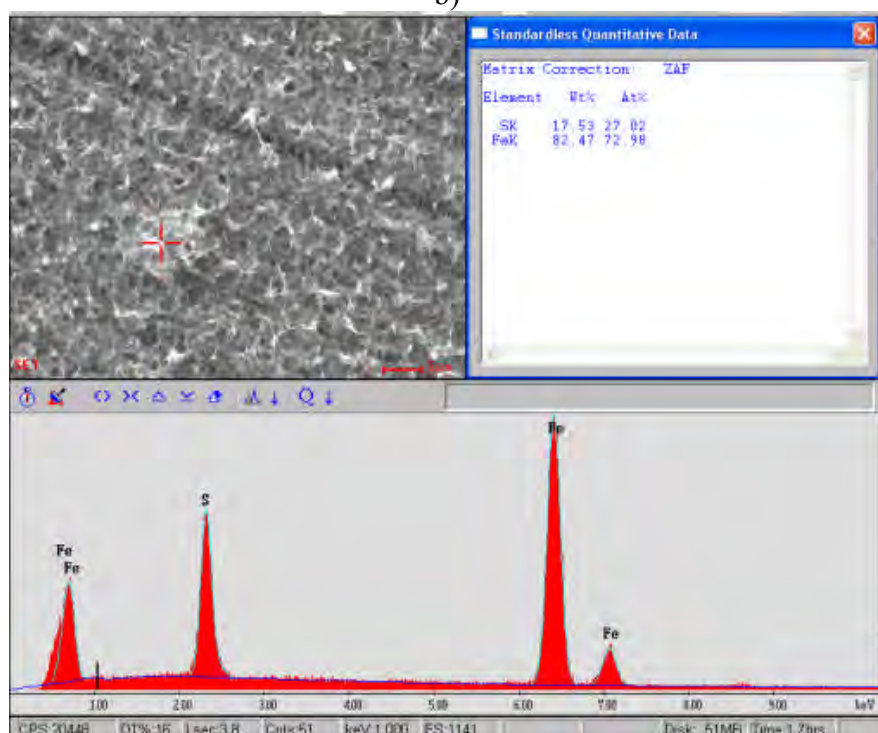
After 6 days exposure to H_2S , iron sulfide layer became much thicker than the layers which formed at the earlier times (Figure 13). In the meantime, a new feature was observed on the iron sulfide scale. Some “bulges” formed on the uniform iron sulfide layer. EDX analysis shows that the iron sulfide content of the balloon scales is much higher than for the rest of the scales. The SEM image of the corrosion product layers suggests that the excess of iron sulfide content may come directly from reaction between H_2S and the metal underneath the uniform FeS scales. This new feature was suspected to show an initiation of localized corrosion.



a)



b)



c)

Figure 13. Corrosion specimen exposed to H_2S for 6 days at 0 wt% NaCl, 25°C, with corrosion product layer.

An SEM image of the specimen surface after corrosion product layer removal is shown in Figure 14. This confirms what was suspected to occur. Several points showing pitting attack were observed on the metal surface. The diameter of these small pits was from 6 μm to 15 μm .

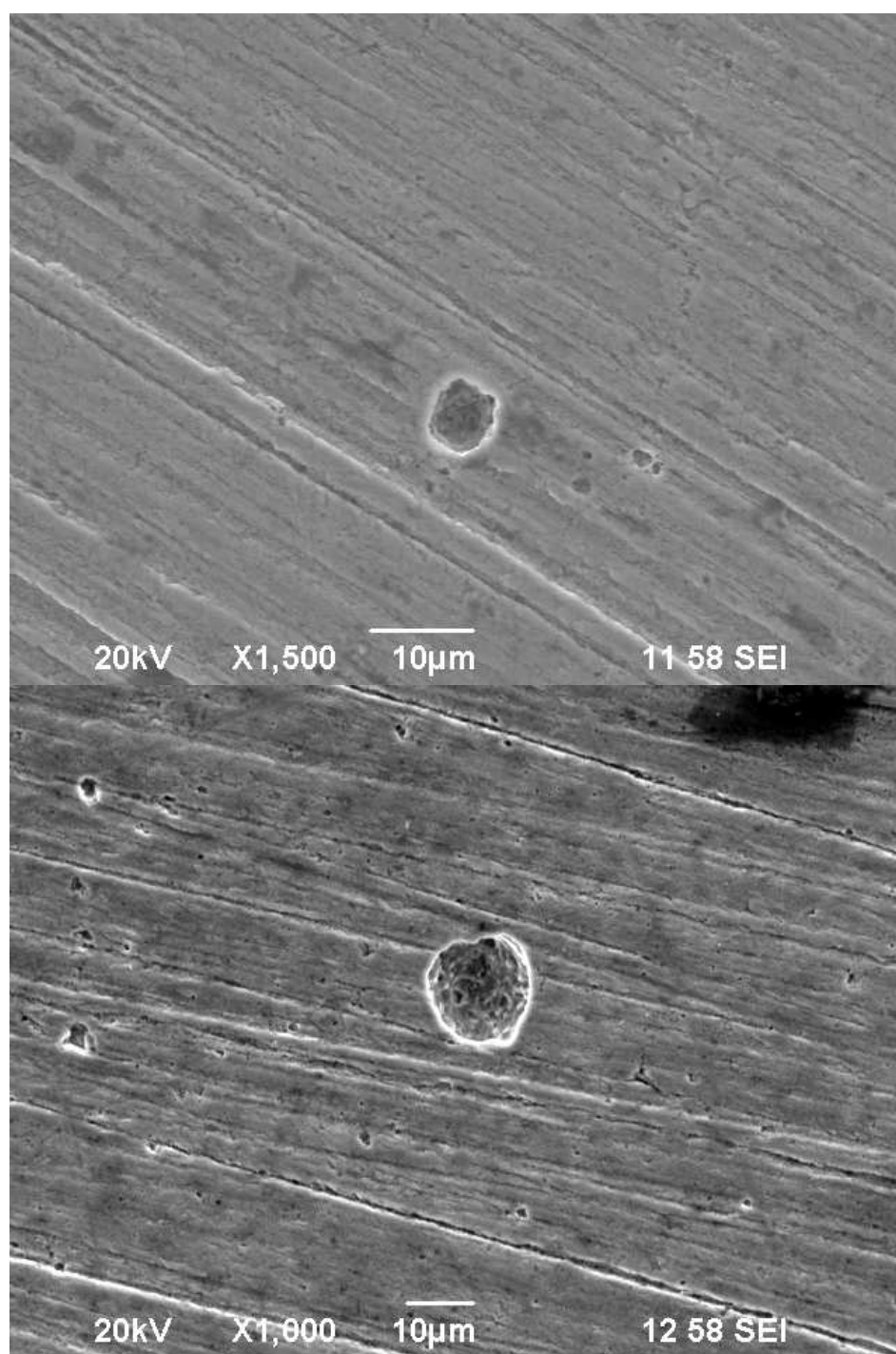


Figure 14. Corrosion specimen exposed to H₂S for 6 days at 0 wt% NaCl, 25°C, without corrosion product layer.

The MEX- 3D reconstruction of SEM Images software was used to analyze the pit depth. Figure 15 shows the 3D view of one pit. The pit depth is around 40 μm and the pitting rate is around 2.4 mm/yr. Compared with the general corrosion rate of 0.017 mm/yr, the localized corrosion rate is over two orders of magnitude higher. The results suggest that even without the aid of chloride ion, localized corrosion was still initiated. The cause for these phenomena must be further investigated.

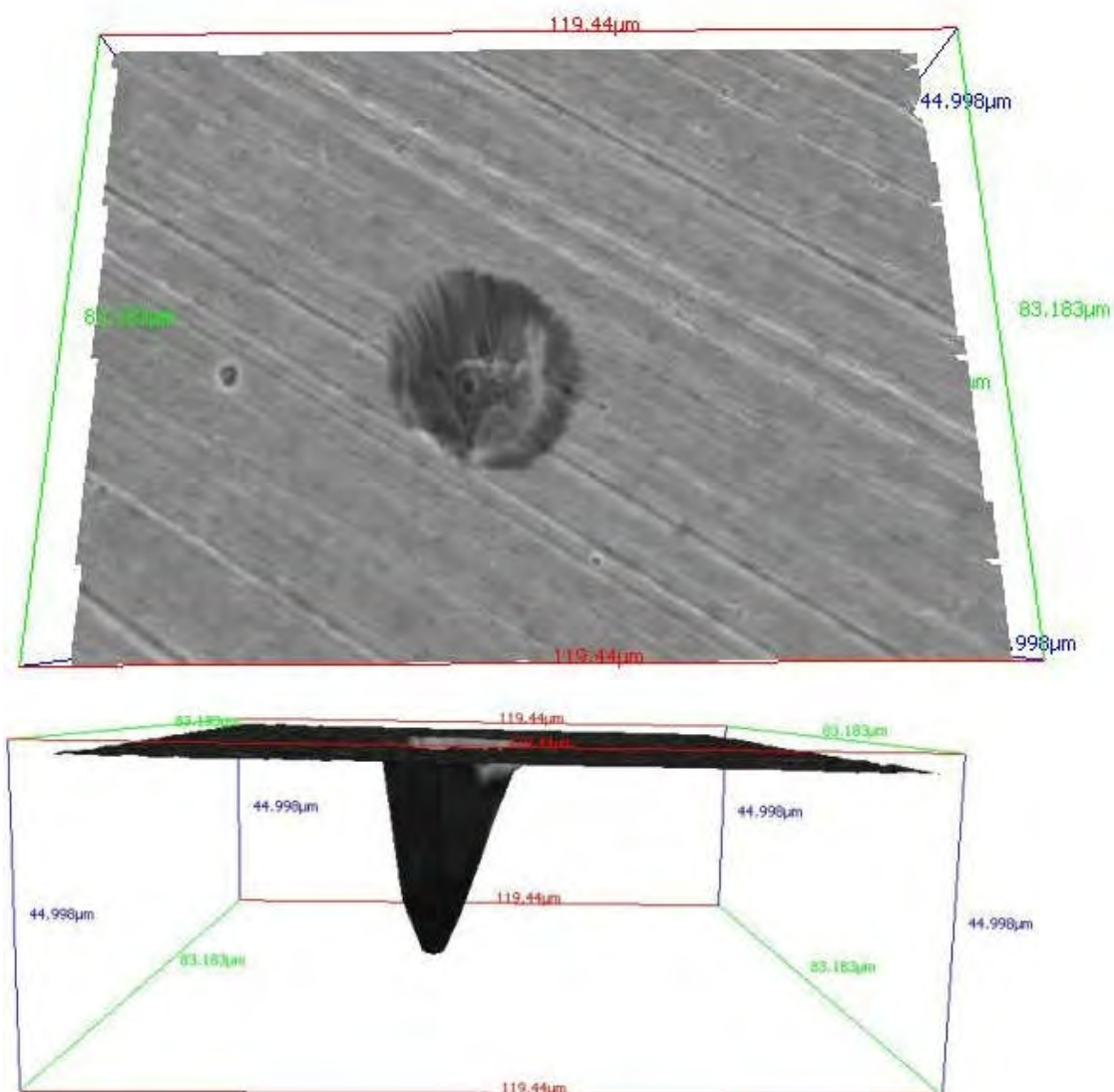


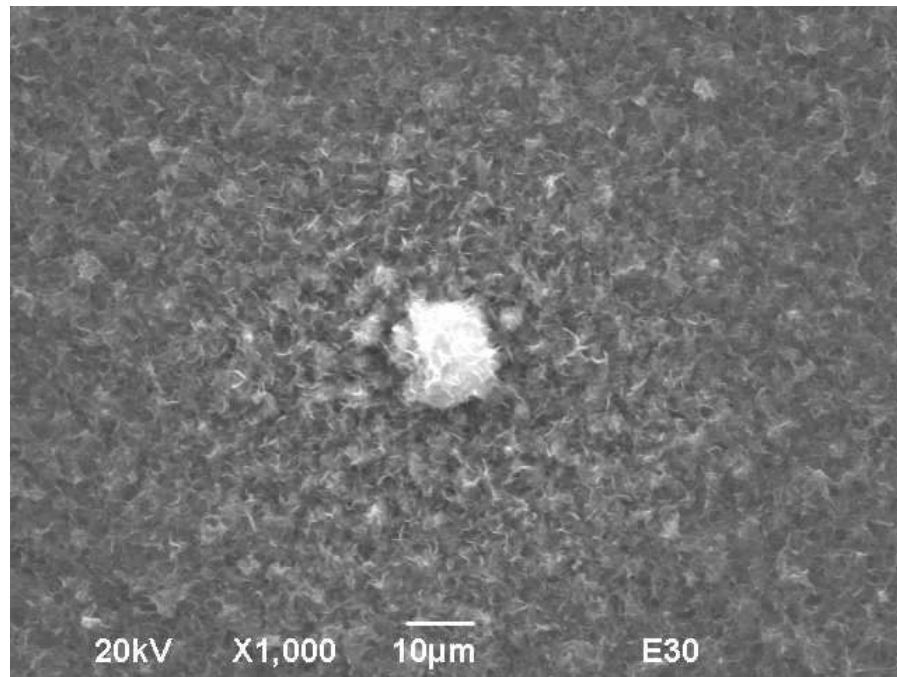
Figure 15. 3D view of corrosion specimen exposed to H_2S for 6 days at 0 wt% NaCl, $25^\circ C$, without corrosion product layer.

3.4.1.4 12th day

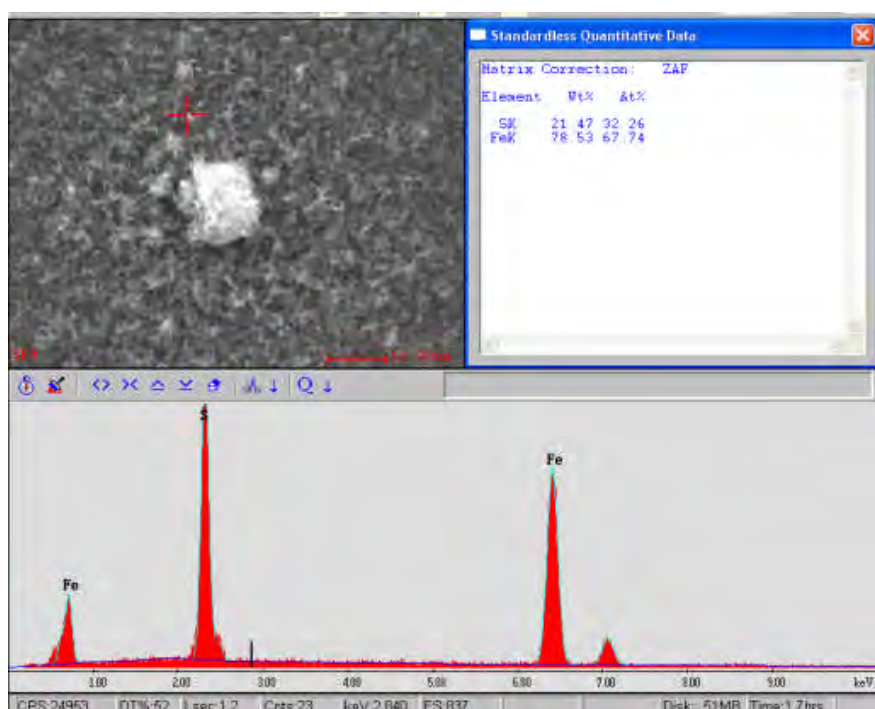
From the SEM image shown in Figure 16, it is clearly seen that the iron sulfide layer kept growing with time. The polishing marks could not be observed on the steel

surface. “Bulges” formed on the iron sulfide surface layer more frequently (Figure 16).

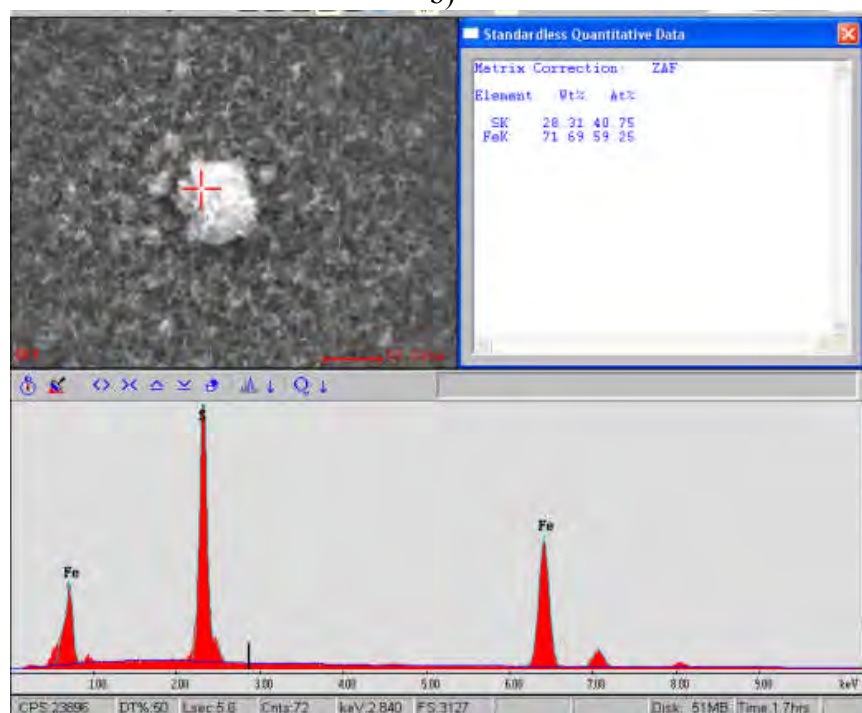
Composition of the iron sulfide “bulge” at 12 days is similar with the one at 6 days.



a)



b)



c)

Figure 16. Corrosion specimen exposed to H_2S for 12 days at 0 wt% NaCl, 25°C, with corrosion product layer.

Pitting corrosion was also observed at 12 days after the specimen surface was revealed by Clarke's solution treatment. The pitting density at 12 days is higher than at 6 days (Figure 17). More and more small pits were observed after the corrosion product layer was removed by Clarke's solution. It appears that pit size did not change with time. The deepest pit depth observed is around 14 μm (Figure 18). This suggested that the pit did not grow with time, which means no propagation of localized corrosion occurred.

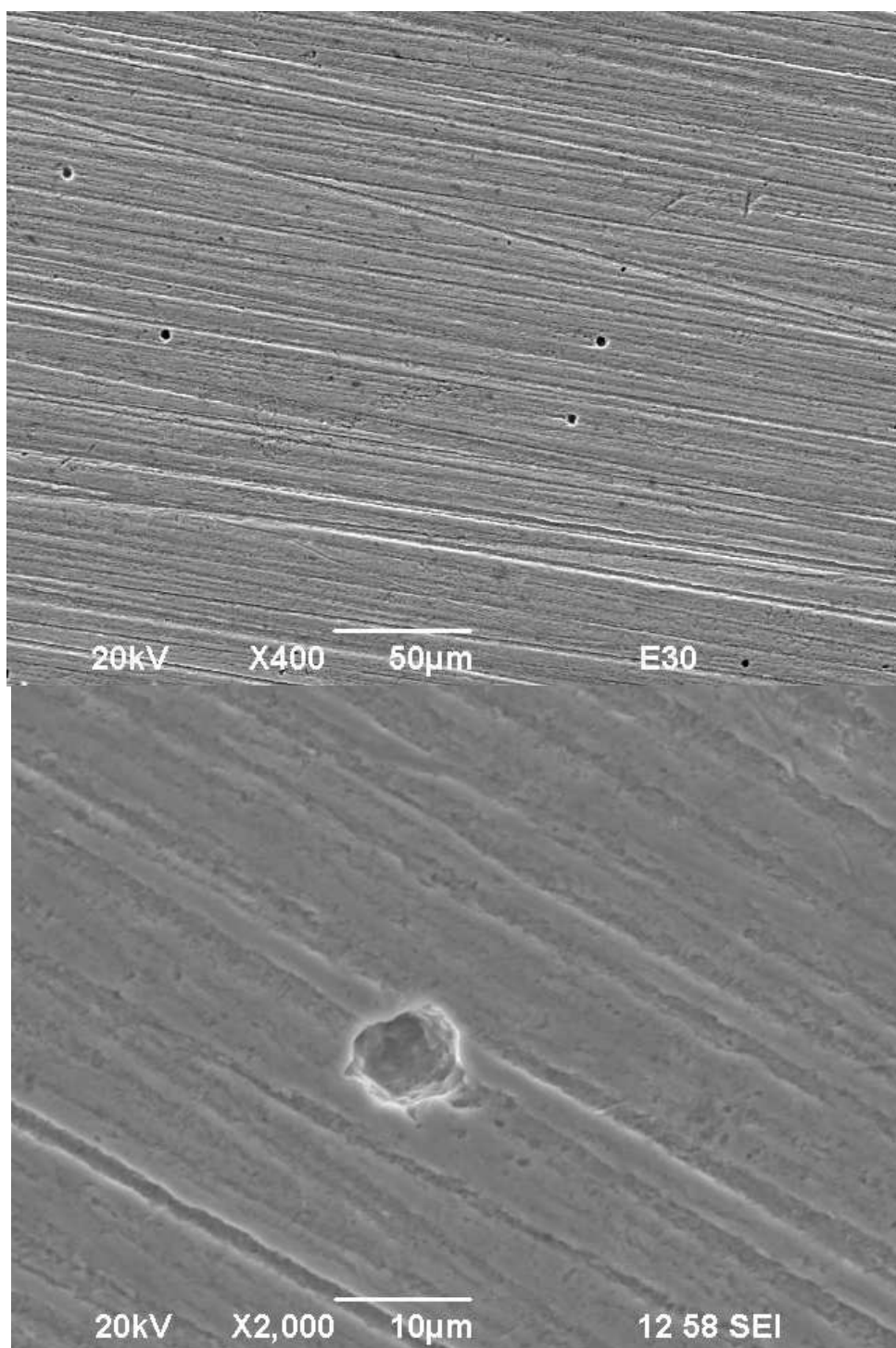


Figure 17. Corrosion specimen exposed to H₂S for 12 days at 0 wt% NaCl, 25°C, without corrosion product layer.

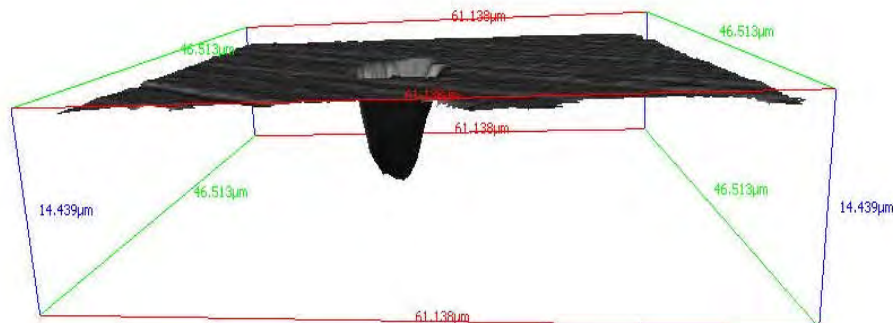


Figure 18. 3D view of corrosion specimen exposed to H₂S for 12 days at 0 wt% NaCl, 25°C, without corrosion product layer.

It is interesting that the localized corrosion was detected at the low H₂S concentration and salt free condition. From the experimental results, it appears that the presence of the chloride ion is not required for the initiation of pitting attack on the steel surface. It is also worth mentioning that the pitting seemed not to propagate with time. Before trying to explain these results, it was decided to investigate what is going to occur to the steel in the presence of a high content of chloride ions. Therefore, 10 wt.% sodium chloride was added into the test solution in the next set of experiments. The results are shown below.

3.4.2 25°C, 50 ppm H₂S (0.05 mbar H₂S at P_{total} 1 bar), 10 wt.% NaCl

To investigate the effect of a high content of chloride ion on the localized H₂S corrosion, 10 wt.% sodium chloride was added into the test solution. The test duration for this experimental set was 26 days. Steel specimens were taken out for analysis at the first day, third day, seventh day, fifteenth day and twenty-sixth day.

3.4.2.1 1st day

The SEM image of the steel specimen surface after one day exposure to H₂S is shown in Figure 19. There is barely any iron sulfide layer formed on the metal surface compared to similar observations in salt-free conditions. This suggests that the addition of a high content of salt significantly slowed down the uniform corrosion rate, which was confirmed by the weight loss measurement (Figure 20). A considerable quantity of sodium chloride is observed in the SEM image, crystallized on the metal surface due to rapid dehydration of alcohol used to dry the steel specimen after exposure. This is apparent as both cubic crystals and dendritic structures on the specimen surface.

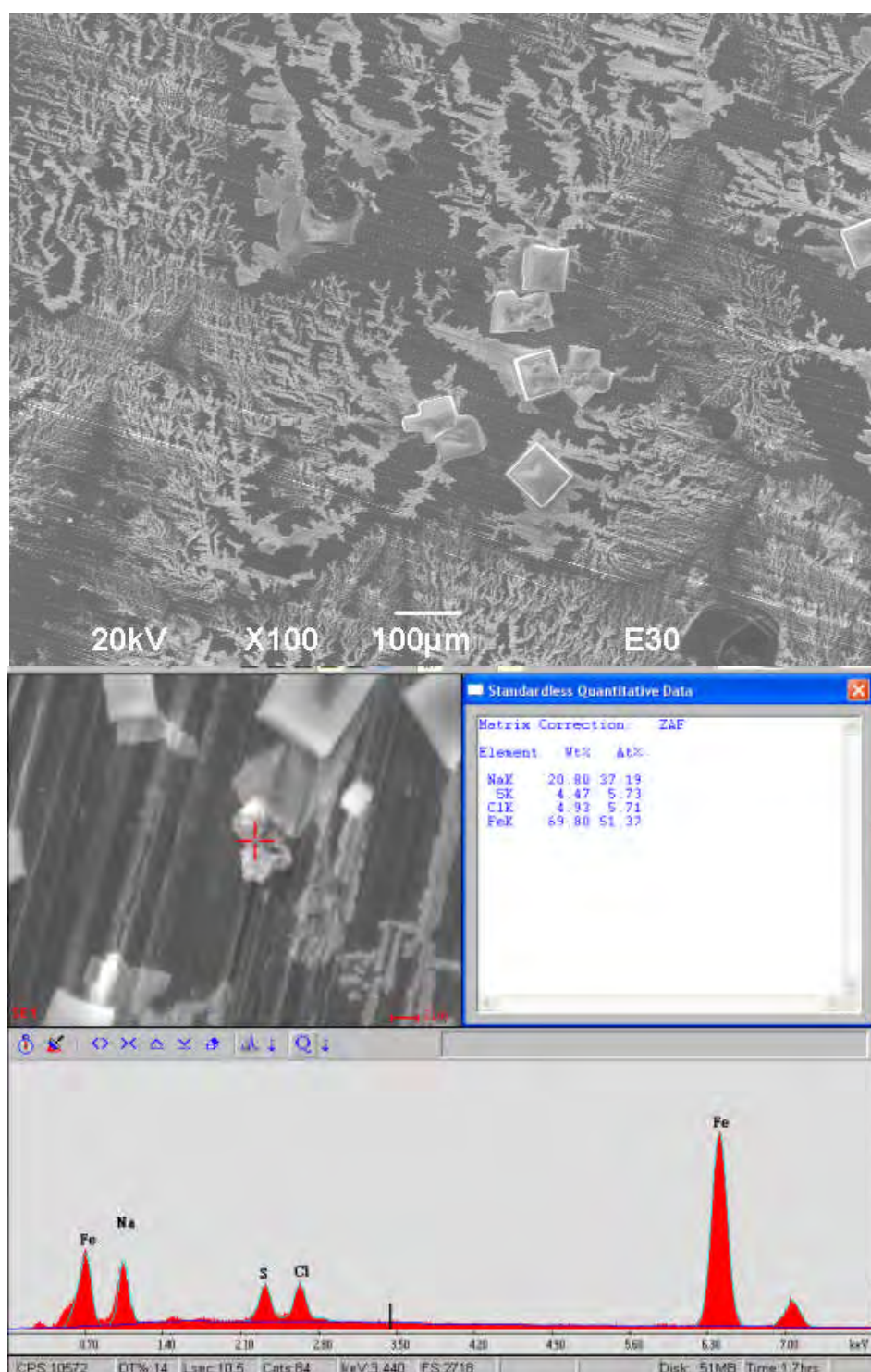


Figure 19. Corrosion specimen exposed to H_2S for 1 days at 10 wt% NaCl, 25°C, with corrosion product layer.

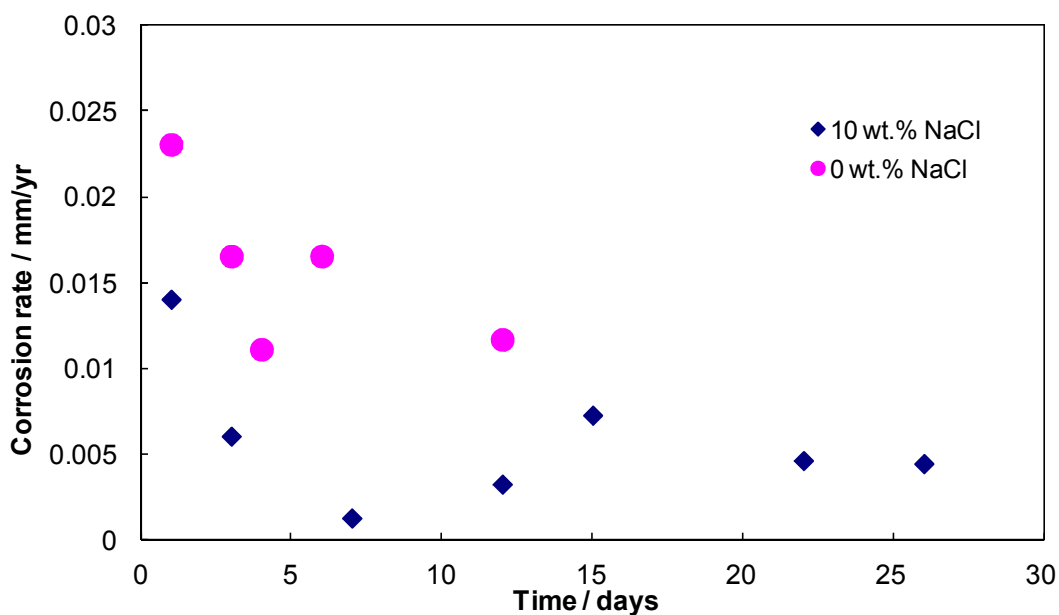


Figure 20. Uniform corrosion rates versus time at 25°C, 50 ppm H₂S, 0 wt% and 10 wt. % NaCl.

3.4.2.2 3 days

In this case, the corrosion specimen was first rinsed with deoxygenated deionized water to remove sodium chloride after retrieval from the glass cell. Therefore, no NaCl crystals were observed on the specimen surface. After three days exposure to H₂S, it appears that most of the specimen surface still showed little corrosion (Figure 21). Small amounts of iron sulfide layer were unevenly distributed on the steel surface. It appears that the addition of chloride ions slowed down the reaction rate between steel and H₂S instead of accelerating the reaction, as was suggested by the literature.

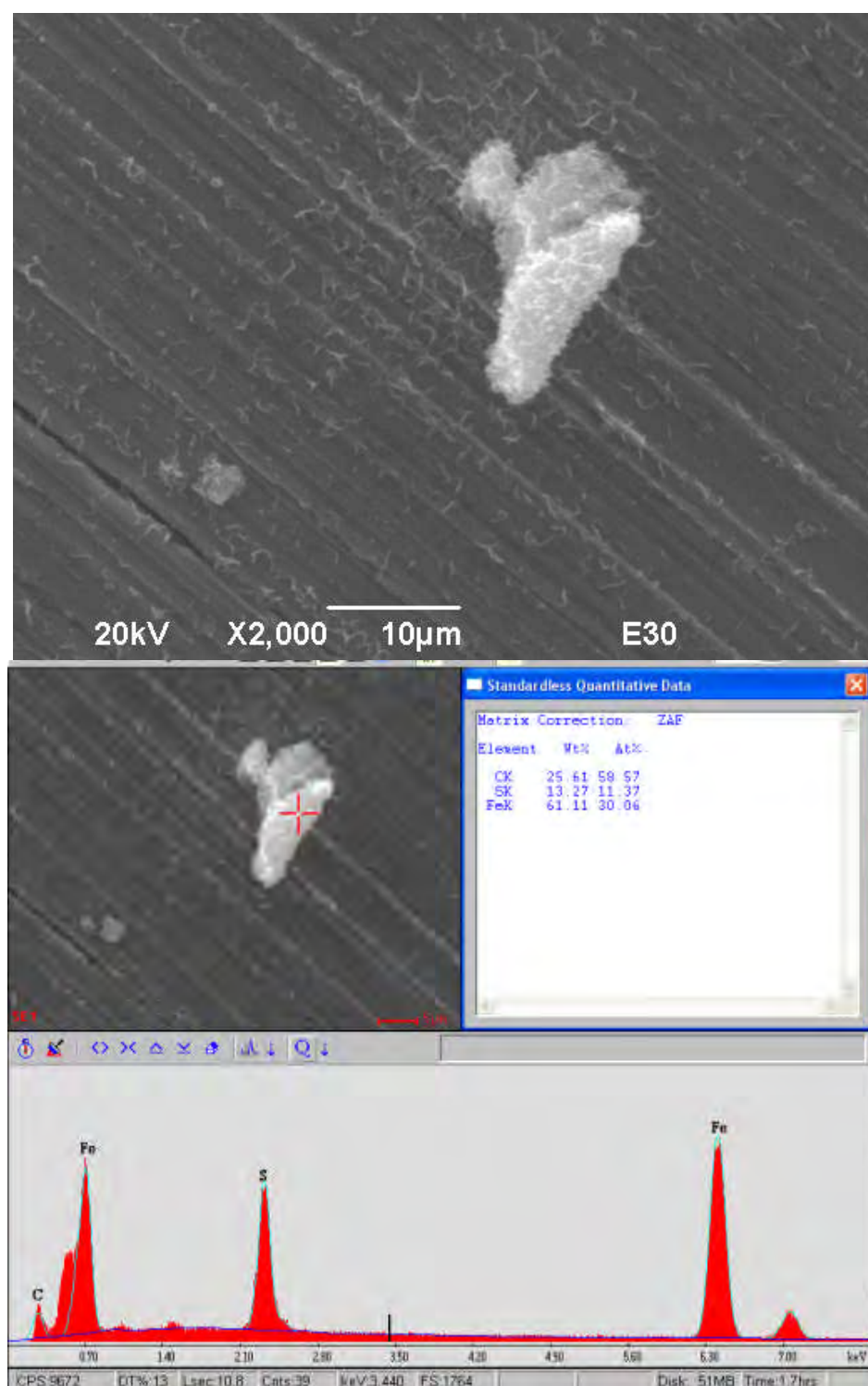
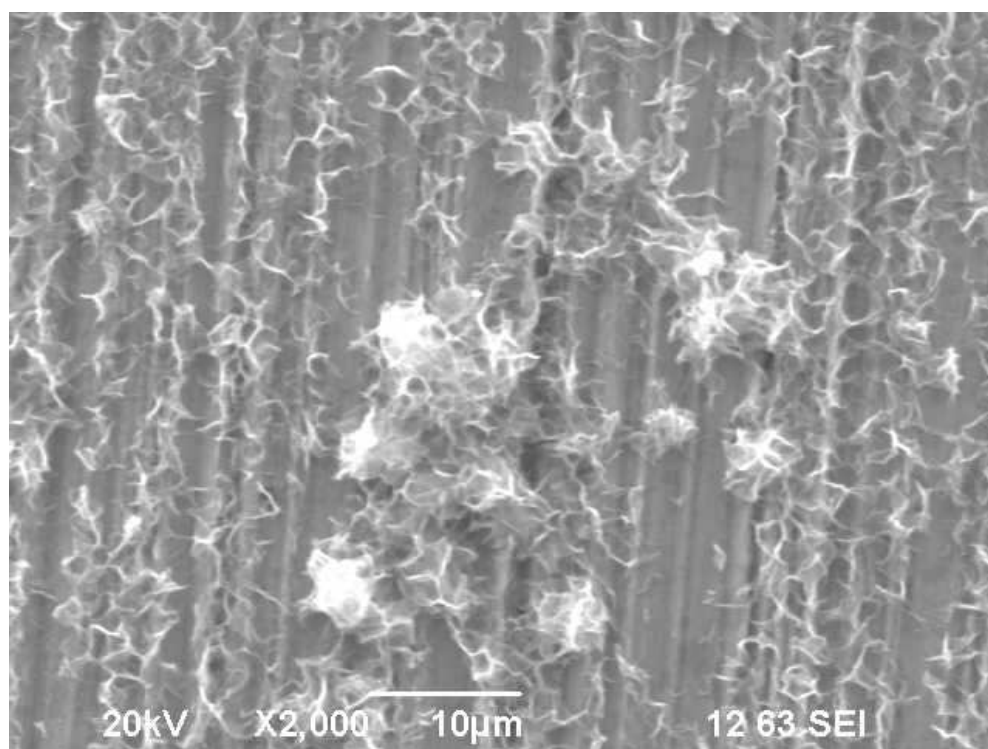


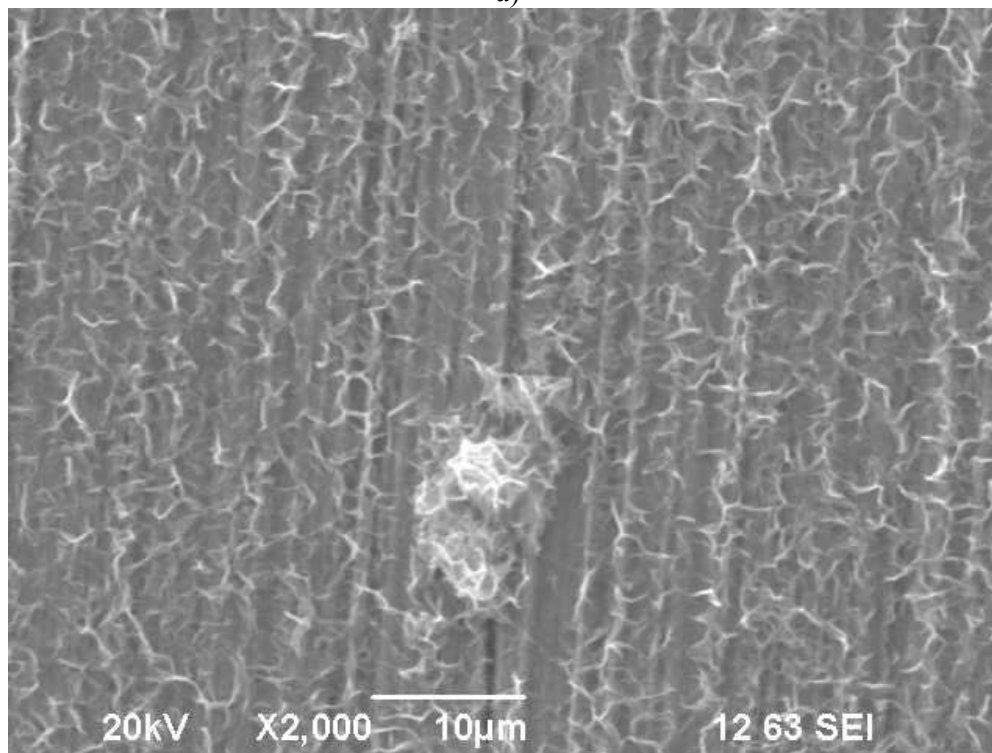
Figure 21. Corrosion specimen exposed to H₂S for 3 days at 10 wt% NaCl, 25°C, with corrosion product layer.

3.4.2.3 7 days

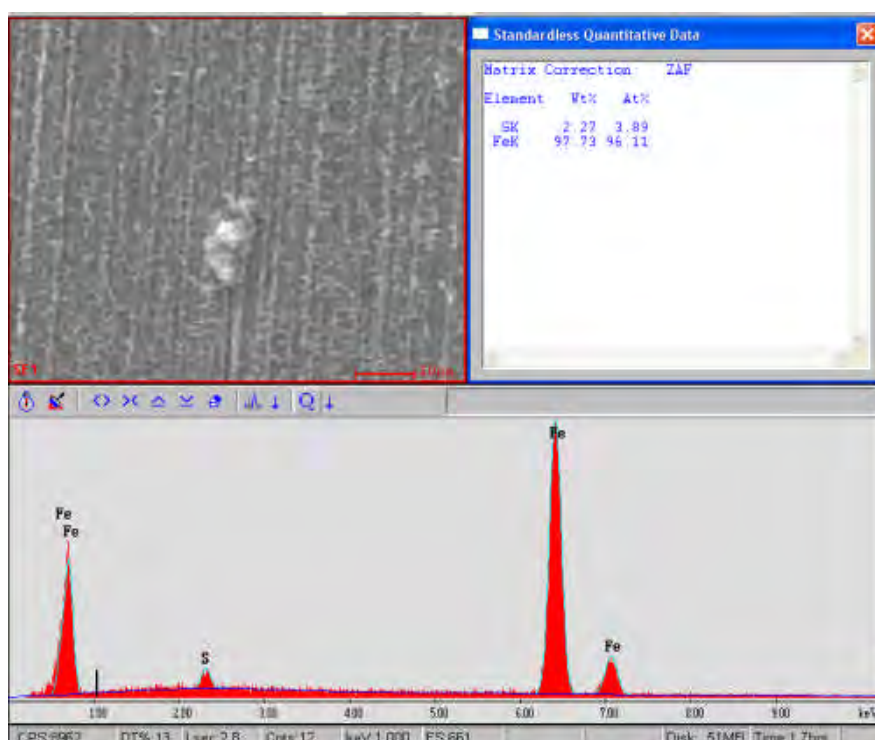
“Blooms” in the iron sulfide layer appeared on the specimen surface (Figure 22), which were more concentrated when compared with the “bulges” found on corrosion product layers observed at 7 days in salt-free conditions. However, the rest of the corrosion product layer is relatively thin. The general corrosion rate at the high salt concentration condition was still very low. Some pitting attack was evident after the iron sulfide layer was removed by Clarke’s solution (Figure 23). However, the pits were too small to quantify in depth.



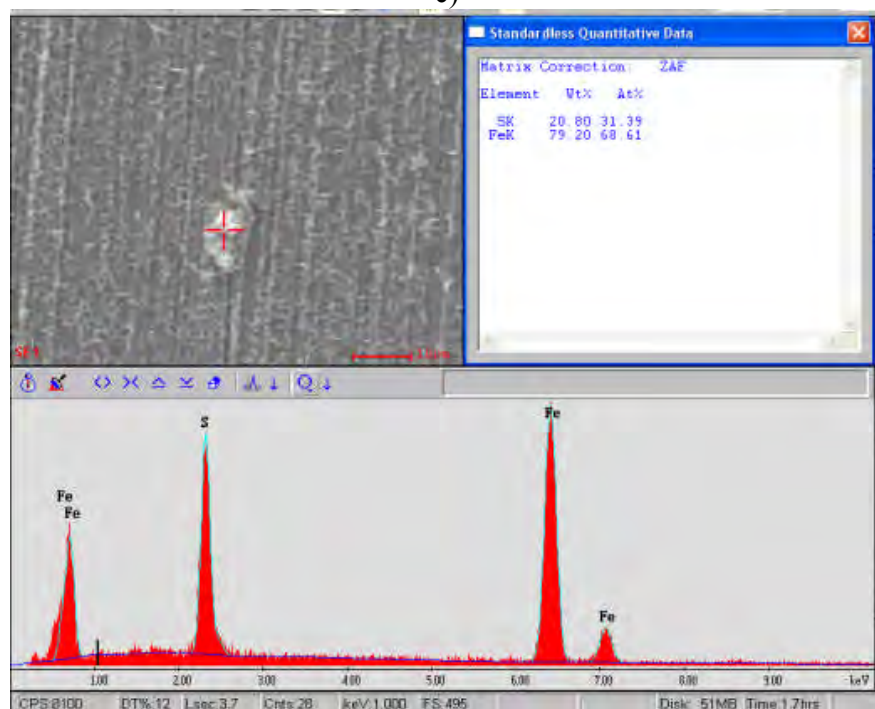
a)



b)



c)



d)

Figure 22. Corrosion specimen exposed to H_2S for 7 days at 10 wt% NaCl, 25°C, with corrosion product layer.

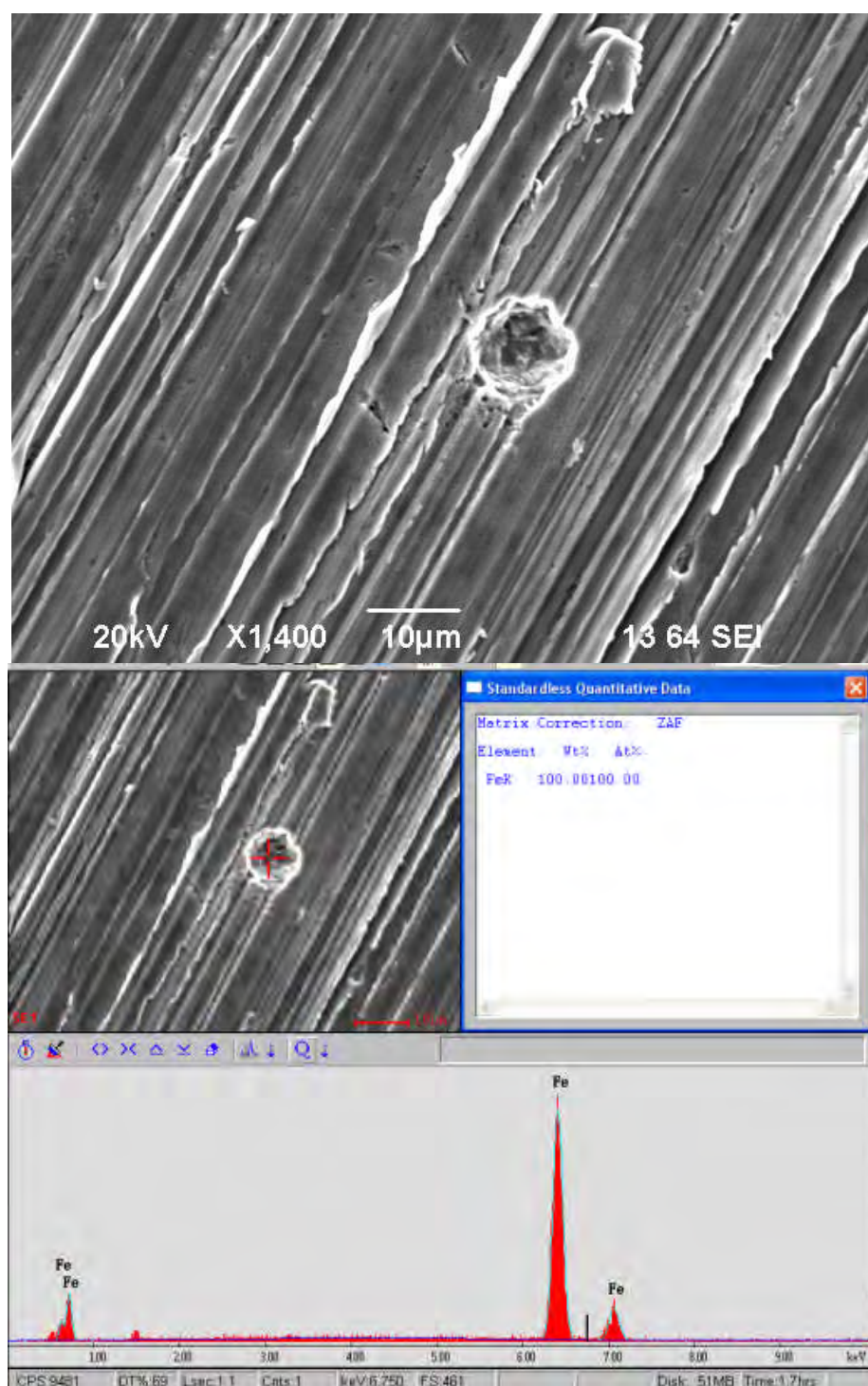
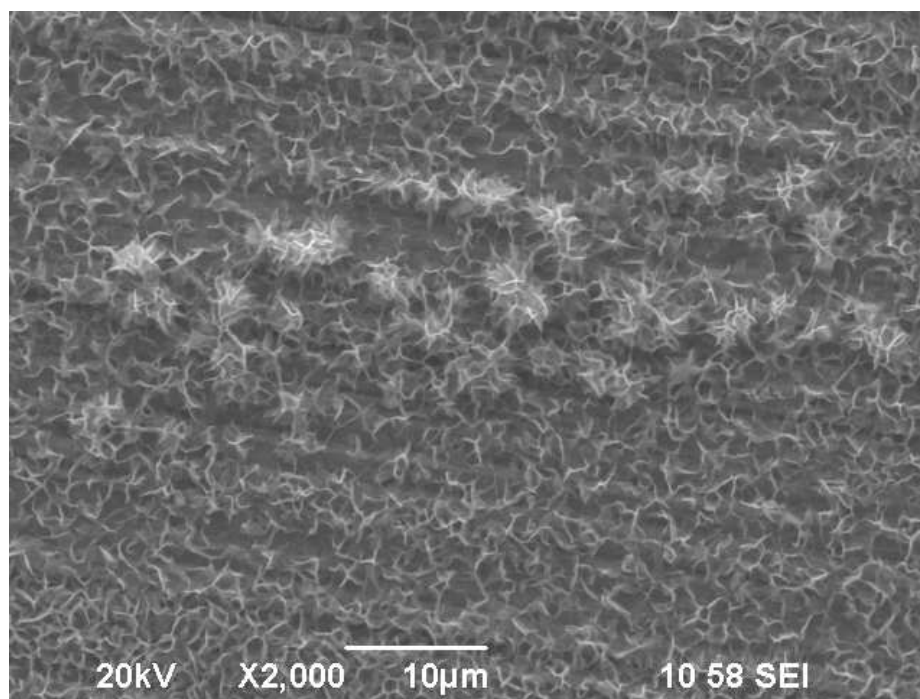


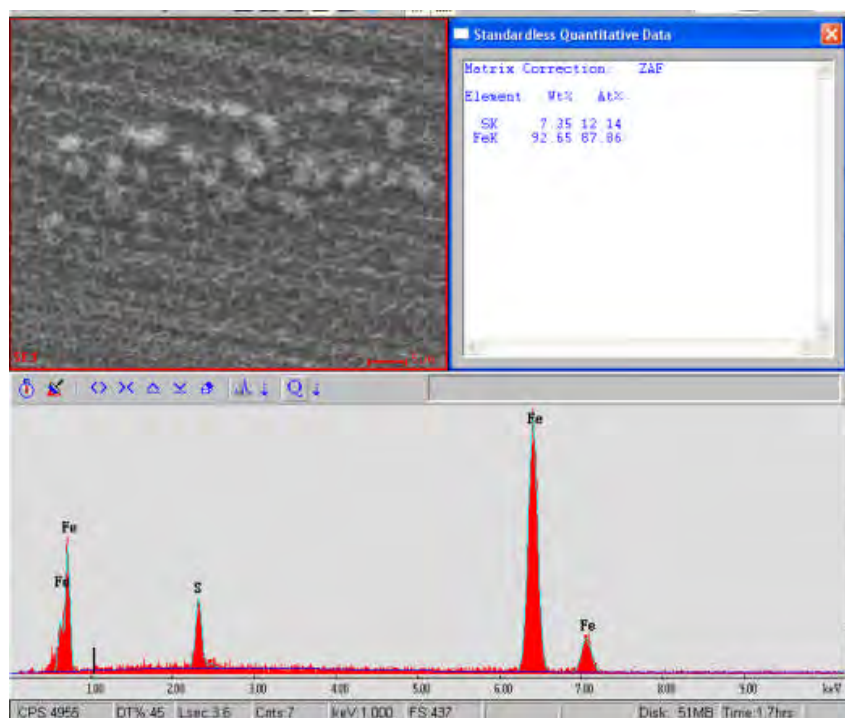
Figure 23. Corrosion specimen exposed to H₂S for 7 days at 10 wt% NaCl, 25°C, without corrosion product layer.

3.4.2.4 15 days

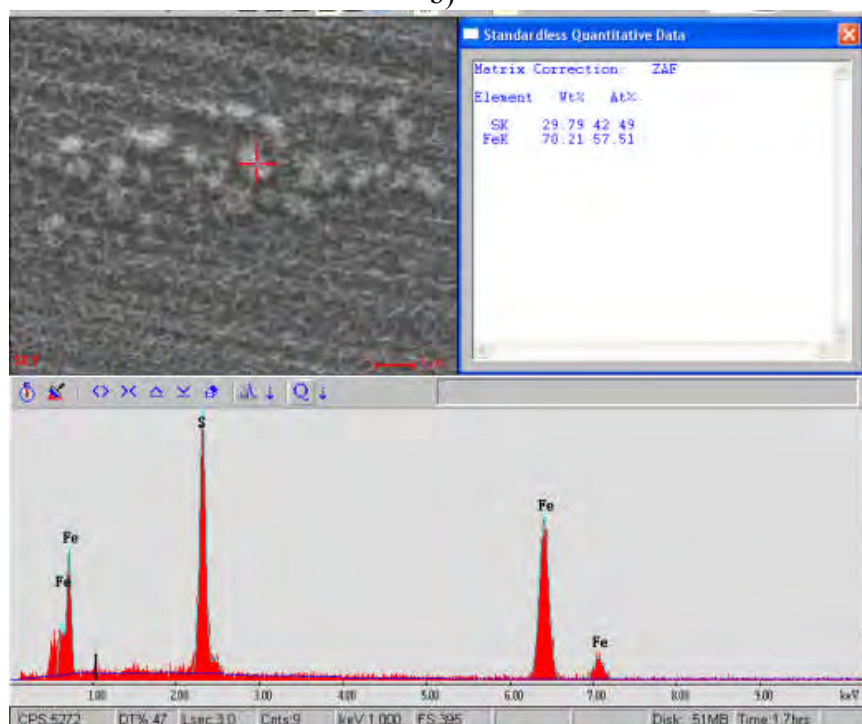
The morphology of iron sulfide layers at 15 days was similar to the layer morphology observed at 7 days (Figure 24). The difference is that the iron sulfide layer at 15 days was visibly thicker as suggested by the SEM image. Figure 25 shows the SEM image of the specimen surface without iron sulfide layers at 15 days. Some pitting attack was observed. A 3D analysis of the pit is shown in Figure 26.



a)



b)



c)

Figure 24. Corrosion specimen exposed to H_2S for 15 days at 10 wt% NaCl, 25°C, with corrosion product layer.

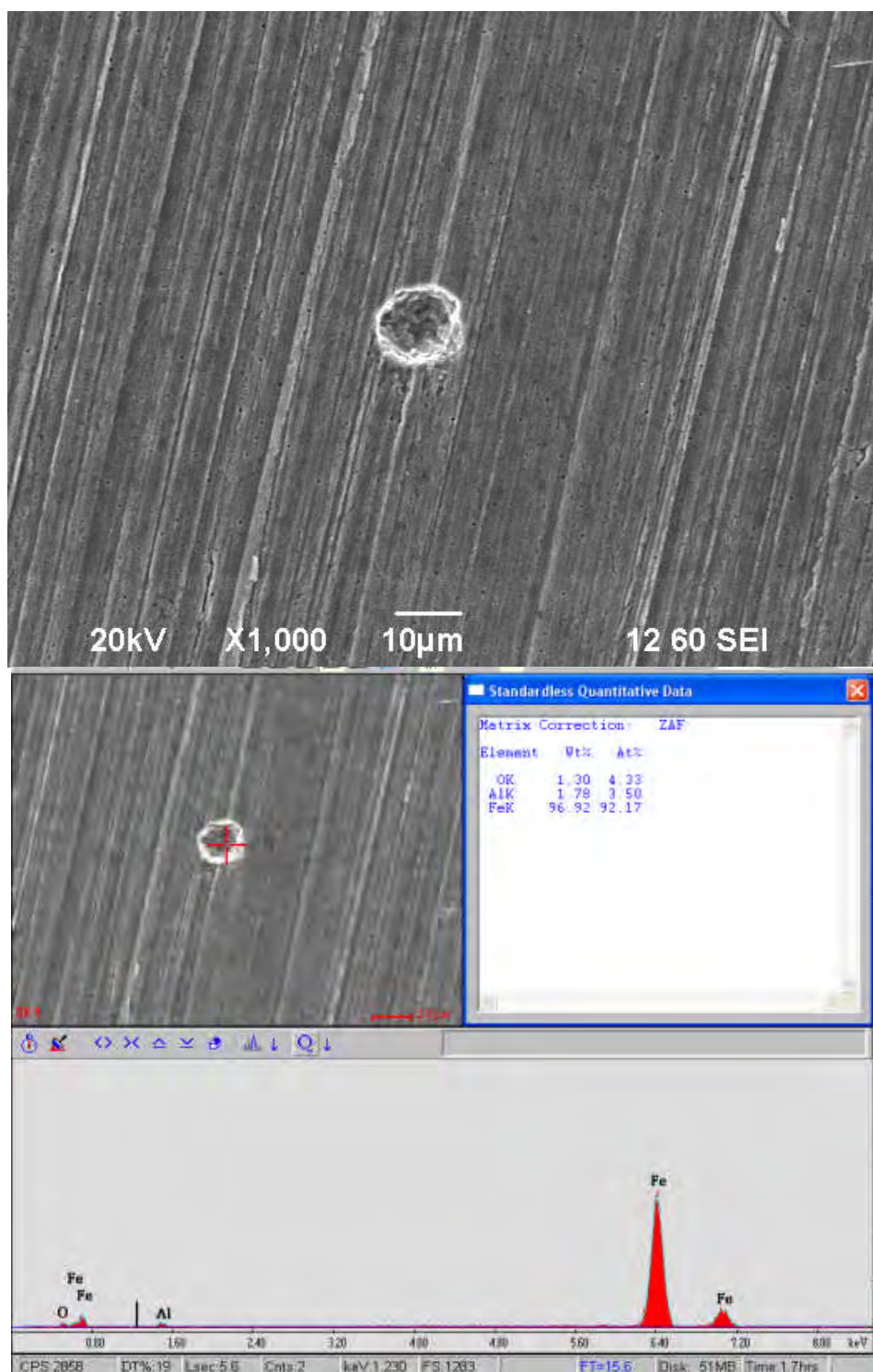


Figure 25. Corrosion specimen exposed to H_2S for 15 days at 10 wt% NaCl, 25°C, without corrosion product layer.

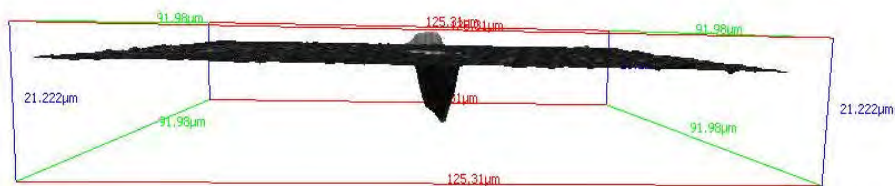


Figure 26. 3D view of corrosion specimen exposed to hydrogen sulfide for 12 days at 0 wt% NaCl, 25°C, without corrosion product layer.

3.4.2.5 26 days

Figure 27 shows the iron sulfide layer morphology after the corrosion specimen was exposed to H₂S for 26 days. Some major cracks of the iron sulfide layers were observed. Large and deep pits were expected; however, no severe pitting corrosion was observed after the iron sulfide layer was removed.

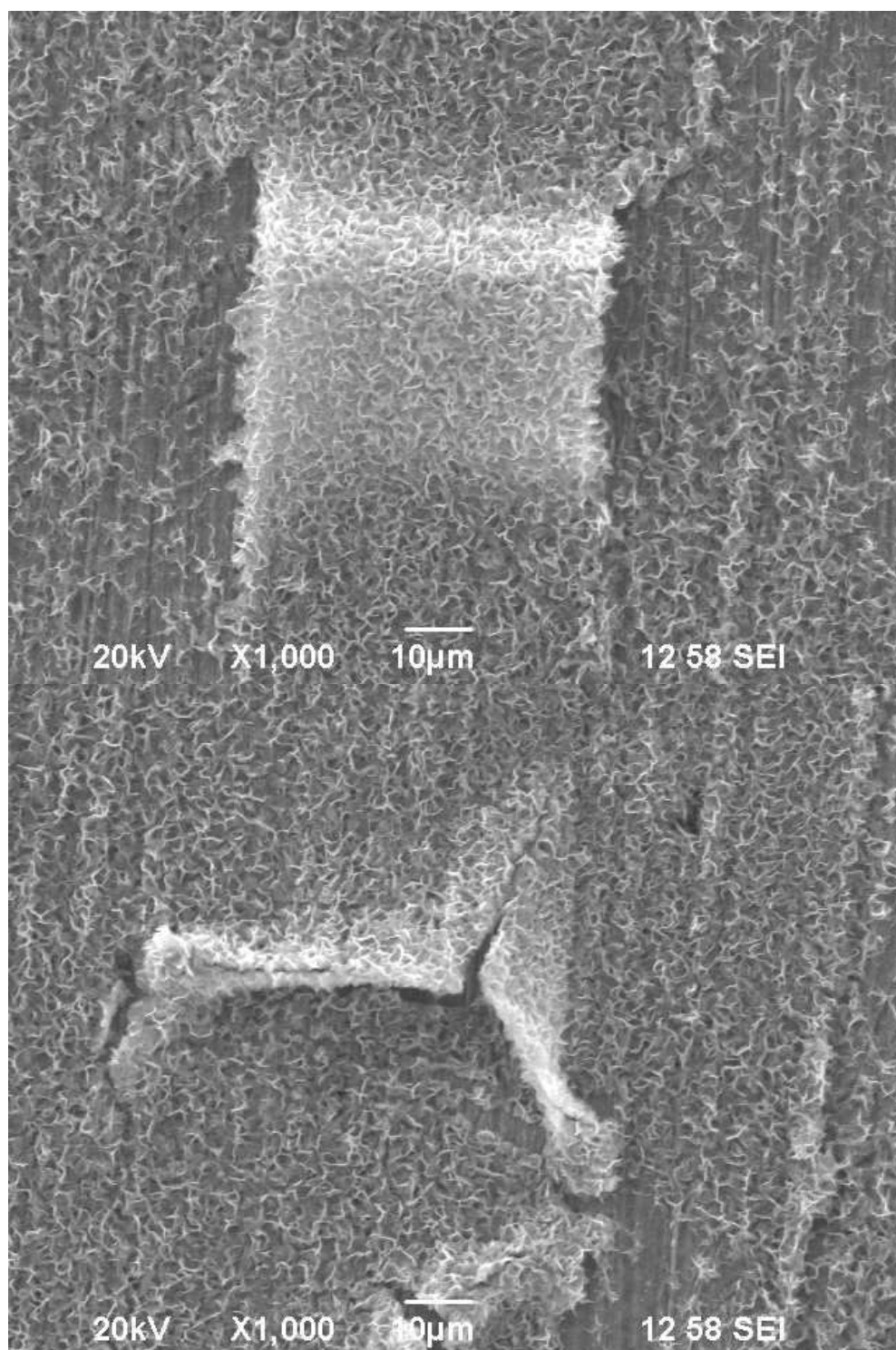


Figure 27. Corrosion specimen exposed to H₂S for 26 days at 10 wt% NaCl, 25°C, with corrosion product layer.

The initiation of pitting attacks was observed in both salt free and high chloride ion concentration conditions. Interestingly, in both cases, the pitting corrosion did not propagate with time. A hypothesis was formulated to explain the cause of the pitting corrosion phenomena observed in these experiments.

3.4.3 Why Did Pitting Attack Initiate but Not Propagate?

As stated above, some pitting (localized corrosion) was observed on the specimen surface even in the salt-free test conditions. Exposed specimens were re-examined by SEM and EDX to try to establish the cause of pitting initiation. Figure 28 shows one location of the specimen surface without the iron sulfide layer at 6 days exposure to a salt-free solution at 25°C, showing what appears to be a bead of a different material at the bottom of the pit. The same was found at several locations. EDX results confirmed the presence of aluminum and magnesium inside the pits. It is suspected that these may have been present as inclusions in the parent steel or were introduced by the surface polishing process. The feasibility of the first assumption was confirmed by looking at steel composition and consulting a metallurgist. The second assumption needed further investigation. Figure 29 shows a freshly prepared bare metal surface polished by sand paper: aluminum and magnesium were also found at a few locations. Gold sputter-coated sand paper was analyzed by EDX and the same elements were found (Figure 30) confirming that the metal inclusion in the steel may have been related to specimen preparation.

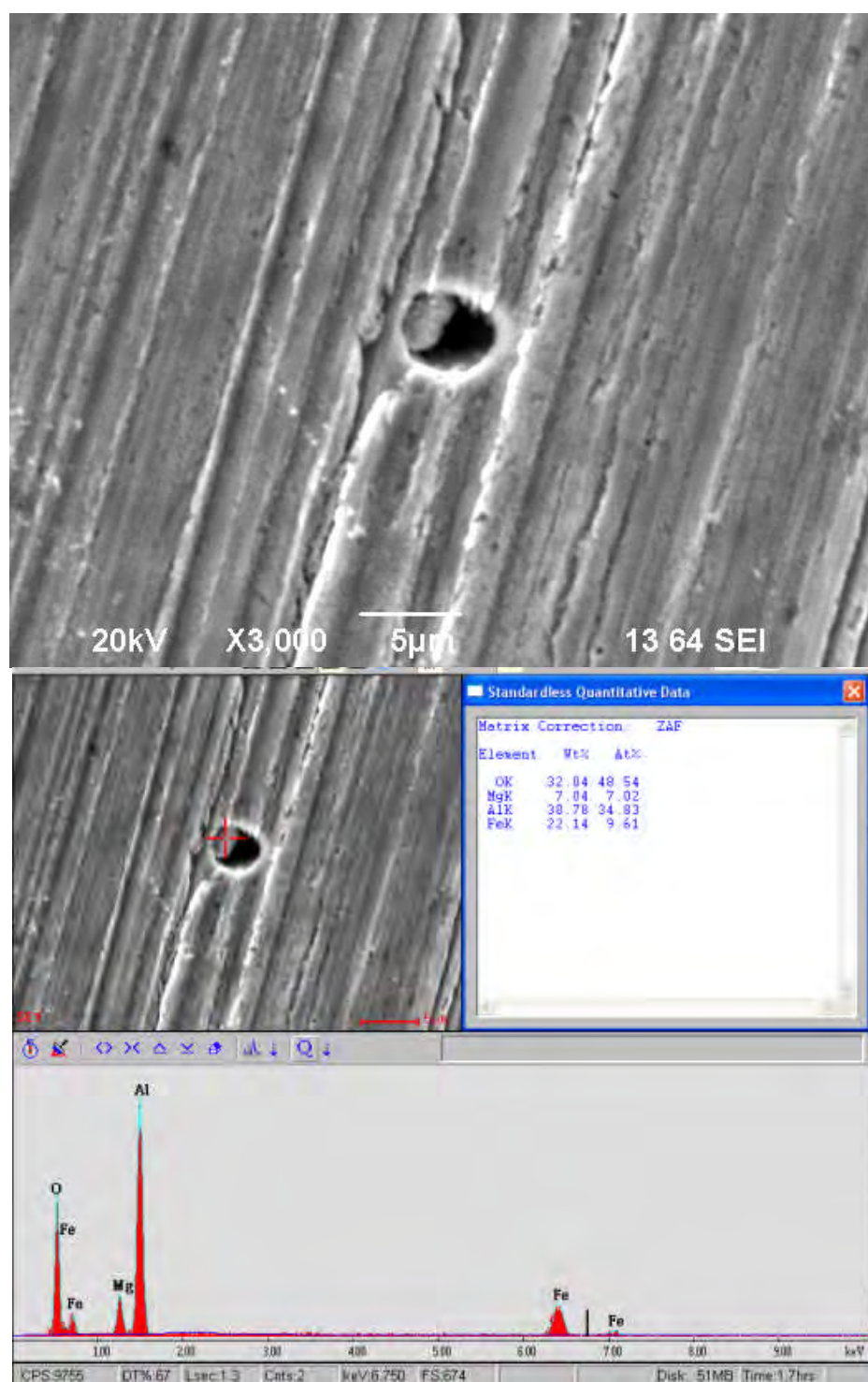


Figure 28. Corrosion specimen exposed to H₂S for 6 days at 0 wt% NaCl, 25°C, without corrosion product layer.



Figure 29. Freshly prepared bare corrosion specimen surface polished to 600 grit sand paper.

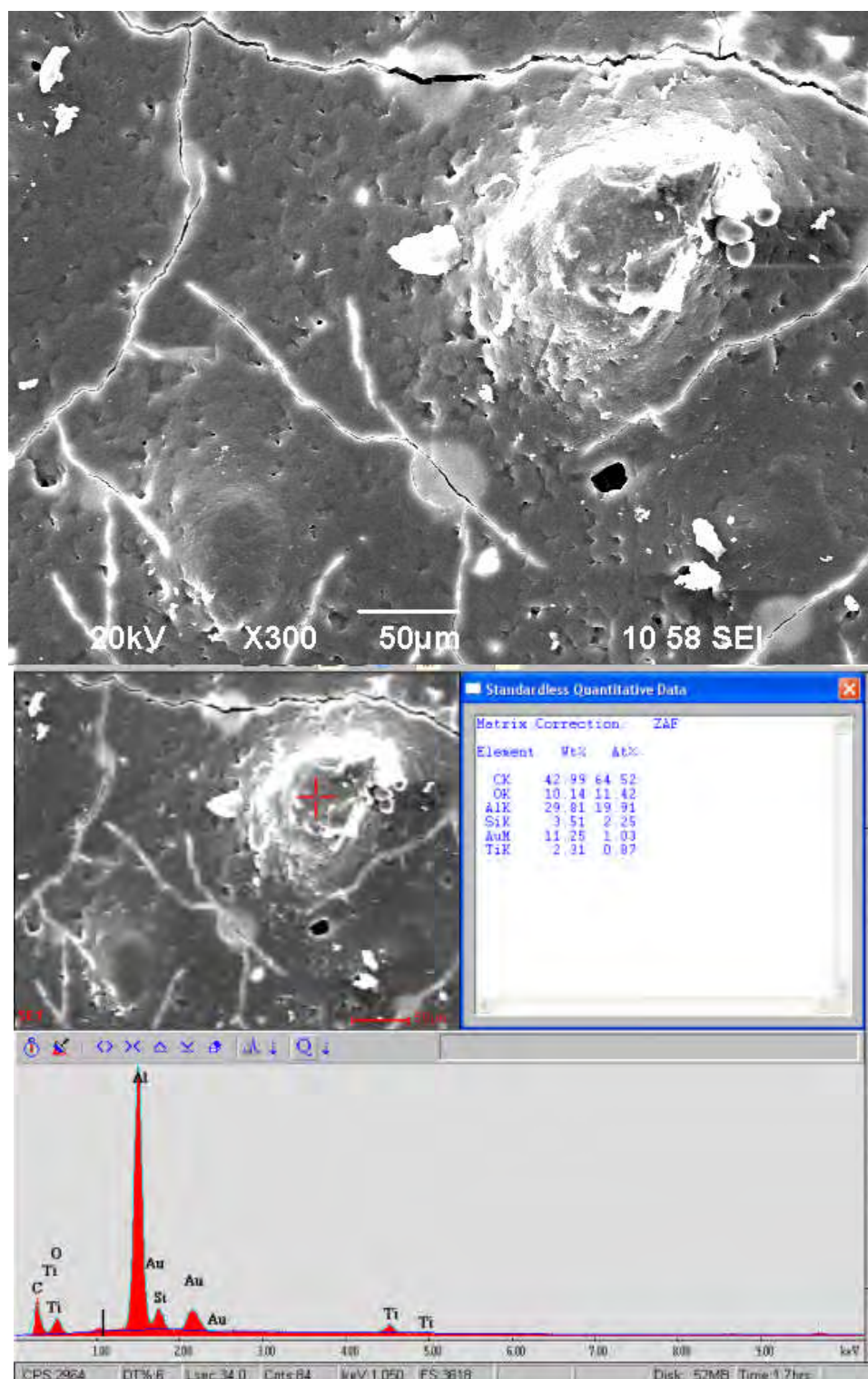


Figure 30. Analysis of gold sputter-coated sand paper.

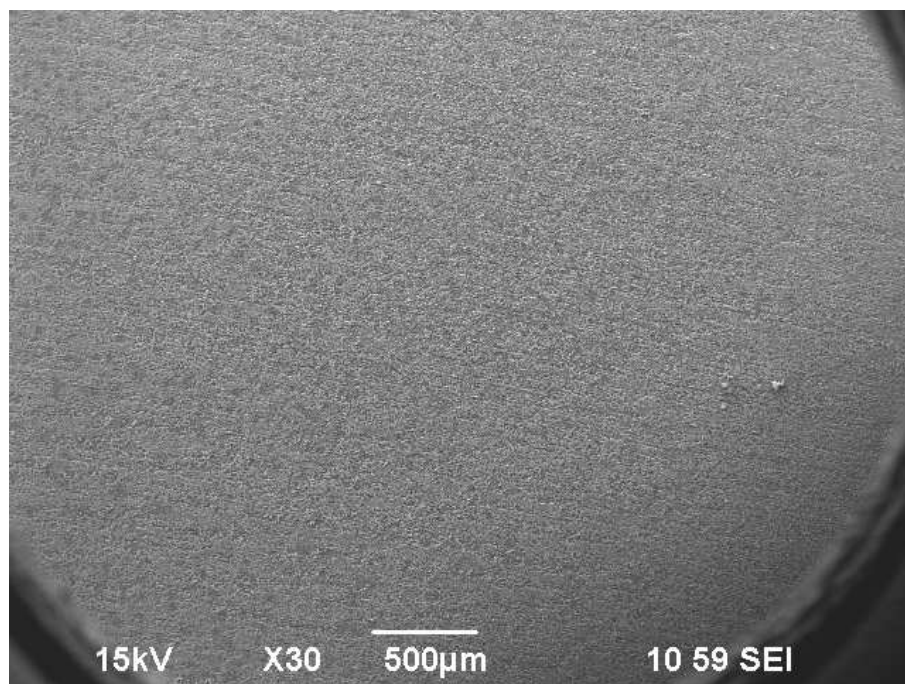
It can be hypothesized that pitting was initiated due to the presence of the inclusions in the steel surface since the pit density was observed to increase with time, yet the examination of a freshly prepared surface had very few indications of the suspect elements on the steel surface. Observations signify that once the steel around the inclusions was dissolved away sufficiently, the inclusions “fell out” and pit propagation stopped. However, more experimental verification is needed to confirm this hypothesis, with a future research goal to include study of the links between material inclusions and pitting.

Overall, these series of experiments were performed to investigate the effects of high salt concentration on the corrosion of carbon steel from the low partial pressure of H_2S . From the experimental results shown above, it appears that the addition of chloride ions actually slowed down the reaction rate between iron and H_2S . This may be due to the adsorption of chloride ions which generated a mass transfer barrier to the corrosive species, such as hydrogen ion and H_2S . In the next series of experiments, similar tests were performed at high partial pressure of H_2S and high temperature.

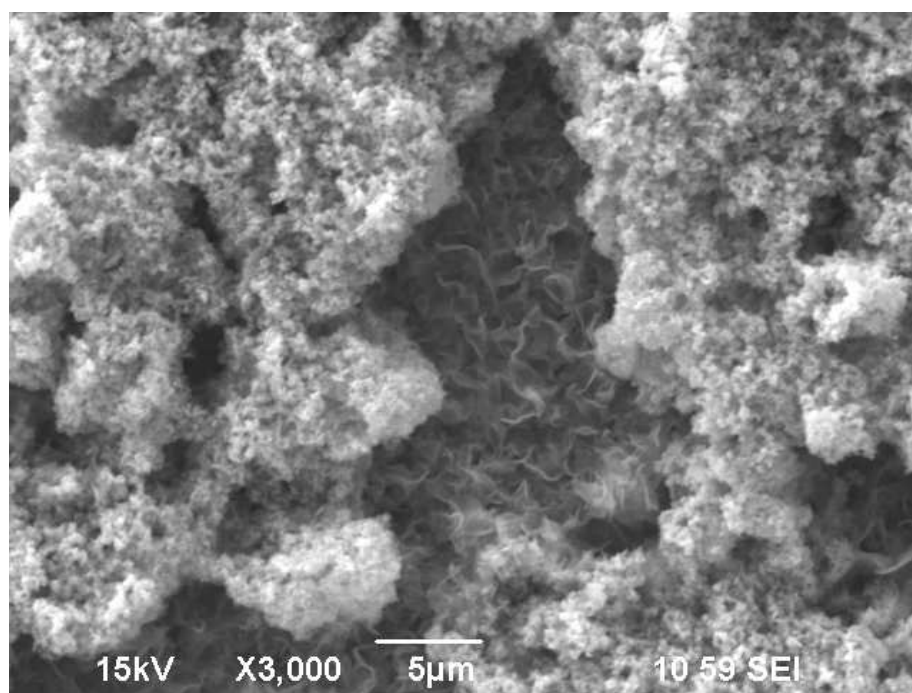
3.4.4 80°C, 5000 ppm H_2S (0.01 bar H_2S at P_{total} 2 bar), 10 wt.% NaCl

Figure 31 shows the SEM image and EDX spectrum of a specimen surface after a 7 days exposure. A uniform layer of corrosion product layer was formed on the specimen surface. A further enlargement of the surface shows that the layer appears amorphous with a layered structure. The composition of the corrosion product layer was shown, by using EDX, to have a high sulfur content. The layer was then removed by Clarke’s solution. The final surface morphology is shown in Figure 32. A large amount of small

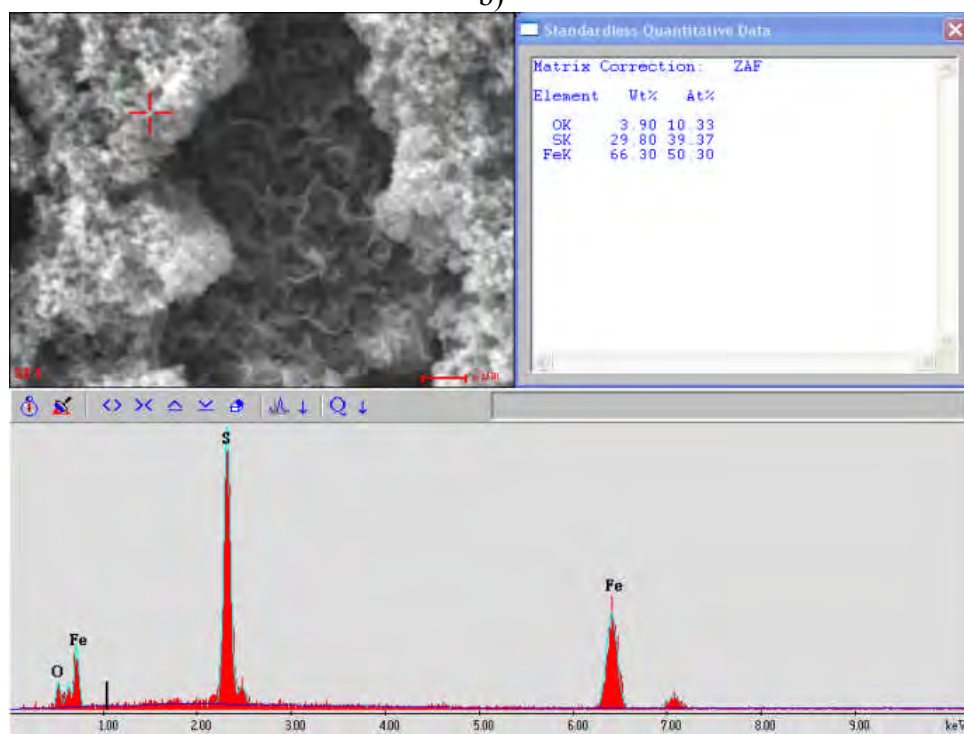
pits were observed on the specimen surface, over 2,000 per square millimeter. However, the pit depth is too small to be quantified, so a pitting ratio would be small as well. The general corrosion rate measured by the weight loss method is 0.08 mm/yr, which is considered low.



a)



b)



c)

Figure 31. Corrosion specimen exposed to 0.01 bar H_2S for 7 days at 10 wt% NaCl, $80^\circ C$, with corrosion product layer.

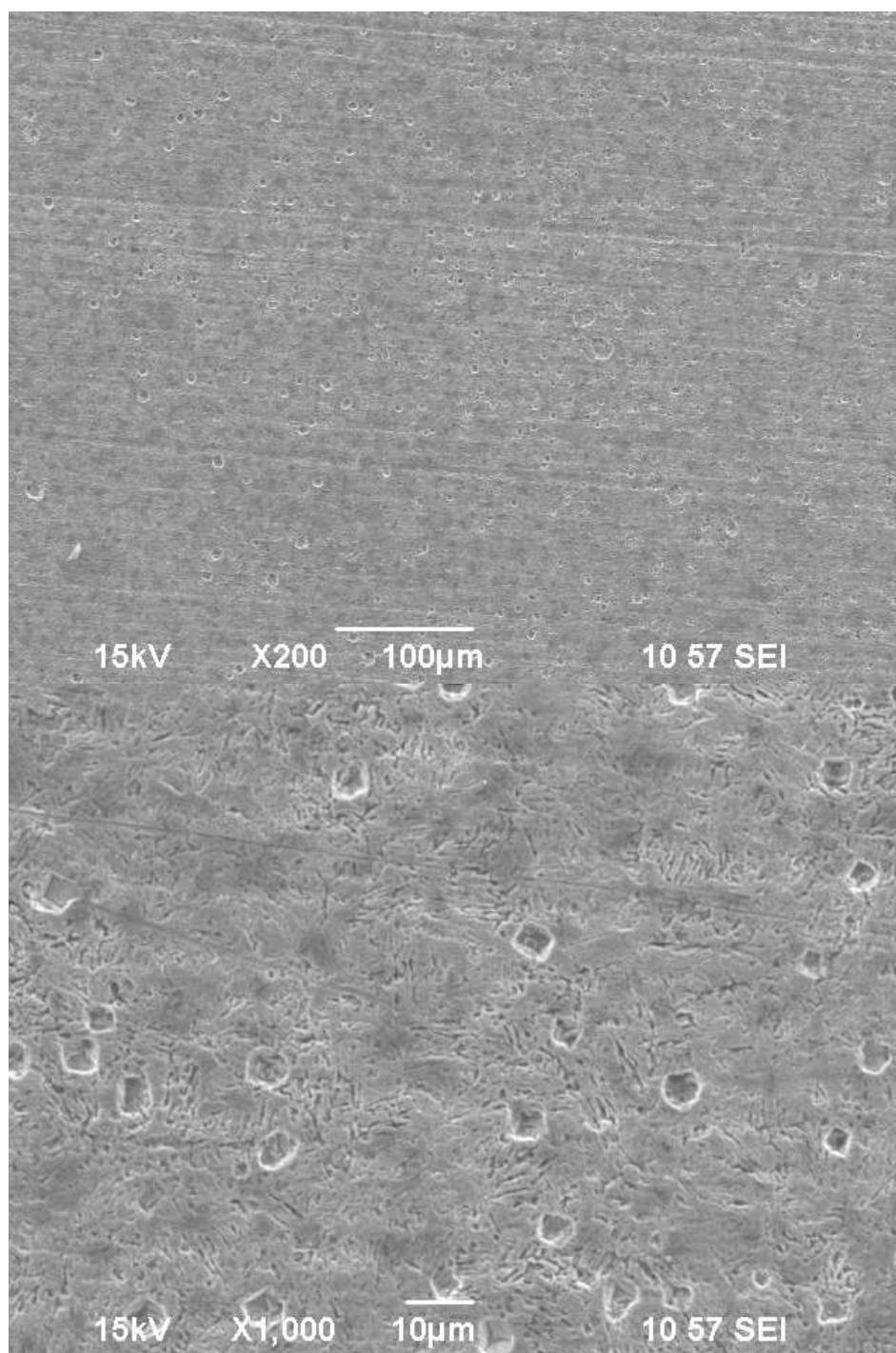


Figure 32. Corrosion specimen exposed to 0.01 bar H₂S for 7 days at 10 wt% NaCl, 80°C, without corrosion product layer.

The SEM image and EDX spectrum of a cross-section of another parallel specimen are shown in Figure 33. A thin layer of iron sulfide formed on the specimen surface. The thickness of the sulfide layer is around 8 μm . The specimen surface underneath the sulfide layers is flat. No pitting attack was observed.

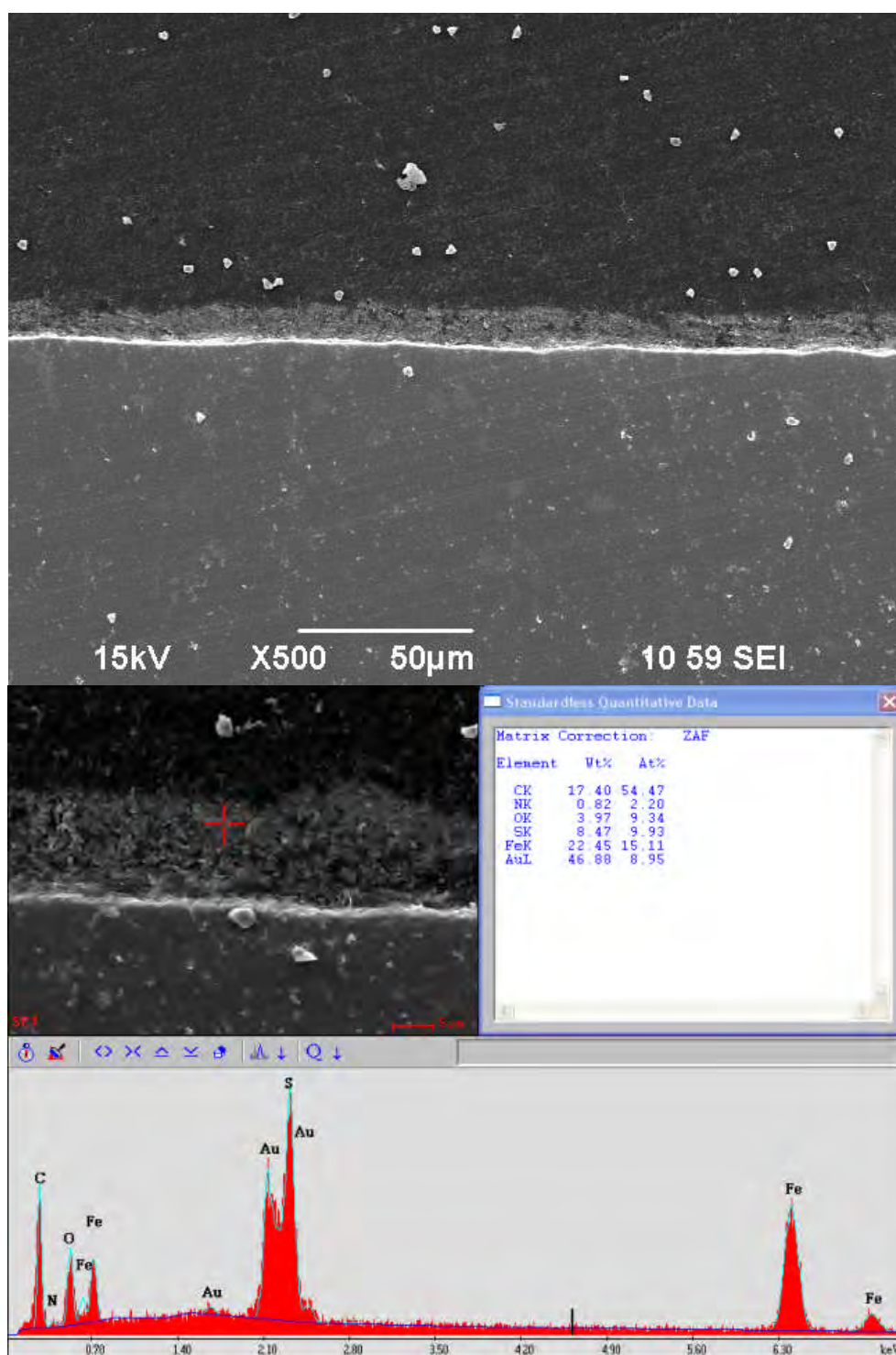
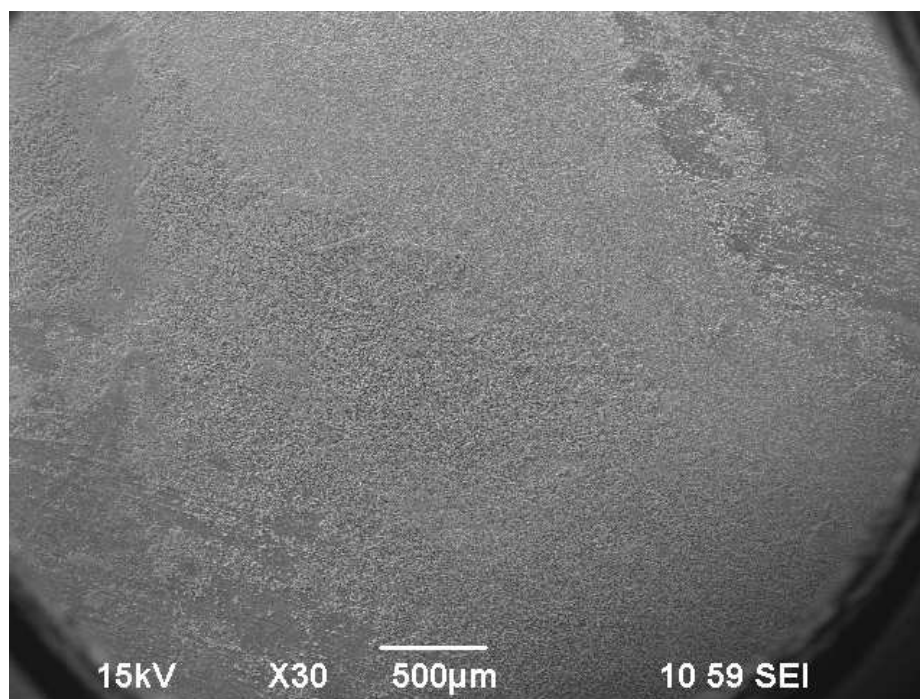


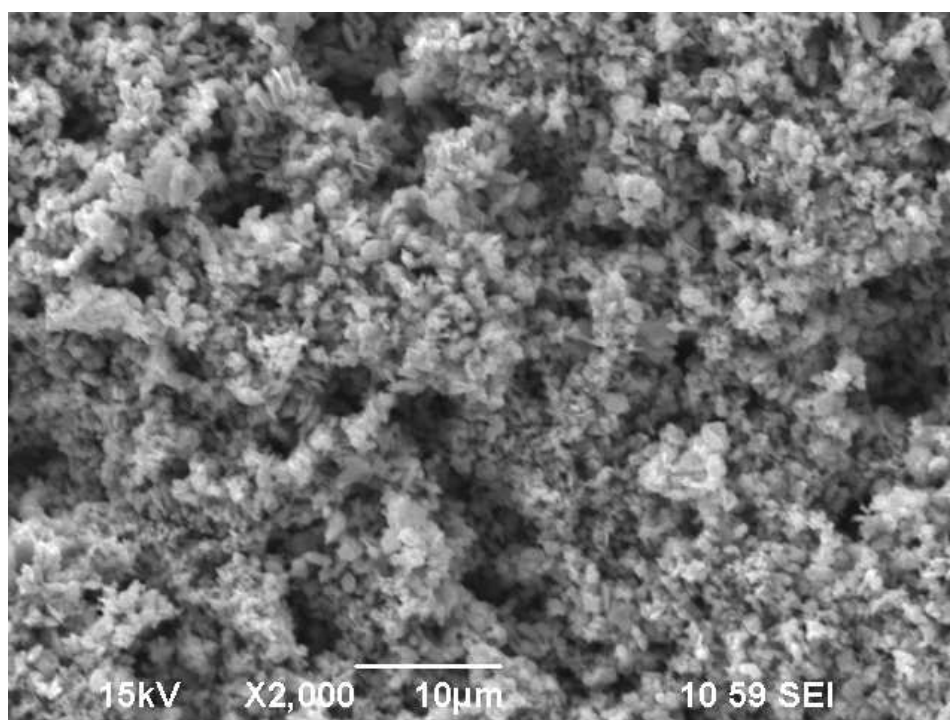
Figure 33. Cross-section of a corrosion specimen exposed to 0.01 bar H₂S for 7 days at 10 wt.% NaCl, 80°C, with corrosion product layer.

3.4.5 80°C, 50000 ppm H₂S (0.1 bar H₂S at P_{total} 2 bar), 10 wt.% NaCl

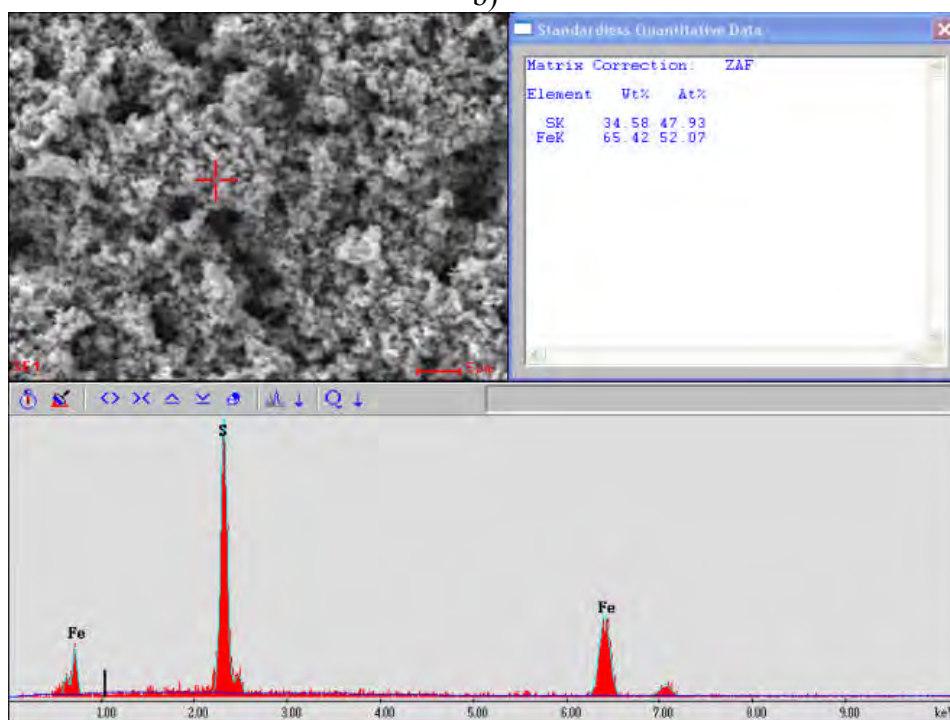
H₂S partial pressure was set at 0.1 bar at 80°C in this autoclave test. The specimen surface with corrosion product layer was analyzed by SEM and EDX to determine layer morphology and composition. Representative SEM/EDX data for the corrosion specimen surface is shown in Figure 34. Most of the surface was covered by a sulfide layer (top left SEM image). A further enlargement of the small area shows that the corrosion product layer appears amorphous with no well-defined crystals present. EDX result confirms the presence of iron and sulfur species.



a)



b)



c)

Figure 34. Corrosion specimen exposed to 0.1 bar H₂S for 7 days at 10 wt.% NaCl, 80°C, with corrosion product layer.

Figure 35 shows the SEM image of the specimen surface after corrosion product layer removal. Similar to the experimental result at 0.01 bar partial pressure of H₂S, pitting attacks were not observed. General corrosion rate is 0.1 mm/yr.

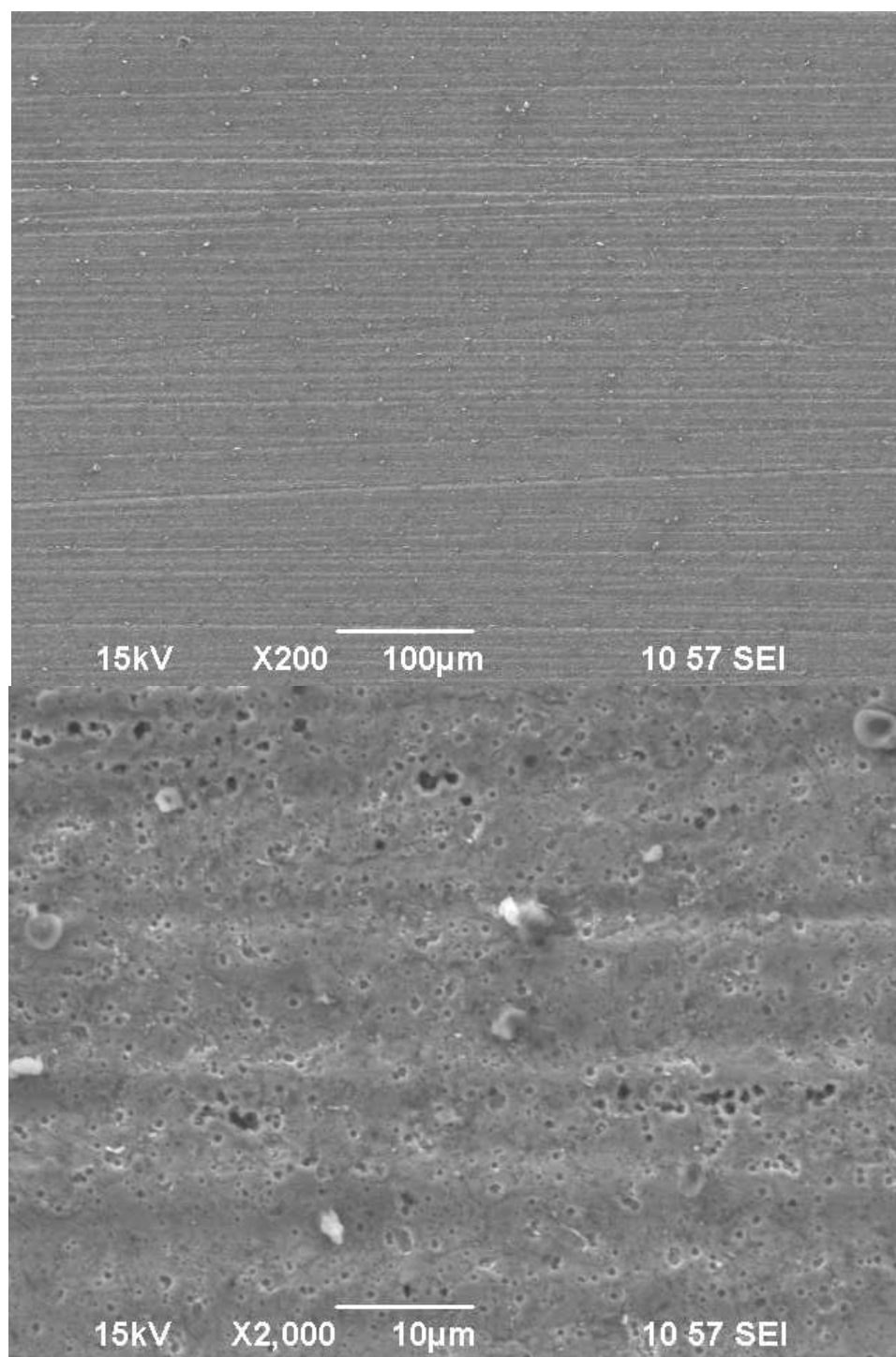
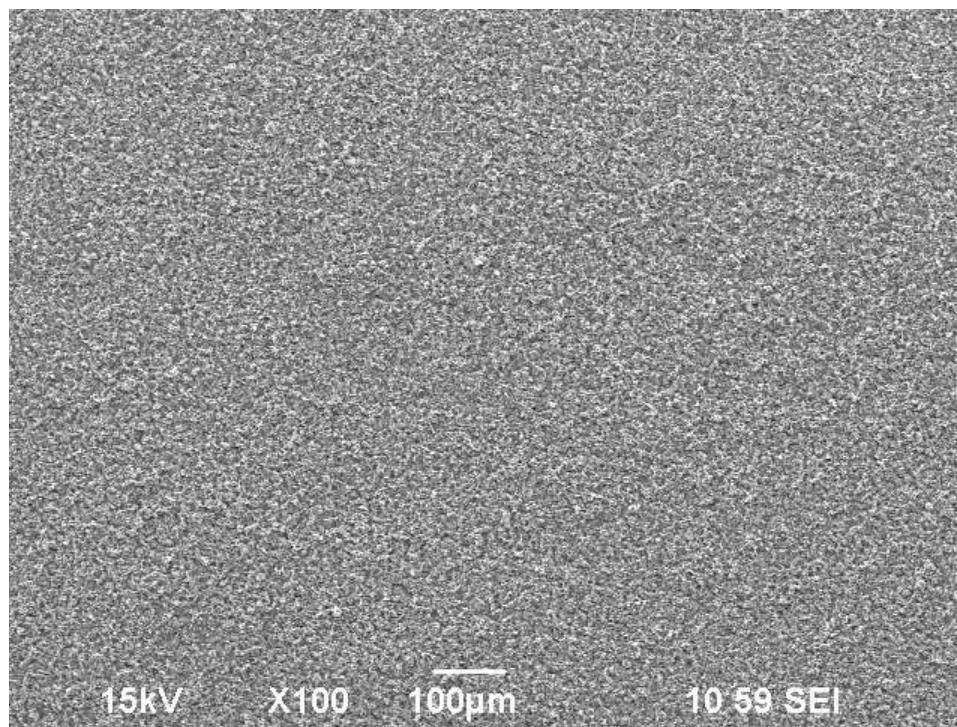


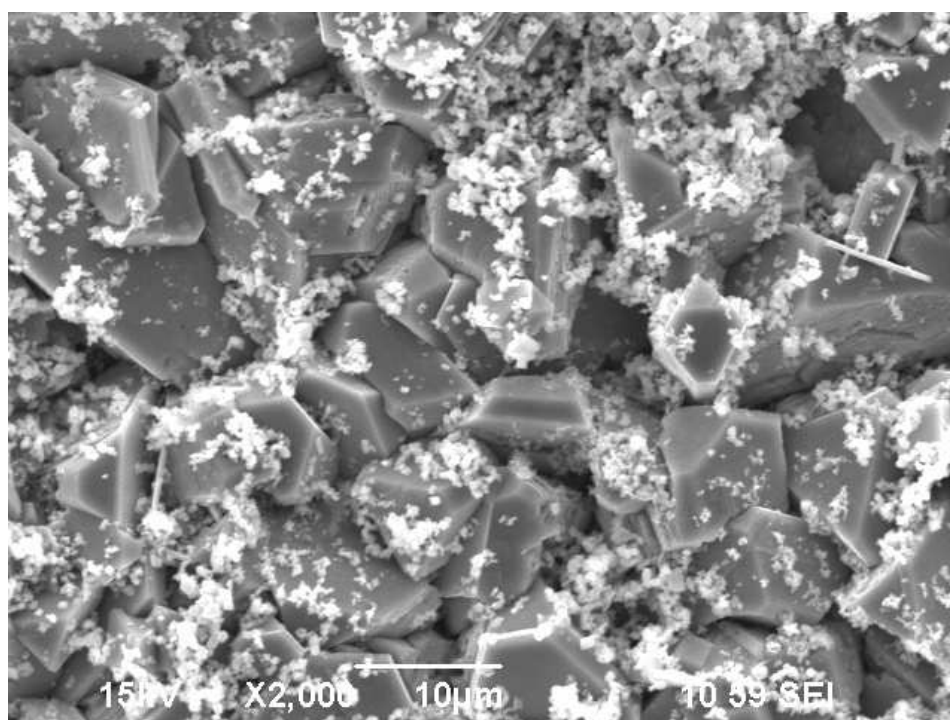
Figure 35. Corrosion specimen exposed to 0.1 bar H₂S for 7 days at 10 wt.% NaCl, 80°C, without corrosion product layer.

3.4.6 80°C, 50 % H₂S (1 bar H₂S at P_{total} 2 bar), 10 wt.% NaCl

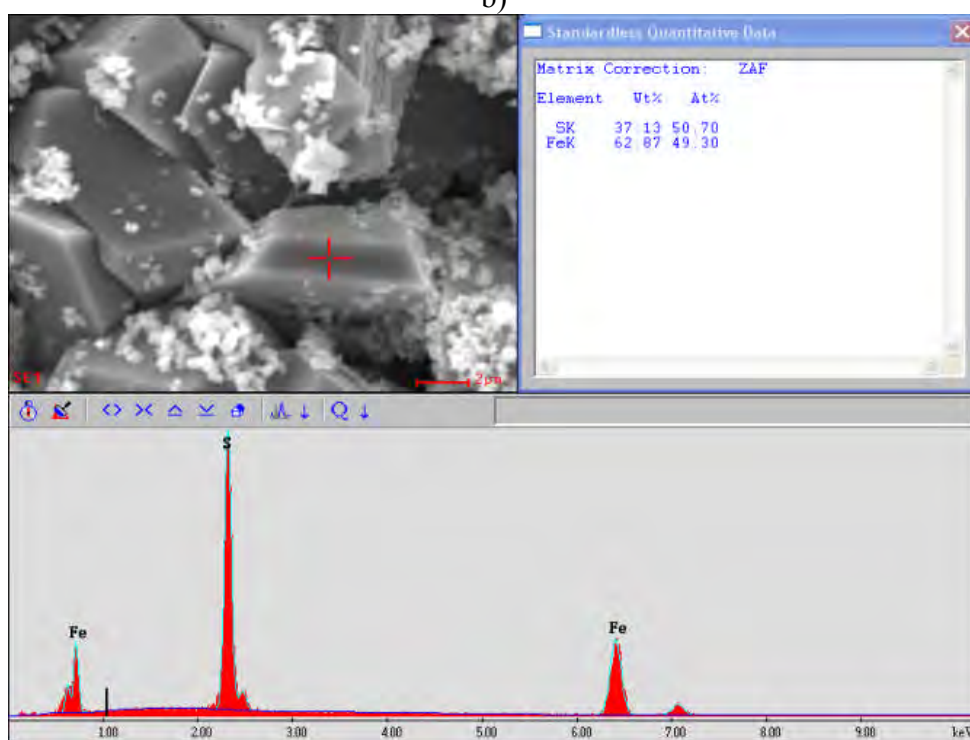
The SEM image and EDX spectrum of a specimen surface after 7 days exposure to 1 bar H₂S are shown in Figure 36. The surface layer appears much more uniform and denser. The enlarged image reveals that the corrosion product layer is crystalline, which is different from what has been observed at the lower H₂S partial pressure. This suggests that the iron sulfide phase may have changed when the H₂S partial pressure was increased to 1 bar. From the hexagonal crystal morphology of the corrosion product layers shown in the SEM image, this would be consistent with pyrrhotite formation. However, XRD analysis needs to be conducted to further confirm that this occurred.



a)



b)



c)

Figure 36. Corrosion specimen exposed to 1 bar H₂S for 7 days at 10 wt.% NaCl, 80°C, with corrosion product layer.

The specimen surface after corrosion product layer removal was then scanned by SEM. The result is shown in Figure 37. It is clearly seen that the polish marks still remain on the surface. This suggests a low corrosion rate. An enlarged SEM image of a small area reveals more detailed appearance of the specimen surface after corrosion. A significant number of small holes were found over the entire specimen surface. It is hard to define the holes as pits, because the size and the depth are too small to be quantified and the holes are all over the surface. “Widespread localized attack” may be a proper expression to be used to illustrate this distinctive corrosion attack, but should be considered to fall under the banner of general corrosion.

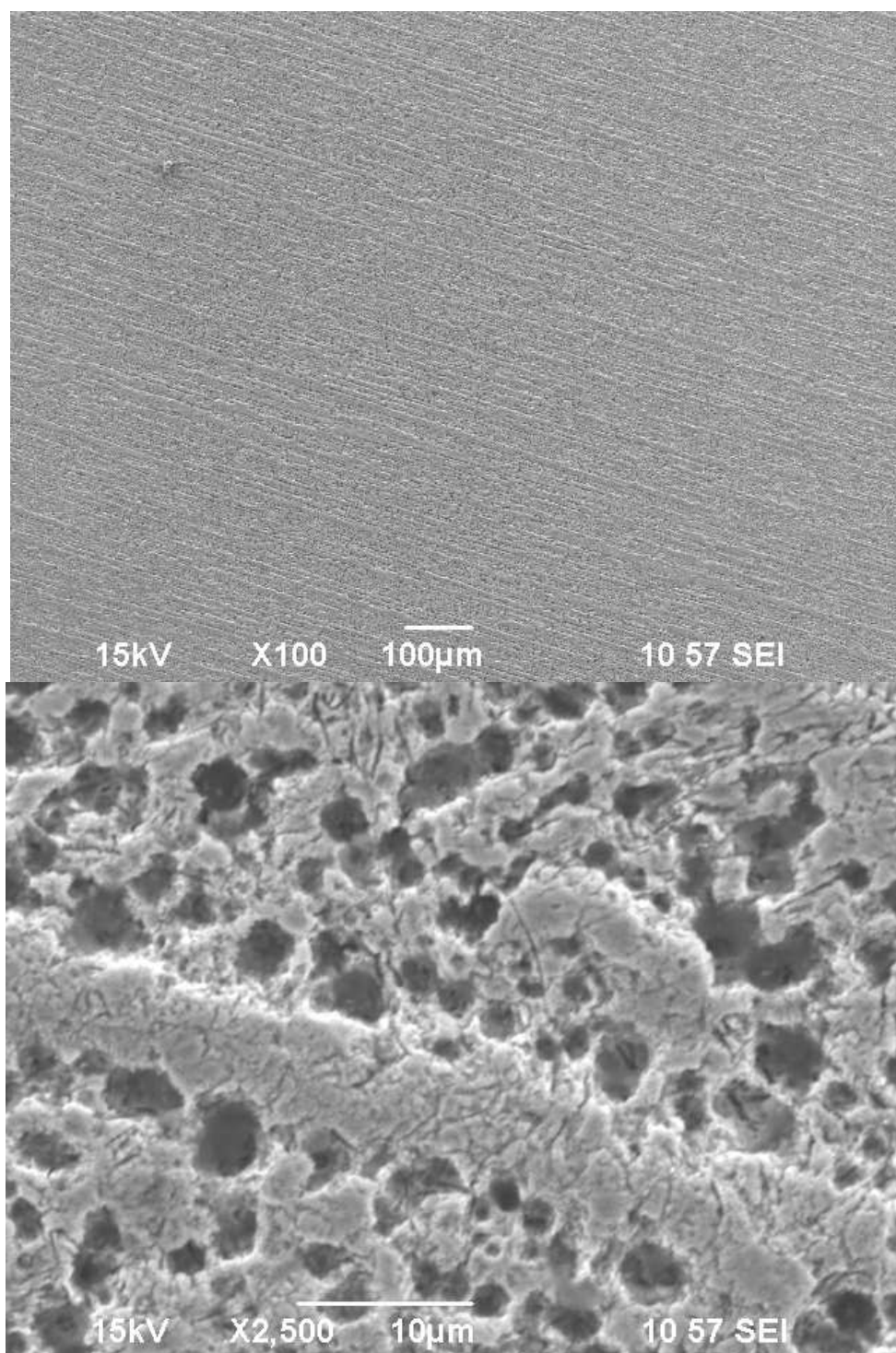


Figure 37. Corrosion specimen exposed to 1 bar H_2S for 7 days at 10 wt.% NaCl, 80°C, without corrosion product layer.

Another corrosion specimen was cut to do the cross-section analysis. The SEM image of the cross-section is shown in Figure 38. The iron sulfide layer is indentified by EDX. The maximum penetration depth was measured to be 10 μ m, which represents a corrosion rate of approximately 0.5 mm/yr. The penetration rate calculated based on the cross-section is about two and a half times higher than the general corrosion rate measured by weight loss, 0.2 mm/yr. However, from the SEM image of the specimen surface after corrosion product layer removal, it is clearly seen that most of the weight loss was caused by the corrosion which occurred more or less evenly over the entire surface area. If the general corrosion rate measured by weight loss is recalculated by using the surface area of the holes seen in the SEM images, the result is approximately the same as the observed penetration rate. Therefore, the corrosion attack detected in this test condition cannot be defined as localized corrosion.

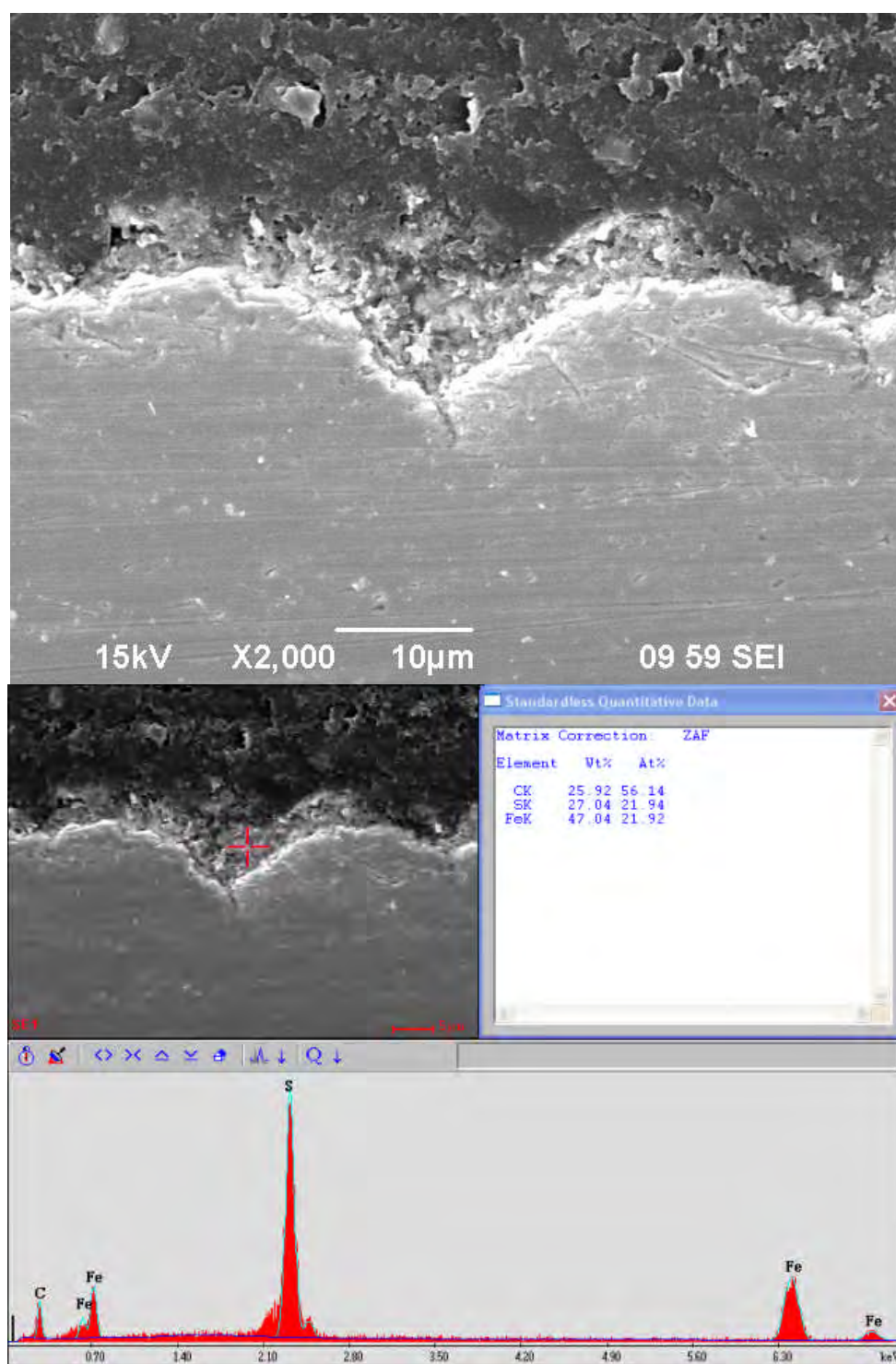


Figure 38. Cross-section of a corrosion specimen exposed to 1 bar H₂S for 7 days at 10 wt.% NaCl, 80°C, with corrosion product layer.

In this series of tests, the experiments were conducted at 80°C, 10 wt.% NaCl with three different H₂S partial pressures of 0.01 bar, 0.1 bar and 1 bar. The comparison of the corrosion rates for the different H₂S partial pressures is shown in Figure 39. It is clearly seen that the overall general corrosion rate increased with an increase of H₂S partial pressure. However, the magnitude of the corrosion rate for each partial pressure of H₂S is rather low. No severe localized corrosion was detected in all three test conditions. It is still questionable whether a high concentration of chloride can initiate localized corrosion in H₂S systems.

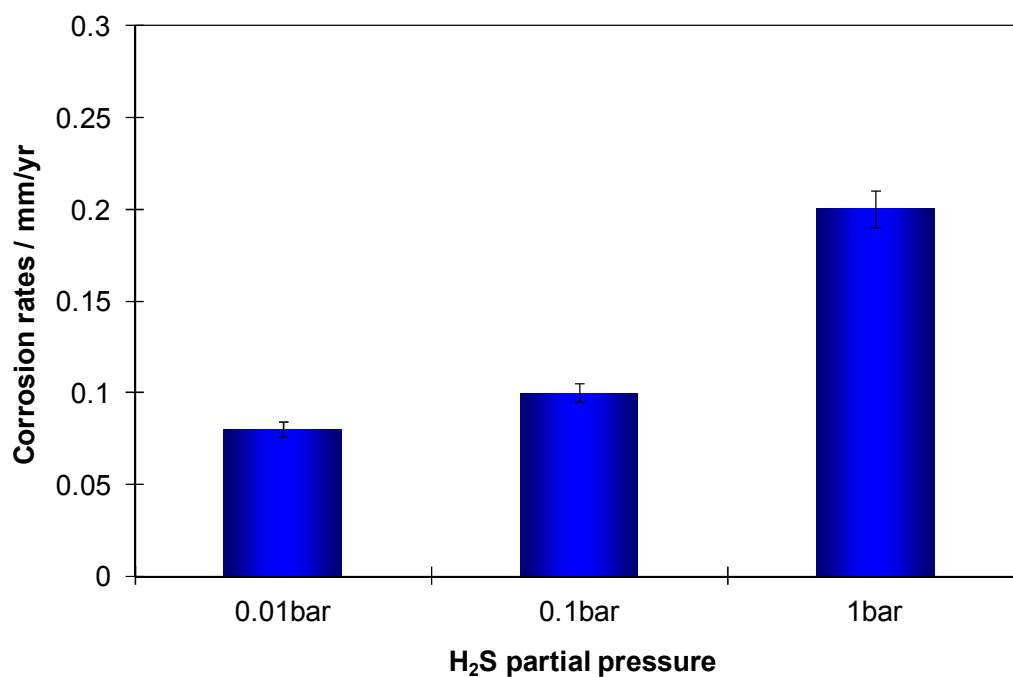


Figure 39. Comparisons of general corrosion rates for different H₂S partial pressures tested.

3.5 Summary

The chloride effects on the initiation of localized H₂S corrosion have been investigated in both the low H₂S concentration (0.05 mbar in one bar total pressure) and high H₂S partial pressure (0.01 bar, 0.1bar and 1 bar).

At low H₂S concentration, the initiation of localized corrosion was observed in both chloride free and high concentration of chloride ions conditions. Interestingly, the localized corrosion did not propagate with time and the general corrosion rate decreased with an increase of chloride concentration. Further surface analysis suggests that the initiation of pitting attacks observed was due to the imperfection of the steel surface (inclusions).

At high H₂S partial pressure, similar experiments were conducted only at high chloride ions concentration. The corrosion under these conditions appeared to be by uniform attack.

Therefore, from the current experimental data, there is no direct evidence that the chloride ion can initiate localized corrosion in sour systems. However, the role of chloride ions on initiation of localized corrosion in sour systems cannot be excluded altogether as a possibility. Future experimentation focused on the chloride effects should be conducted at even higher temperatures, in the presence of CO₂, with other electrolyte components, etc.

CHAPTER 4 INVESTIGATION OF GALVANIC EFFECTS ON THE PROPOGATION OF LOCALIZED CORROSION IN H₂S SYSTEMS

4.1 Introduction

Similar to the initiation of localized corrosion in H₂S systems, the propagation of localized corrosion is also poorly understood. To investigate the propagation of localized H₂S corrosion, and to serve as a starting point, it could be helpful to look at similar experiments conducted in sweet systems.

Localized corrosion of carbon steel in sweet systems (CO₂ dominant corrosion) has been studied for many years. The initiation of localized CO₂ corrosion is believed to be caused by partial protective layer removal. Corrosion product layer removal can be caused by flow or chemical dissolution. Once the passive layer is partially removed, a fresh metal surface is exposed. The initiation of localized corrosion occurs. At this time, the potential difference between the fresh metal surface and the corrosion product layer covered surface becomes the driving force of galvanic current between the corrosion product layer free surface and layer covered surface⁸⁴. If the corrosion environment does not allow the exposed fresh metal surface to be repassivated, then due to the galvanic current, the fresh metal surface corrodes much faster than the surface covered with a layer of corrosion product. This amounts to propagation of localized corrosion by a galvanic mechanism.

Once the initiation of localized corrosion in H₂S system occurs (by chemical or mechanical means), the propagation of localized corrosion may follow the same principle as in sweet systems. A simple experimental plan has been made to test the feasibility of

galvanic current theory in sour systems. The results are described in the following sections.

4.2 Objectives and test Matrix

The objective of this set of experiments is to investigate the galvanic effect on pitting propagation in an aqueous system with dissolved H₂S.

An experimental plan was defined to achieve this objective. The details as well as the test matrix are shown below.

Table 4. Test conditions

Parameters	Conditions
Total Pressure	1 bar
H ₂ S concentration	50 ppm ($P_{\text{H}_2\text{S}} = 0.05 \text{ mbar at } P_{\text{total}} = 1 \text{ bar}$)
Temperature	25°C
Solution	1 wt.% NaCl
pH	5.0
Material	C1018

4.3 Experimental set-up

An overall experimental set-up is shown in Figure 40. A cylinder containing mixed nitrogen and approximately 500 ppm H₂S gas was used as the source of the H₂S. A second cylinder containing pure nitrogen was used to dilute the H₂S concentration from the source with a mixing gas rotameter. Before the gas was bubbled into the test solution, the H₂S concentration in the gas phase was measured with a H₂S colorimetric detection tube.

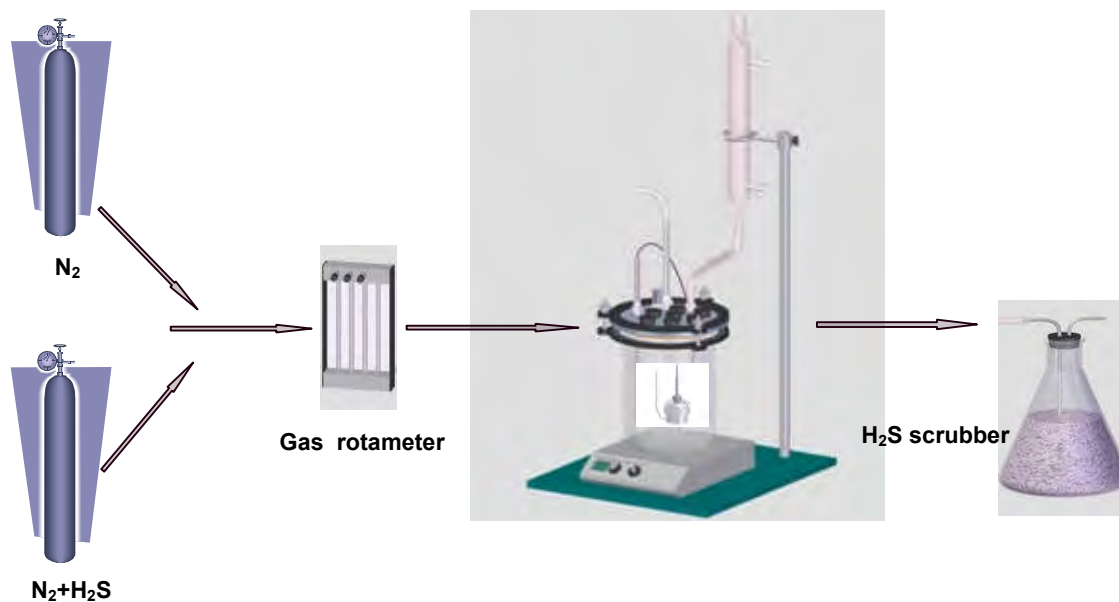


Figure 40. Experimental setup.

Experiments were performed in a glass cell filled with 2 liters of 1 wt.% sodium chloride solution. Initially the test cell was deoxygenated by purging with nitrogen. After that, H_2S gas of a defined concentration was added. The temperature was controlled by a hot plate with a thermocouple. The pH was adjusted to 5.0 by addition of deoxygenated hydrochloric acid.

An artificial pit, designed in-house, was used in this experiment⁸⁴. Figure 41 shows a schematic of the artificial pit design. The area ratio between cathode and anode is 1000:1. At the beginning of the experiment, the cathode was put into the solution. Linear polarization (LPR) measurements were conducted to monitor the corrosion rate. Then 50 ppm H_2S (0.05 mbar H_2S at 1 bar total pressure) was added into the solution.

When a stable corrosion rate and corrosion potential of the cathode were obtained, a fresh polished “anode” surface was inserted into the middle hole of the “cathode” surface. The depth of the artificial pit is easily adjusted and measured externally to the glass cell. After the corrosion potential of the anode reached a stable value (less than $\pm 0.5\text{mV}$ change), galvanic current measurement was conducted between the cathode and the anode.

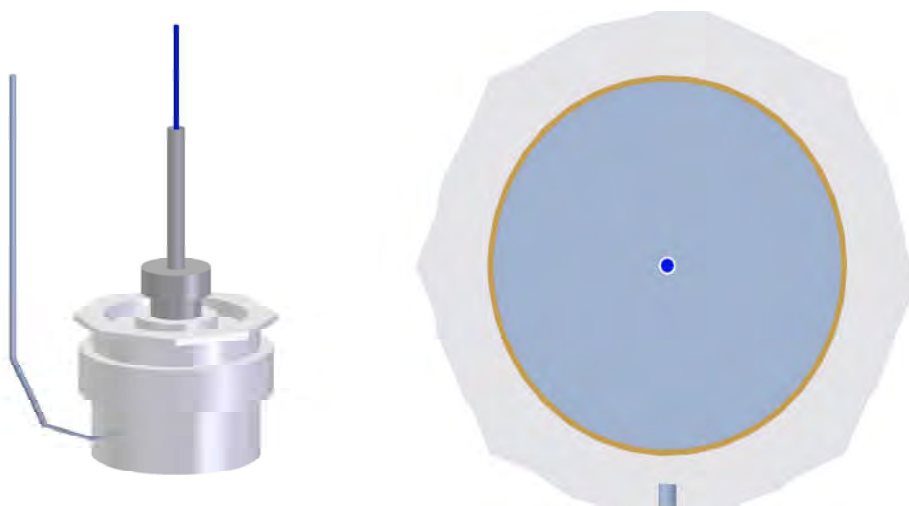


Figure 41. Schematic of an artificial pit.⁸⁴

4.4 Experimental results and discussion

4.4.1 Experimental results

Figure 42 shows the corrosion rate during the iron sulfide layer building process on the cathode. Corrosion rate of the cathode started at 0.4 mm/yr in the nitrogen purged system, H_2S was then added into the system. After 10 hours, the corrosion rate was stabilized at around 0.1 mm/yr. The corrosion potential of the cathode also stabilized. This suggests that a well protective layer was generated on the cathode surface.

Interestingly, the corrosion rate, as well as the corrosion potential, decreased dramatically right after H₂S was added into the system. It is worth noting that the potential change during the layer formation process in pure H₂S systems is different from in CO₂. In a sweet system, it has been observed that the corrosion potential will increase after a very protective layer of iron carbonate film formed on the steel surface. Detailed comparisons will be described later.

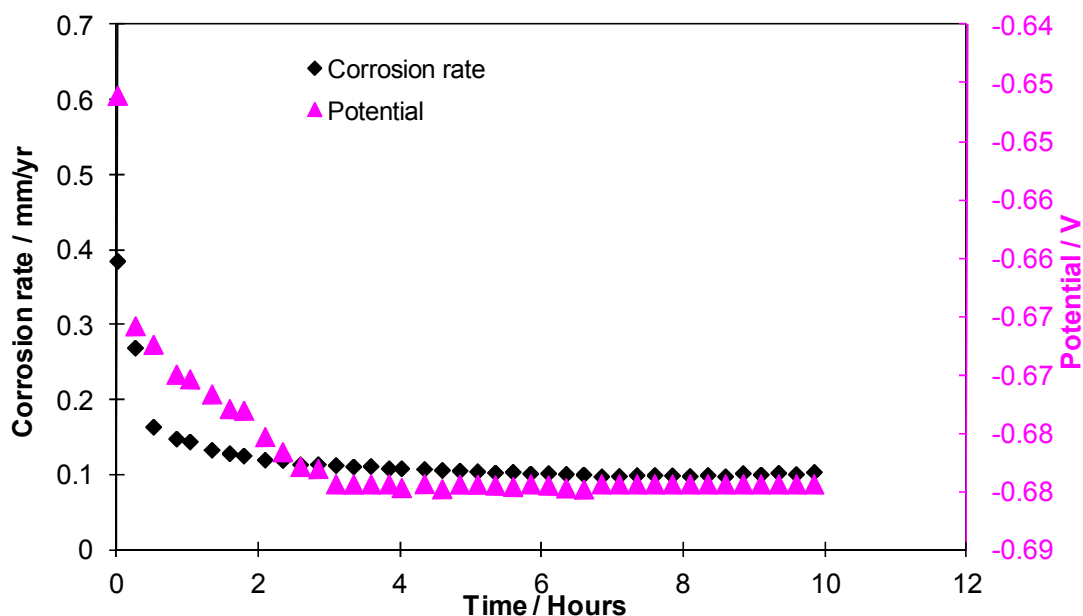


Figure 42. Uniform corrosion rates vs. time at 25°C, 50 ppm H₂S, 0 wt.% NaCl.

Figure 43 shows the galvanic current between the cathode and the anode. The anode was flush mounted. The result shows a small amount of galvanic current flowing from anode to cathode. The simply converted galvanic corrosion rate of 0.3 mm/yr is of the same magnitude as the general corrosion rate of the anode. Figure 44 and Figure 45

show the galvanic current measurement results with different pit depths of 4 mm and 6 mm, respectively. The converted galvanic corrosion rates are 0.2 and 0.4 mm/yr, which are not significantly different from the result with flush mounted anode. This suggests that the galvanic current does not depend on the depth of a pit. The detection of galvanic current between the cathode and anode indicate that it is possible that the galvanic effect may contribute to the pit propagation.

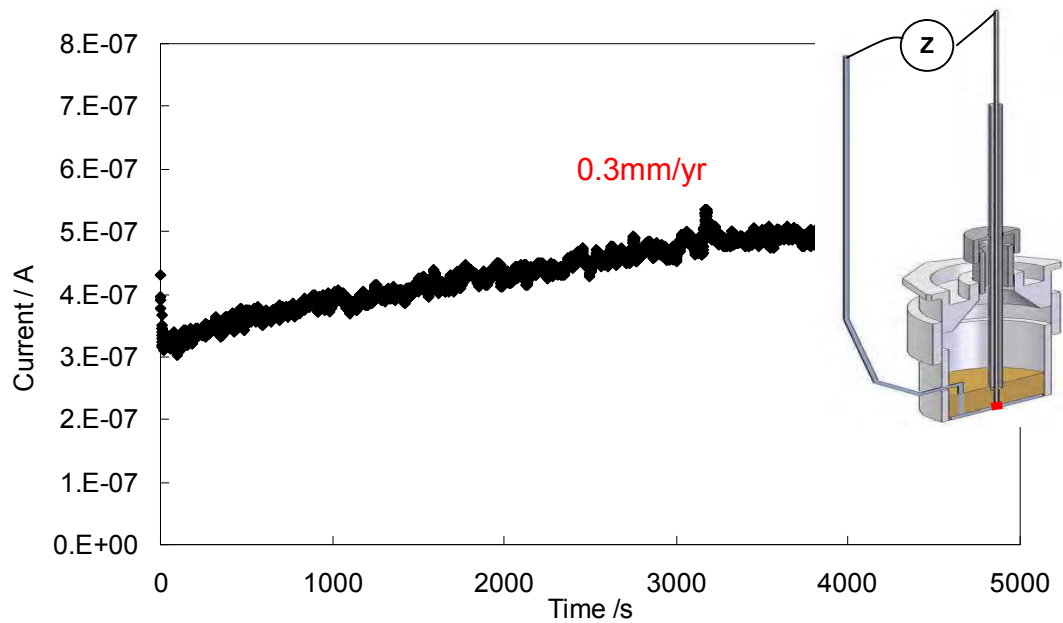


Figure 43. Galvanic current between cathode and anode, pit depth 0 mm.

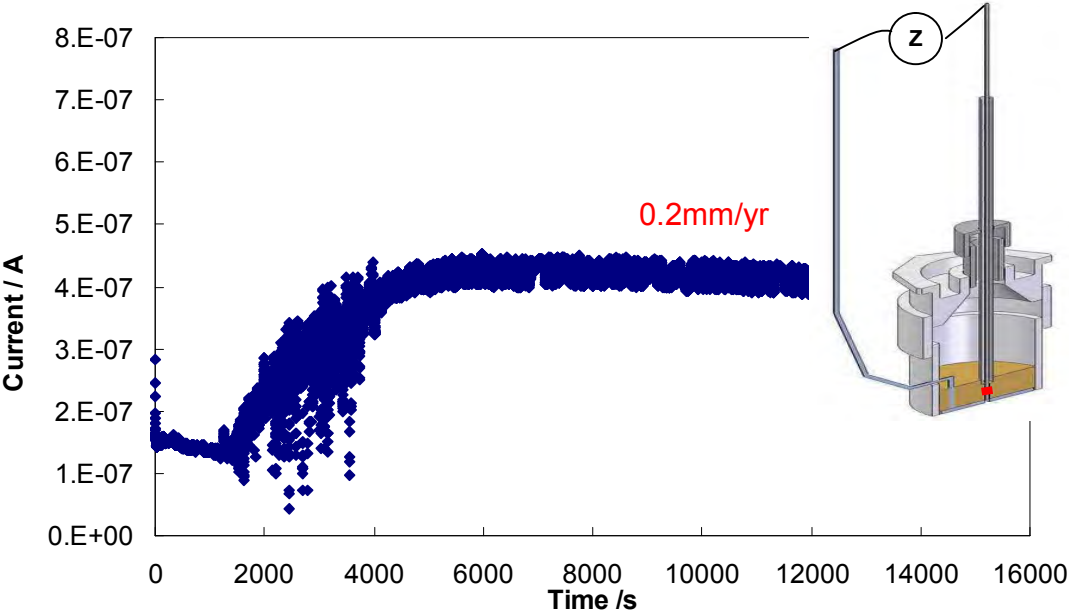


Figure 44. Galvanic current between cathode and anode, pit depth 4 mm.

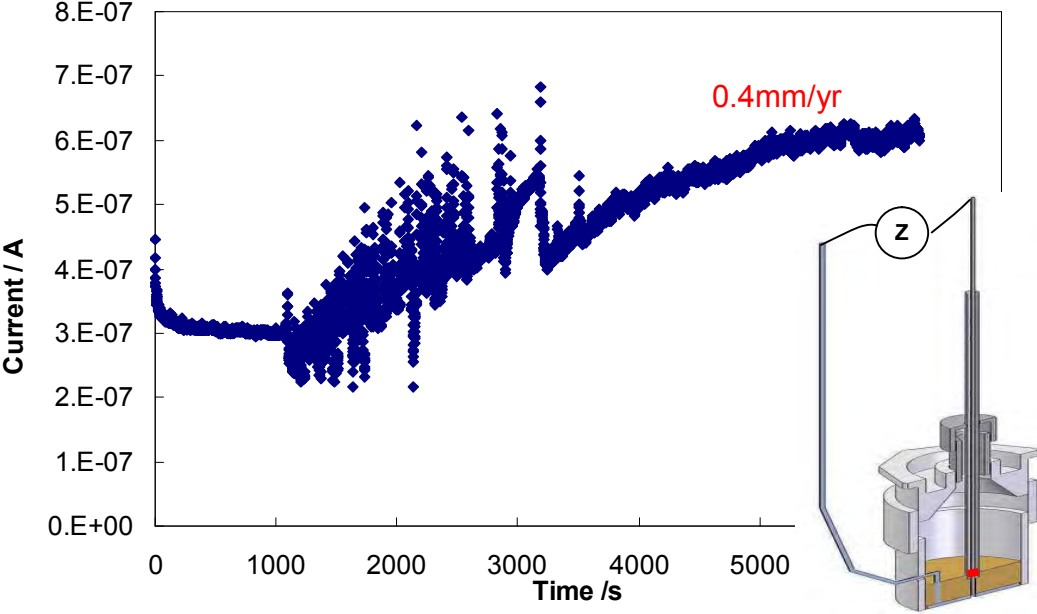


Figure 45. Galvanic current between cathode and anode, pit depth 6 mm.

To confirm the results of the first set of experiments, a set of repeat tests were conducted. Figure 46 shows the corrosion product layer forming process of the cathode. Corrosion rate decreased from 0.6 mm/yr to 0.1 mm/yr after the H₂S was added. The corrosion potential of the cathode decreased as well. The corrosion potential of anode was monitored in this set of experiments. Figure 47 shows a comparison of the stabilized cathode potential and the anode potential with time. The stabilized corrosion potentials of cathode and anode are similar, which suggests that the galvanic current between these two is negligible. The galvanic current measurement shown in Figure 48 confirmed this observation. The converted galvanic corrosion rate is around 0.06 mm/yr, much less than the general corrosion rate. When the pit depth was set to 6 mm, the stabilized corrosion potential of anode is much higher than the cathode potential (Figure 49). The galvanic current measurement is consistent with the potential measurement. The galvanic current is a negative value (Figure 50). It means that the current was flowing from cathode to anode. At this time the anode is protected.

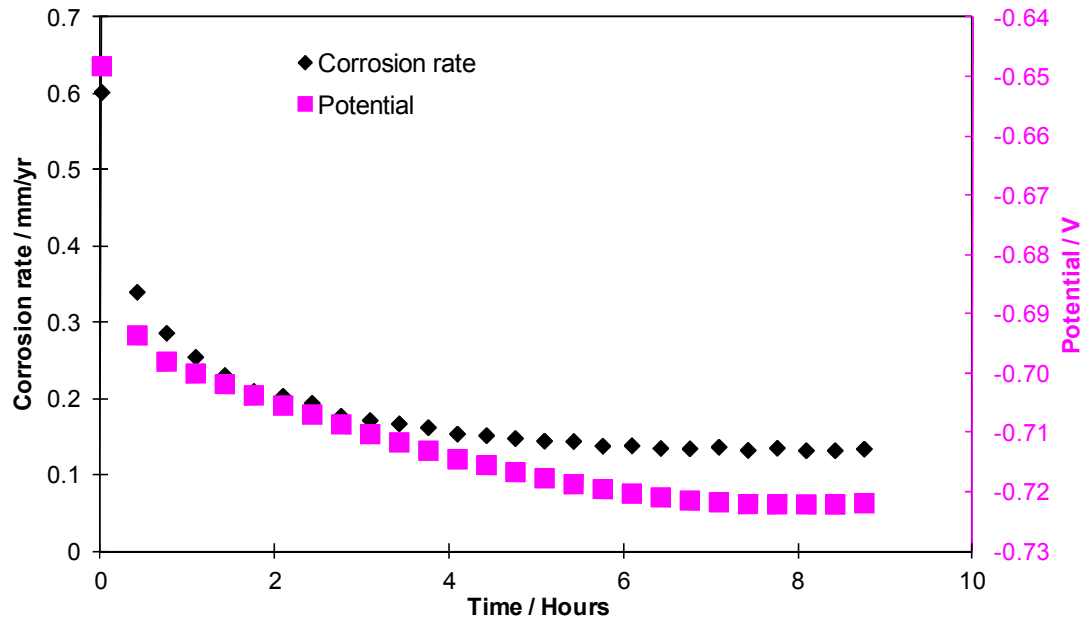


Figure 46. Corrosion rate and potential of cathode vs. time.

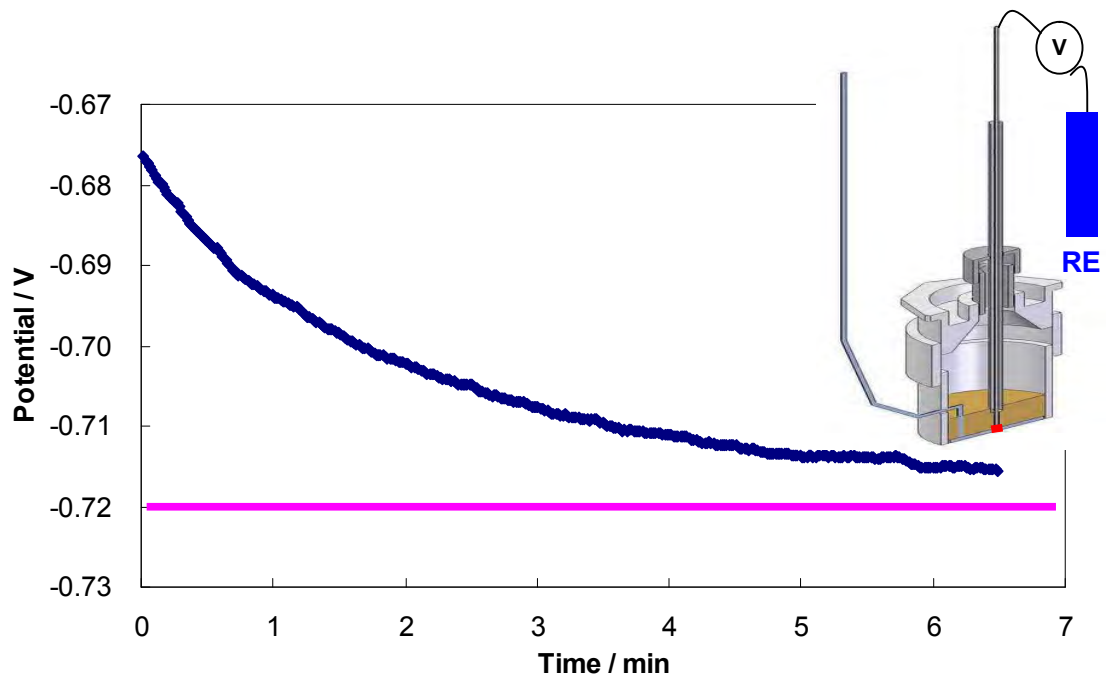


Figure 47. Comparison of potential change during iron sulfide layer forming process between cathode and anode. (pit depth 0 mm)

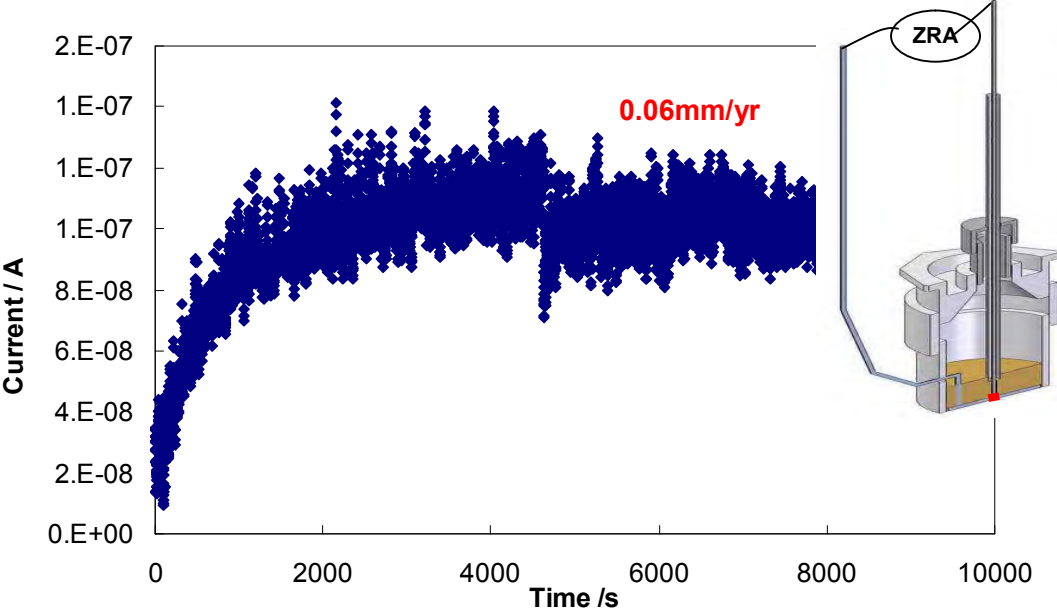


Figure 48. Galvanic current between cathode and anode, pit depth 0 mm.

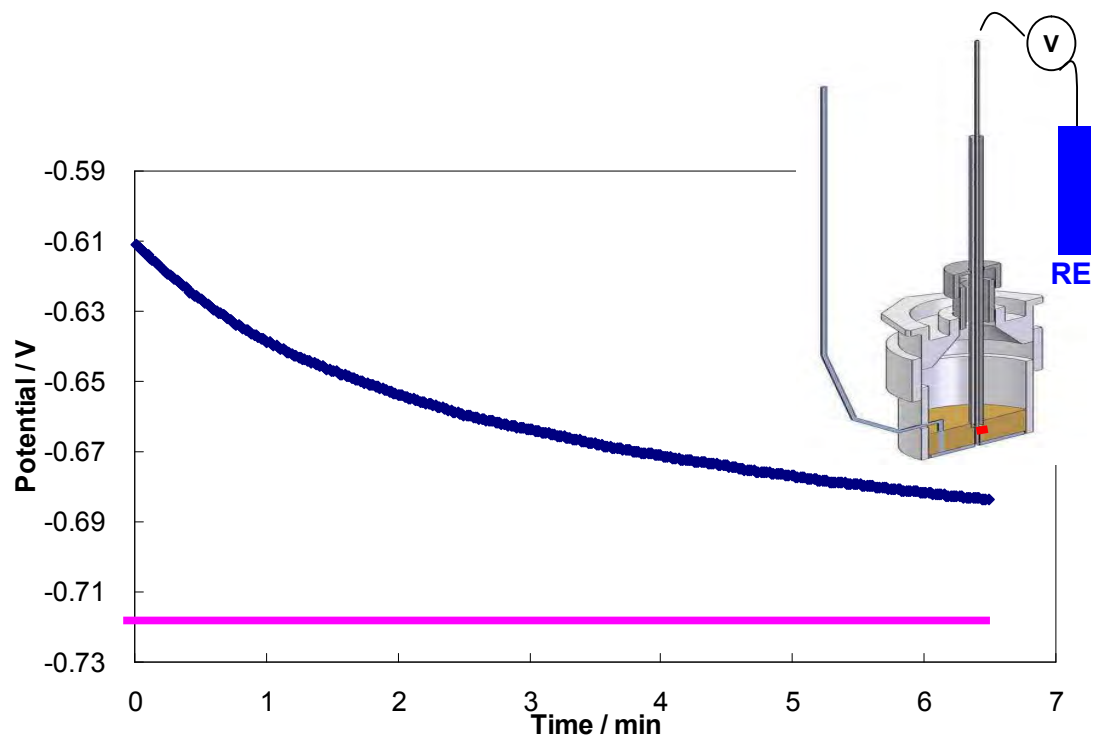


Figure 49. Comparison of potential change during iron sulfide layer forming process between cathode and anode. (pit depth 6 mm)

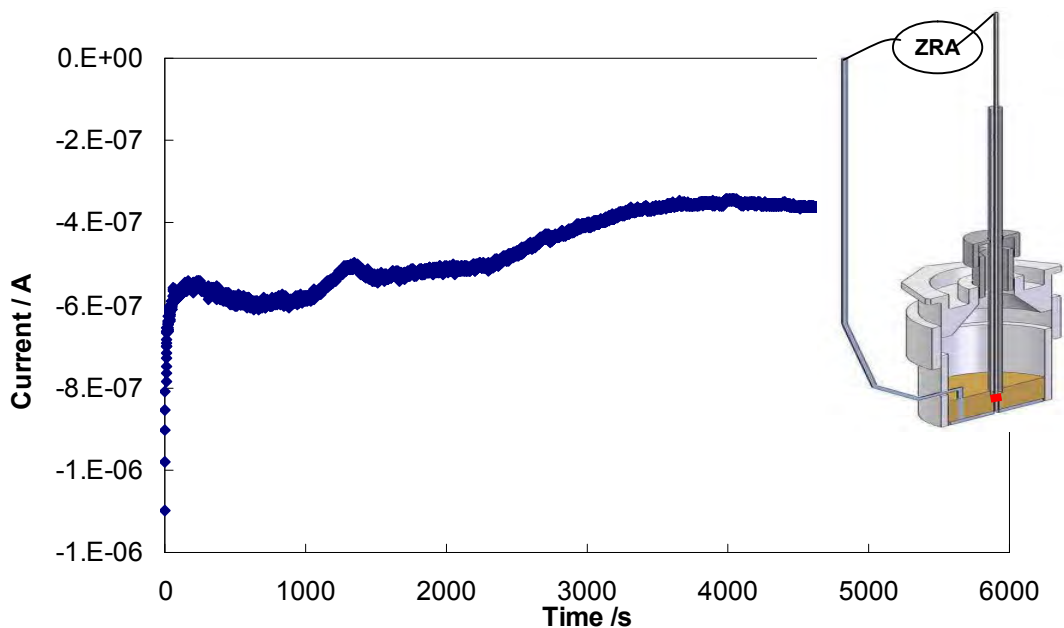


Figure 50. Galvanic current between cathode and anode, pit depth 6 mm.

4.4.2 Discussion

The presence of galvanic corrosion on the propagation of localized corrosion in sweet system has been observed and measured⁸³. However, from the experimental results described here, it appears that this mechanism does not hold in a pure H₂S system. In a sweet system, the corrosion potential of steel increases after a corrosion product layer forms on a steel surface. This is because the formation of passive layer alters the corrosion mechanism, as sketched in Figure 51. However, in a pure H₂S system, the observation was that the corrosion potential of steel decreased when iron sulfide layer formed on the steel surface. This is because the H₂S dominant corrosion is controlled by mass transfer as shown by a decrease in the limiting current (Figure 52).

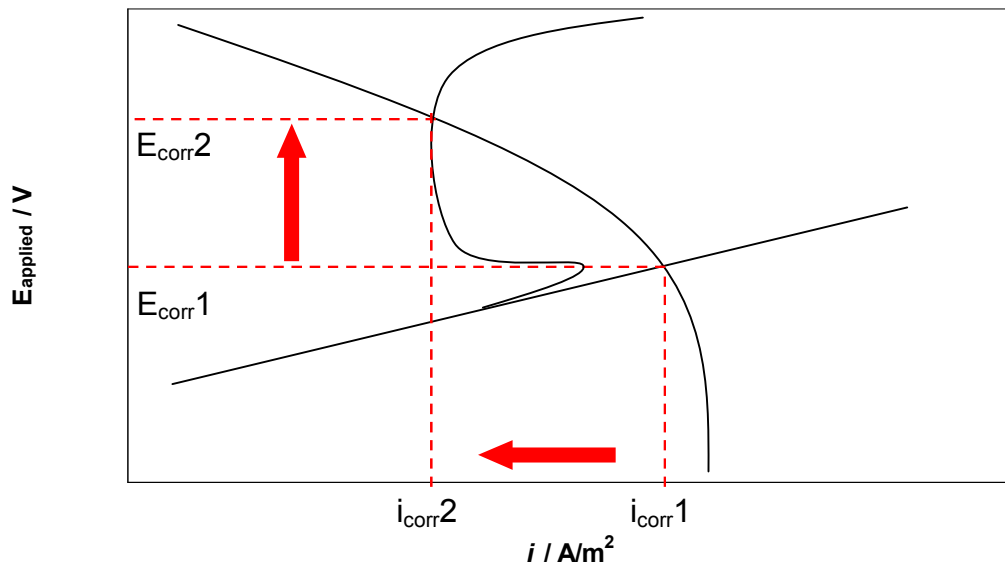


Figure 51. Simplified sketch of corrosion mechanisms in a sweet system showing the change in corrosion potential and corrosion current when a passive layer forms on the steel surface.

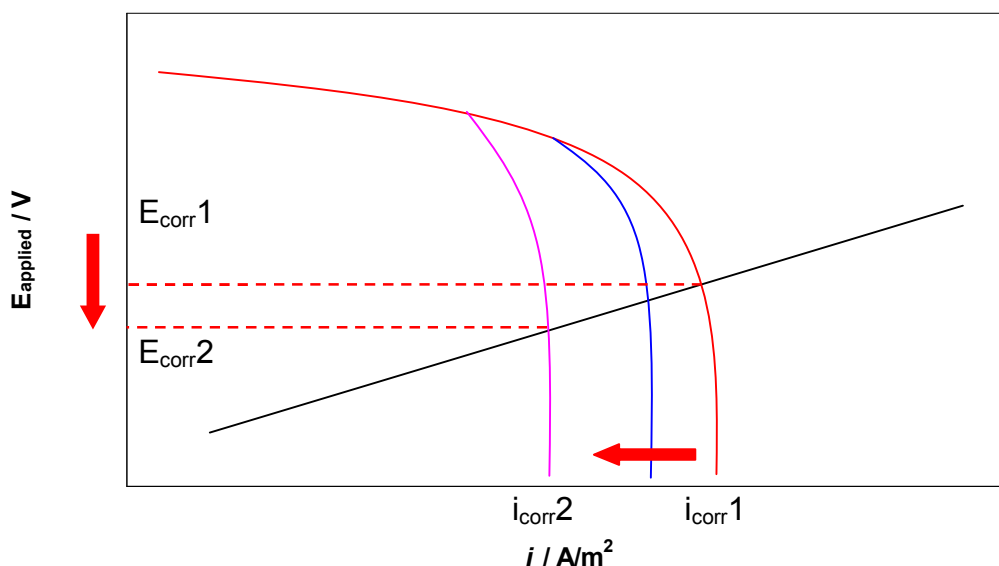


Figure 52. Simplified sketch of corrosion mechanisms in a sour system showing the change in corrosion potential and corrosion current for an iron sulfide layer building process in a pure H_2S system.

In order to understand propagation of localized corrosion for an iron sulfide layer covered surface, Figure 53 shows the three possibilities of potential difference between the cathode and anode that could happen after the pit is initiated. In the first case, the pit area is not covered by the iron sulfide layer and maintains its initial corrosion rate; therefore, the potential of the pit area stays unchanged. Since this is much higher than the potential of the surrounding steel area, the pit area would be protected. In the second case, the iron sulfide layer is reformed in the pit area right after it is initiated. Because of the mass transfer effect, the corrosion potential of the pit area will decrease. The final stabilized potential of the pit area is close to the potential of the surrounding steel area. At this time, the galvanic current between the pit and surrounding steel surface is negligible.

This case is closest to what was experimentally observed. The last case is for the corrosion potential of a pit to become lower than the potential of the surrounding steel. The galvanic current between the two surfaces would cause the pit to propagate. However, this case is not what was recorded in the present series of experiments. In the H₂S environment, the concentration of H₂S in a pit should be similar to that of the rest of the environment, or could be lower due to mass transfer effects. Consequently, the pit potential could only be virtually equal or slightly higher than the potential of steel already covered by iron sulfide layer. Therefore there could be no significant galvanic current flowing from a pit to the iron sulfide layer covered steel surface in a system with only H₂S as the corrosive species.

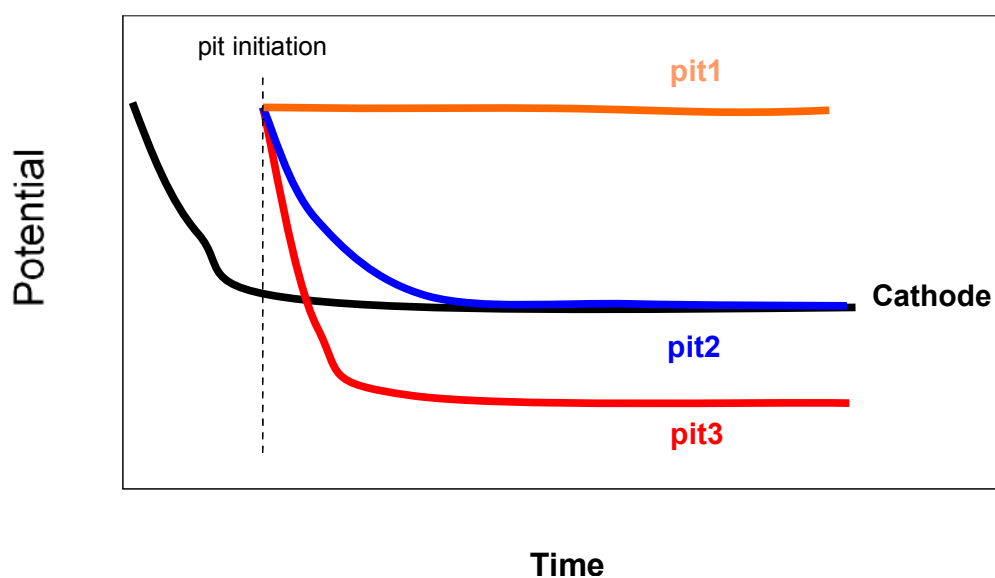


Figure 53. Simulation of three possible potential difference scenarios during pit growth.

4.4.3 Summary

In the experiments described above, it appears that the propagation of localized corrosion cannot be caused by galvanic effects when only H₂S is present in the system. This is due to a decrease of potential of iron sulfide layer covered surface. When iron sulfide layer is locally broken down, the potential of the bare metal surface is higher than the iron sulfide covered surface. Therefore, even if pitting attack is initiated it will not necessarily propagate. However, this galvanic theory cannot be simply excluded. Similar studies need to be done in the H₂S/CO₂ system to verify the feasibility of galvanic effects.

CHAPTER 5 INVESTIGATION OF THE ROLE OF ELEMENTAL SULFUR IN LOCALIZED CORROSION OF CARBON STEEL

5.1 Introduction

Elemental sulfur is one of the most abundant elements occurring on Earth. It is typically present as yellow crystals⁸⁵. People have been aware of the presence of sulfur for several thousand years and have used it for various purposes such as medicine, fertilizer, explosive powder and many other applications⁸⁶.

Elemental sulfur has different molecular formulae, mainly depending on the temperature. This is known as allotropy, akin to diamond, graphite, C₆₀ and related nanotubes in the carbon system. The number of atoms in sulfur allotropes can vary from 2 to *ca.* 10⁶ (polymeric)⁸⁷. Cyclooctasulfur with formula S₈ is the most thermodynamically stable allotrope under normal conditions⁸⁷. Its melting point is 115.21°C. The boiling point of elemental sulfur is reported to be 444.6°C and it can be made to sublime⁸⁸ at lower temperatures

Cyclooctasulfur itself has various crystallographically distinct allotropes including orthorhombic (α) sulfur, monoclinic (β) sulfur, and monoclinic (γ) sulfur⁸⁷. Orthorhombic (α) sulfur is stable up to 95.2°C⁸⁷; its crystal structure has sixteen molecules of S₈ in each unit cell. Monoclinic (β) sulfur is the form of sulfur stable between 95.2°C and its melting point of 115.21°C. Despite the phase changed at these temperatures, the structure of the S₈ ring remains the same⁸⁷. Monoclinic (β) sulfur has six molecules of S₈ in one unit cell⁸⁹. At temperatures between the melting point and boiling point, (β) sulfur is converted to (γ) sulfur⁸⁷.

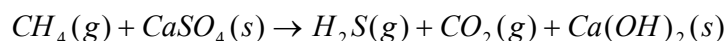
Elemental sulfur is extremely soluble in carbon disulfide. The solubility of sulfur in carbon disulfide is increasing with an increase of temperature. Other than carbon disulfide, elemental sulfur is not very soluble in other organic solvents. Elemental sulfur is barely soluble in water. The solubility of elemental sulfur in water is $(1.9 \pm 0.6) \times 10^{-8}$ mole of sulfur/kg⁸⁹.

Similar to H₂S, elemental sulfur is also of concern to the oil and gas industry. As sweet fields are being depleted, more and more sour oil and gas wells are developed. Elemental sulfur is readily found in the field especially in extremely sour reservoirs, which may present severe problems to oil and gas production.

5.2 Literature review

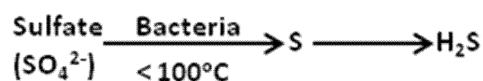
Elemental sulfur is originally present in some sour gas reservoirs, especially in extremely sour gas environments (H₂S concentrations exceeding ~ 10000 ppm): and can be formed by a number of pathways.

Elemental sulfur can be generated by thermochemical sulfate reduction as shown below⁸⁹:

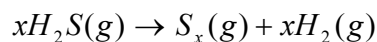


As stated previously for H₂S formation, this can involve higher alkanes⁸⁹.

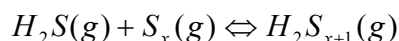
Microbial reduction of sulfate can also lead to the formation of elemental sulfur⁸⁹:



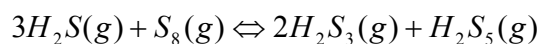
At high H₂S concentration and high temperature, H₂S may dissociate and form elemental sulfur⁸⁹:



Elemental sulfur is mixed in the sour gas either in physical mixture or in chemical equilibrium with hydrogen polysulfide⁹⁰. It has been hypothesized that hydrogen sulfide, elemental sulfur and hydrogen polysulfides can coexist in an equilibrium system in elevated temperatures³⁴. The simplest way to write this reaction corresponds to:



However, such processes will involve more than one hydrogen polysulfide species, for example³⁴:



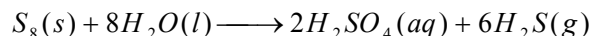
When temperature and pressure drops elemental sulfur will deposit on the internal pipeline surface when its saturation value has been exceeded, i.e., the sulfur is no longer soluble in the acid gas phase. This deposition process can be considered as being the reverse of sublimation.

In the presence of water, sulfur has been reported to cause catastrophic corrosion problems.

Researchers have attempted to investigate the mechanism of elemental sulfur corrosion of mild steel since the 1970's. However, the mechanism is still not well established.

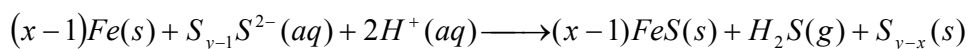
Maldonado-Zagal and Boden⁹¹ studied the sulfur hydrolysis reaction. A decrease of aqueous pH to 2.0 was observed after sulfur was mixed with deionized water at

ambient temperature. A sulfur hydrolysis reaction was proposed based on this observation:



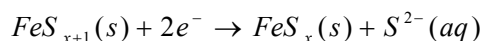
The acidification caused by sulfur hydrolysis was believed to be the dominant factor of elemental sulfur corrosion. According to this mechanism, elemental sulfur does not need to have a direct contact with the steel surface to cause severe corrosion problems. Elemental sulfur corrosion was reduced to acid corrosion by sulfuric acid.

MacDonald, *et al.*,⁹² hypothesized that an electrochemical reaction between iron and polysulfide is the driving force for corrosion in systems where elemental sulfur is present.



According to the reaction, H₂S was generated during the elemental sulfur corrosion process.

In 1991, G. Schmitt⁸⁵ performed similar studies on sulfur hydrolysis. However, no significant acidification was observed after sulfur was mixed with water. The sulfur hydrolysis reaction proposed by Maldonado-Zagal and Boden was still believed to be proceeding, but at a very slow rate. Sulfur/iron corrosion studies were also performed in this study. Significant corrosion attack was observed when sulfur was in direct contact with the steel surface. In the end, an electrochemical mechanism for elemental sulfur corrosion was proposed:

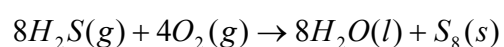


Based on this mechanism, to have severe corrosion, sulfur has to be in a direct contact with the steel surface. However, there is no direct experimental evidence to prove the electrochemical nature of elemental sulfur corrosion.

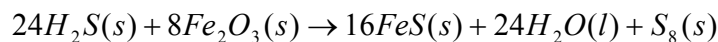
Later on, Dowling^{93,94} studied the corrosion of materials used in handling and storage of solid elemental sulfur. Following that work, the further mechanistic studies of elemental sulfur corrosion could not be found in the open literature. Most of the studies on elemental sulfur corrosion focused on how to mitigate the corrosion. A number of studies⁹⁵⁻¹⁰¹ were performed on the inhibition of elemental sulfur corrosion. However, due to the severity of elemental sulfur corrosion, most of the attempts on inhibition were not successful. Physical coating (aluminum and epoxy coating) as physical barrier and chemical inhibitor including chromate (CrO_4^{2-}), vanadate (VO_3^-), and hydrogen peroxide (H_2O_2) have been reported to be applied for the inhibition of elemental sulfur corrosion⁹³. However, neither of these approaches works well. Therefore, a good understanding of the elemental sulfur corrosion mechanism would be helpful as a baseline to find a good way to mitigate the sulfur corrosion problem in the oil and gas industry.

As stated above, in most cases, sulfur generated through geological processes is originally present in the gas reservoir. However, in oil and gas fields, elemental sulfur may arise from various sources. Oxygen contamination can happen in many different situations including shutting in production, upstream compression and injection of chemicals such as inhibitors. This may result in the formation of elemental sulfur³⁴:

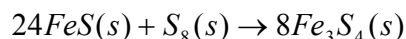
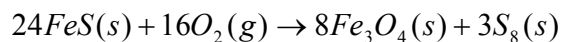
Oxidation of H_2S :



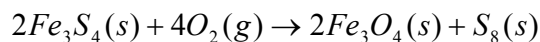
Reaction between iron(III) oxide and H₂S (reduction of ferric oxide to ferrous sulfide):



Laboratory studies have shown that formation of elemental sulfur by iron sulfide oxidation is possible^{102,103}. Boursiquot¹⁰², *et al.*, have performed experimental work on dry oxidation of mackinawite powder. In their studies, iron sulfide was synthesized by a reaction of iron wire with sodium sulfide in acetic acid. The produced iron sulfide was then freeze dried and exposed to air. Figure 54¹⁰² shows the X-ray diffraction data of the oxidation products. The data clearly show that after a three month exposure to air, elemental sulfur (labeled S) became a dominant species. Based on the results, the reaction sequence equations have been proposed as¹⁰²:



According to the reactions above, mackinawite is first oxidized to magnetite and elemental sulfur, then sulfur reacts with mackinawite and forms greigite. Boursiquot¹⁰², *et al.*, reported that the generated magnetite was “poorly crystalline”, consequently, as an amorphous phase it will not be detected by X-ray diffraction. Longer exposure to oxygen leads to the oxidation of greigite:



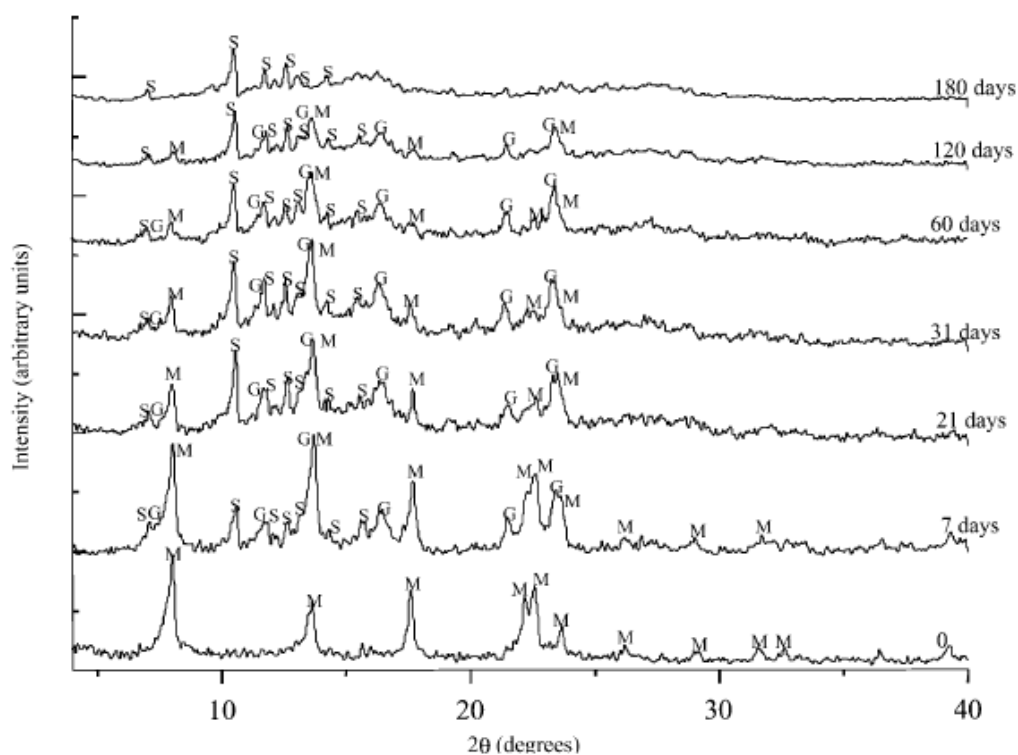
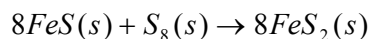


Figure 54. X-ray diffraction data from S. Boursiquot¹⁰² (S: sulfur [S₈]; M: mackinawite [FeS]; G: greigite [Fe₃S₄]).

The experimental results performed by Boursiquot *et al.*, suggests that it is very possible that iron sulfide layer formed on the steel surface can be oxidized to elemental sulfur.

Benning, *et al.*,¹⁰³ did similar studies on oxidation of iron sulfide powder. However, they conducted the oxidation process in an aqueous solution. Figure 55. X-ray diffraction data shows their X-ray Diffraction data. Data sets 1 and 2 shown in the figure are the diffraction patterns before oxygen was introduced. Mackinawite is the only component detected. Data sets 3 to 5 correspond to diffraction patterns acquired after air was introduced to the solution. After 24 hours exposure to oxygen, sulfur was detected.

With time, the sulfur content first increased and then decreased. After 10 days, the dominant oxidation product became pyrite. This is likely due to the reaction between sulfur and mackinawite (with greigite acting as an intermediate):



Although in the end elemental sulfur was not the dominant phases detected by X-ray diffraction, the presence of high content of pyrite suggests elemental sulfur was generated by oxidation of mackinawite.

It is worth noting, the peak positions of elemental sulfur and iron sulfide species were different in the XRD data from Boursiquot's and Benning's experiments. This is due to the different X-ray sources used in their experiments. In Boursiquot's study, a classical powder diffractometer with transmission geometry equipped with a Mo tube was used. In Benning's experiments, the oxidation products were characterized with a Rigaku Geigerflex. (CuK_α radiation, scanning rate 2° / minute for a 2θ range of 5 – 65°)

Both Boursiquot's and Benning's experimental studies on oxidation of mackinawite indicate that elemental sulfur can be formed by oxidizing this iron sulfide powder. Therefore, the oxygen contamination could cause a severe corrosion problem if associated with pipelines containing iron sulfide because of the high possibility of producing elemental sulfur.

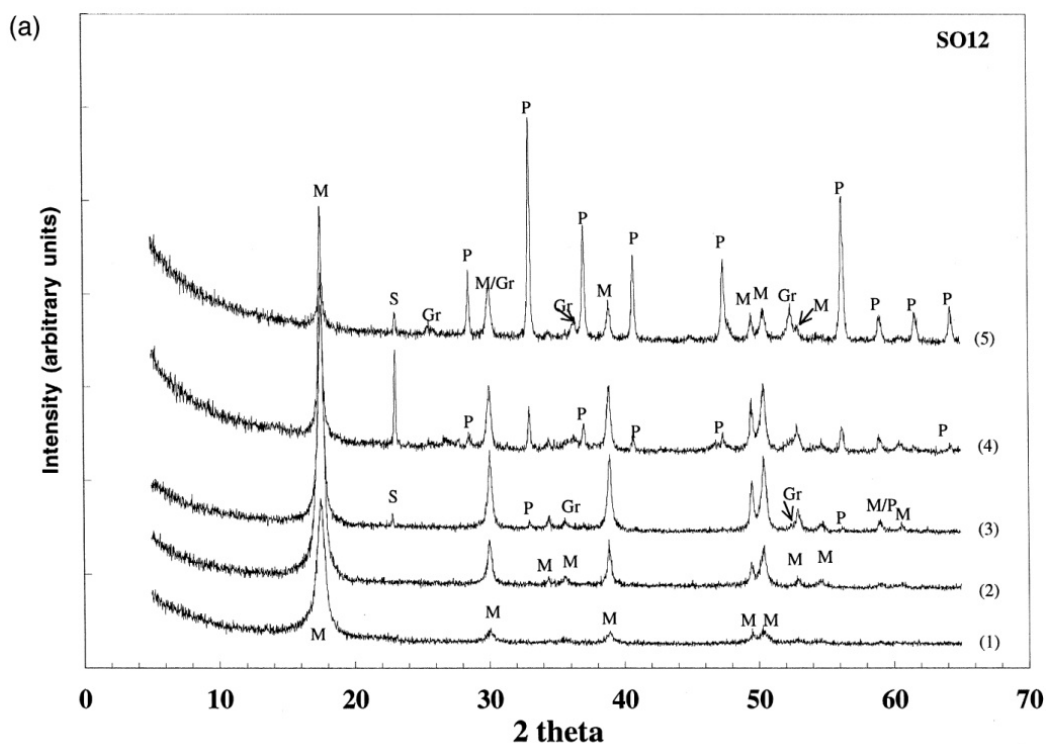


Figure 55. X-ray diffraction data for mackinawite oxidation in aqueous solution (S: sulfur [S_8]; M: mackinawite [FeS]; G: greigite [Fe_3S_4]; P: pyrite [FeS_2]).¹⁰³

5.3 Objectives and test matrices

The objective of this work was to investigate the corrosion mechanism of carbon steel in the presence of elemental sulfur. According to the current literature on elemental sulfur corrosion, the experimental work was divided into two directions: aqueous sulfur hydrolysis reaction mechanisms and direct sulfur/iron reaction mechanisms. The effects of various parameters on sulfur/iron reaction were investigated, such as salt effects, pH effects, CO_2 and H_2S .

The first step was to investigate formation of elemental sulfur. The objective of this study was to see if elemental sulfur can be generated in the lab by oxidation of iron

sulfide formed on a steel surface. This scenario represents the case in which elemental sulfur is not originally present on the steel and then forms upon exposure to oxygen. The iron sulfide layer building experiments were conducted at two different H₂S concentrations, 100 ppm and 10,000 ppm. The gas source for the oxidation process is air (20.9% oxygen content). The test material was X65, which is normally used in pipeline construction. The detailed test condition is shown in Table 5.

Table 5. Test conditions

Parameters	Conditions
Total Pressure	1 bar
Temperature	80°C
H ₂ S Concentration	100 ppm ($P_{\text{H}_2\text{S}} = 0.1 \text{ mbar}$ at $P_{\text{total}} = 1 \text{ bar}$), 10000 ppm ($P_{\text{H}_2\text{S}} = 10 \text{ mbar}$, $P_{\text{total}} = 1 \text{ bar}$)
Solution	1 wt.% NaCl purged with nitrogen
Initial pH	6.5
Material	X65

5.4 Experimental setup

The experimental setup for oxidation of iron sulfide is shown in Figure 56. A cylinder containing approximately 500 to 12000 ppm H₂S gas mixed with nitrogen was used as the source of the H₂S. A second cylinder containing pure nitrogen was used to dilute the H₂S concentration from the source with a mixing gas rotameter. Before the gas was bubbled into the test solution, the H₂S concentration in the gas phase was measured with a H₂S colorimetric detector tube.

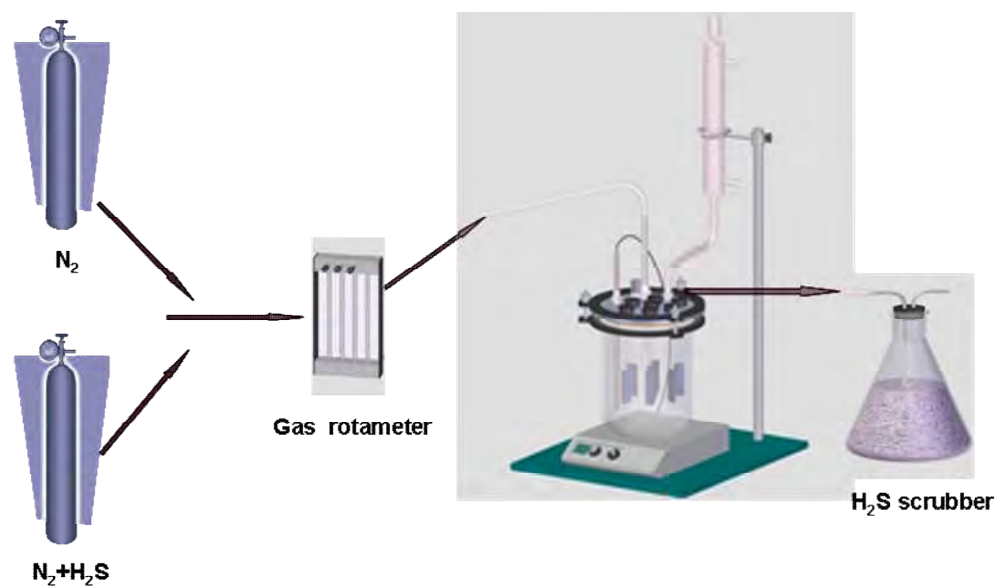


Figure 56. Experimental setup

Experiments were performed in a glass cell filled with 2 liters of deionized water at a salt concentration of 1 wt.%. Initially the test cell was deoxygenated by purging with nitrogen. After that, H_2S gas of a defined concentration was added. The temperature was controlled by a hot plate with a thermocouple. The initial pH was 6.5. After 2 to 4 days, the purging gas was changed from a H_2S/N_2 mixture to Certified Breathing Air. Specimens were taken out at various time intervals (1 day, 4 days, etc.) to analyze produced layers.

Parallel to this study, sulfur hydrolysis experiments were performed to investigate the temperature effects on the acidification of pure water with elemental sulfur. This involved adding elemental sulfur to deoxygenated deionized water purged with nitrogen and measuring the pH of each test system with time. The chosen temperature range was 25-150°C. Experiments were conducted in both glass cells and autoclaves. Additional

high temperature sulfur hydrolysis experiments were conducted in an autoclave, see Figure 57.

In these experiments, a droplet of sulfur was first weighed and then put in a glass Petri dish. Approximately 1 gram of sulfur was used for each experiment. The Petri dish was then transferred to the autoclave, previously filled with 500 ml deionized water. Nitrogen was purged through the solution to facilitate deoxygenation. After 40 minutes of purging, the autoclave was pressurized to 300 psi with nitrogen and heated to the desired temperature. After 24 hours, the autoclave was depressurized and the test solution sampled. During the depressurizing process, a GASTECTM pump with a colorimetric tube was used to determine the possible presence of H₂S in the gas phase. The reaction solution was sampled and analyzed by ion chromatography to identify the anionic species present in the test solution after equilibration. The system was cooled down to room temperature and the pressure released. pH measurements were conducted after each test.

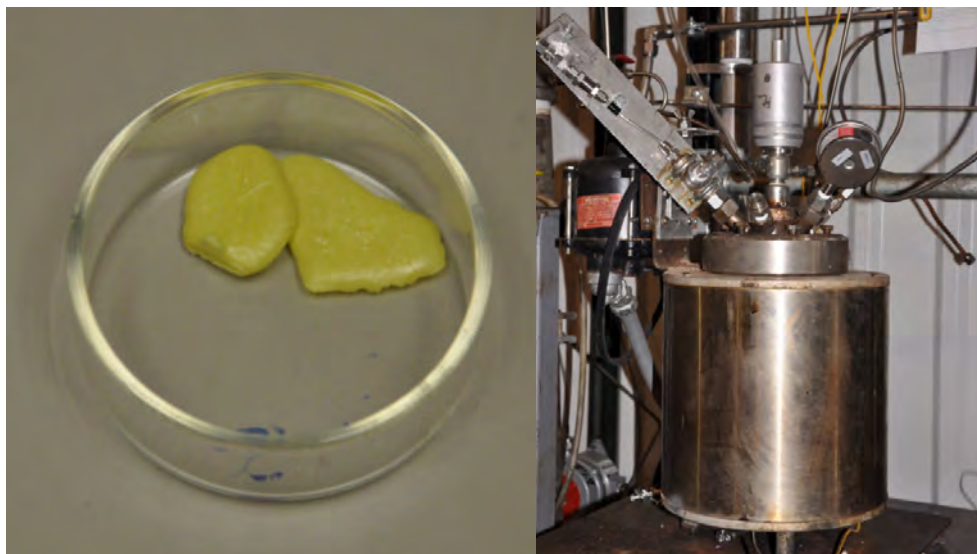


Figure 57. Sulfur in a glass Petri dish and the autoclave used in the sulfur hydrolysis experiments.

For the corrosion experiments (investigating direct sulfur/iron reaction), elemental sulfur (ACROS 99.999%) was deposited onto polished specimens by heating it slightly above its melting-point (115°C) then poured onto the X65 steel specimen surface. This gave uniform coverage of adherent sulfur to the steel specimen surface. Care was taken not to oxidize the sulfur as it was heated. Prior to depositing sulfur, the steel specimen polishing followed the same general procedure. The sand paper with increasing grit number was used in the increasing order: 240, 400, 600. After polishing, specimens were immersed in isopropyl alcohol in an ultrasonic cleaner for 1 to 2 minutes, and then air dried.

Specimens thus prepared were then transferred to a glass cell for corrosion experiments. Depending on the test conditions, the test solution was either deionized

water or different salt solutions. The test solution was either purged with nitrogen, carbon dioxide or H₂S.

Corrosion specimens were removed from the glass cell and characterized after certain durations (1 day, 4 days or 5 days). Prior to analysis, un-reacted sulfur was mechanically removed from the specimen surface. Samples were characterized with a scanning electron microscope (SEM), EDAX energy dispersive X-ray spectroscopy attachment (EDX), infinite focus microscope (IFM). Select specimens were analyzed by a X-ray diffractometer (XRD). XRD data was taken from layers directly on the corrosion specimens. Corrosion products were then removed by treatment with Clarke's solution, and the specimen's surface re-characterized by IFM. Localized corrosion rates were determined by analysis of IFM data whereas general corrosion rates were obtained by the weight loss method.

5.5 Experimental results and discussion

The experimental results are illustrated below in two parts. The results of in situ oxidation of iron sulfide to give elemental sulfur are shown first followed by the results related to the mechanisms of elemental sulfur corrosion of mild steel.

5.5.1 Oxidation of iron sulfide

This section of the experimental results is separated into two parts, 100 ppm H₂S and 10000 ppm H₂S. The following paragraphs further describe each condition.

5.5.1.1 100 ppm H₂S (0.1 mbar H₂S at P_{total} 1 bar)

5.5.1.1.1 LPR measurement

Figure 58 shows the LPR corrosion rate of RCE specimen with time. The initial corrosion rate (nitrogen purged) is around 0.1 mm/yr. The corrosion rate decreased immediately right after 100 ppm H₂S was bubbled through the test solution. This suggests that a protective iron sulfide corrosion product layer was formed on the specimen surface. The corrosion rate kept decreasing with time and stabilized at a very low value after four days. At the fourth day, the purging gas was changed from the H₂S/N₂ mixture to the air. The corrosion product started to be oxidized. It is clearly seen that the LPR corrosion rate increased instantly after air was purged through the system. It appears that oxygen thereafter dominated the corrosion process.

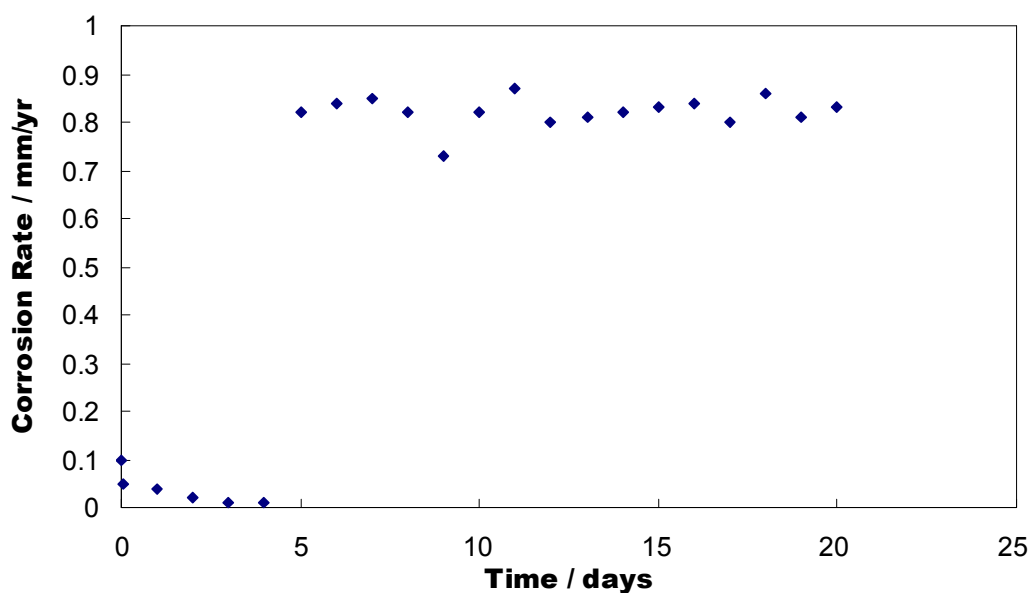


Figure 58. LPR corrosion rate vs. time at 100 ppm H₂S (layer formation)

5.5.1.1.2 Analysis of corrosion and oxidation products

Corrosion and oxidation products were analyzed by SEM, EDX, XRD, and Raman Spectroscopy.

Figure 59 shows the SEM image and EDX spectrum of a specimen surface after a 1 day exposure. A very thin layer of corrosion product formed on the specimen surface, this appears to be discontinuous. EDX data show that sulfur and iron are the main components of this product, consistent with the formation of FeS.

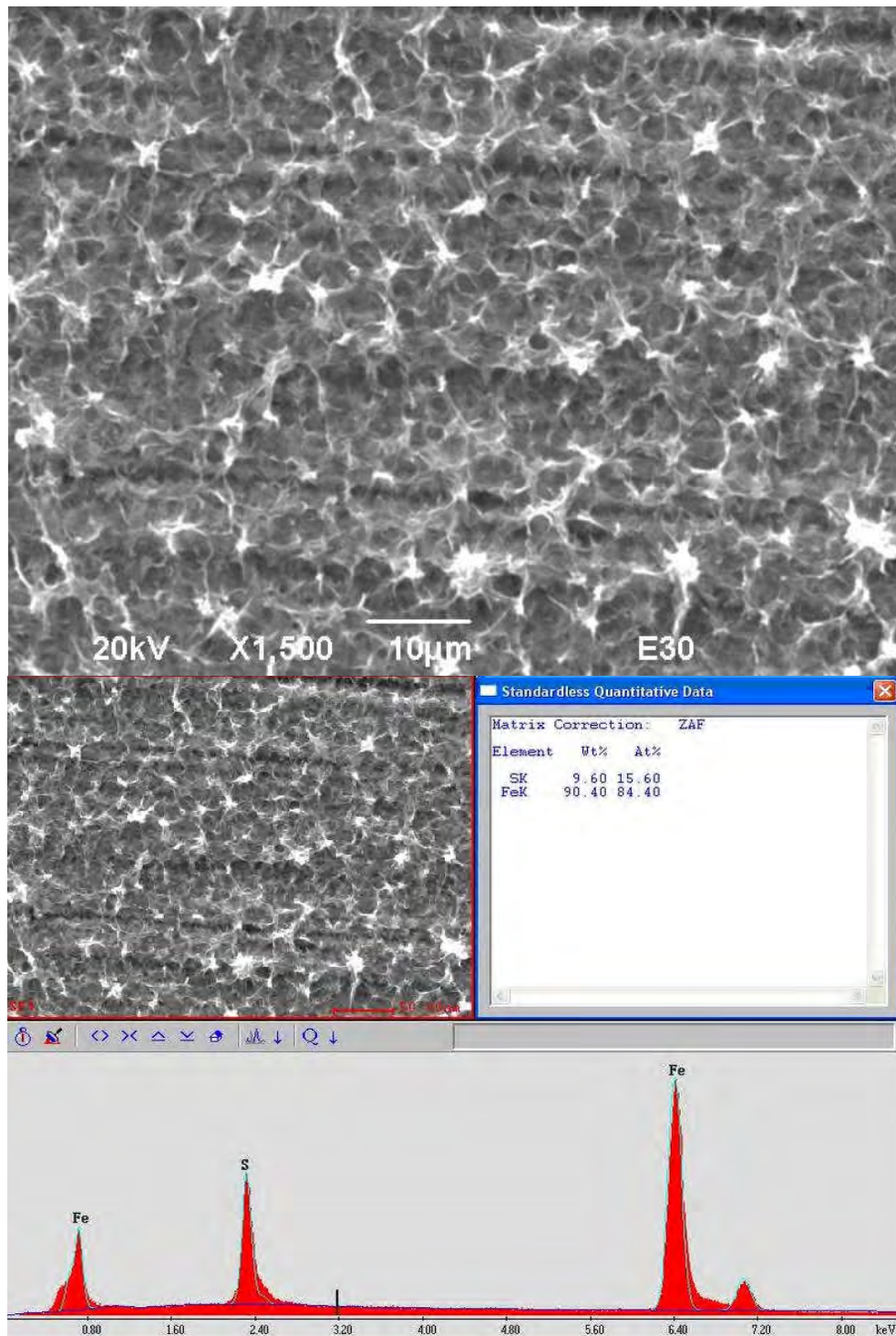


Figure 59. SEM image and EDX spectrum of a specimen surface after a 1 day exposure to 100 ppm H₂S.

In Figure 60 the morphology of the iron sulfide and oxidation product layer formed on the specimen surface after a 1 day exposure to air is shown. In the SEM image, it is clearly seen that a layer with new features formed on the specimen surface – one with a much less well defined structure. Its EDX spectrum shows an oxygen peak, which suggests that it could be some type of iron oxide.

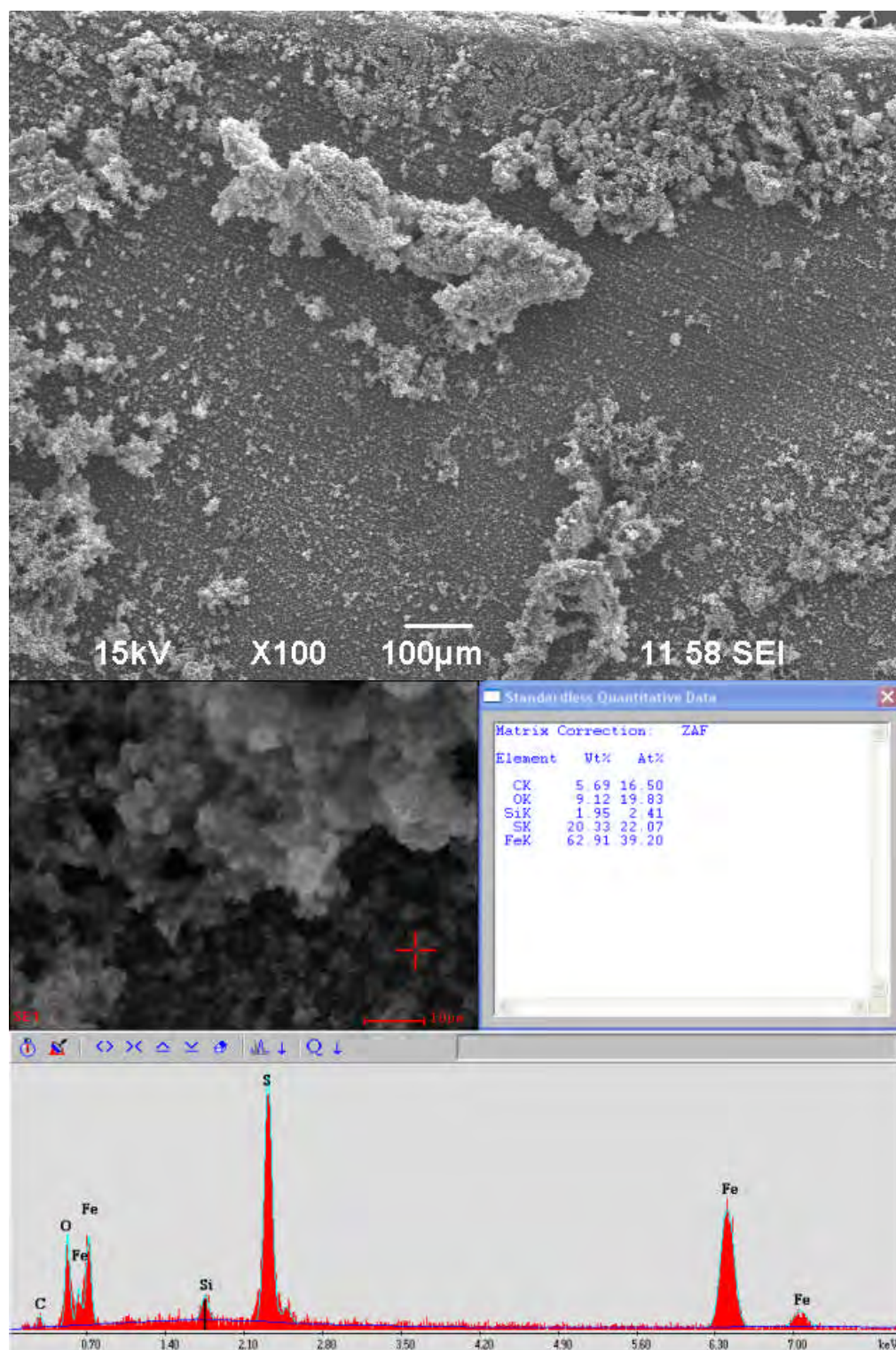


Figure 60. SEM image and EDX spectrum of a specimen surface after a 1 day exposure to air (H_2S was stopped purging)

After 5 days exposure to air, the layer on the specimen surface (Figure 61) shows a similar morphology as the corrosion product layer formed after the first day. However, EDX shows much higher oxygen content.

Figure 62 and Figure 63 show the SEM images and EDX spectra of specimen surfaces after 10 and 16 days exposure to air, respectively. The morphology of the corrosion products formed on these two specimens does not show any significant differences. The corrosion product layer has become much denser and thicker compared with the one formed at the earlier time. EDX spectra indicate similar composition, with the peak for oxygen now being of the highest intensity.

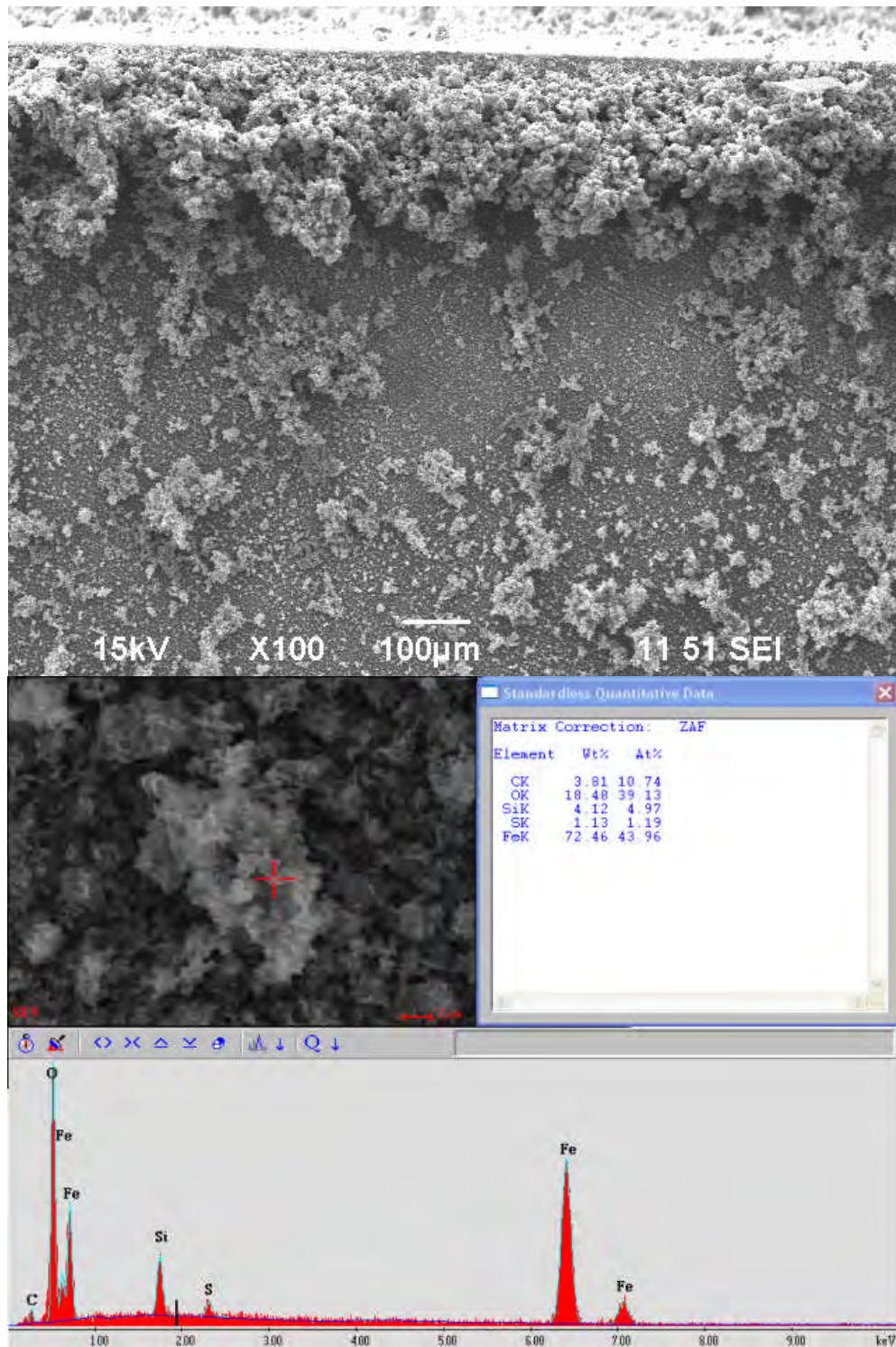


Figure 61. SEM image and EDX spectrum of a specimen surface after a 5 days exposure to Certified Breathing Air (H_2S was stopped purging)

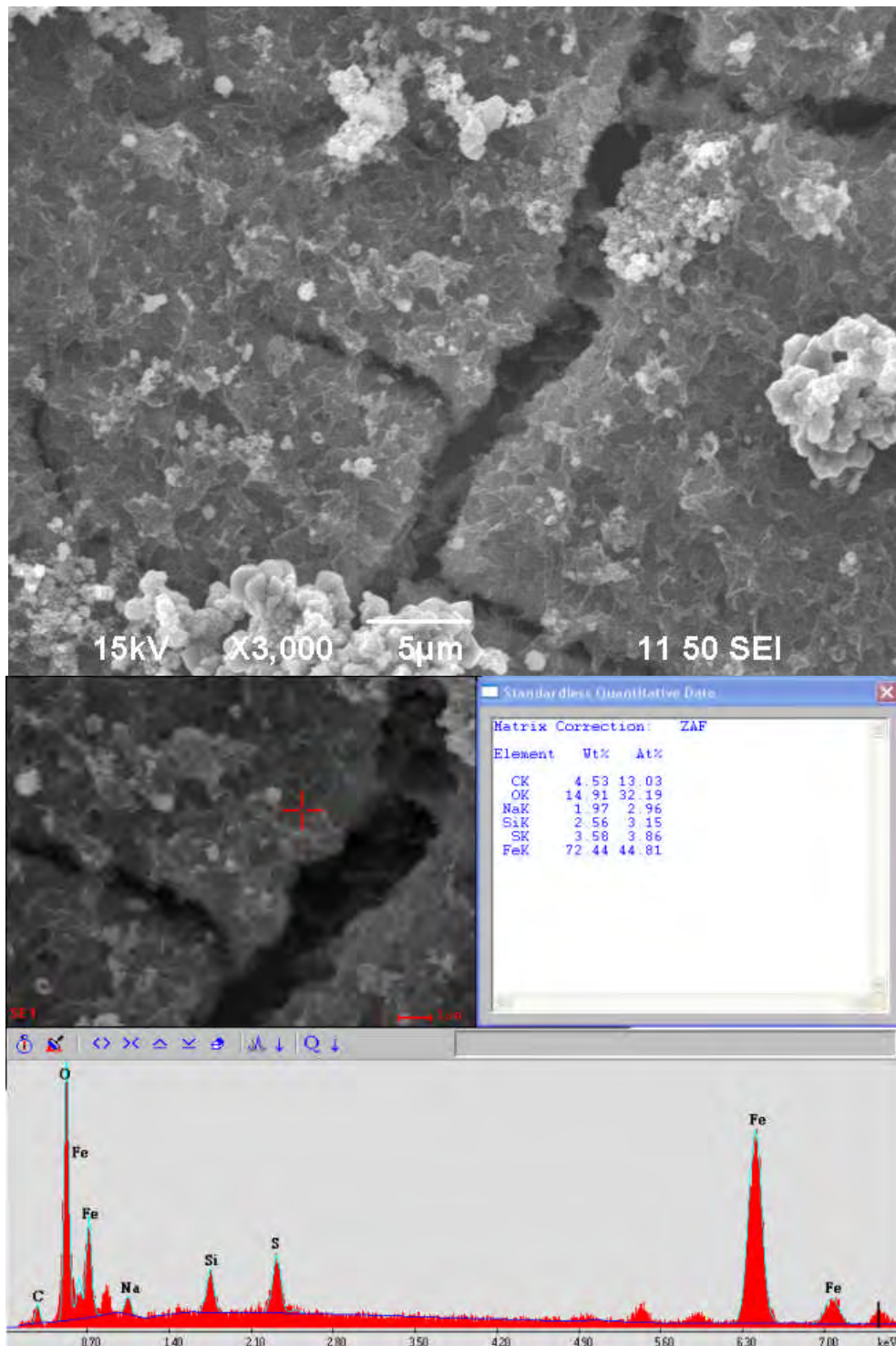


Figure 62. SEM image and EDX spectrum of a specimen surface after a 10 days exposure to Certified Breathing Air (H_2S was stopped purging)

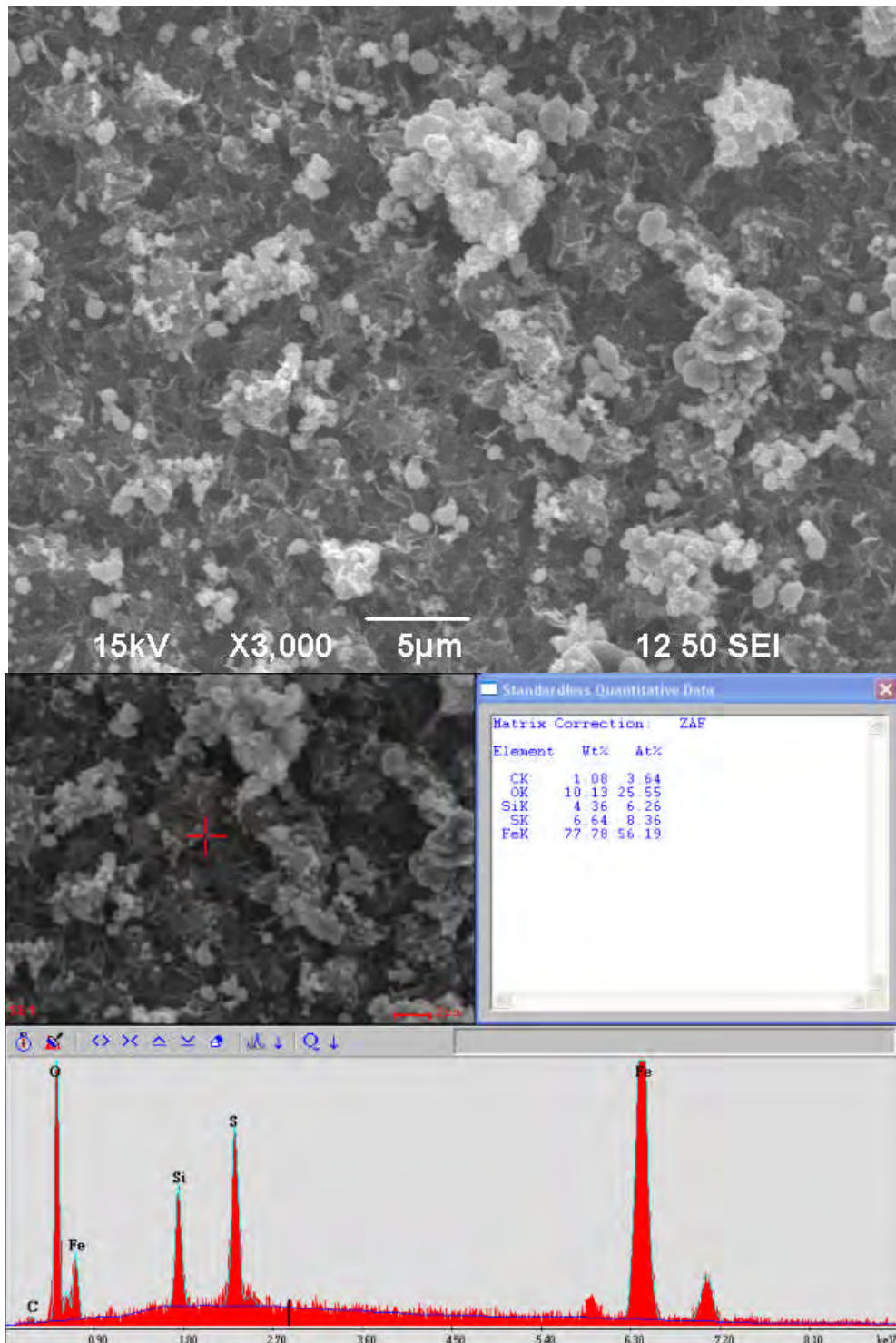


Figure 63. SEM image and EDX spectrum of a specimen surface after a 16 days exposure to Certified Breathing Air (H_2S was stopped purging)

Based on the observations of the SEM and EDX analysis, elemental sulfur was not positively detected after 16 days exposure as no crystals of pure sulfur were apparent. Therefore, another technique, X-ray diffraction was used to further analyze the composition of the corrosion and oxidation products.

Figure 64 shows the XRD data of specimen surfaces with different test periods. The black line represents the XRD data of the specimen surface after four days exposure to 100 ppm H₂S. Only substrate steel (as Fe) and mackinawite were indentified from this data. After oxygen was introduced to the system, a new peak, consistent with magnetite, appears in the XRD data (purple line, 1 day exposure to air), with the intensity of the mackinawite peak decreased. This suggests that the iron sulfide was partially oxidized. With time, the intensity of magnetite increased and more magnetite peaks appeared. However, no elemental sulfur was detected.

The specimen after ten days exposure to air was analyzed next. Before the XRD scan, corrosion product layers were removed from the specimen surface because the specimen was too large for direct analysis with the X-ray diffractometer. The data is shown in Figure 65. The iron peaks shown in Figure 64 disappeared due to the different treatment of the corrosion product layer before scanning. From this XRD data, magnetite is proven to be the dominant species after 10 days oxidation. Boursiquot hypothesized that magnetite would form in FeS oxidation system¹⁰². Elemental sulfur may also have been detected by the X-ray diffraction data, however, the intensity of the sulfur peaks is very low and the match against reference data was poor. It is difficult to conclude that sulfur was generated under the current test conditions.

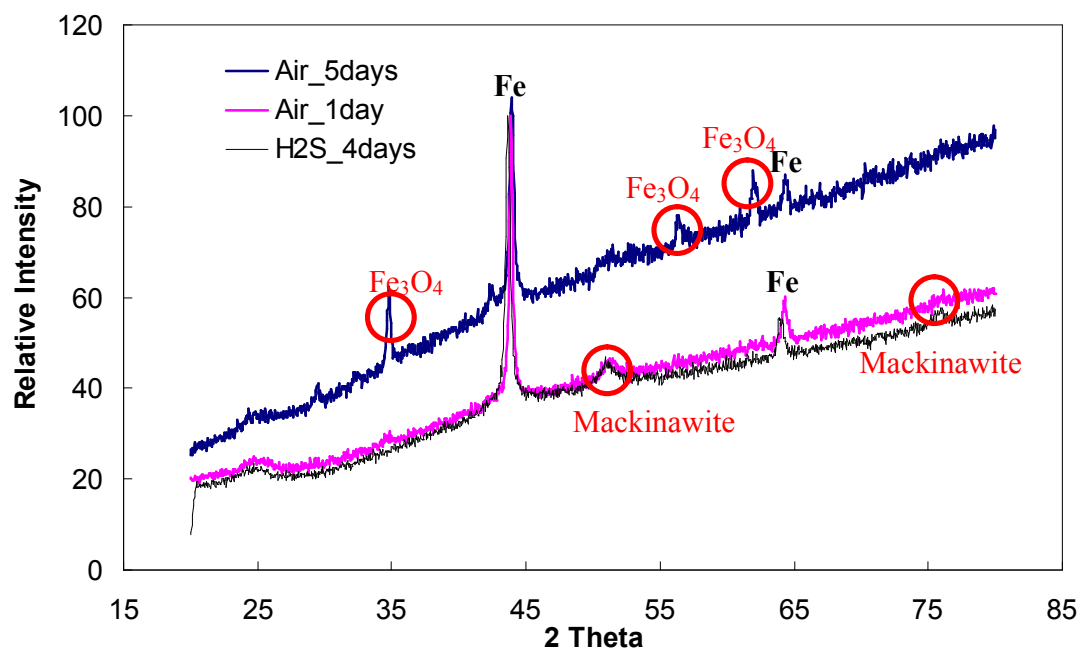


Figure 64. X-ray diffraction data of corrosion and oxidation products (4 days exposure to H₂S, 1 day and 5 days exposure to air).

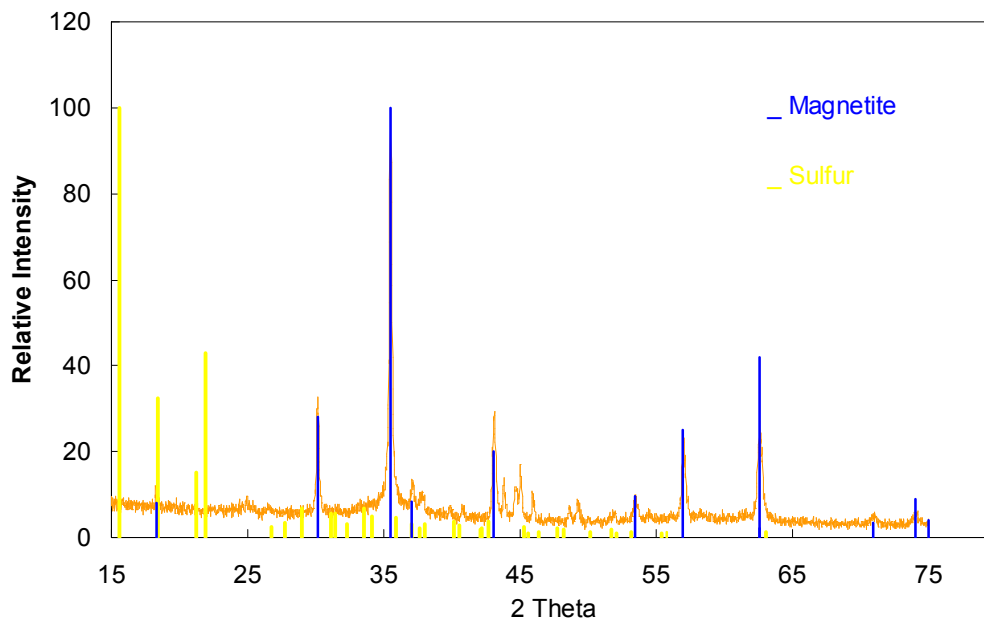


Figure 65. X-ray diffraction data of corrosion and oxidation products (10 days exposure to air).

5.5.1.2 10000 ppm H₂S (0.01 bar H₂S at P_{total} 1 bar)

Following the unsuccessful detection of elemental sulfur in low H₂S concentration experiments, a new experiment with a higher H₂S concentration (0.01 bar H₂S at total pressure 1 bar) as conducted.

5.5.1.2.1 LPR measurement

Figure 66 shows the LPR corrosion rate with time of the experiment with 10,000 ppm H₂S (0.01 bar H₂S at total pressure 1 bar) during the corrosion product layer building process. The dashed lines separate the data into three phases. The first phase is the pre-corrosion, in which only nitrogen was purged into solution. The second phase is the iron sulfide building process. During this process, 10000 ppm H₂S was purged

through the test solution. The oxidation process is the final phase when H₂S was stopped and air was used as the gas purged through the solution.

In the pre-corrosion phase, the LPR corrosion rate is around 0.1 mm/yr. Interestingly, when 10000 ppm H₂S was purged into solution, the corrosion rate immediately increased instead of decreasing. This is contradictory to the result obtained for the experiment with 100 ppm H₂S. The sudden increase of corrosion may be due to a decrease of pH from 7.0 to 5.4 after 10,000 ppm H₂S was added to the system. However, with time, the corrosion rate kept decreasing and stabilized at 0.1mm/yr. It appears that a protective layer formed on the steel surface and became more protective with time. After the corrosion rate was stabilized, air replacing H₂S was purged through solution. The corrosion rate then increased to around 1.1 mm/yr in one day. This suggests that oxygen dominated the corrosion reactions, which is similar to the result of the previous test.

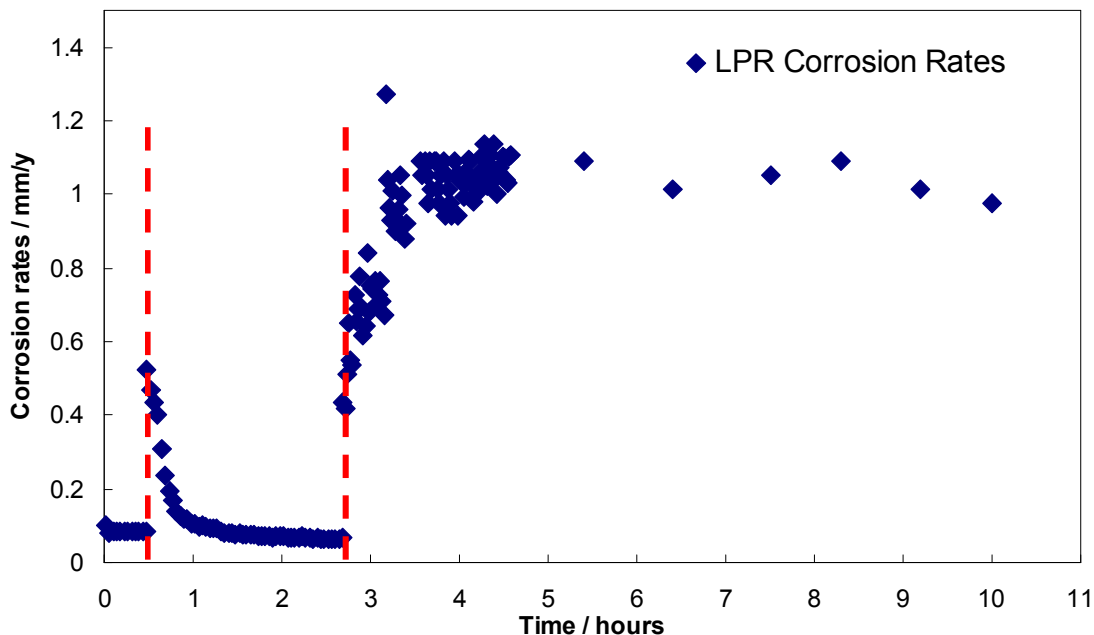


Figure 66. LPR corrosion rate vs. time at 10000 ppm H₂S (corrosion product layer formation).

5.5.1.2.2 Analysis of corrosion and oxidation products

The specimens were taken out from the test solution at different times to do the surface analysis. Figure 67 shows the SEM image and EDX data of corrosion products after 2 days exposure to 10000 ppm H₂S. Corrosion product layers appeared to be much more uniform and dense. The SEM image reveals that the corrosion product is more crystalline, which is totally different from what has been observed at the lower H₂S partial pressure. This suggests that the iron sulfide phase may have changed when the H₂S concentration was increased to 10,000 ppm.

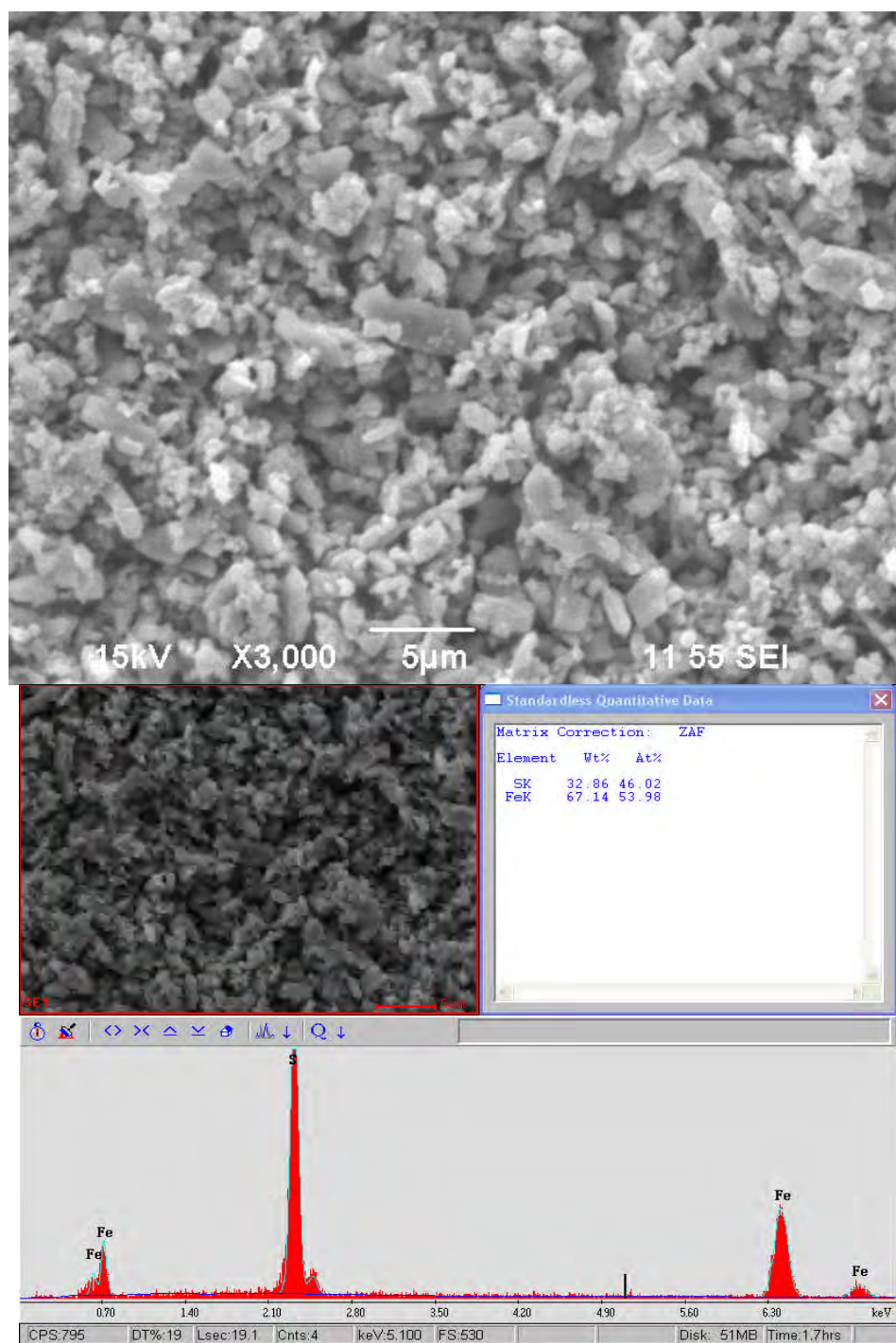


Figure 67. SEM image and EDX spectrum of a specimen surface after a 2 days exposure to 10,000 ppm H₂S.

The SEM image and EDX spectrum of a specimen surface after 1 day exposure to air is shown in Figure 68. It appears that the input of oxygen significantly changed the corrosion product layer morphology. Corrosion product layers became more amorphous. This may cause a higher corrosion rate due to development of a less protective layer structure. This hypothesis is consistent with the LPR corrosion rate results. The EDX spectrum shows the oxygen peak, which suggests that the iron sulfide layer was oxidized.

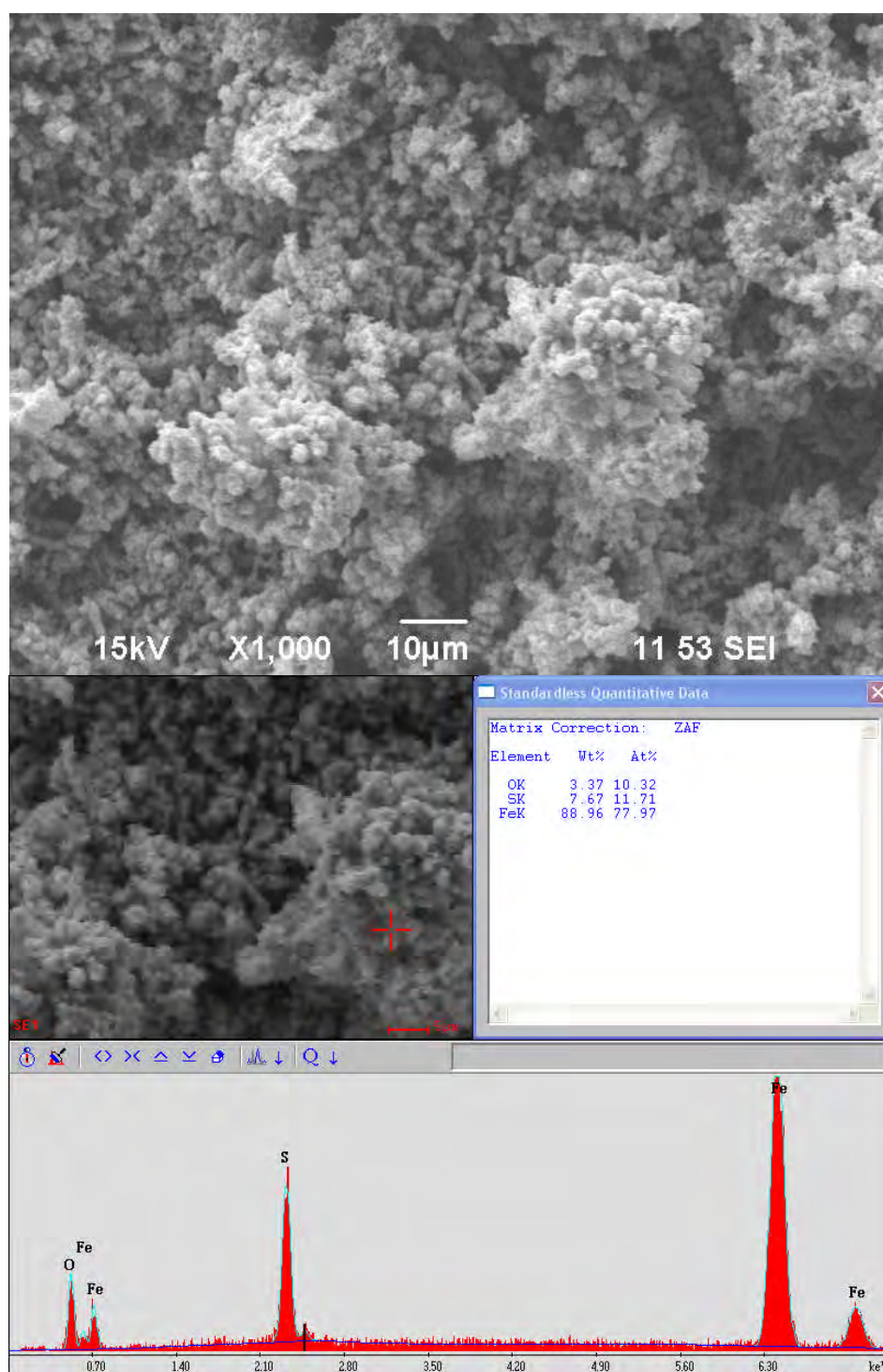


Figure 68. SEM image and EDX spectrum of a specimen surface after a 1 day exposure to air. (H_2S was stopped purging)

Figure 69 and Figure 70, respectively show the SEM image and EDX spectrum of a specimen surface after 5 and 10 days exposure to air. There is no significant difference in layer morphology between these two specimens. Corrosion product layer appears amorphous and has a high oxygen peak in its EDX spectrum. However, even after ten days exposure to air, sulfur crystals were not observed anywhere on the specimen surface.

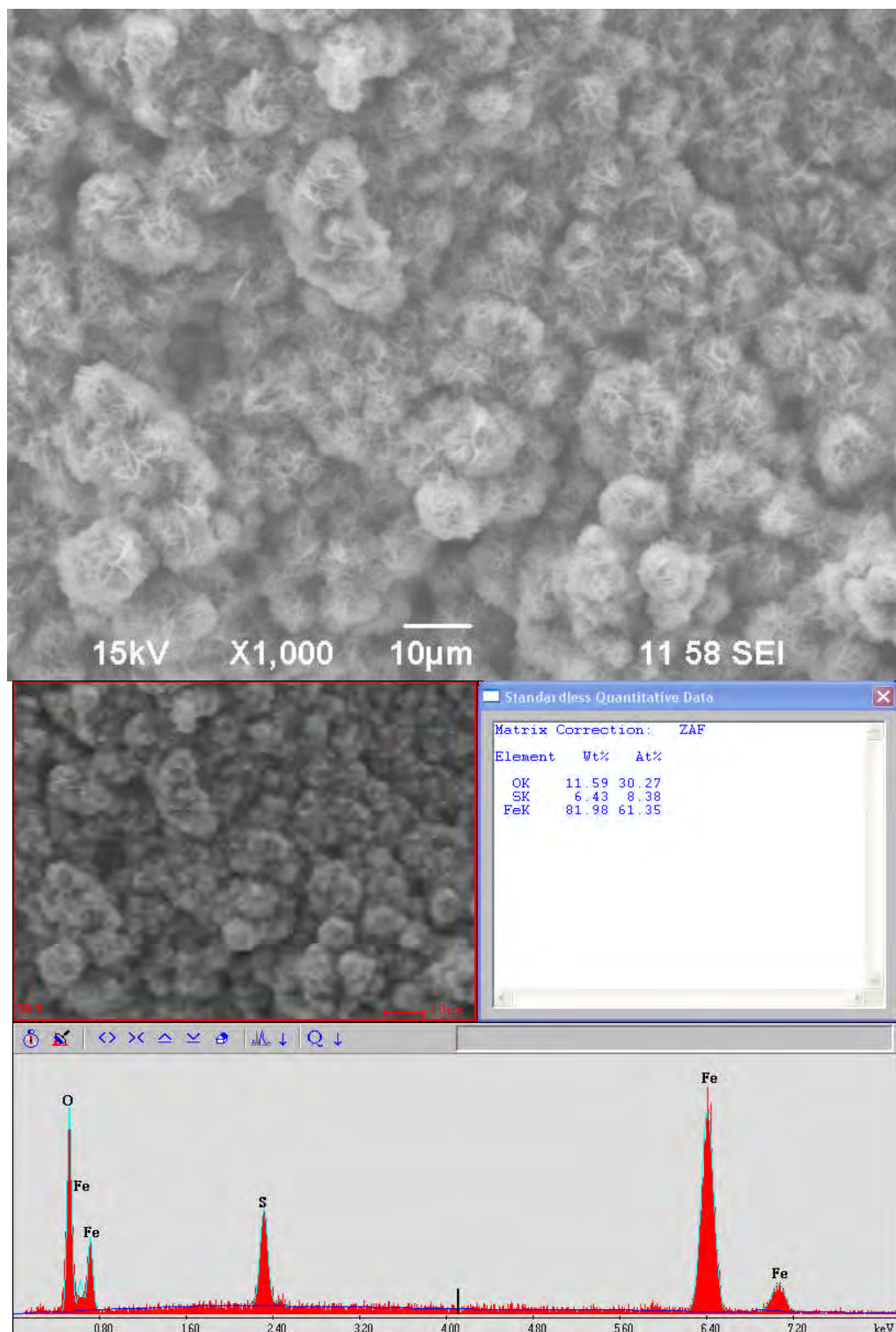


Figure 69. SEM image and EDX spectrum of a specimen surface after a 5 days exposure to Certified Breathing Air. (H_2S was stopped purging)

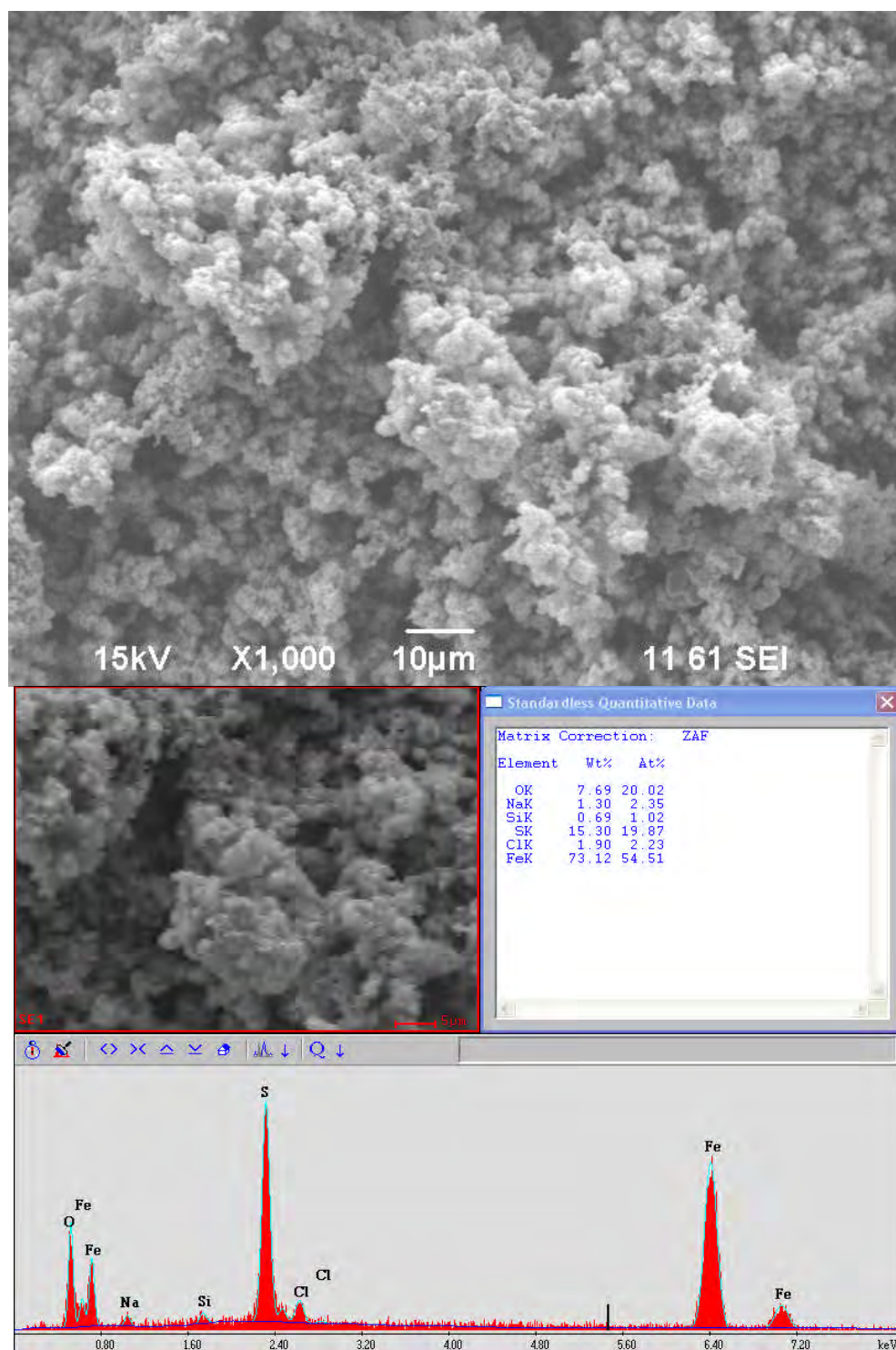
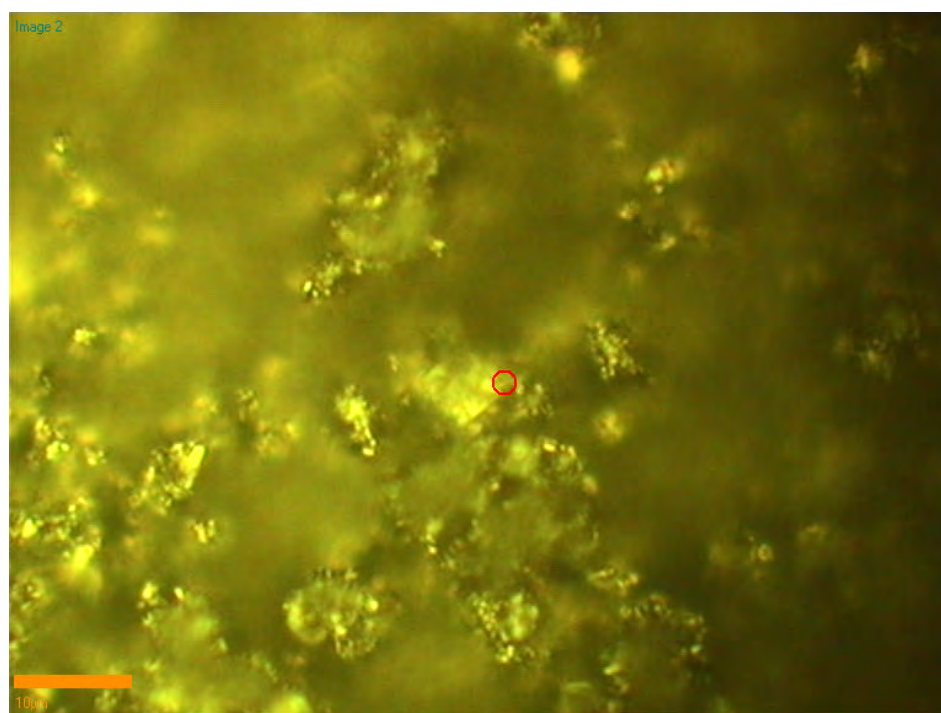


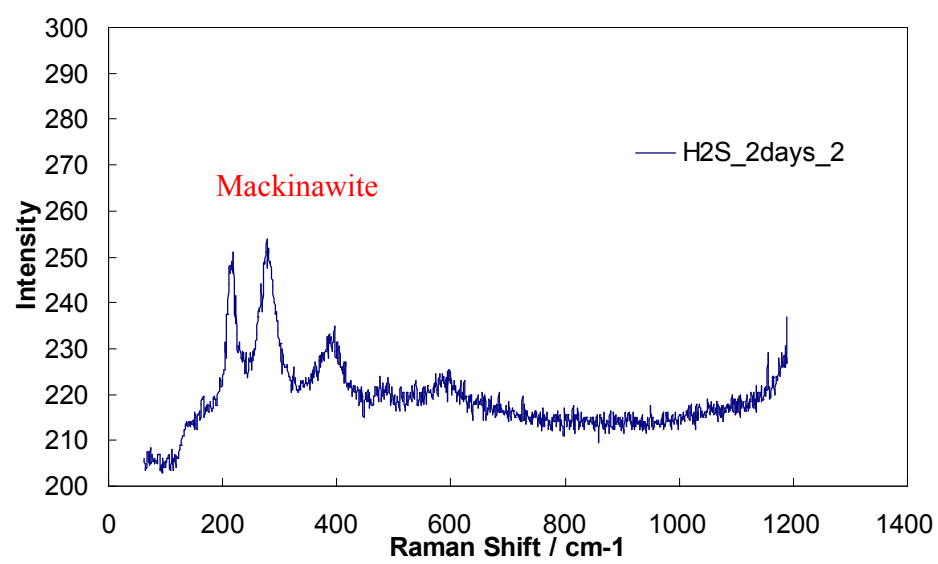
Figure 70. SEM image and EDX spectrum of a specimen surface after a 10 days exposure to air. (H_2S was stopped purging)

Raman spectroscopy was used to identify the corrosion and oxidation products at 10000 ppm H₂S conditions. Figure 71 shows the Raman data of a specimen surface after 2 days exposure to 10000 ppm H₂S. The upper two pictures were taken by Raman spectroscopy and the other two figures show the Raman shift data corresponding to the two red points in the first two pictures. It is clearly seen that mackinawite and pyrrhotite were identified. It suggests that at high H₂S concentration conditions, it is easy for mackinawite to transfer to pyrrhotite.

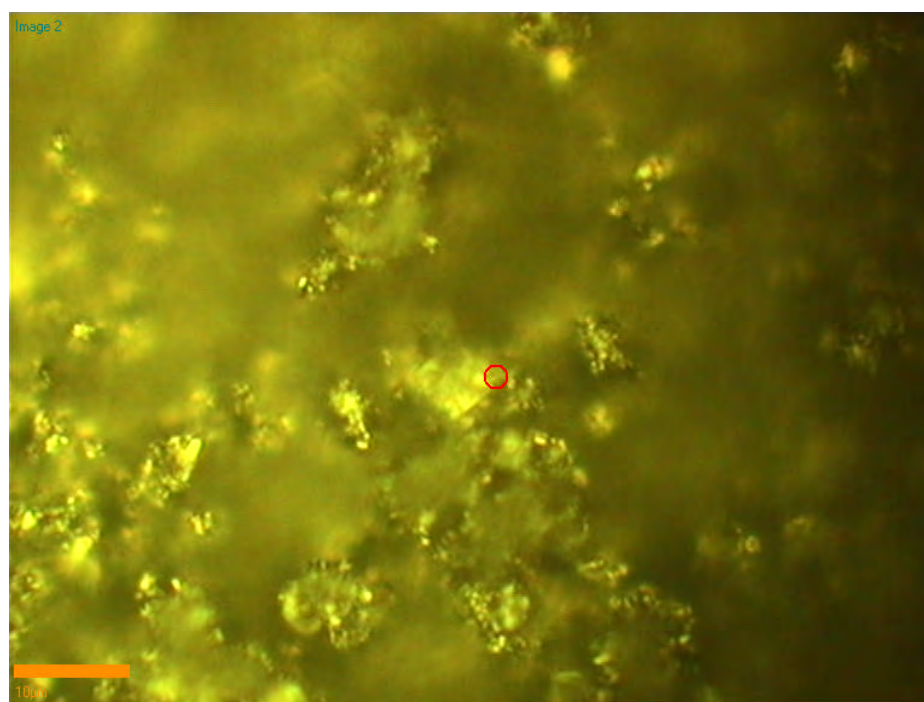
Figure 72 shows the Raman data of the corrosion product layers on the specimen surface after 1 day exposure to Certified Breathing Air. Data were taken from three different locations along the specimen surface. Mackinawite was first identified. Magnetite as well as hematite was discovered from Raman shift data. It appears that parts of the iron sulfide layers were oxidized, likely during the analysis itself.



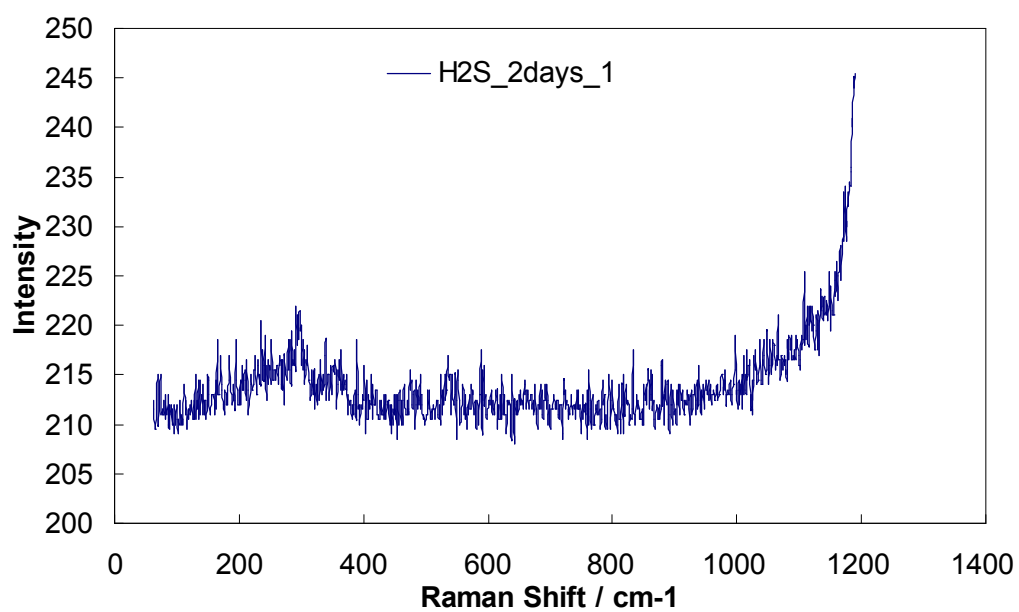
a)



b)

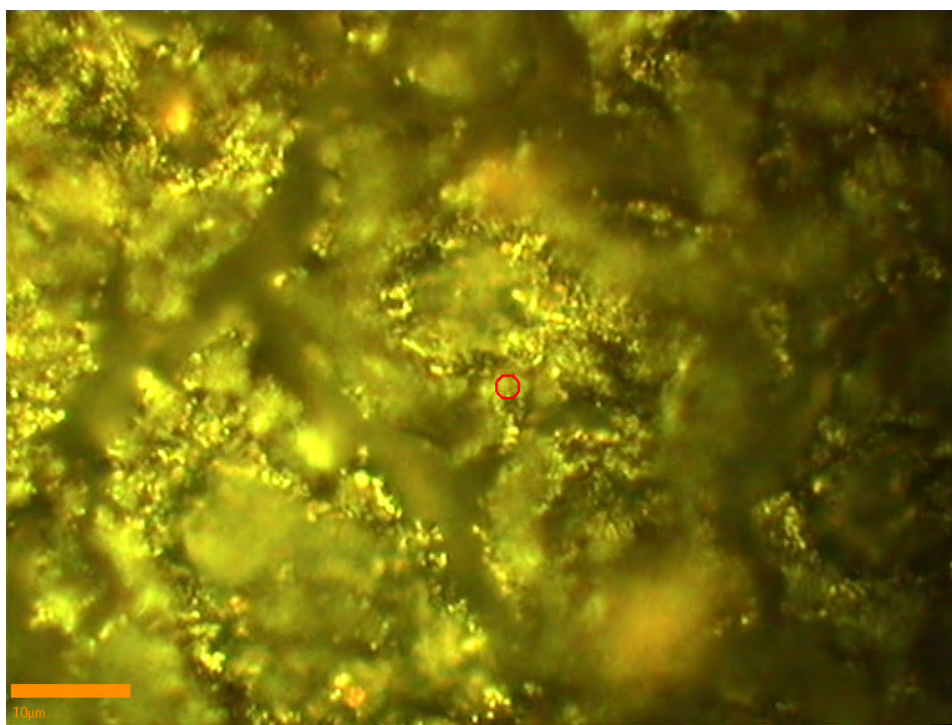


c)

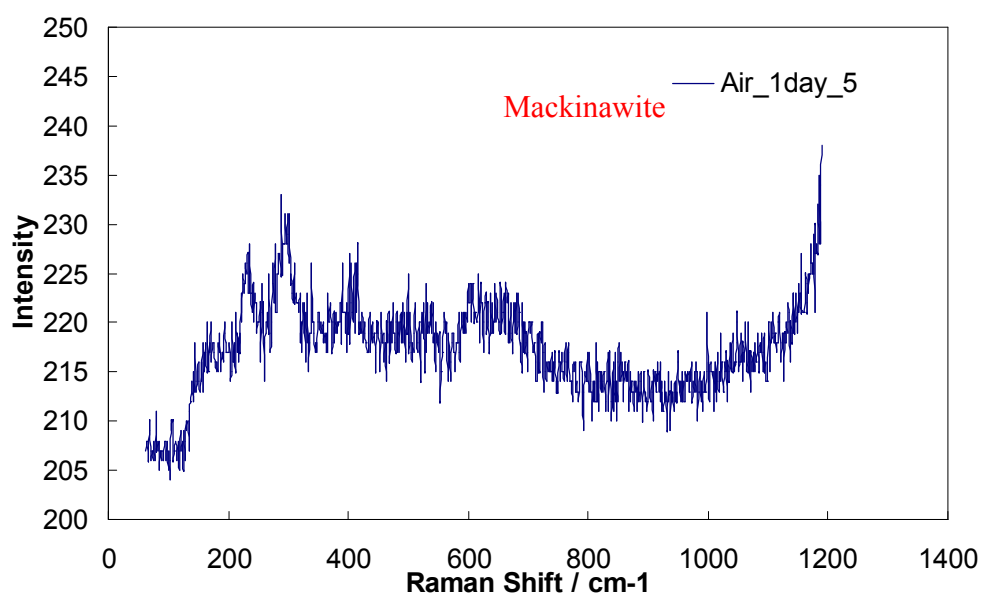


d)

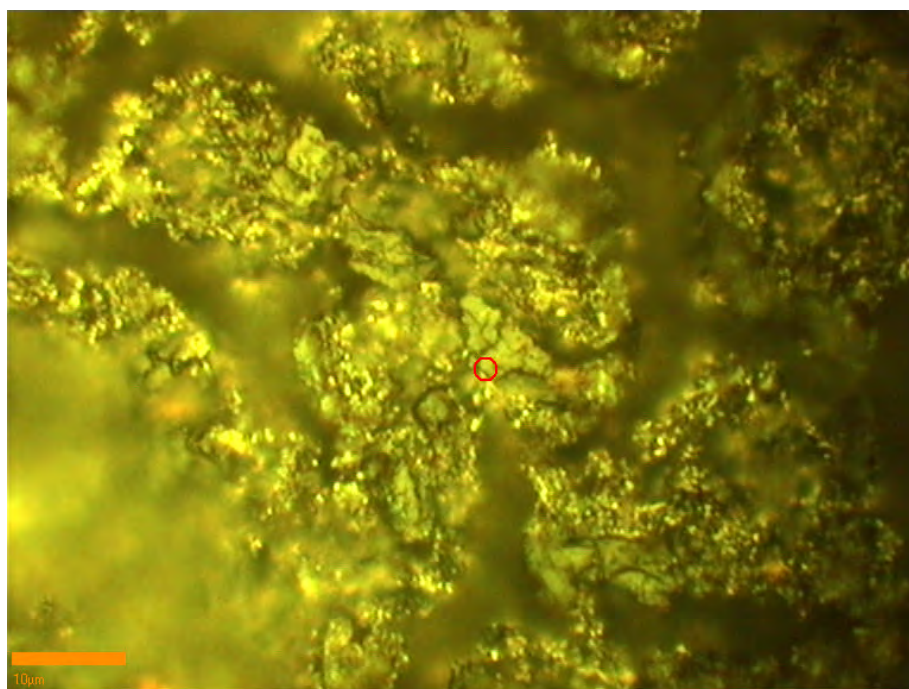
Figure 71. Raman data of corrosion products (two days exposure to 10000 ppm H₂S).



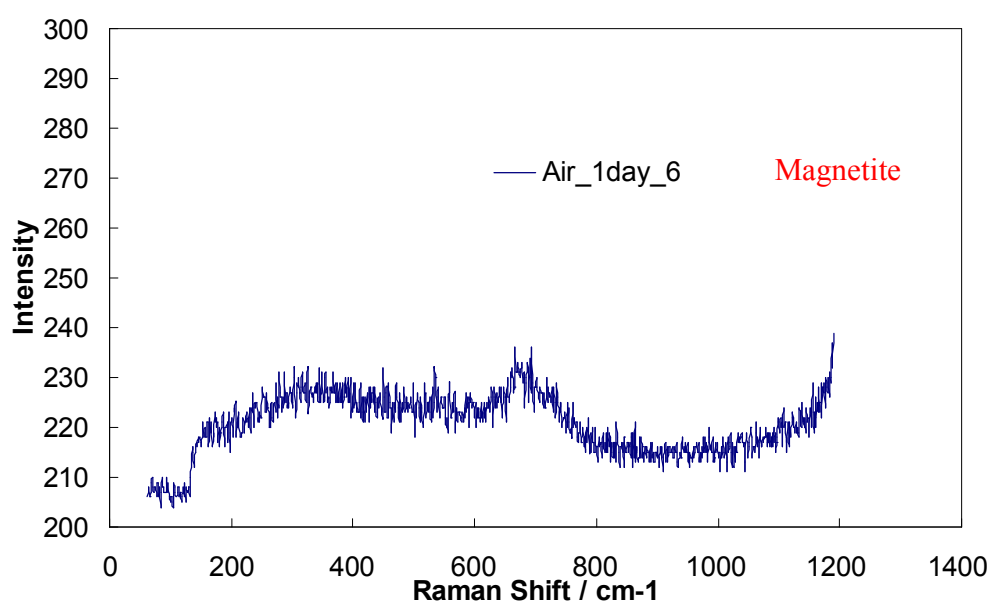
a)



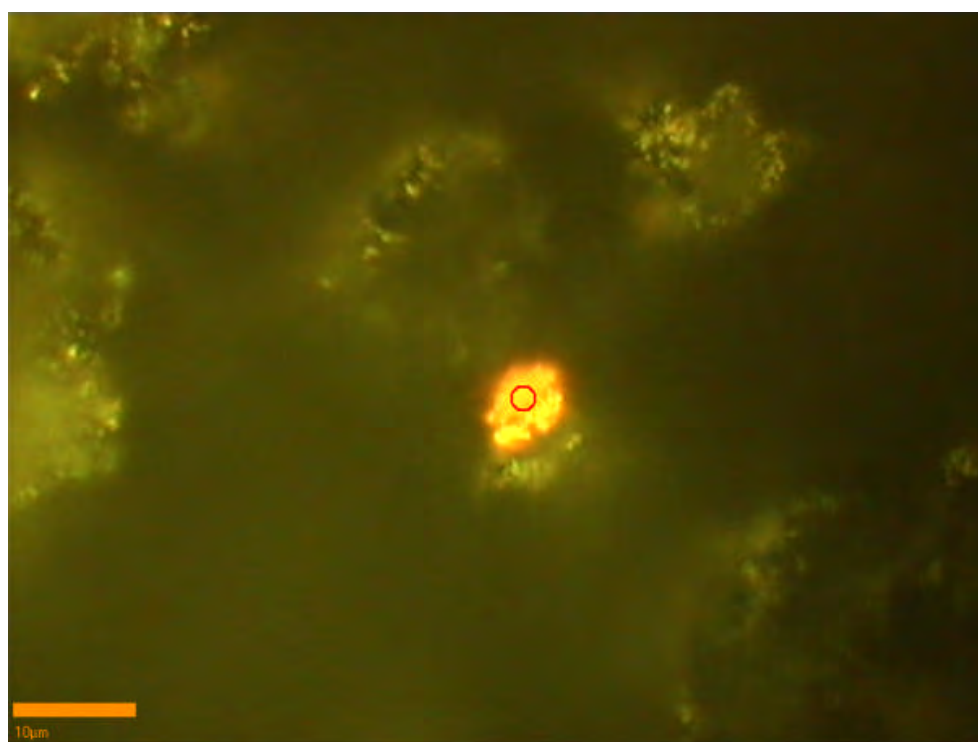
b)



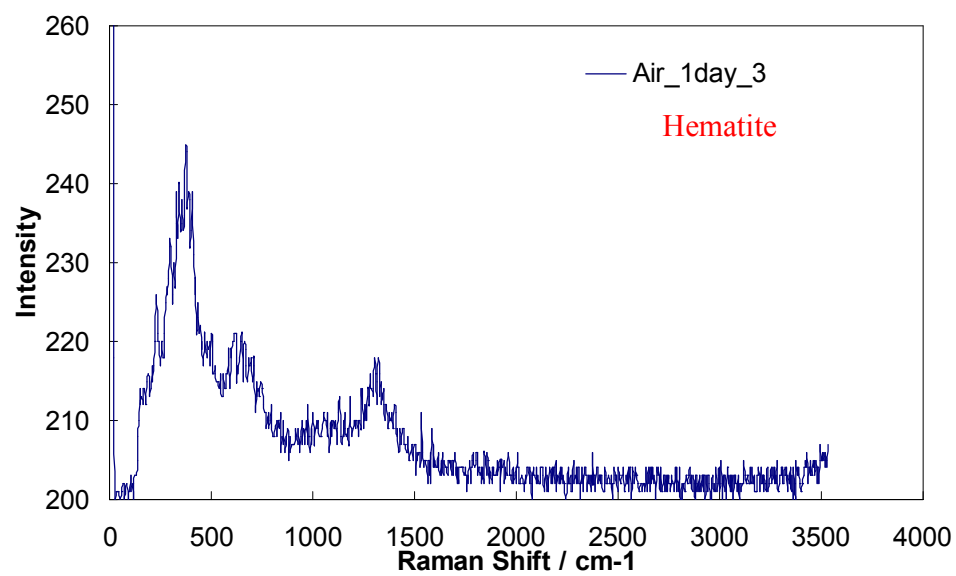
c)



d)



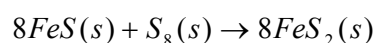
e)



f)

Figure 72. Raman data of corrosion products (1 day exposure to air).

The specimen surface after 10 days exposure to air was scanned by Raman Spectroscopy. The result is shown in Figure 73. Mackinawite, pyrrhotite, hematite and pyrite were detected by the Raman shift data. The appearance of pyrite suggests that sulfur was generated by oxidizing the iron sulfide and then combined with iron sulfide to form the pyrite (FeS_2) as suggested below:



Both this work and Benning's work were conducted in aqueous solution. Benning generated iron sulfide in the solution by reacting H_2S and iron powder. Iron sulfide (mackinawite) was precipitated in the aqueous solution. By doing this, mackinawite and oxygen had enough contact area, which might lead to a completed oxidation reaction. In this work, mackinawite was also a reaction product of H_2S and iron but was formed on the steel substrate. Since the mackinawite layer was thin, oxygen may penetrate and react with iron directly (Mackinawite was still easily detectable after 5 days exposure to oxygen). This might be the reason why hematite was the dominant oxidation product. However, sulfur is a weak Raman scatterer and may have been present, but just went undetected. It also may have been amorphous, and hence directly undetectable by X-ray diffraction.

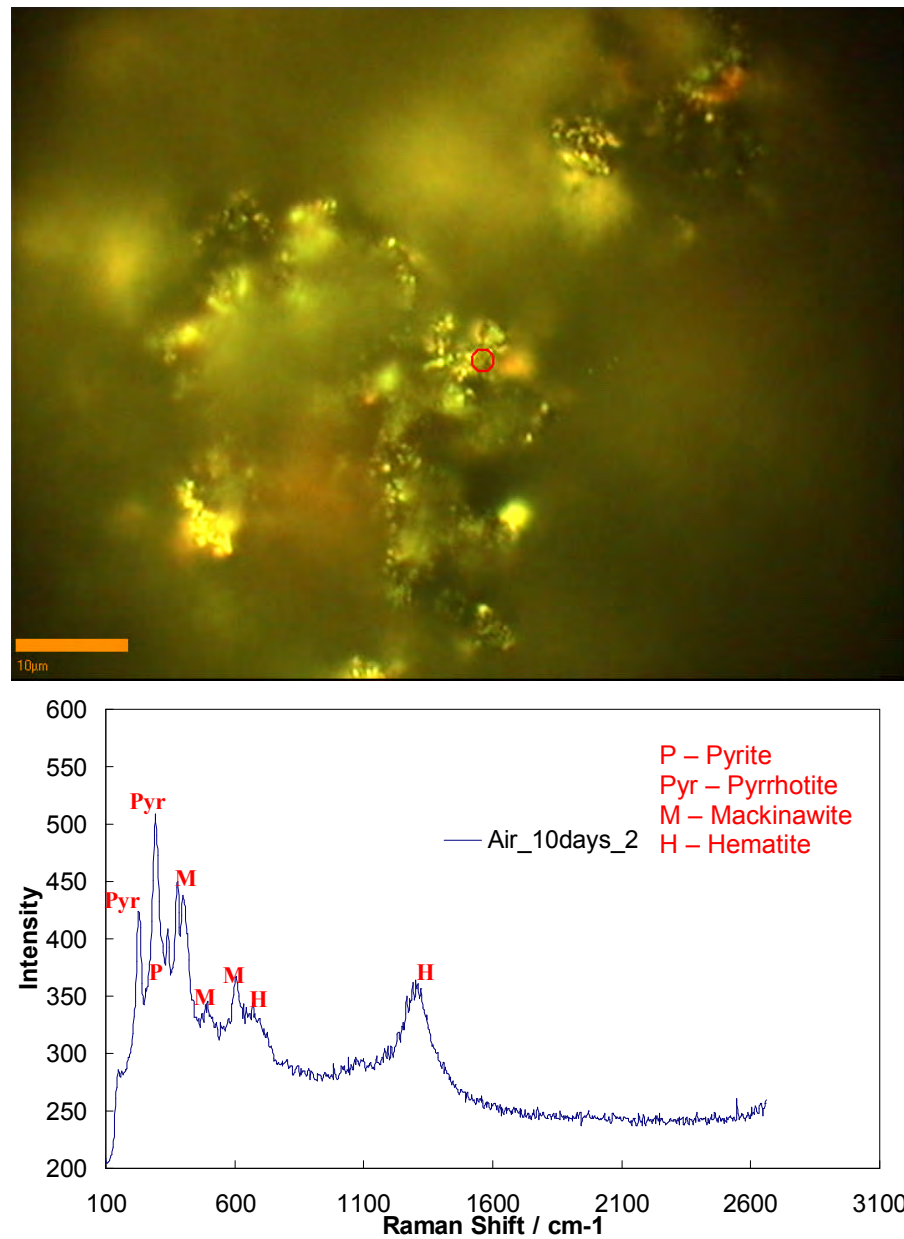


Figure 73. Raman data of corrosion products (10 days exposure to air).

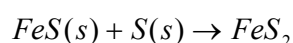
5.5.1.3 Summary

The possibility of sulfur generation by oxidation of iron sulfide was investigated in this study. Iron sulfide was generated first by reacting steel specimens with two

different concentrations of H₂S (100 ppm and 10000 ppm). Then fresh air was introduced into the system to react with iron sulfide. The final reaction products were analyzed by SEM, EDX, XRD and Raman spectroscopy.

During the iron sulfide generation process, the stabilized general corrosion rate measured by LPR decreased after H₂S was introduced. LPR corrosion rate immediately decreased after low concentration of H₂S was introduced. However, at the high H₂S concentration condition, the corrosion rate first increased and then readily decreased. The first increase of corrosion rate may be due to the initially high corrosivity of high concentration of H₂S as an acid. However, after iron sulfide was formed, a mass transfer barrier was established on the steel surface, which resulted in a further decrease of corrosion rate.

According to the experimental data, elemental sulfur was not directly detected at both low and high H₂S concentrations by using SEM, EDX, XRD and Raman spectroscopy. XRD data shows possible signs of the presence of sulfur after the iron sulfide layer was oxidized over a protracted period of time under the condition of low H₂S concentration. However, the intensity of the sulfur peaks is very low. It is hard to unequivocally conclude that sulfur was generated under the current test conditions. The discovery of pyrite by Raman spectroscopy at high H₂S concentration suggests that elemental sulfur was generated by oxidizing the iron sulfide because of the following reaction¹⁰³:



This is consistent with Benning's observation that pyrite is a dominant FeS oxidation product in such environment¹⁰³.

Magnetite and hematite were other dominant oxidation products under the test conditions according to the XRD and Raman results. It appears that the oxygen concentration is too high, so it diffused through the iron sulfide layer and directly oxidized the steel substrate. Decreasing oxygen concentration and longer exposure is recommended to be the next step for anyone going further in this research direction.

5.5.2 Elemental sulfur corrosion mechanism

No matter where elemental sulfur comes from, when sulfur and water are present in the pipeline, severe corrosion may occur. These sections further described key parameters relating to the elemental sulfur corrosion mechanism.

5.5.2.1 Sulfur hydrolysis reaction

In the present work, significant acidification of water upon exposure to elemental sulfur was measurable only at temperatures in excess of 80°C, as shown in Figure 74. The pH values shown were obtained after waiting for at least a few hours while the measured pH stabilized. The results confirmed that hydrolysis products were indeed being formed by reaction of elemental sulfur with water, be they H₂S, H₂SO₂, H₂SO₃, H₂SO₄ and/or polysulfide species. The pH values measured were significantly higher than those reported in a similar study by Maldonado-Zagal and Boden⁹⁰, however it is difficult to establish why. Also, it is not clear if this mechanism can be used as an explanation for localized attack on mild steel by elemental sulfur, as the lowest pH values

observed fall within the typical range of pH seen in water/CO₂ systems. In addition buffering effects of dissolved CO₂ and H₂S would have minimized this acidification.

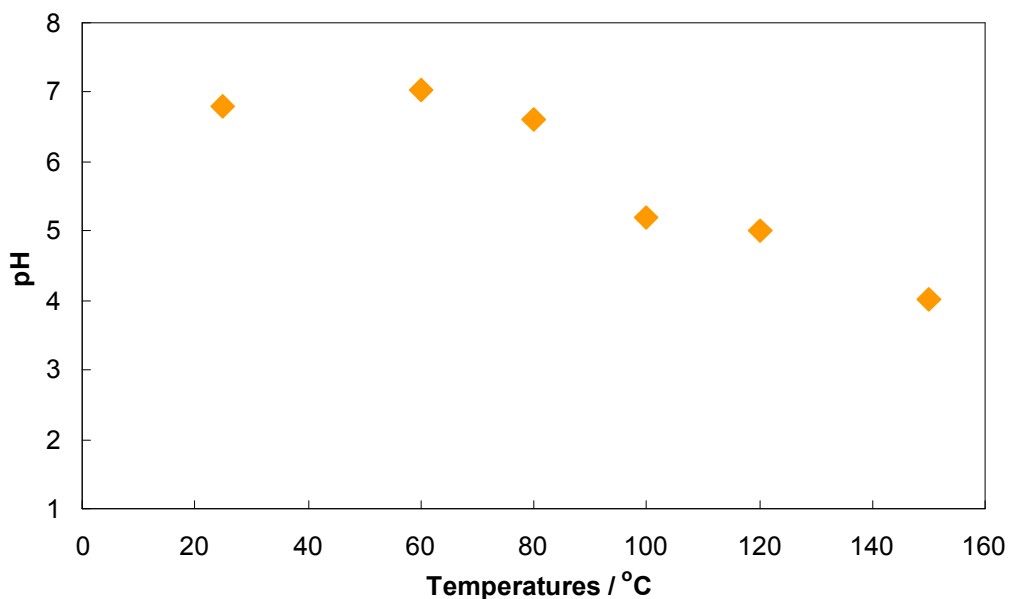


Figure 74. pH at equilibration after mixing water with sulfur at various temperatures.

However, these tests were conducted without the presence of iron, and the pH measured was the bulk pH. The surface pH of steel may be extremely low when it has a direct contact with elemental sulfur. To clarify this hypothesis, follow up surface pH measurements in the presence of sulfur were performed.

A flat pH probe was used to measure the surface pH. Figure 75 shows the schematic of the instrument set up. A mild steel mesh with a sulfur drop deposit in the middle was fitted onto the end of the pH probe by a plastic coupling. The fabricated sets were put into a 1 wt.% NaCl solution deoxygenated by nitrogen. The pH changes were monitored with time.

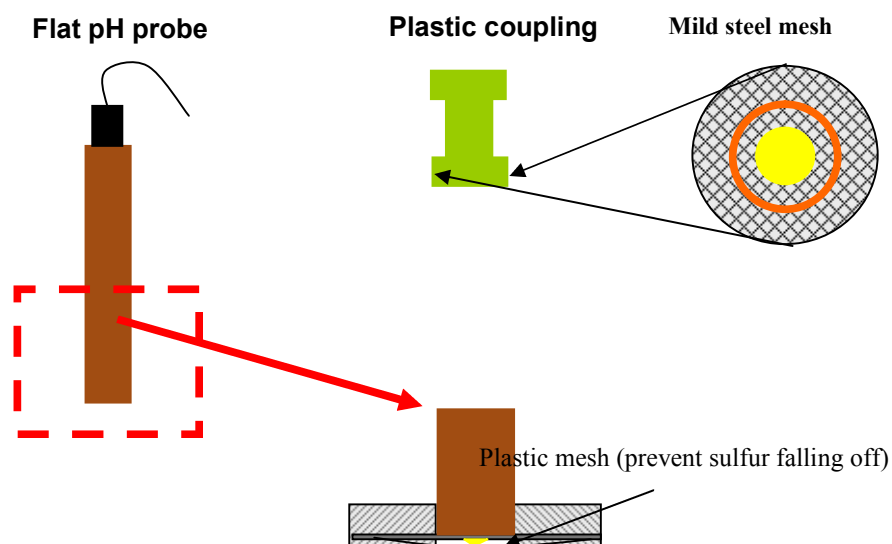


Figure 75. Mesh-capped pH probe⁸⁷ applied to the sulfur corrosion system.

Figure 76 shows the surface pH change with time measured at 25°C and 80°C. The diamonds correspond to results at 25°C, the squares to 80°C. It is clearly seen that at 25°C, the surface pH underneath the sulfur increased from 6.5 to around 8.0. Acidification proposed by Maldonado-Zagal and Boden was not observed at 25°C. The increase of pH is probably due to the corrosion underneath the sulfur pellet. More hydrogen ions were consumed and more ferrous irons released at the specimen surface.

The results at 80°C are different. The pH was decreased from 6.5 to around 5.5 in a day. This is consistent with the sulfur hydrolysis experiment conducted at the same temperature but without steel specimens. The acidification observed here is probably due to the reaction between elemental sulfur and water. However, the acidification caused by sulfur hydrolysis is not significant.

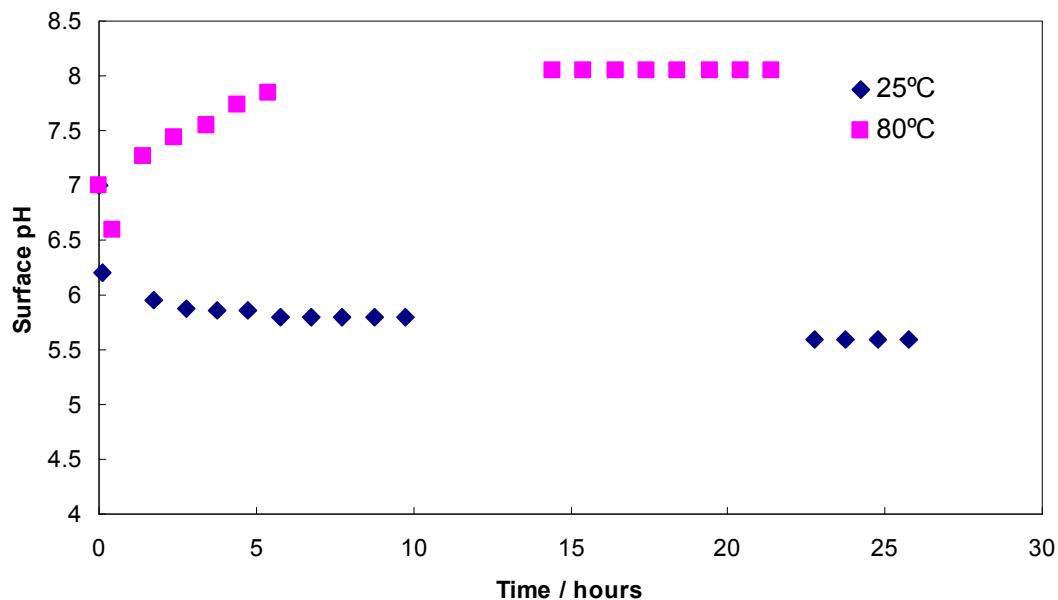


Figure 76. Surface pH measurements for sulfur hydrolysis on a corroding steel mesh.

Minimal acidification observed after sulfur was mixed with water suggests that sulfur hydrolysis does not occur appreciably. Although the reaction rate is low and may not be the dominant process in elemental sulfur corrosion, it is still useful to determine the products of sulfur hydrolysis reactions. Therefore, additional experiments were performed to identify the reaction products. The results from these are shown and discussed below.

In previously discussed ion chromatography results, sulfuric acid had previously been proposed to be the product of the sulfur hydrolysis reaction. Therefore, a standard solution with aqueous sulfate ion (SO_4^{2-}) was first prepared and tested by ion chromatography to obtain a standard chromatogram for comparison with data obtained from the experimental solutions. The results are shown in Figure 77. Sulfate ion

appeared at a retention time of 8.3 minutes. In order to avoid contamination of the chromatography column by the standard solution, pure deionized water was injected into the instrument to clear the column. Figure 78 shows the results for DI water after column purging, note the absence of any SO_4^{2-} peak in the chromatogram. This confirmed that the column was free from SO_4^{2-} and ready for reinjection.

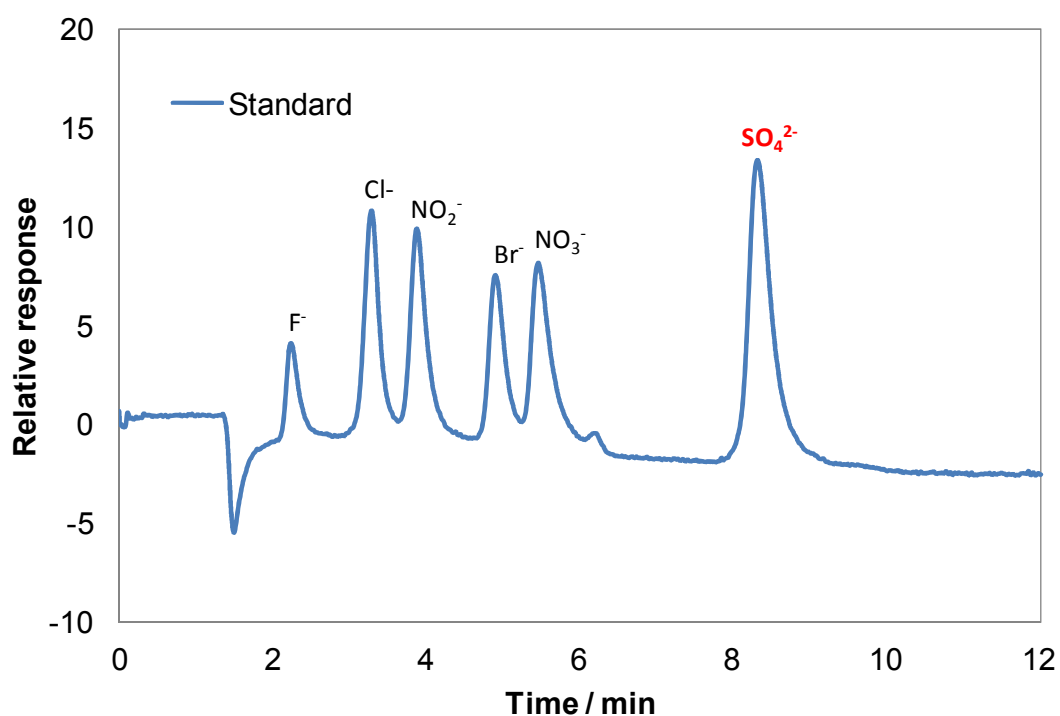


Figure 77. Ion chromatogram for standard solution with SO_4^{2-} .

Figure 79 shows the chromatogram for different test solutions recovered at various temperatures (25°C, 80°C, 135°C and 150°C) after equilibration. These results indicate that sulfate ions are present in all test solutions and that the concentration increases with temperature (peak area increases with increase of temperature). This

qualitatively indicates that sulfuric acid, H_2SO_4 , is a likely product of sulfur hydrolysis. Interestingly, H_2S was only detected at 150°C and the concentration was extremely low (less than 1 ppm). This may be because the reaction rate is low and insufficient gaseous H_2S was generated for detection in lower temperature tests.

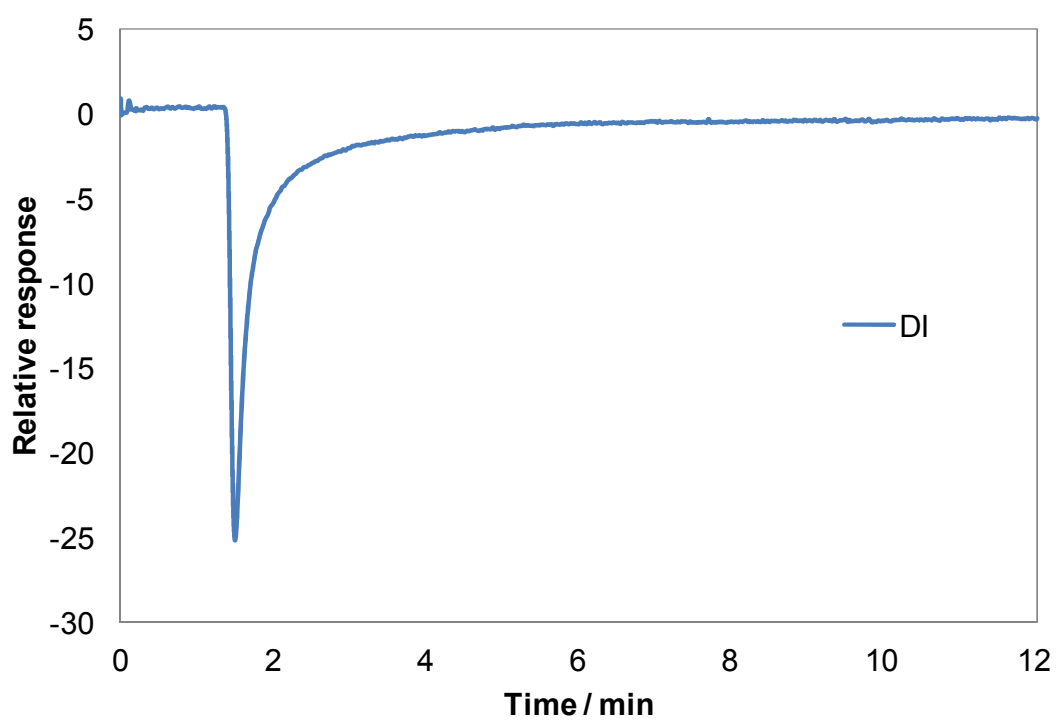


Figure 78. Chromatogram for deionized water after purging of the chromatographic column.

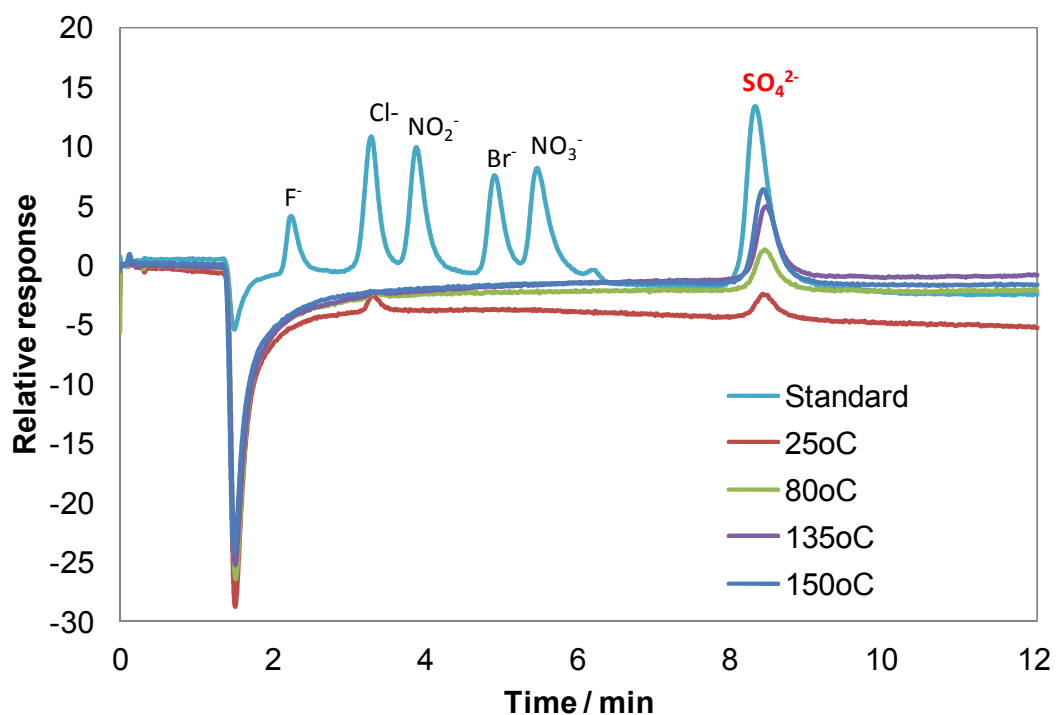


Figure 79. Chromatograms for water/sulfur solutions exposed at different temperatures.

The pH measurements after each 24 hour experiment at different temperatures are shown in Figure 80. The pH value of 2.9 observed at 150°C strongly suggests the presence of a strong acid in the test solution. According to the chromatography results that showed the presence of SO_4^{2-} , the acid is believed to be sulfuric acid (H_2SO_4). Although no H_2S was detected in the gas phase, hydrogen sulfide and sulfuric acid are still considered to be the most likely products of the sulfur hydrolysis reaction, therefore one can write:



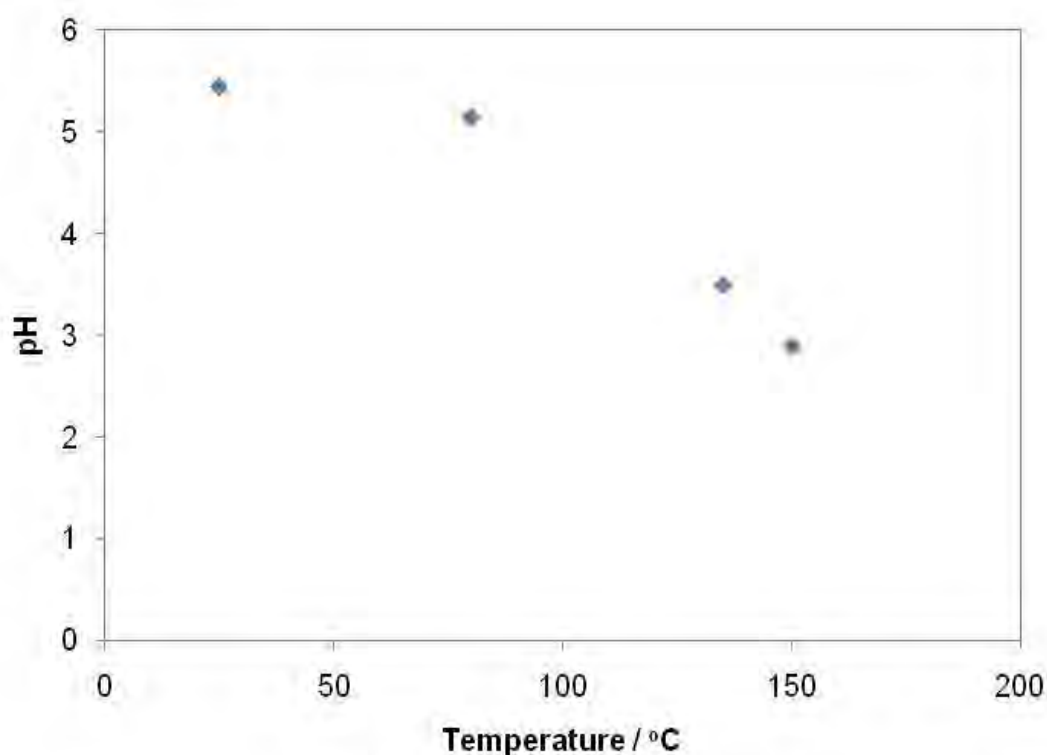


Figure 80. pH of the test solution after degassing for the studied temperatures.

5.5.2.2 Direct sulfur/iron reaction mechanism

The effects of various parameters such as salt, pH, CO₂ and H₂S partial pressure have been studied to clarify the sulfur/iron reaction mechanism. The results are described in the following sections.

5.5.2.2.1 Sulfur/iron reaction in salt free condition (deionized water)

The first set of experiments for the sulfur/iron reaction was conducted in salt free conditions. A specimen with elemental sulfur on the surface prior to exposure is shown in Figure 81. The portion of the specimen surface which was in direct contact with the elemental sulfur was significantly blackened after exposure; this was due to the formation of iron sulfide. A typical specimen surface, after the reaction, is shown in Figure 82.



Figure 81. Elemental sulfur deposited on the surface of a corrosion specimen before exposure.

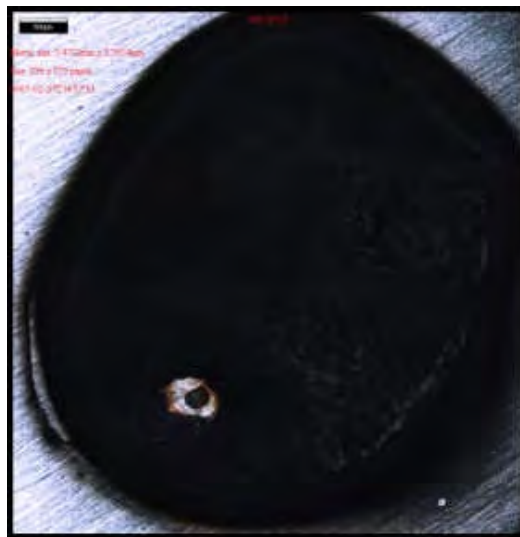


Figure 82. The overall surface of a corrosion specimen after exposure to elemental sulfur (25°C, 3 days).

Representative SEM/EDX data for the corrosion specimen surface that has been in direct contact with elemental sulfur for one day at 25°C is shown in Figure 83. Note

that most of the surface layer resembles a blistered layer (top left SEM image). Cracking of the layer, shown in the enlarged image, reveals that it is very thin and seems to be exfoliating from the surface. A further enlargement of the small area shows that the layer appears amorphous, with no well defined morphologies present; this was confirmed by XRD. The composition of the layer was shown to be consisting with iron sulfide using EDX. IFM image of the corrosion specimen after the iron sulfide has been removed reveals some pitting corrosion, Figure 84. The top right image corresponds to the small region marked on the “whole specimen” picture, to the left. The line across the “twin pits” corresponds to the profile data at the bottom of the figure. Note that the first pit has a depth of *ca.* 18 μm , whereas the second pit is *ca.* 12 μm . Comparison of general and localized corrosion rate data of generated samples is given below.

After four days at 25°C a thicker layer has formed at the surface, see Figure 85. The exfoliation of the layer is obvious on the enlarged image on the top right. The origin of the lines on the underside of the exfoliated layer are due to the polishing marks on the original steel substrate, which have left an imprint on the sulfide layer formed by a direct reaction. Cracking of the layer is more severe on this specimen than the one exposed for only one day. From EDX and XRD, it is clear that the layer chemistry remains fundamentally unchanged in the longer exposure. Pit depths appear similar to those observed after 1 day; however, the profile shown in Figure 86 seems to indicate a broadening effect. After a 5 day exposure at 25°C, see Figure 87, the layers seem to be even thicker and coarser than before, but pit depth remains similar, see Figure 88.

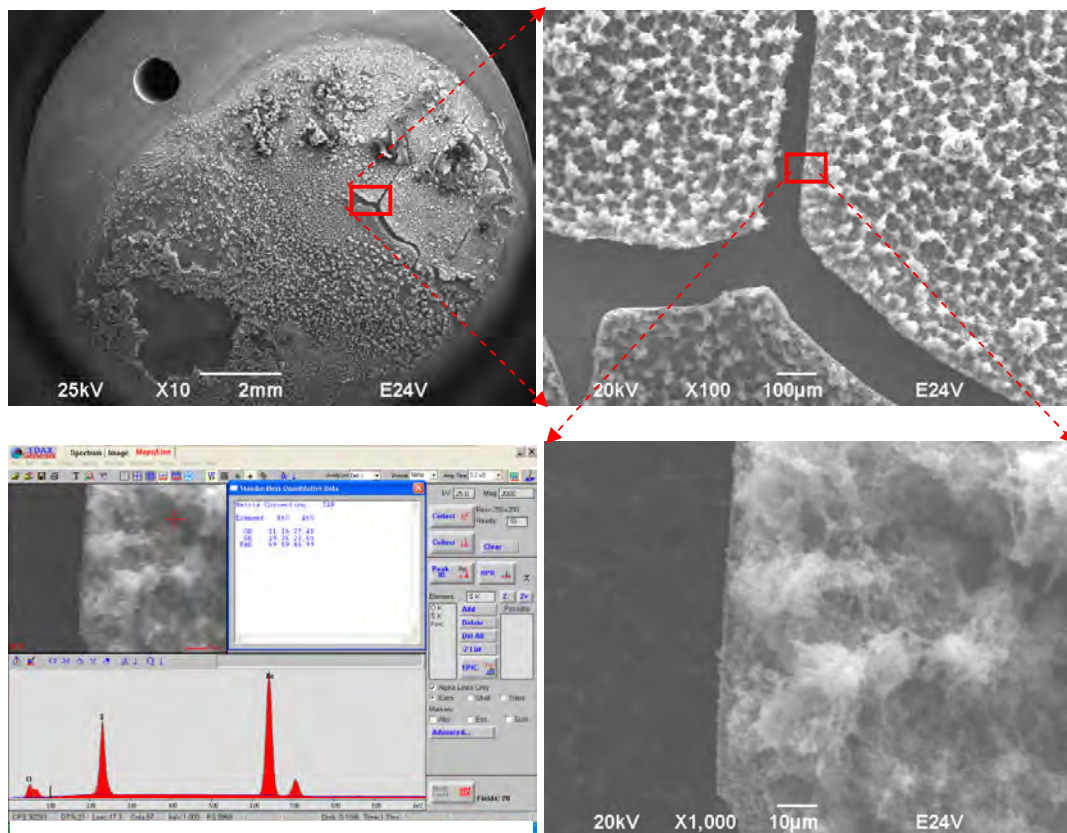


Figure 83. Corrosion specimen contacted with elemental sulfur for 1 day at 25°C, with corrosion product layer.

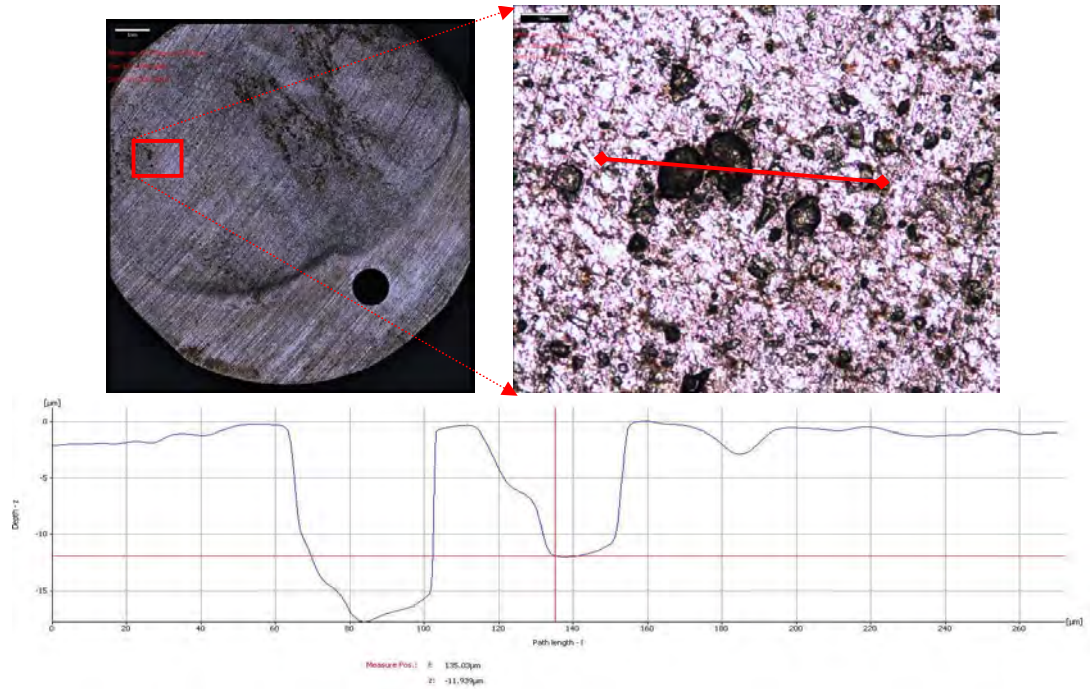


Figure 84. IFM data for corrosion specimen contacted with sulfur for 1 day at 25°C, without corrosion product layer, appearance of the surface (top images) and a line profile.

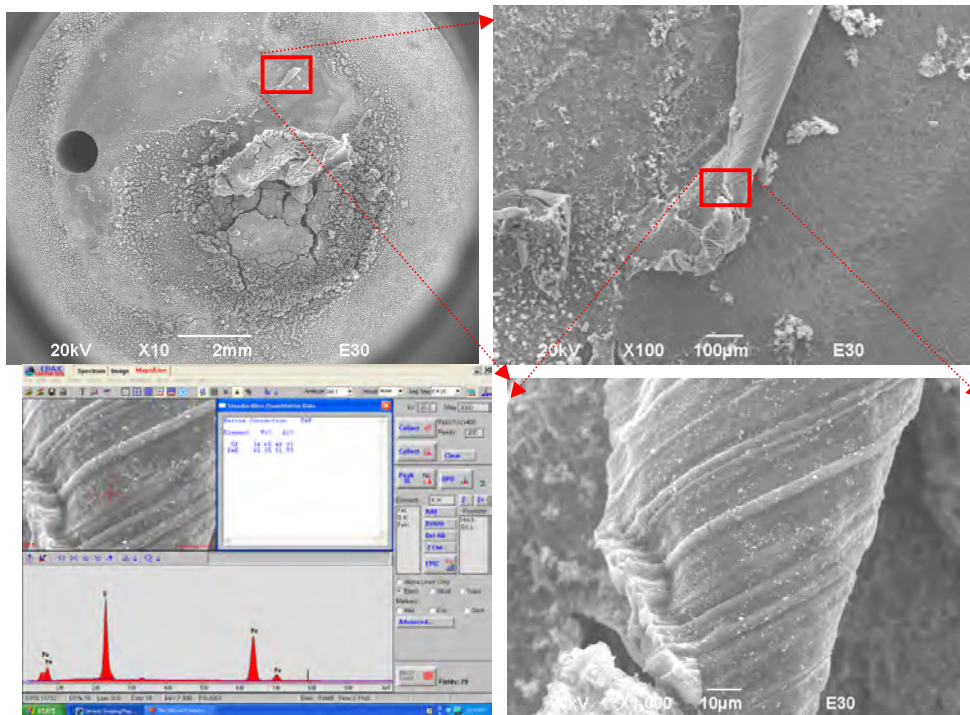


Figure 85. Corrosion specimen contacted with elemental sulfur for 4 days at 25°C, with corrosion product layer.

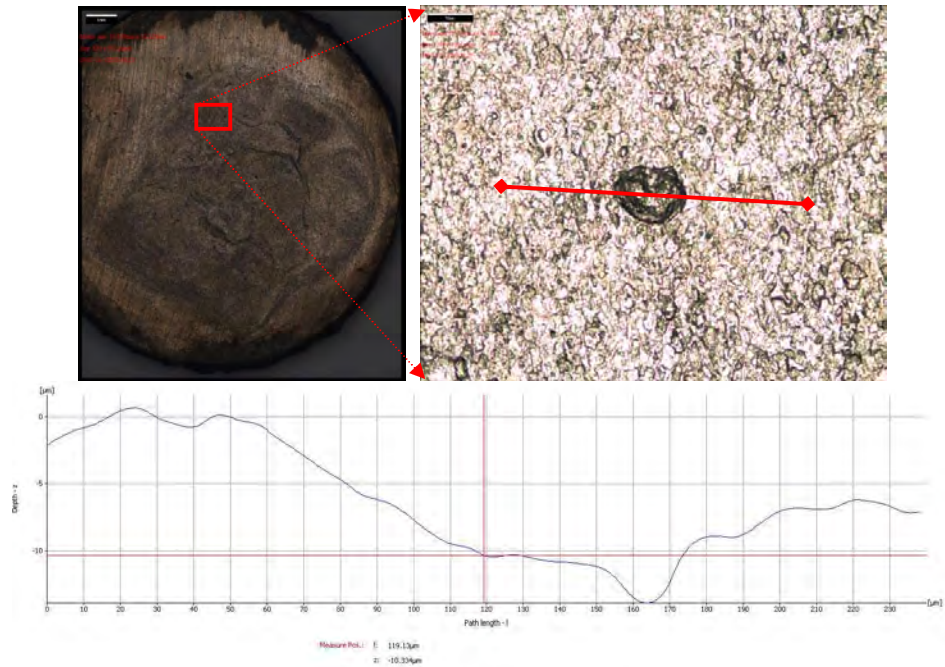


Figure 86. IFM data for specimen contacted with sulfur for 4 days at 25°C, without corrosion product layer.

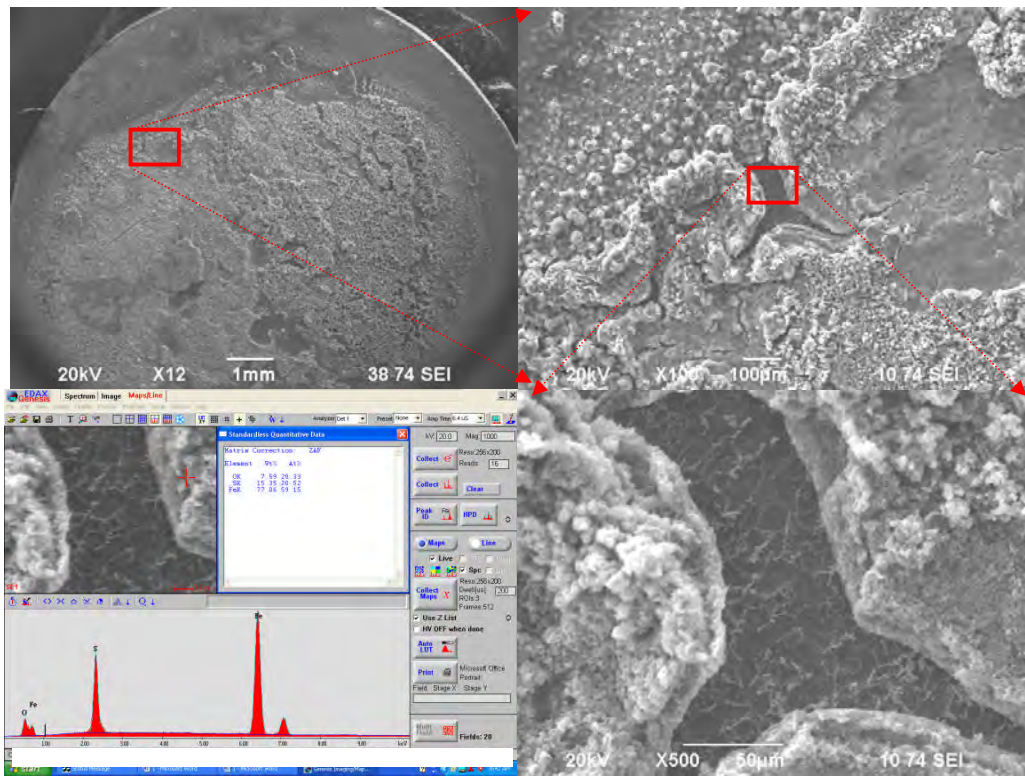


Figure 87. Corrosion specimen contacted with elemental sulfur for 5 days at 25°C, with corrosion product layer.

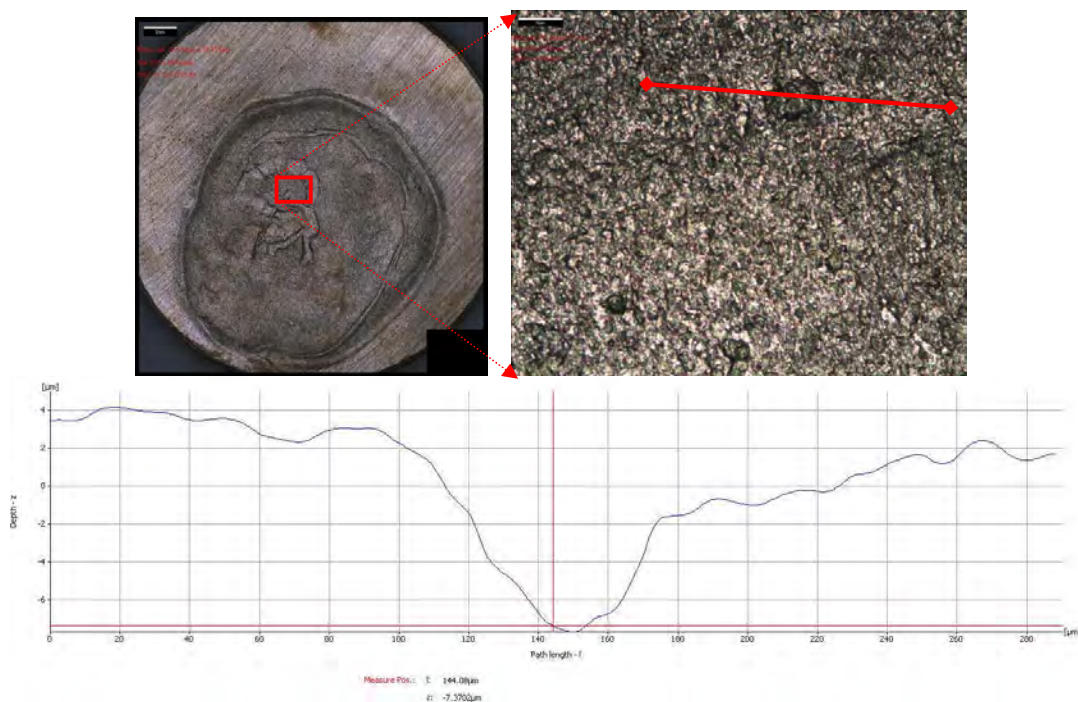


Figure 88. IFM data for specimen contacted with sulfur for 5 days at 25°C, without corrosion product layer.

Another similar series of experiments was conducted at 80°C. After one day at 80°C there is a much thicker layer present on the specimen surface than was observed at 25°C, see Figure 89. Distinct iron sulfide microcrystallites seem to have formed. The pitting depth is again about 15 µm, see Figure 90. After 4 days at 80°C, Figure 91, the layer has become thicker and coarser, appearing more crystalline. Pitting depth remains at *ca.* 15 µm, Figure 92, but broadening is again observed. Pit density on the surface also appears to be increasing. After 5 days at 80°C, Figure 93, the entire surface seems to be covered by a coarse and cracked layer. From XRD, the dominant phase is the crystalline iron sulfide mackinawite, see Figure 94. Mackinawite is a layered structure which is common in aqueous environments under mildly sour conditions¹⁰⁴.

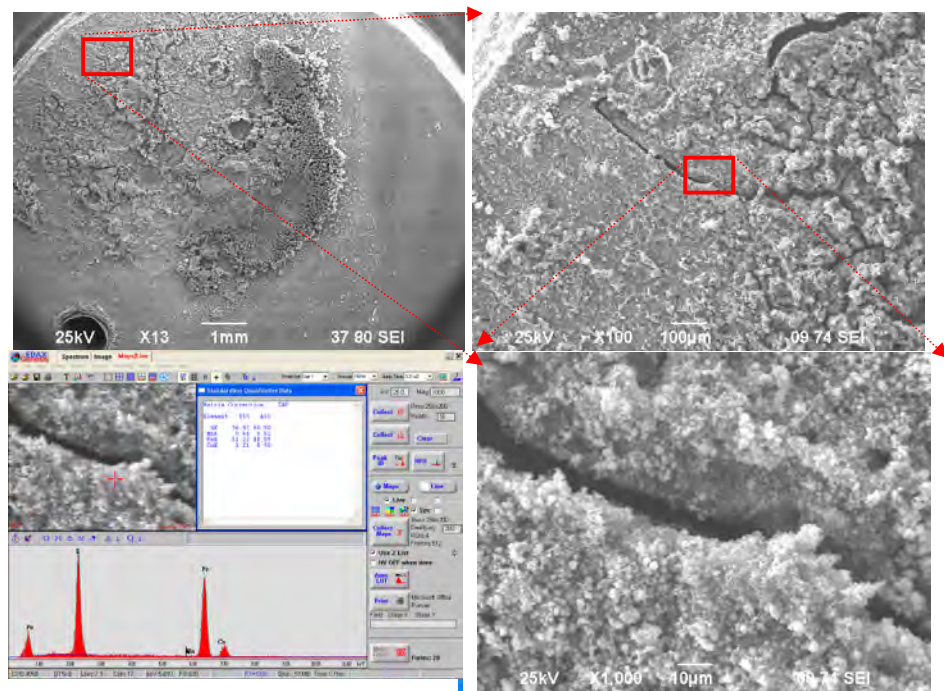


Figure 89. Corrosion specimen contacted with elemental sulfur for 1 day at 80°C, with corrosion product layer.

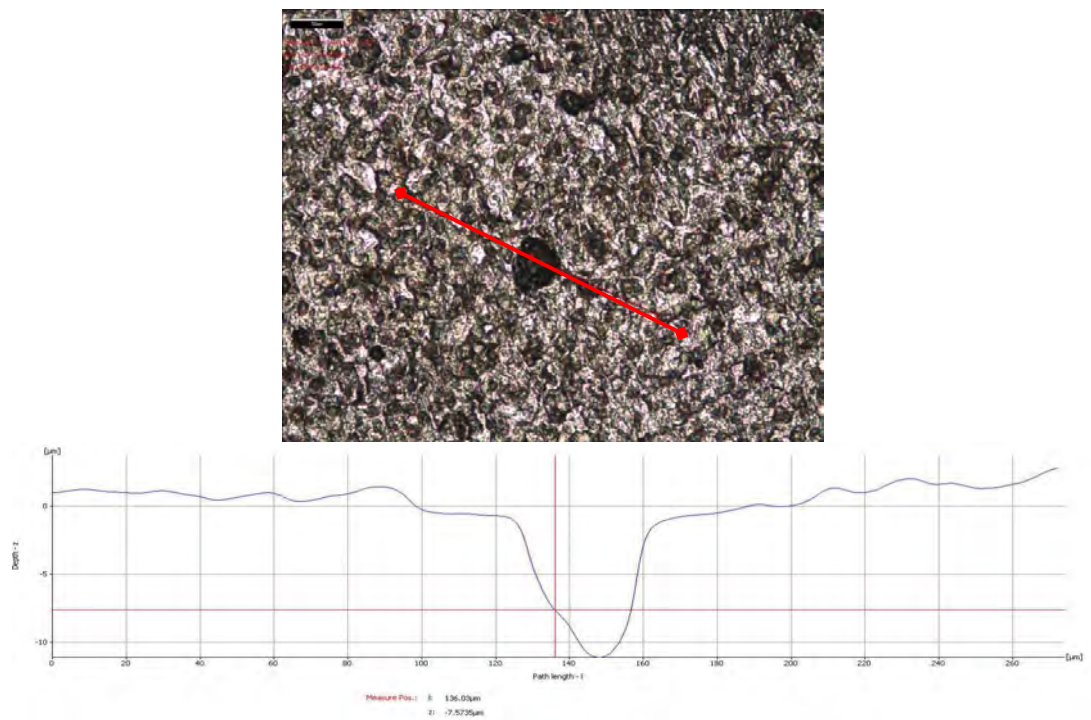


Figure 90. IFM data for specimen contacted with sulfur for 1 day at 80°C, without corrosion product layer.

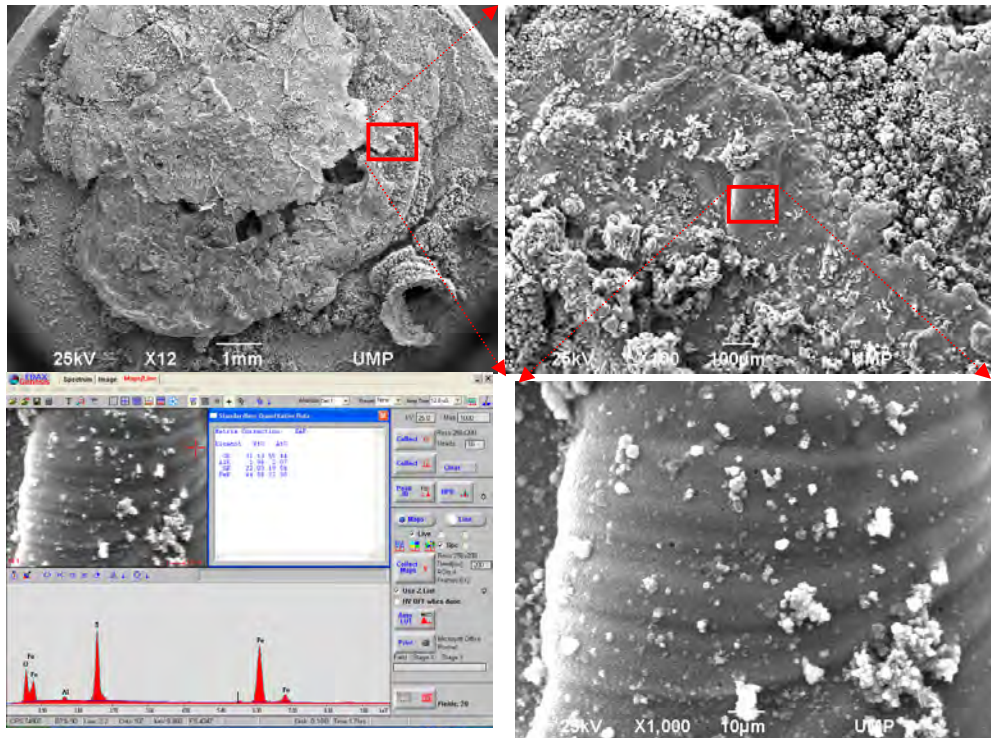


Figure 91. Corrosion specimen contacted with elemental sulfur for 4 days at 80°C, with corrosion product layer.

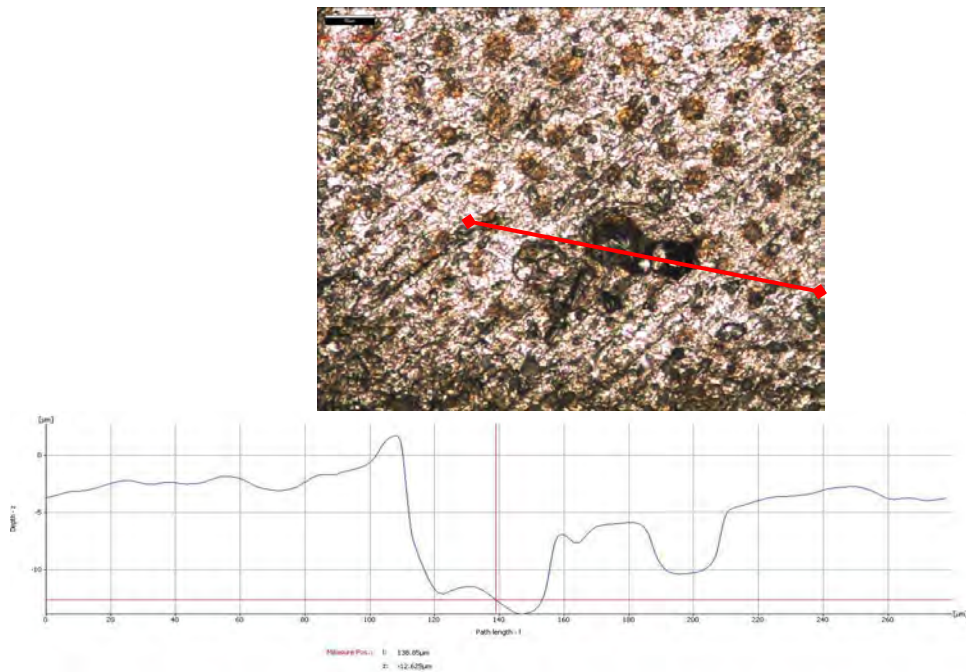


Figure 92. IFM data for specimen contacted with sulfur for 4 days at 80°C, without corrosion product layer.

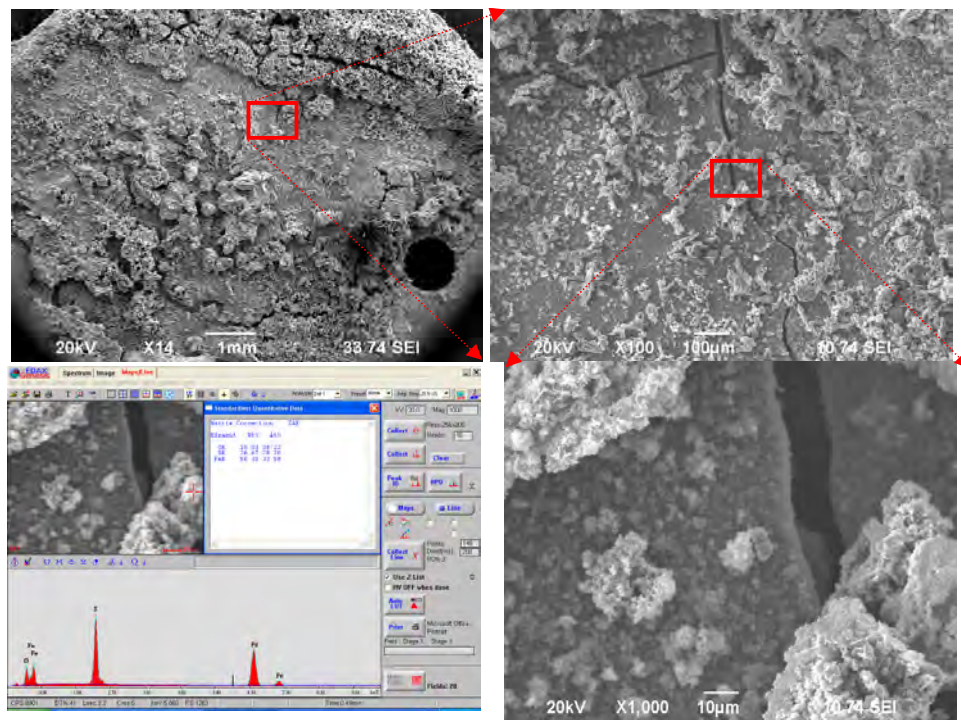


Figure 93. Corrosion specimen contacted with elemental sulfur for 5 days at 80°C, with corrosion product layer.

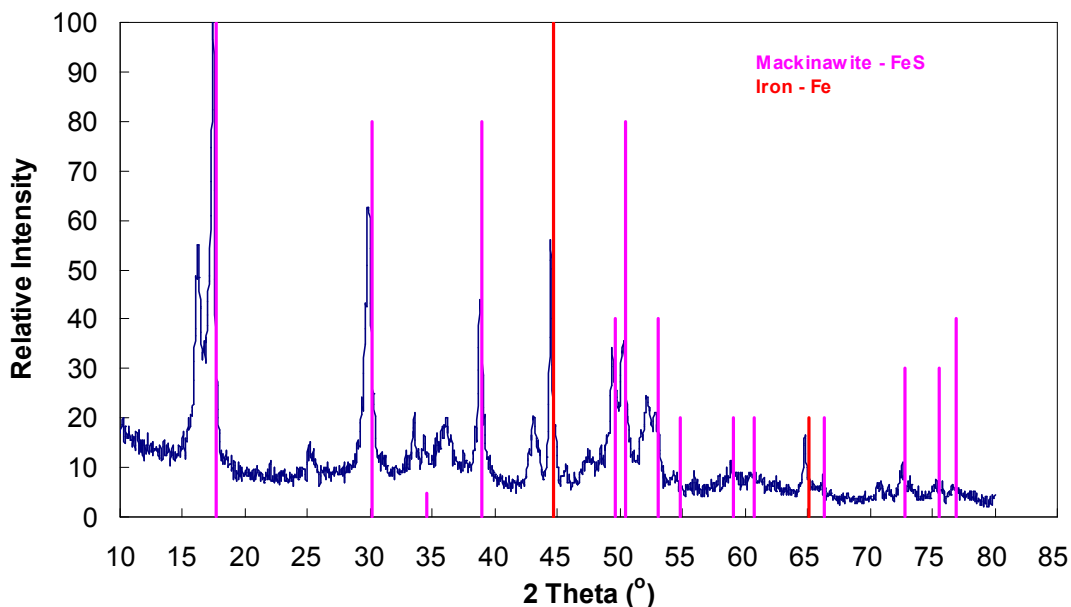


Figure 94. XRD data of the corrosion product after 4 days at 80°C.

Comparison of general and localized corrosion rates are shown in Figure 95 and Figure 96. Both refer to the steel surface area underneath the elemental sulfur deposit. At 25°C, the localized corrosion rate (pitting) decreased from 7.2 mm/yr after one day to 1.7 mm/yr after 5 days. The general corrosion rate remained essentially unchanged at *ca.* 0.80 mm/yr. At 80°C, the localized corrosion rate was 5.1 mm/yr after one day, but was reduced to 3.0 mm/yr after 5 days. The general corrosion rate was 1.6 mm/yr at 80°C, double the general corrosion rate measured at 25°C.

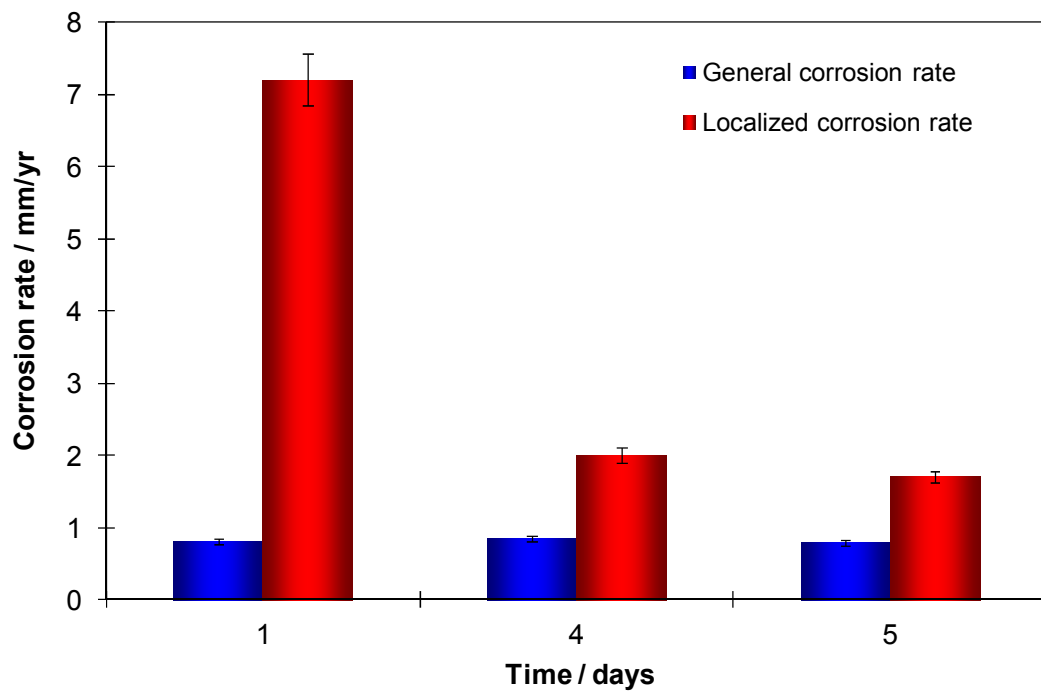


Figure 95. Comparison of general and localized corrosion rates at 25°C, DI water.

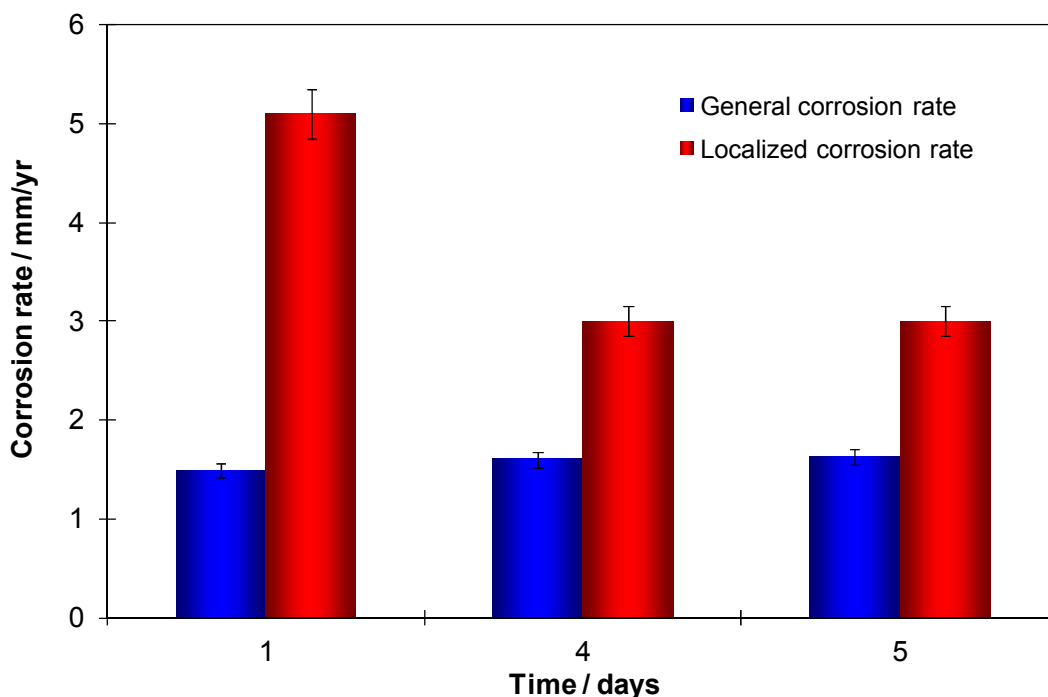
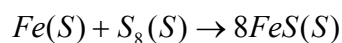


Figure 96. Comparison of general and localized corrosion rates at 80°C, DI water.

It is worth noting that the thick deposits of iron sulfide on the steel substrate formed directly beneath the elemental sulfur. Consequently, a direct solid-state reaction for the formation of iron sulfide from elemental precursors is a more likely process which may occur in these systems:



Such a reaction path does not depend on the generation of acidic species when water is exposed to elemental sulfur.

5.5.2.2.2 Sulfur/iron reaction in dry condition (solid state reaction)

In the preceding section, experimental evidence was shown that a direct reaction between sulfur and steel may occur when they are in contact and in water. To further

prove the feasibility of this theory, a set of experiments for the sulfur/iron reaction were conducted in dry conditions (air). Figure 97 shows a schematic experimental setup. A transparent PVC tube with a plastic cap was glued onto an aluminum sheet and then put on a hot plate. Nitrogen was purged through the tube to remove the oxygen. After 1 hour of purging, a carbon steel specimen with a sulfur deposit was put into the tube. Temperature was varied from 25°C to 125°C by adjusting the hot plate temperature. The test duration was from 6 hours to 2 days. After the test, the steel surface was examined.

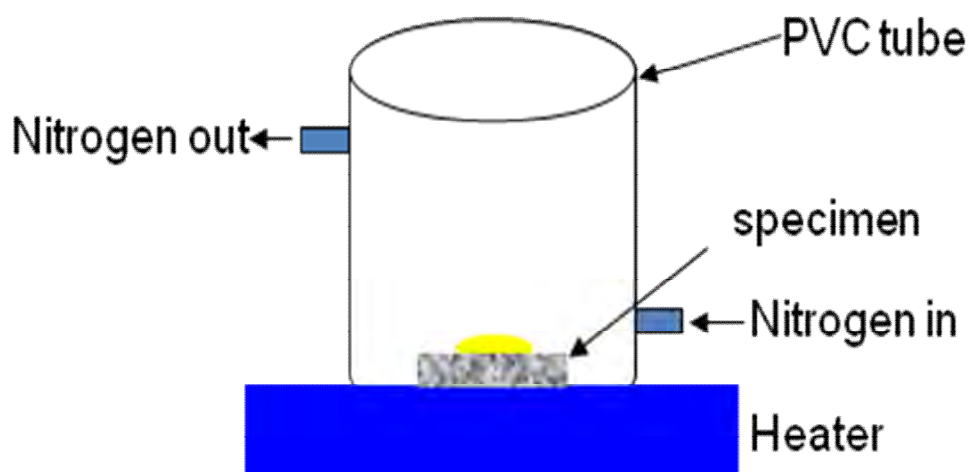
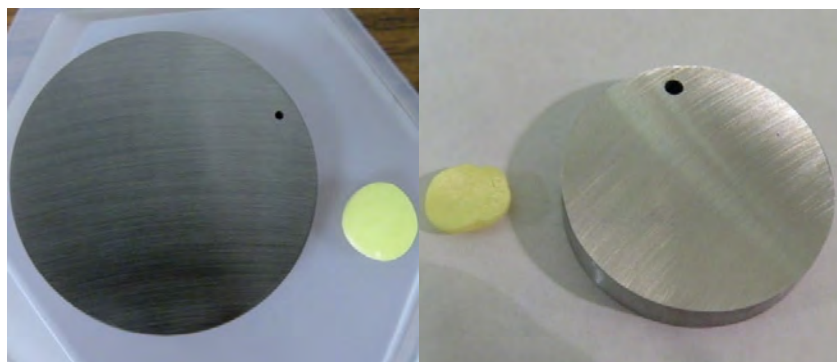


Figure 97. Experimental set-up for solid state reaction.

Experiments for the dry sulfur/iron reaction were started at low temperatures (25°C and 60°C). Figure 98 shows the specimen surface and bottom of sulfur after 6 hour of direct contact at 25°C and 60°C. It is clearly seen that there is no difference between the specimen surface and the fresh polished steel surface. No black iron sulfide layer was detected on the specimen surface as well as the bottom of the sulfur droplet. Weight loss measurement confirms no weight change on both sulfur and the steel specimen. This

suggests that at low temperature (25°C and 60°C), sulfur appears not to react with iron at dry condition.



a) 25°C

b) 60°C

Figure 98. Specimen surface after 6 hour exposure at 25°C and 60°C.

Since no reaction between sulfur and iron was observed at low temperature and short exposure time, the test temperature was increased to 80°C and exposure was increased to 2 days. Figure 99 shows the steel specimen and sulfur surface after experiment. Similar to the low temperature test, no corrosion products were detected on the specimen and sulfur surface.

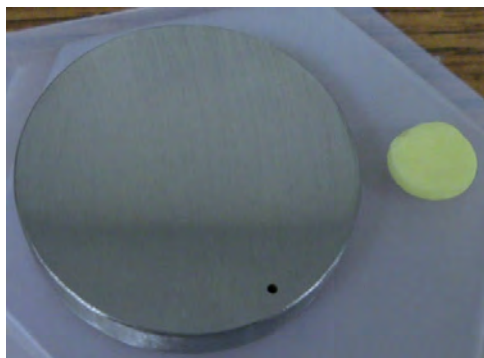


Figure 99. Specimen surface after 2 days exposure at 80°C.

Temperature was then further increased to 125°C, which is slightly higher than the melting point of elemental sulfur. Figure 100 shows the specimen surface during and after the experiment. The picture in the left side shows the specimen surface during the experiment. It appears that the sulfur has been melted on the specimen surface. After six hours exposure, sulfur was mechanically removed from the steel surface. Still, no iron sulfide layer was detected on the surface. A small amount of sulfur residue remained on the steel surface because of the strong adhesive bond between sulfur and steel.

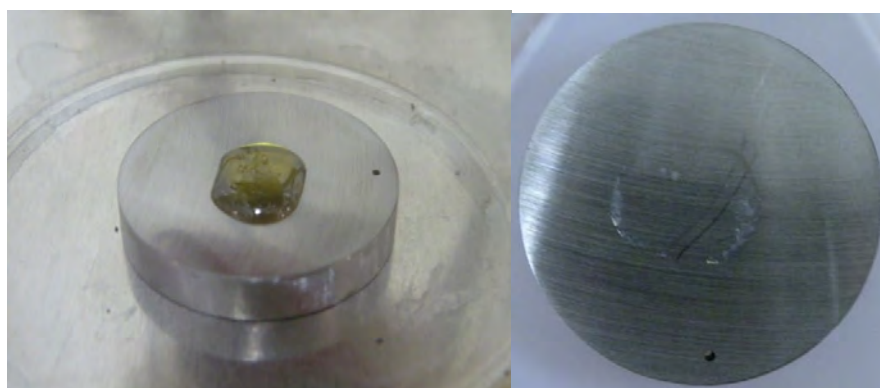


Figure 100. Specimen surface during and after 6 hours exposure at 125°C.

Experimental results suggest that sulfur cannot react with steel, or the rate is extremely low when water is not present even at a temperature above the sulfur melting point. Therefore, the previous hypothesis of a direct solid state reaction between sulfur and iron is less likely to be the main corrosion mechanism of elemental sulfur corrosion when water is not present.

5.5.2.2.3 Investigation the nature of the sulfur/iron reaction

In the new experiments, either an electrically insulating or conductive barrier was placed between the sulfur droplet and the metal sample surface, separating the steel and sulfur to eliminate direct, physical contact between them. The design of these experiments was meant to reveal the mechanisms of sulfur corrosion by distinguishing the importance of two main parameters: direct physical proximity *vs.* electrical contact of sulfur and steel. In other words the distinction is between a chemical and an electrochemical reaction. The barriers placed between the sulfur droplet and sample surface in three different series of tests were: a non-conductive nylon mesh and a conductive graphite sheet with and without an array of small holes (Figure 101). Samples thus prepared were then transferred to a glass cell for corrosion experiments. Glass cell tests were performed in a salt free and a 1.5 M salt solutions (NaCl).

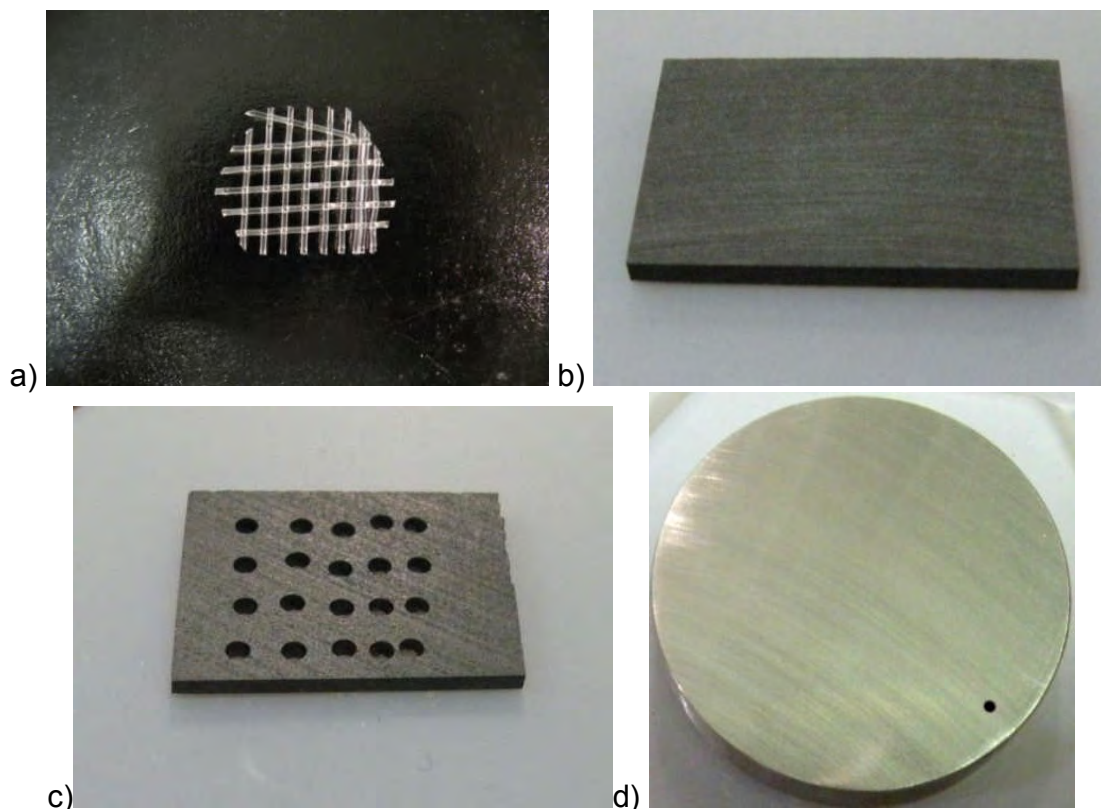


Figure 101. Materials used for the physical separation of sulfur and iron: a) plastic mesh, b) graphite sheet, c) graphite sheet with 0.043" ID holes, d) X65 steel sample.

After removal from the glass cell following the experiment, corrosion samples were immediately put into deoxygenated deionized water to dissolve any soluble salts from the sample surface. Prior to surface analysis, the unreacted sulfur was mechanically removed from the sample surface. Samples were characterized by scanning electron microscopy (SEM), energy dispersive X-ray fluorescence microanalysis (EDX) and infinite focus microscopy (IFM). Corrosion products were then removed by treatment with Clarke's solution and the bare corroded steel sample surface was re-characterized by

IFM. Localized corrosion rates were determined by analysis of IFM data whereas general corrosion rates were obtained by weight loss methods.

5.5.2.2.3.1 Experiments with the plastic mesh

A plastic mesh was placed between the sulfur droplet and the sample surface (Figure 102). By doing that, sulfur was both physically separated (if only for a small distance) and electrically insulated from the steel sample surface. The thickness of the mesh is about 2 mm, which still puts the sulfur and the sample in close proximity to each other.

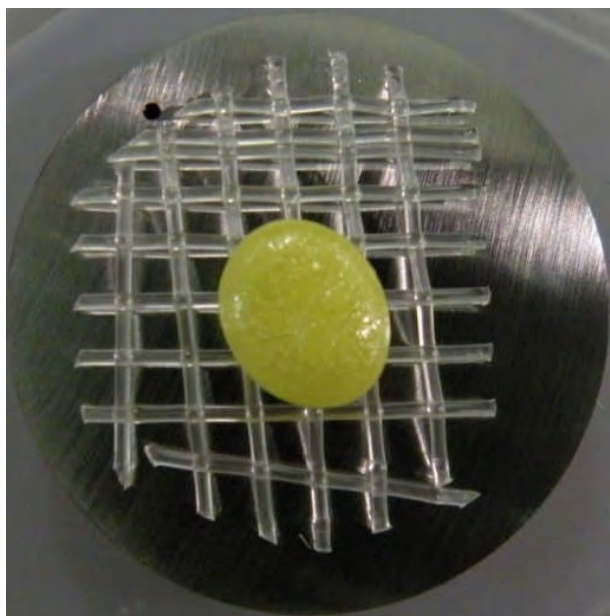


Figure 102. Sample arrangement for the sulfur/plastic-mesh/steel test, where steel surface is in close proximity to sulfur but electrically insulated from each other.

The experiment was conducted at 25°C in pH neutral de-ionized water. Figure 103 shows a picture of the sample surface after 1 day. The sulfur and plastic mesh were physically removed from the sample surface. A slight black tarnish was observed on the

sample surface. Figure 104 shows the SEM/EDX data for a typical region of the sample surface. The surface morphology is similar to a steel surface exposed to a solution containing a very small amount (traces) of dissolved hydrogen sulfide. EDX data also indicates a small amount of sulfur. This would be consistent with the hypothesis that a small amount of H_2S was generated by the sulfur hydrolysis reaction and its subsequent reaction with the steel surface.

From a series of similar experiments it was concluded that when the sulfur and steel sample were in physical proximity but electrically insulated from each other, corrosion was not measurable and virtually no corrosion product film was obtained. This suggests that the physical proximity between sulfur and steel alone is insufficient to cause corrosion attack.



Figure 103. Steel sample surface after exposure in the sulfur/plastic-mesh/steel test where it was in close proximity to sulfur but electrically insulated from each other.

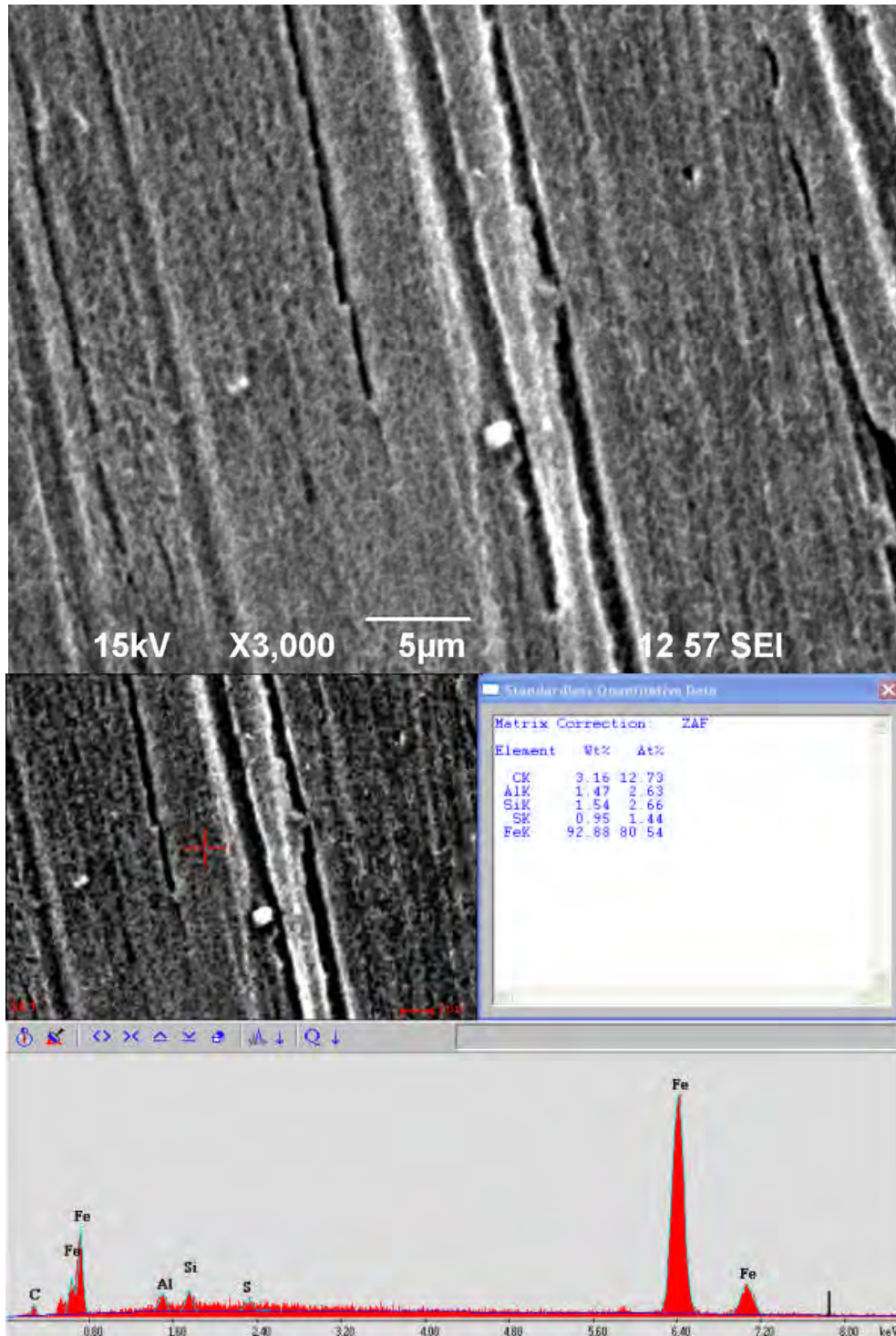


Figure 104. SEM/EDX data for the typical corroded steel surface after exposure in the sulfur/plastic-mesh/steel test where it was in close proximity to sulfur but electrically insulated from each other.

5.5.2.2.3.2 Experiments with the graphite sheet

In this series of experiments, the sulfur and steel surface were physically separated but electrically connected by placing an electrically conductive carbon sheet (2mm thick) between them (Figure 105). This experiment was also conducted at 25°C in pH neutral deionized water. A picture of the sample surface after corrosion is shown in Figure 106.

A thin, tarnish layer formed on the sample surface but only in the area which was covered by the carbon sheet. However, corrosion attack under this condition was not severe. The surface region which was uncovered by the carbon sheet remained untarnished and shiny, which suggests that essentially no corrosion occurred in this area. Figure 107 shows the SEM/EDX data of the surface underneath the carbon sheet. EDX data suggests that most of the corrosion product layer observed in the area covered by the carbon sheet was a mixture of iron oxide and iron sulfide.

This series of experiments suggested that if the steel surface and sulfur are physically separated but electrically connected, the sulfur will be reduced, the iron will be oxidized and iron sulfide will form in between the two. However, because of the separation and due to the impermeability of the carbon sheet, it was difficult for the reactive species to diffuse through, and therefore the degree of attack was not high. It was concluded that electrical connection between sulfur and steel alone does not lead to a severe corrosion attack.

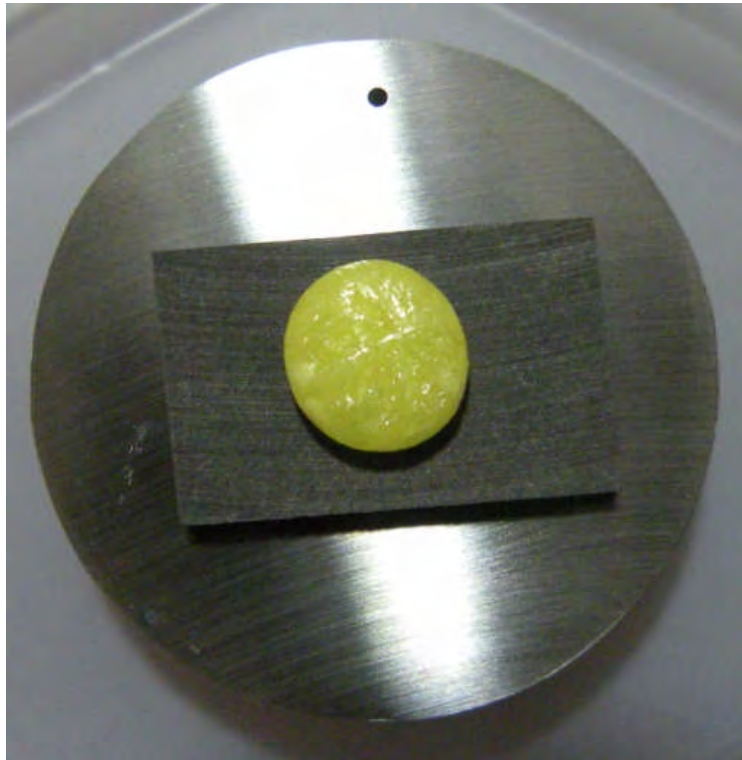


Figure 105. Sample arrangement for sulfur/carbon-sheet/steel test where the steel was separated from the sulfur but electrically connected.

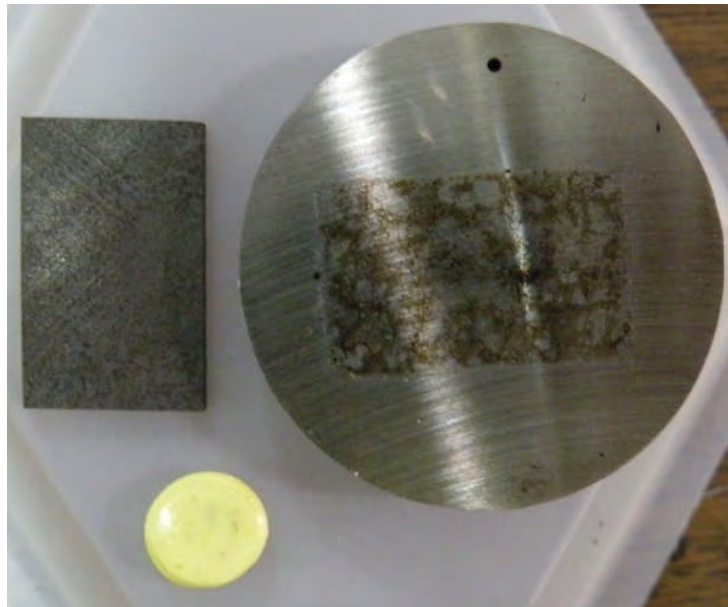


Figure 106. Steel sample surface after exposure in the sulfur/carbon-sheet/steel test where the steel was separated from the sulfur but electrically.



Figure 107. SEM/EDX data for the steel sample surface underneath the carbon sheet after exposure in the sulfur/carbon-sheet/steel test where the steel was separated from the sulfur but electrically connected to it.

5.5.2.2.3.3 Experiments with the graphite sheet with holes

This experiment was meant to investigate the case when sulfur was both electrically connected and in physical proximity to the steel surface. Figure 108 shows the sample arrangement.

The experiment was again conducted at 25°C in pH neutral deionized water. After the experiment, the sulfur and carbon sheet were physically removed from the sample surface. Figure 109 shows the SEM/EDX data for the sample surface beneath a hole. It is apparent that a thin layer of corrosion product formed on the area directly under the hole. EDX data confirmed this to be an iron sulfide.

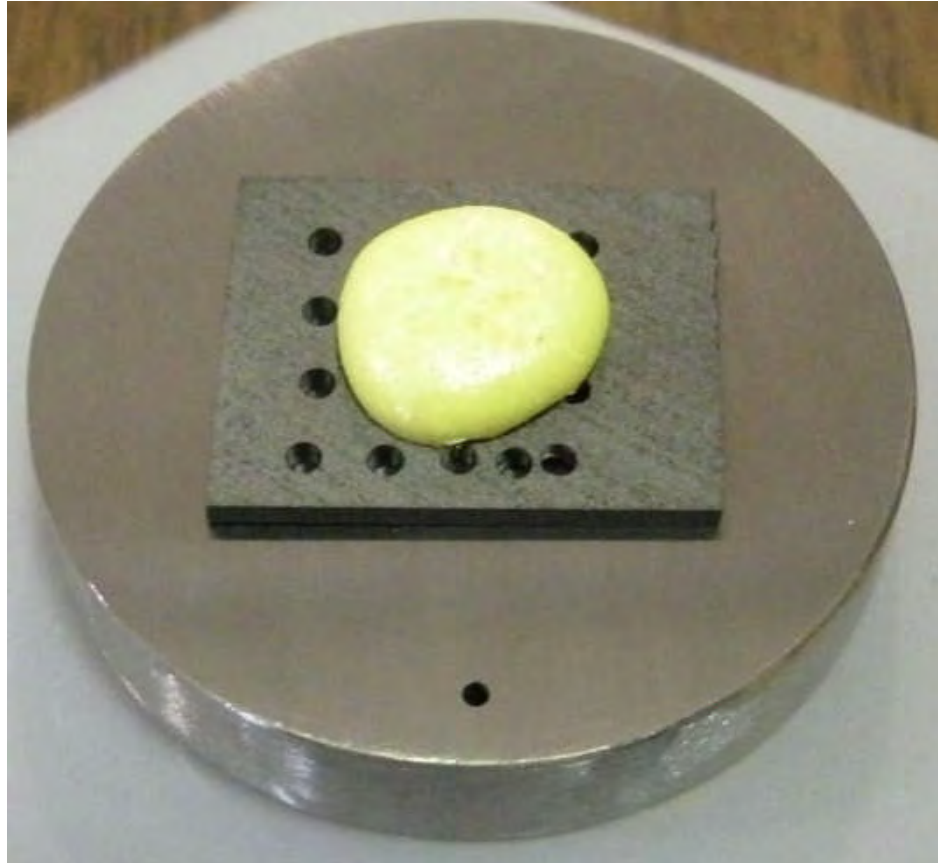


Figure 108. Sample arrangement for sulfur/carbon-sheet-with-holes/steel test where the steel was in physical proximity to the sulfur and electrically connected.

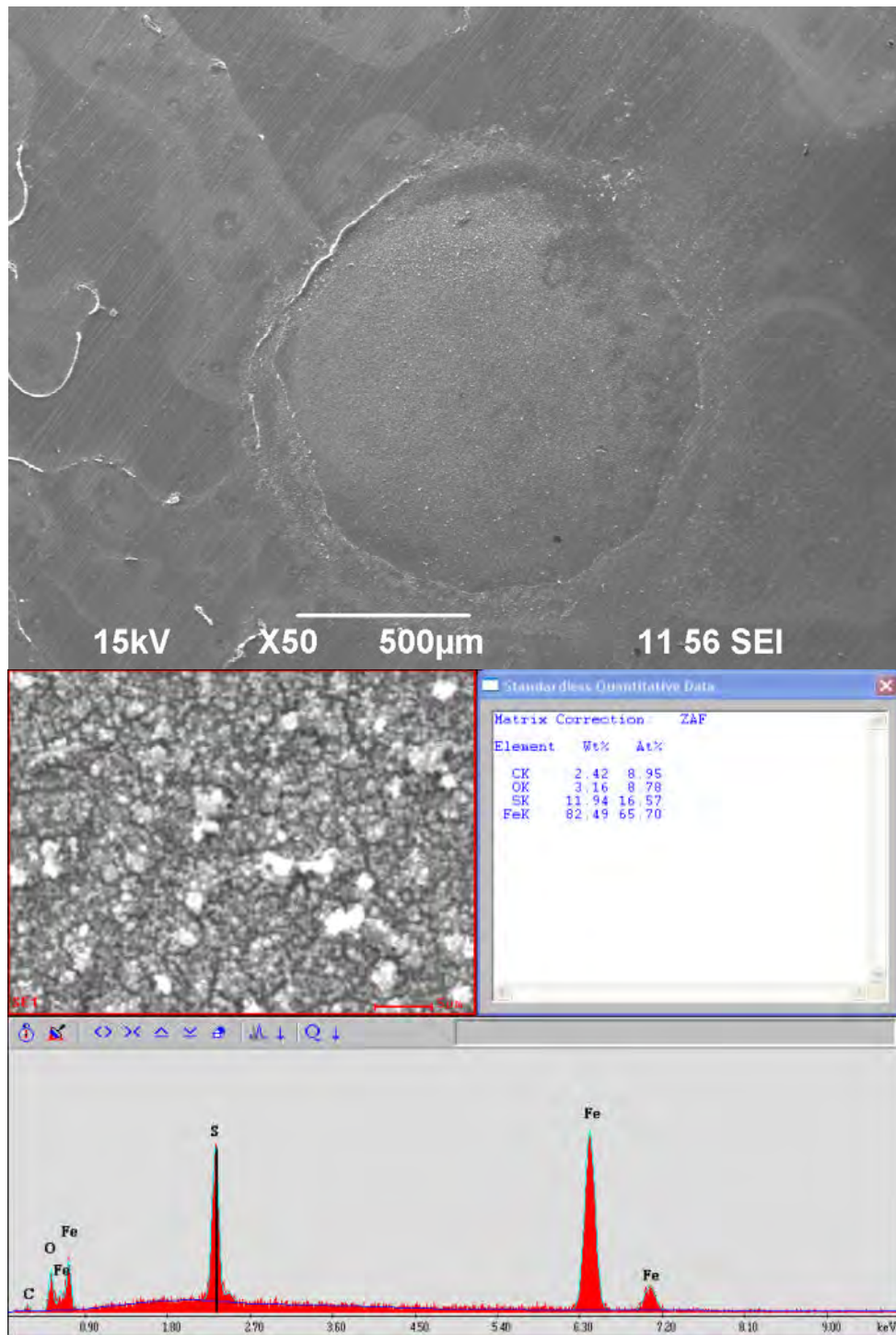


Figure 109. SEM/EDX data for the sample surface underneath the hole from the experiment where the steel was in physical proximity to the sulfur and electrically connected.

Figure 110 shows a SEM image of another location of the specimen surface after the experiment. It is clearly seen that the iron sulfide layer was mostly generated on the specimen surface directly underneath the holes. This is different from what was observed when the plastic mesh or the carbon sheet without holes was used. The experimental results indicate that when the carbon sheet provided a conductive media for the electron transfer between sulfur and steel and the holes enables the mass transfer of species, and the degree of attack was much higher.

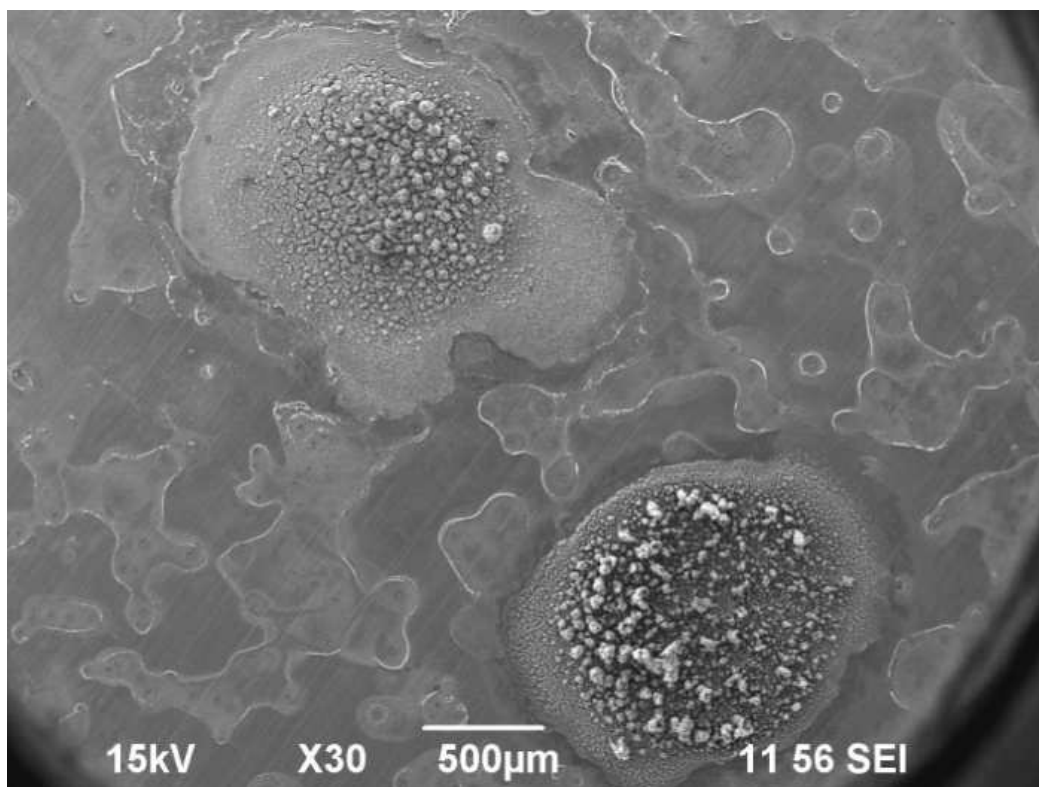


Figure 110. SEM data for the sample surface underneath the hole, from the experiment where the steel was in physical proximity to the sulfur and electrically connected.

In another experiment, the temperature was increased to 80°C to increase the kinetics of the corrosion reaction. Figure 111 shows the SEM image of the sample surface underneath the carbon sheet with holes. A significant amount of sulfide layer was observed directly under the holes. In this case, much more severe corrosion occurred on the metal surface.

From the above investigation, it was concluded that elemental sulfur corrosion can occur without direct contact of sulfur and the steel surface. Severe corrosion may occur when sulfur and steel are electrically connected and in physical proximity to each other. This investigation revealed the electrochemical nature of elemental sulfur corrosion.

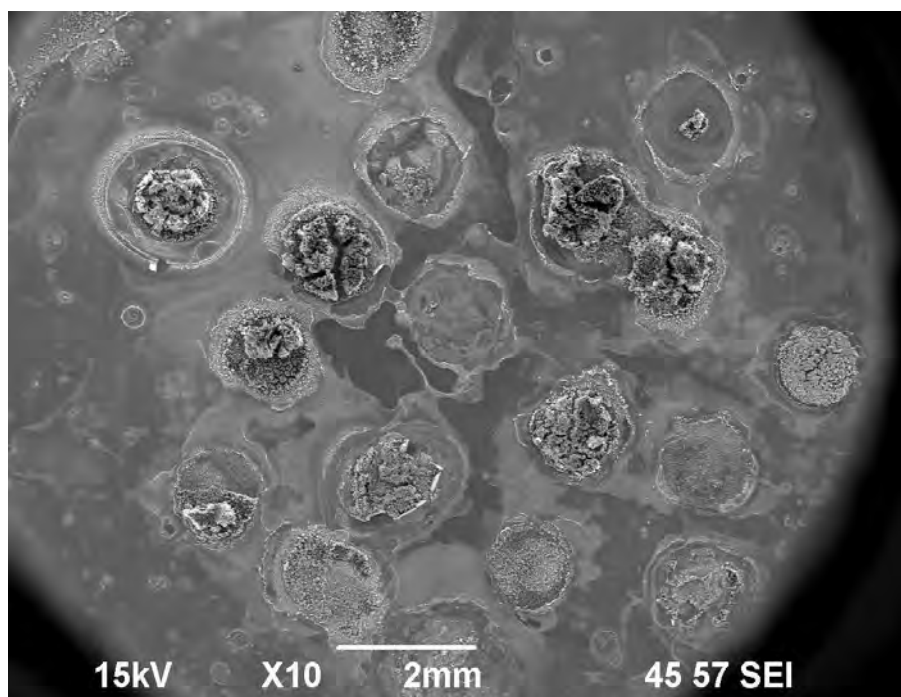


Figure 111. SEM image of the sample surface underneath the carbon sheet with holes from the higher temperature experiment where the steel was in physical proximity to the sulfur and electrically connected.

5.5.2.2.4 Sulfur/iron reaction in 10 wt.% NaCl

In the new series of experiments, 10 wt.% NaCl was added into the test solution. The purpose was to see if the corrosion attack by elemental sulfur may change with the addition of chloride ions or increased solution conductivity.

Specimens with elemental sulfur on the surface before and after 1, 4 and 5 days exposure at 25°C are shown in Figure 112, Figure 113 and Figure 114. Interestingly, a black iron sulfide layer was formed on the specimen area which has no direct contact with elemental sulfur. This is quite different from what has been observed in salt free conditions, where only the portion of specimen surface underneath the sulfur was significantly blackened after exposure. Detailed comparisons of experimental results between salt free and high salt concentration conditions will be shown later.

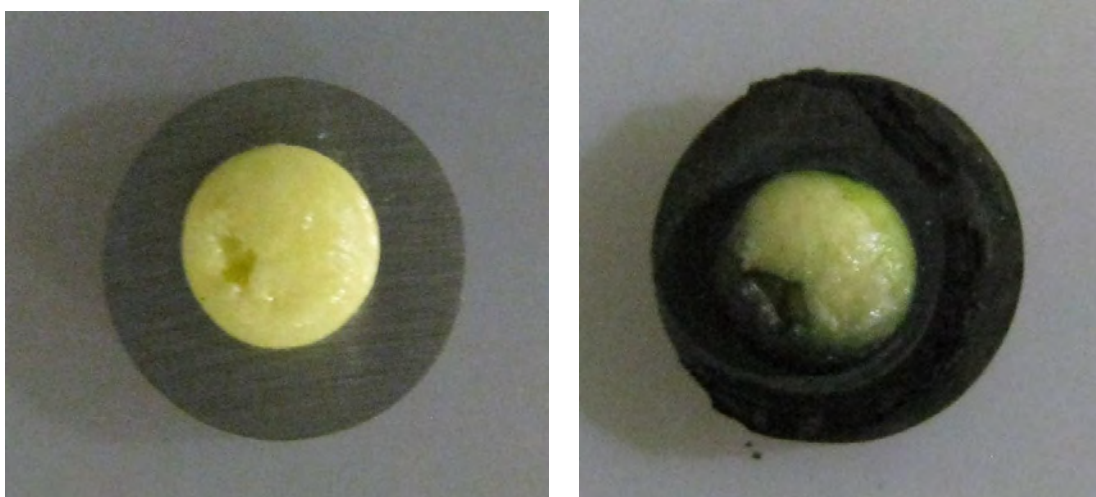


Figure 112. Corrosion specimen before and after 1 day exposure at 25°C.

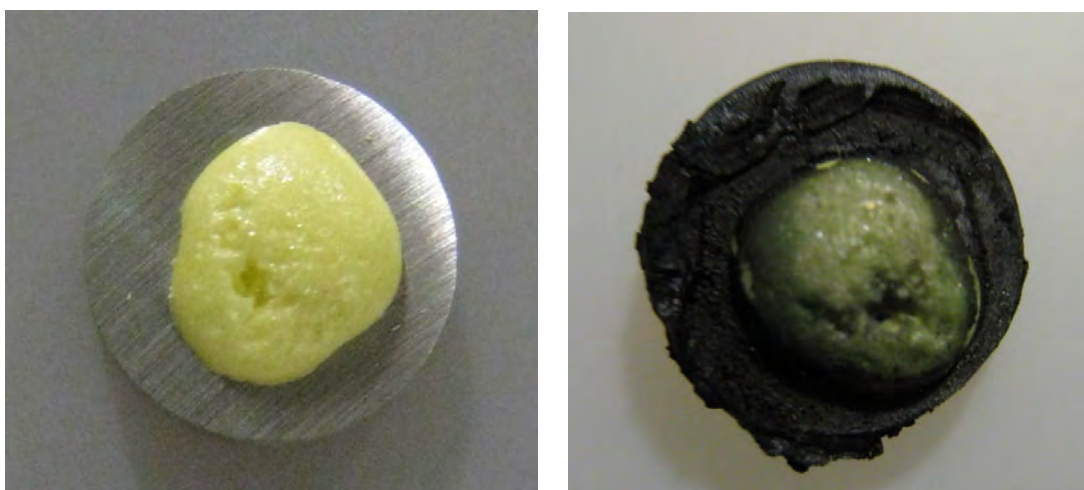


Figure 113. Corrosion specimen before and after 4 days exposure at 25°C.

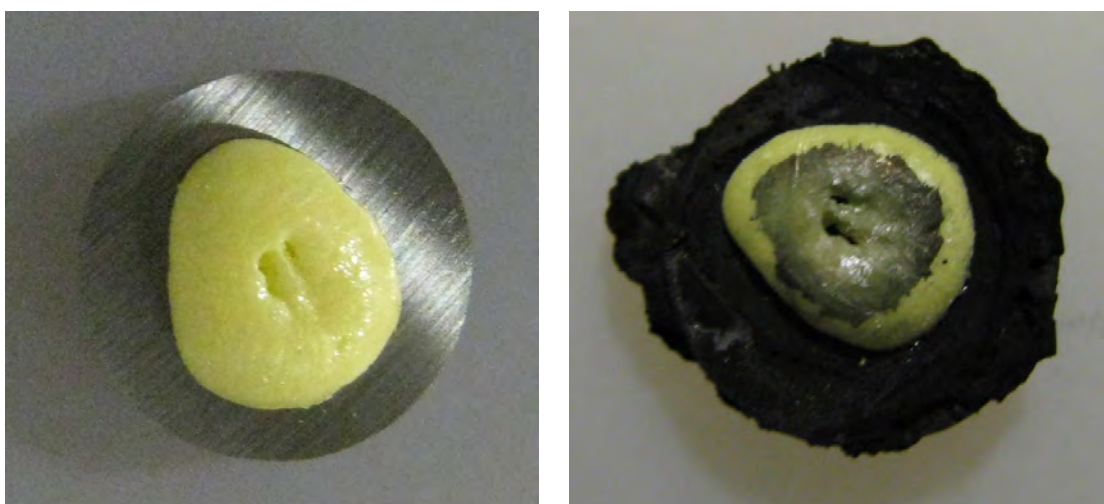


Figure 114. Corrosion specimen before and after 5 days exposure at 25°C.

Representative SEM/EDX data for the corrosion specimen surface that has been in direct contact with elemental sulfur for one day at 25°C is shown in Figure 115. The red circled area represents the area that was covered by the sulfur pellet. Most corrosion product layer generation occurred in close proximity to the periphery of the sulfur pellet. This phenomenon confirms the observation made by Kennelley, et al. in 1990¹⁰⁵. A

further enlargement of the small area underneath the sulfur pellet (top right) shows clear polishing marks covered by a small quantity of corrosion product. A high magnification SEM picture shows the outer area which was uncovered by sulfur, a much thicker corrosion product layer was generated in this area. The composition of the corrosion product layer was shown by EDX to be consistent with iron sulfide. The IFM image of the corrosion specimen, after the iron sulfide has been removed, reveals severe localized corrosion in the outer area (Figure 116). The top right and bottom left images correspond to the small regions marked on the “whole specimen” picture. The line across the top right of the image corresponds to the profile data of the specimen surface. IFM data show that the specimen surface beneath the sulfur pellet was barely corroded. Comparison with the SEM pictures of specimen surface with corrosion product layer reveals that the steel corrodes more severe when more corrosion product layer is generated on the specimen surface. After four days at 25°C a thicker corrosion product layer has formed at both the inner and outer surface, see Figure 117. However, the corrosion product layer on the outer specimen surface is still much thicker than the layer on the inner specimen surface. Cracking of the layer is observed on the specimen surface. From EDX, it is clear that the corrosion product layer chemistry remains fundamentally unchanged with longer exposure. IFM data (Figure 118) shows that several shallow “holes” start to form on the sulfur covered region. This is indicative of initiation of pitting corrosion. Localized corrosion attack on the outer specimen surface is still significant. The corrosion depth is about 25 μm and it increases with time. After a 5 day exposure at 25°C, see Figure 119, the corrosion product layers seem to be even thicker and coarser

than before. However, the polishing marks are still observable in the region which was covered by elemental sulfur. IFM data, Figure 120, show that the shallow pits generated at the fourth day continue to grow. The outer surface also shows greater localized corrosion depth.

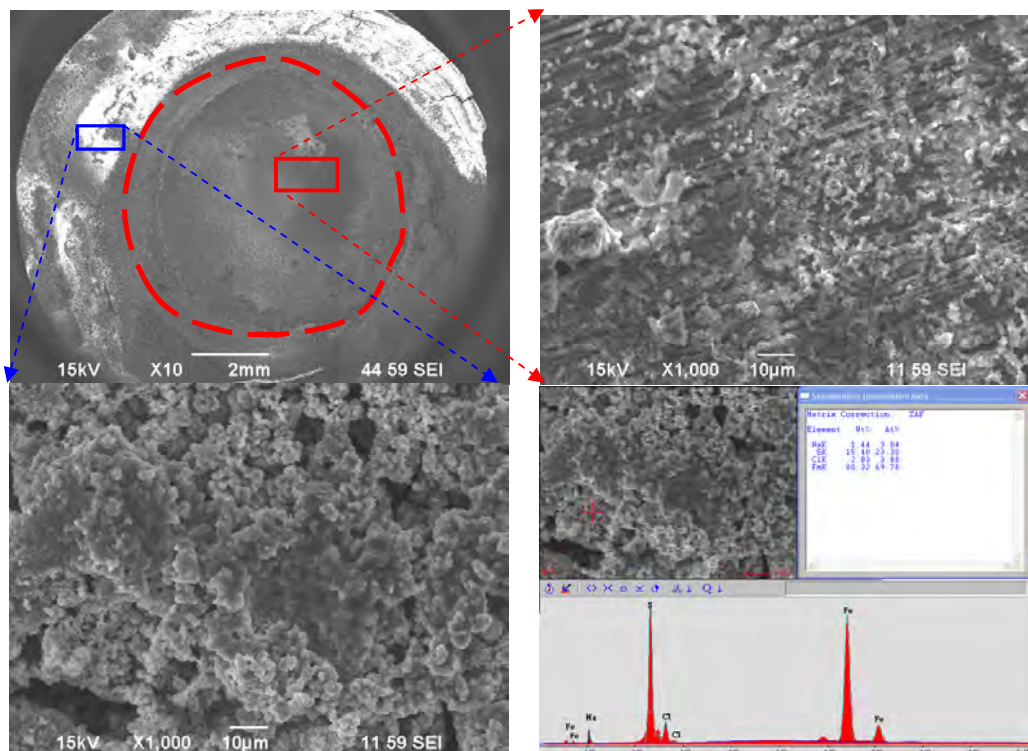


Figure 115. Corrosion specimen contacted with elemental sulfur for 1 day at 25°C, with corrosion product layer.

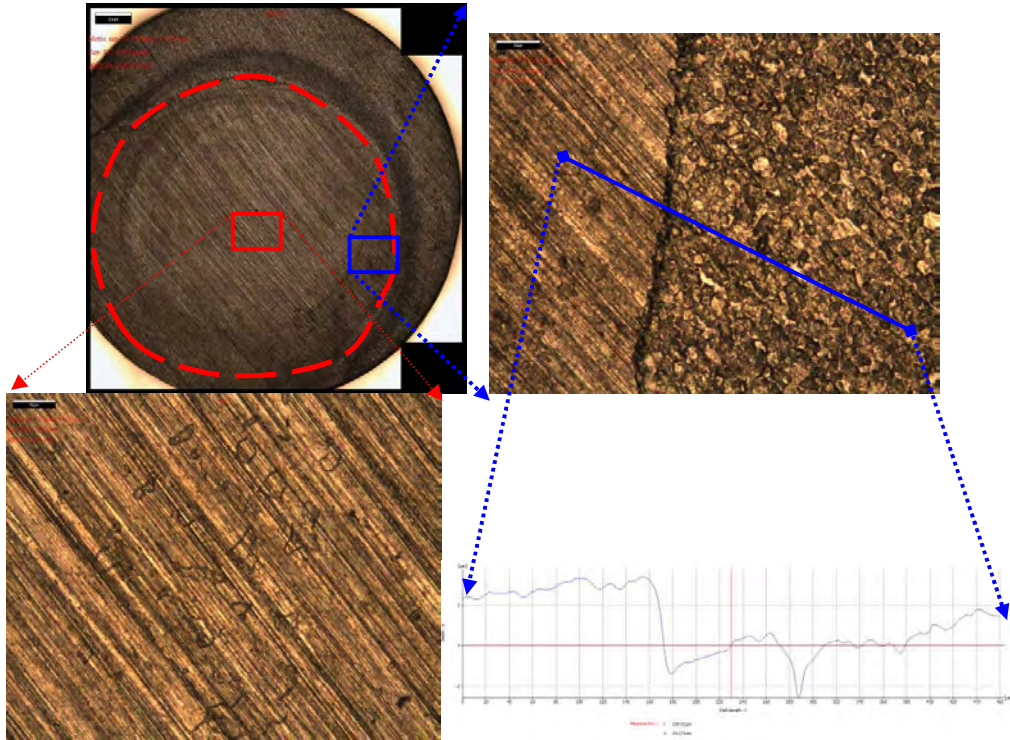


Figure 116. IFM data for corrosion specimen for 1 day at 25°C, without corrosion product layer, appearance of the surface (top images) and a line profile.

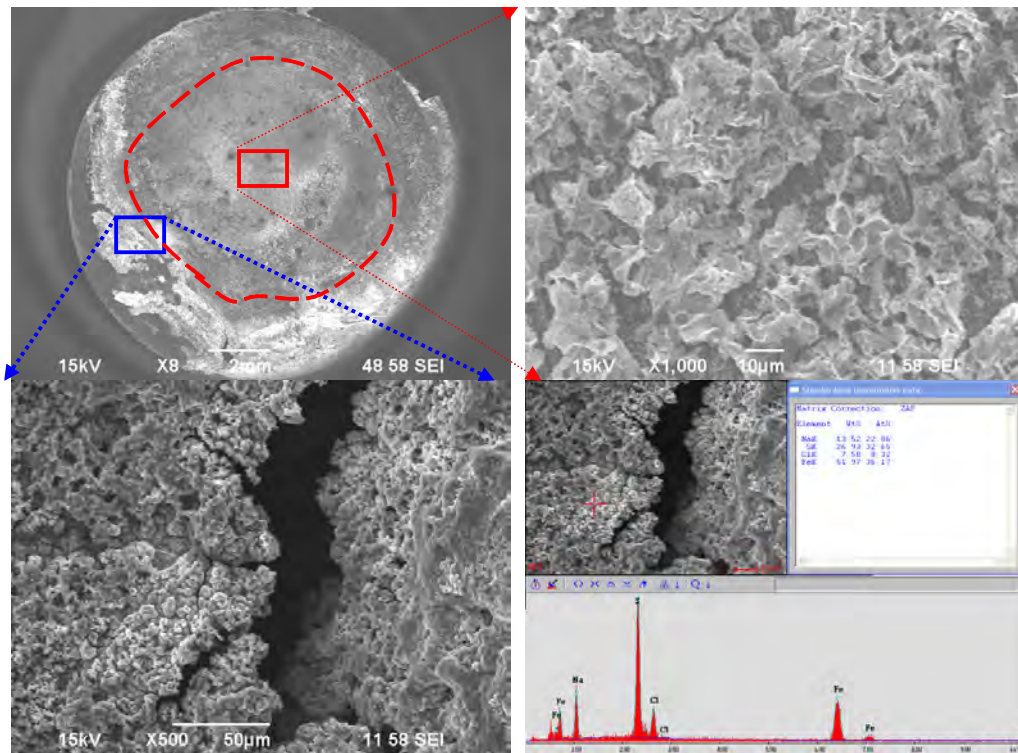


Figure 117. Corrosion specimen contacted with elemental sulfur for 4 days at 25°C, with corrosion product layer.

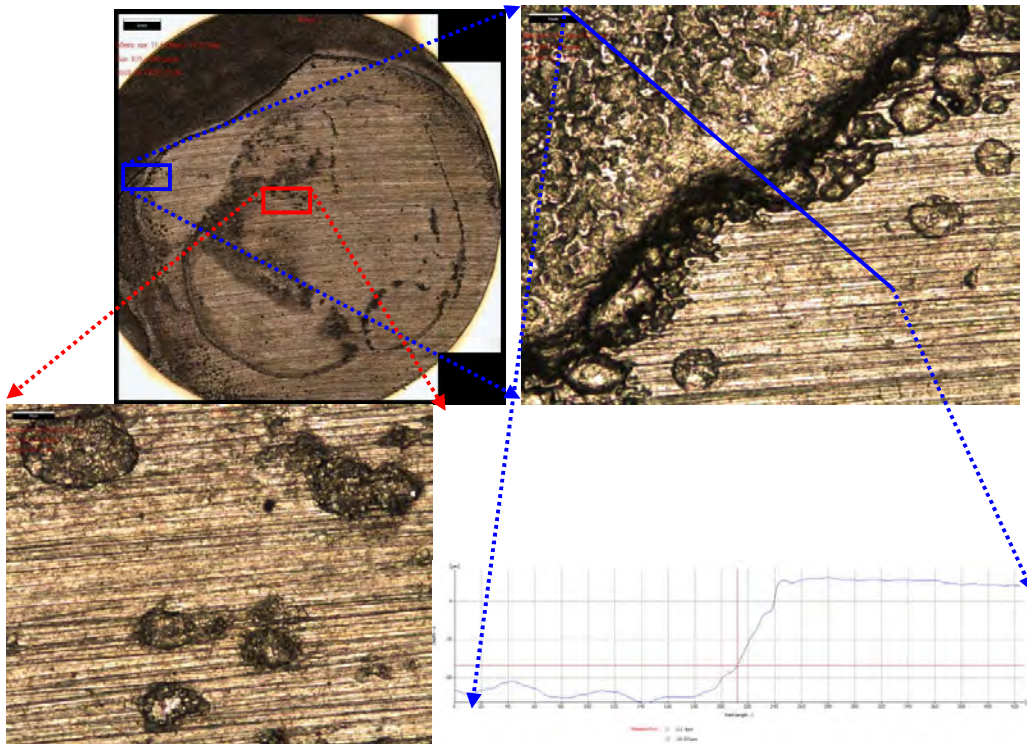


Figure 118. IFM data for specimen contacted with sulfur for 4 days at 25°C, without corrosion product layer.

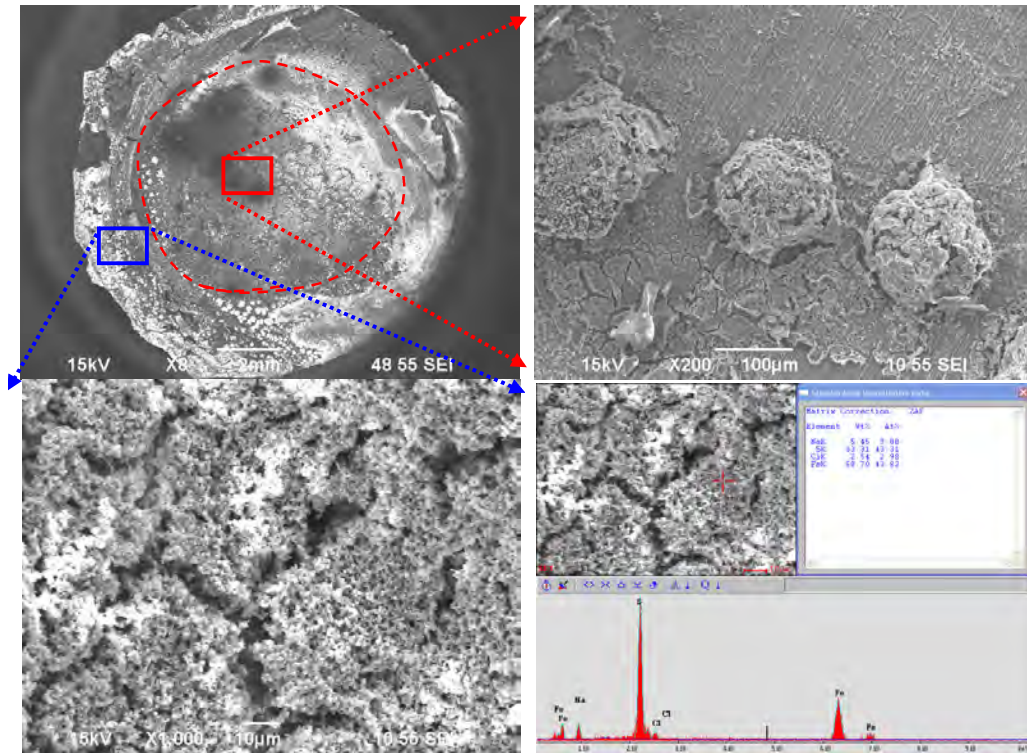


Figure 119. Corrosion specimen contacted with elemental sulfur for 5 days at 25°C, with corrosion product layer.

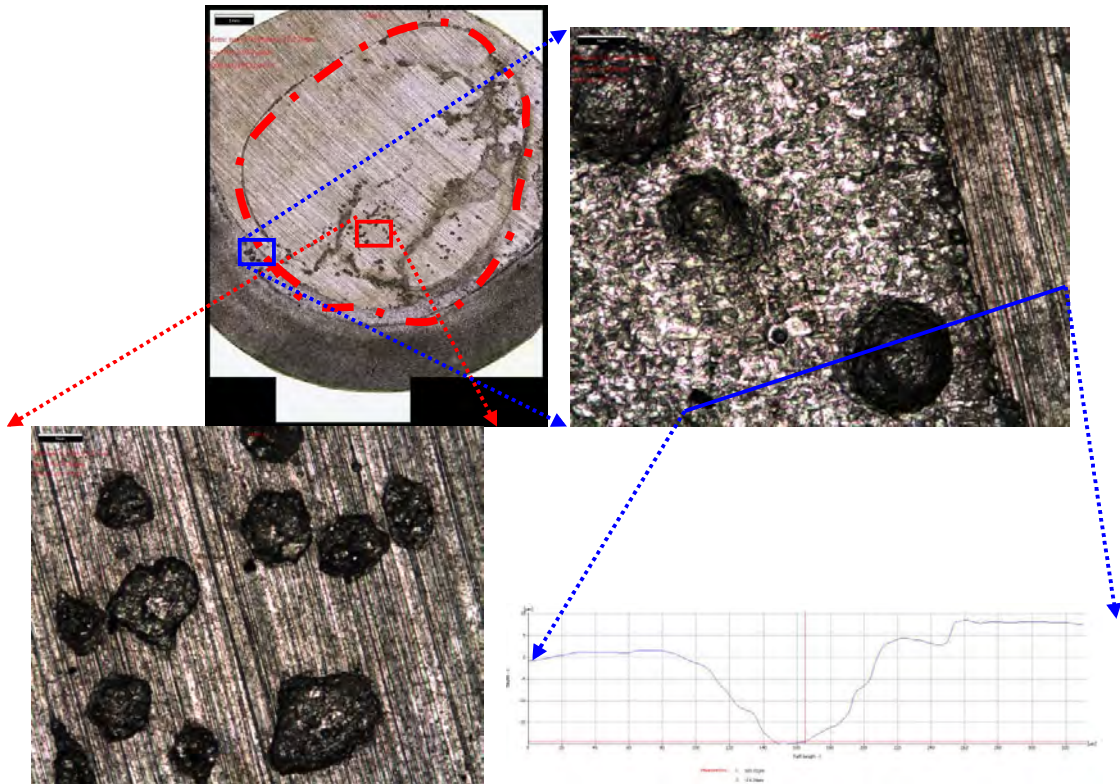


Figure 120. IFM data for specimen contacted with sulfur for 5 days at 25°C, without corrosion product layer.

A similar series of experiments was conducted at 80°C. Specimens with elemental sulfur on the surface before and after 1, 4 and 5 days exposure at 80°C are shown in Figure 121, Figure 122 and Figure 123. Similar to the experimental results at 25°C, the corrosion product layers appeared to be all over the specimen surface.

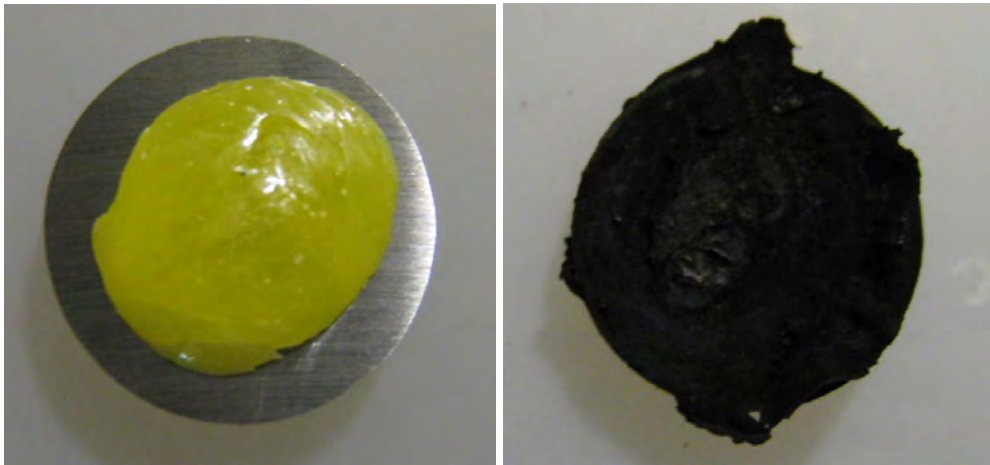


Figure 121. Corrosion specimen before and after 1 day exposure at 80°C.



Figure 122. Corrosion specimen before and after 4 days exposure at 80°C.

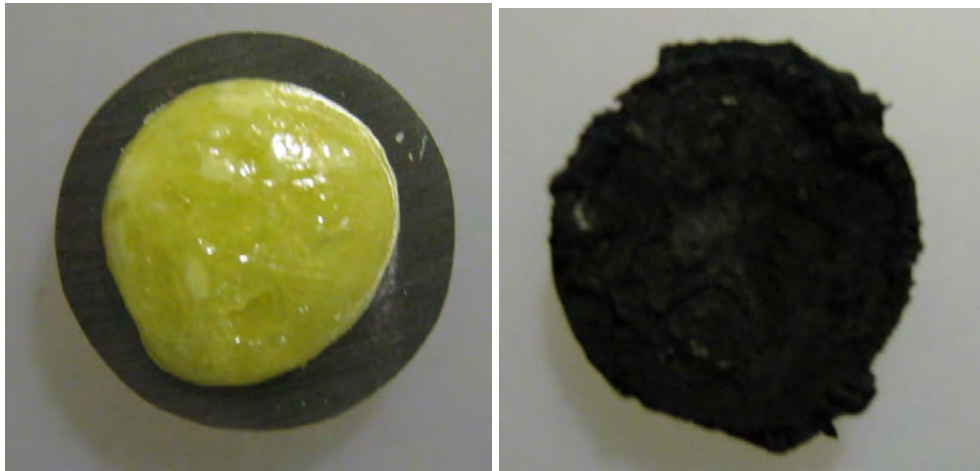


Figure 123. Corrosion specimen before and after 5 days exposure at 80°C.

After one day at 80°C there is a much thicker layer present on the specimen surface than was observed at 25°C, see Figure 124. The white regions of the image are caused by deposition of sodium chloride. The thickness and macroporosity of layer makes it difficult to completely dissolve the salt from the specimen surface. IFM data, Figure 125, of the specimen surface after corrosion product layer removal clearly shows a much more severe localized corrosion attack. Interestingly, in the region of the sulfur covered surface, part of the steel was corroded away yet another region of the specimen surface remained with the original appearance (polishing marks on). The localized corrosion depth around the outer surface is around 55 μm , representing 20 mm/yr corrosion rate. This is an extremely high corrosion rate. After 4 days at 80°C, Figure 126, the corrosion product layer has become thicker and coarser. After 5 days at 80°C, Figure 127, the entire surface seems to be covered by a coarse and cracked corrosion product layer. The corrosion product layers appear to be much denser and highly crystalline. IFM data (Figure 128) show the specimen surface after corrosion product

layer removal. A layer of the original steel surface was corroded away. It is difficult to quantify the localized corrosion depth, because the original specimen surface is gone. However, a surface profile analysis is still given for reference. The depth is around 35 μm . It was noted that the corrosion rate decreased with time.

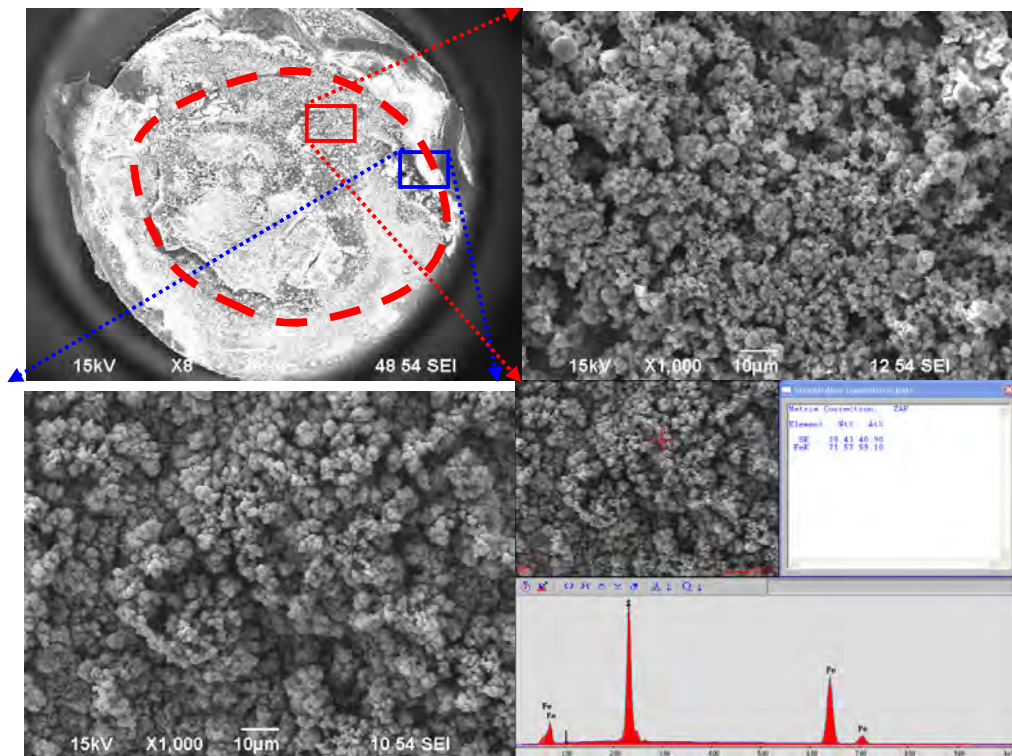


Figure 124. Corrosion specimen contacted with elemental sulfur for 1 day at 80°C, with corrosion product layer

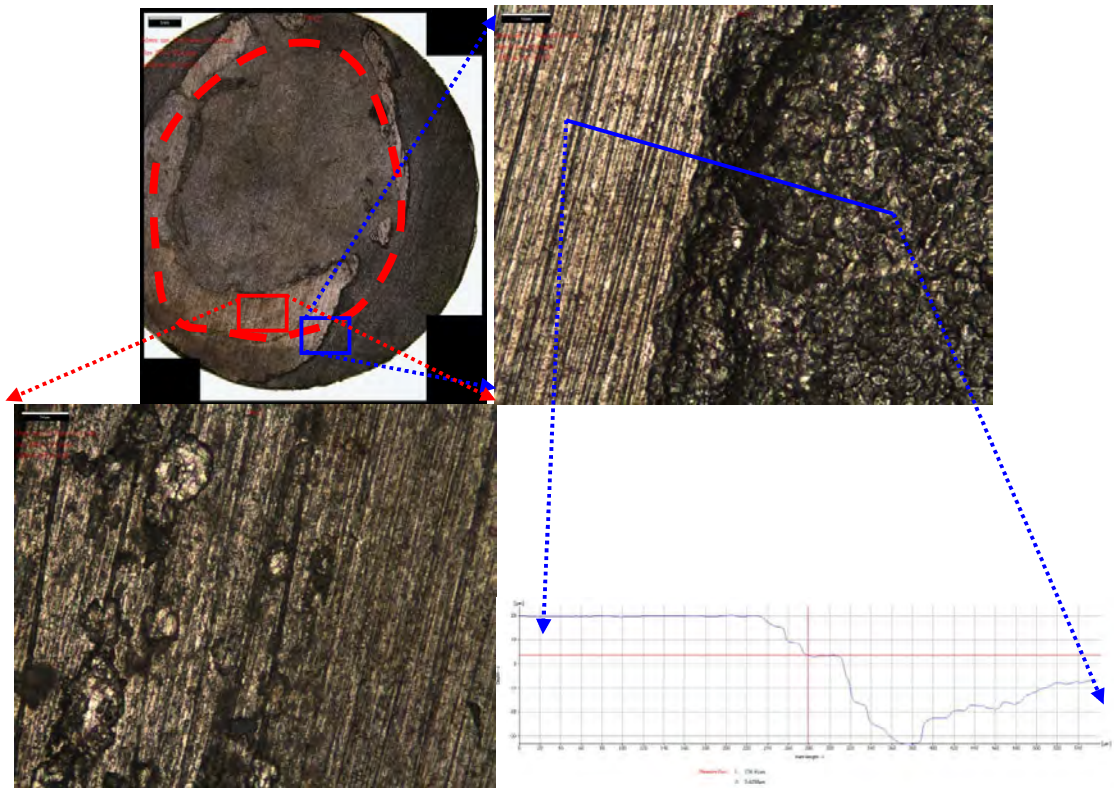


Figure 125. IFM data for specimen contacted with sulfur for 1 day at 80°C, without corrosion product layer.

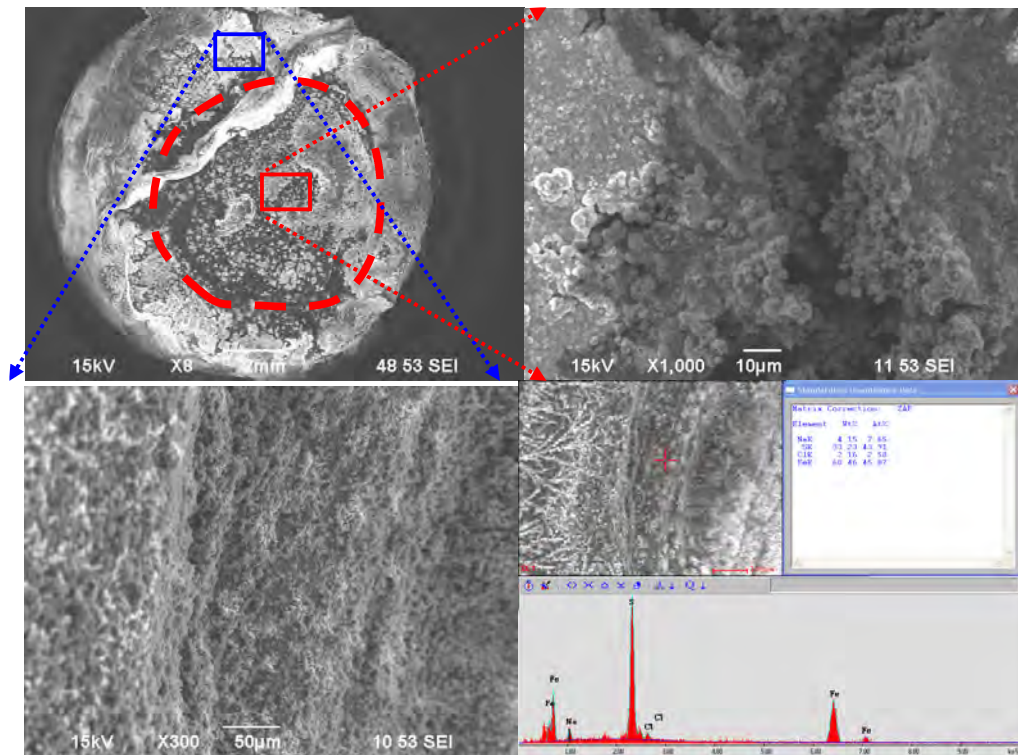


Figure 126. Corrosion specimen contacted with elemental sulfur for 4 days at 80°C, with corrosion product layer.

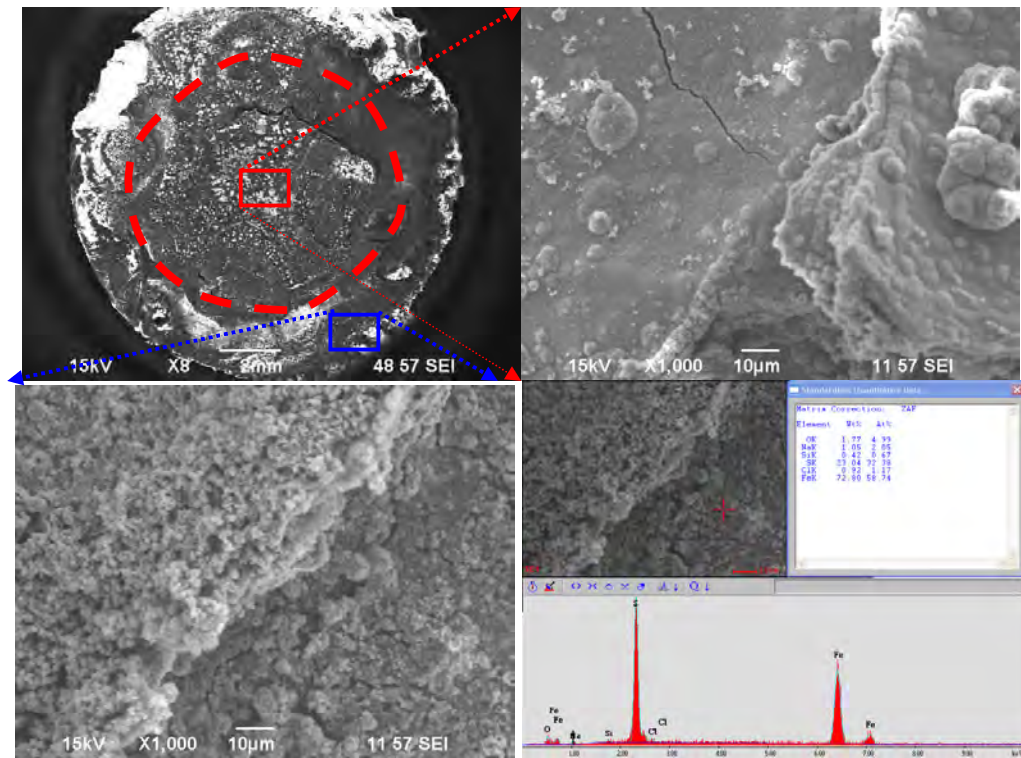


Figure 127. Corrosion specimen contacted with elemental sulfur for 5 days at 80°C, with corrosion product layer.

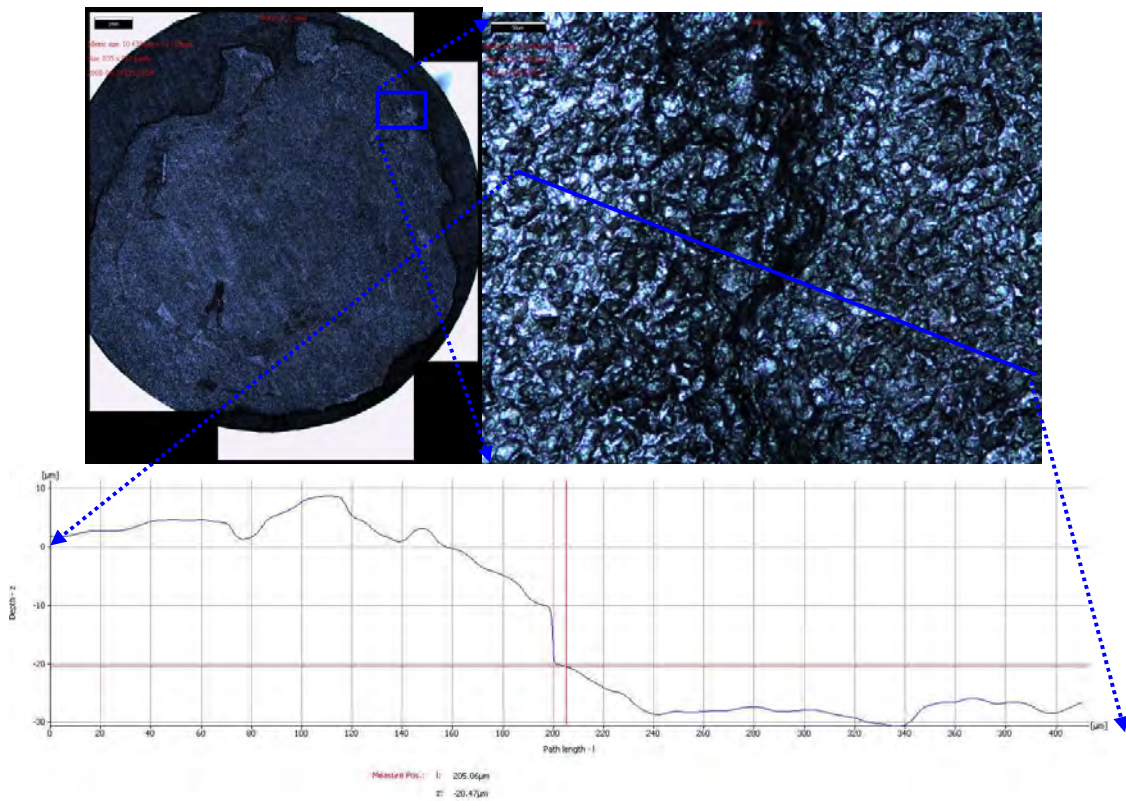


Figure 128. IFM data for specimen contacted with sulfur for 5 days at 80°C, without corrosion product layer.

Figure 129 shows the comparison of general corrosion rates between salt free and 10 wt.% NaCl conditions at 25°C. It is worth noting that the corrosion rate was calculated based on the total specimen area. The local rate may be significantly higher than the general corrosion rate. Results clearly indicate that an increase of salt concentration significantly increases the general elemental sulfur corrosion rates. General corrosion rates increased two to three times when salt concentration was increased from 0 wt. % to 10 wt. %. From Figure 130, it is seen that the thick deposits of iron sulfide on the steel substrate formed directly beneath the elemental sulfur at salt free conditions. However, at high salt concentration, most of the corrosion product layers were generated in the region

which is not covered by elemental sulfur. Therefore, this further proved that the direct reaction mechanism proposed before is unlikely to be the dominant process during elemental sulfur corrosion. The differences in layer formation at different salt concentrations suggest that high concentration of salt plays an important role in the elemental sulfur corrosion.

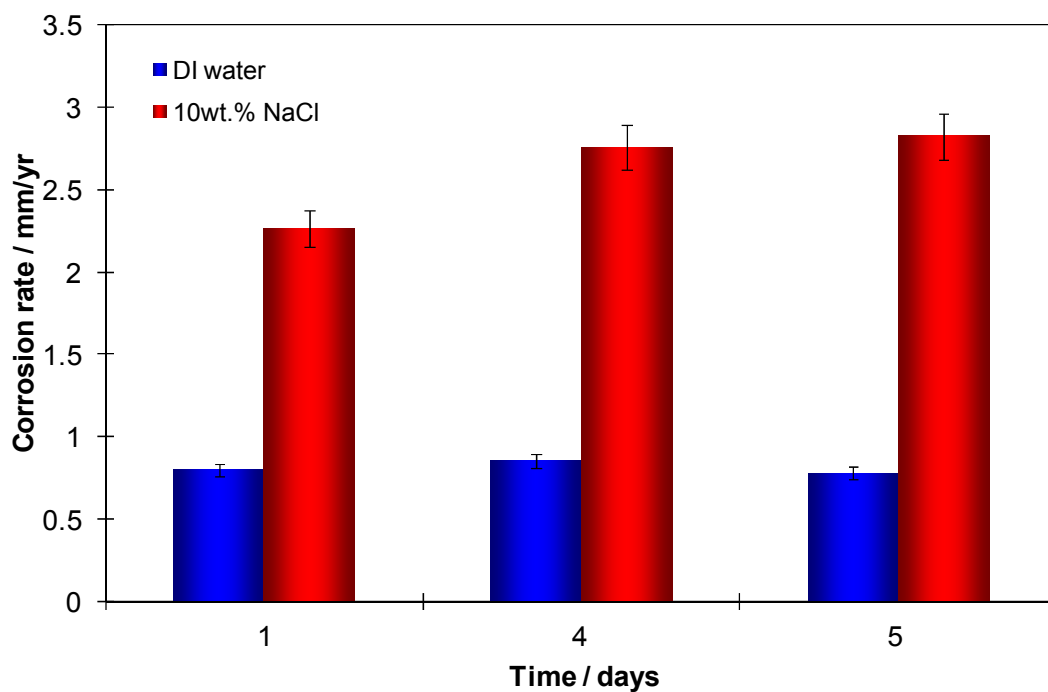


Figure 129. Comparison of general corrosion between salt free and 10 wt.% NaCl conditions at 25°C.

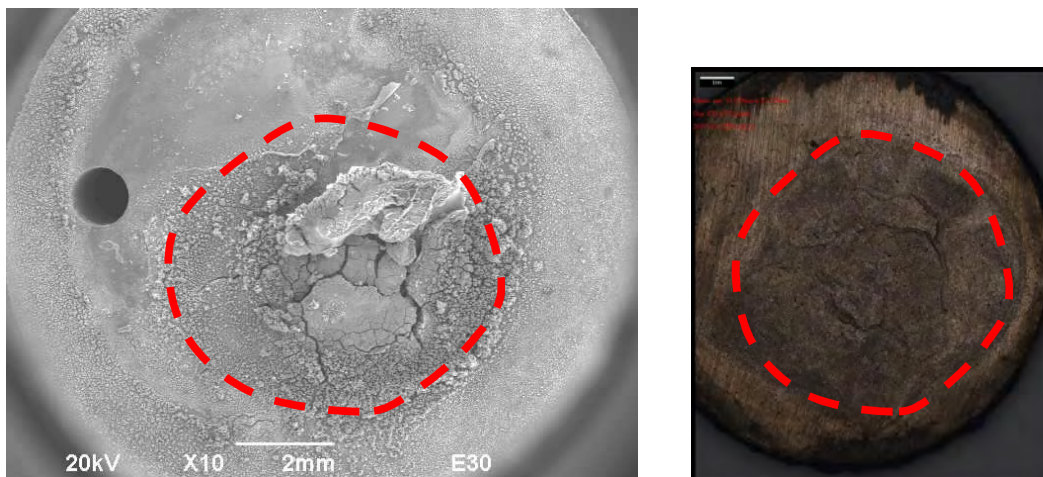


Figure 130. Corrosion specimen contacted with elemental sulfur for 4 days with and without film at 25°C, salt free condition

5.5.2.2.5 Sulfur/iron reaction in various salt solutions (NaCl, NaClO₄, Na₂SO₄, CaCl₂ and KCl)

From the previous experimental results, it has been found that the addition of sodium chloride has large impacts on elemental sulfur corrosion. It not only accelerated the overall general corrosion rate, but also changed the location of the corrosion attack. Solution conductivity is strongly affected by the presence of salt, and the question is whether this is the main factor contributing to the different nature of the attack. To clarify this, elemental sulfur corrosion experiments were conducted in different salt solutions including sodium chloride, sodium perchlorate, sodium sulfate, calcium chloride and potassium chloride. By doing this, the effects of various ionic species on elemental sulfur corrosion were revealed.

It is worth noting that in the new experimental series, the surface area ratio of sulfur to steel specimen was decreased by using specimen with bigger surface area.

Therefore, to have a good comparison, the experiments with deionized water and sodium chloride were repeated.

5.5.2.2.5.1 Experiments in deionized Water, 25°C

The sulfur/iron reaction experiment at 25°C in salt free conditions has been done previously. The purpose of repeating the test was to develop good comparisons between these three test conditions (keeping the specimen size, sulfur weight and size the same). Specimens with elemental sulfur on the surface before and after 1 day exposure at 25°C are shown in Figure 131. Only the portion of specimen surface underneath the sulfur was significantly blackened after exposure. This is consistent with what has been observed before. Representative SEM/EDX data for the corrosion specimen surface that has been in direct contact with elemental sulfur for one day at 25°C is shown in Figure 132. The yellow circled area represents the area that was covered by the sulfur pellet. It is clearly seen that black iron sulfide film was mostly formed on the specimen area which has been covered with elemental sulfur. A high magnification SEM picture shows the outer area which was uncovered by sulfur, no film was formed at all. Figure 133 shows the IFM picture of the specimen surface after the films were removed. It appears that the corrosion behavior mostly happens on the areas which are covered by elemental sulfur. Comparison with the SEM pictures of specimen surface with film reveals that the steel corrodes more severe when more film is generated on the specimen surface. The general corrosion rate was calculated in this case based only on the sulfur covered area. This corrosion rate is around 0.3 mm/yr.

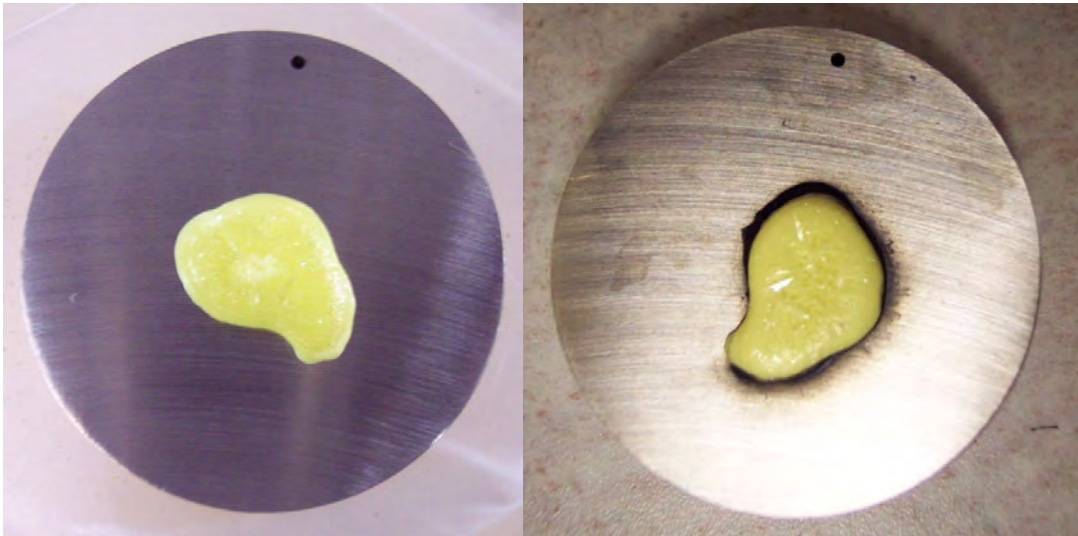


Figure 131. Corrosion specimen before and after 1 day exposure to sulfur at 25°C, salt free condition.

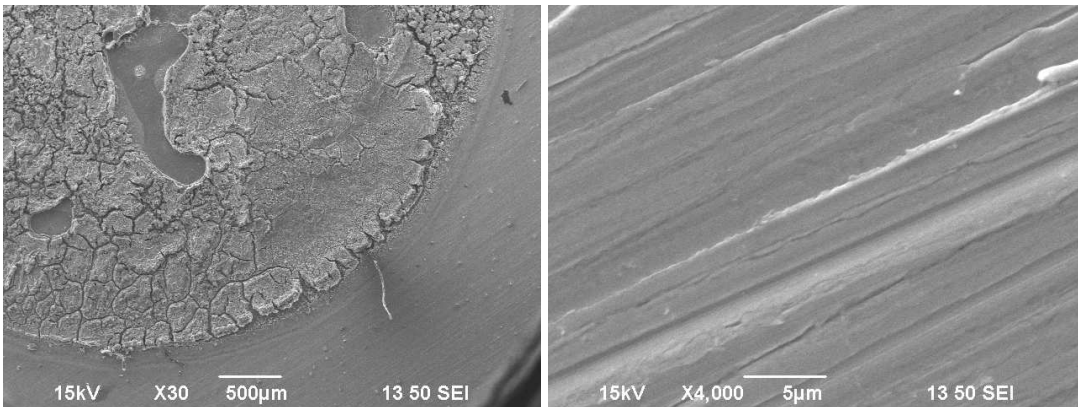


Figure 132. SEM image of specimen surface after 1 day exposure to sulfur at 25°C, salt free condition.

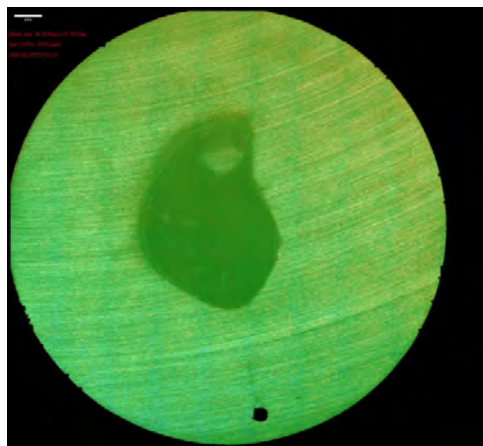


Figure 133. IFM data for corrosion specimen for 1 day at 25°C, salt free condition, without film, appearance of the surface.

5.5.2.2.5.2 Experiments with 0.175 M NaCl, 25°C

The same experiment was done at 25°C, 0.175 M NaCl solution. Figure 134 shows the specimen surfaces before and after corrosion. Interestingly, black iron sulfide film was formed on the specimen area which has no direct contact with elemental sulfur. This is quite different from what has been observed in salt free conditions, where only the portion of specimen surface underneath the sulfur was blackened after exposure.

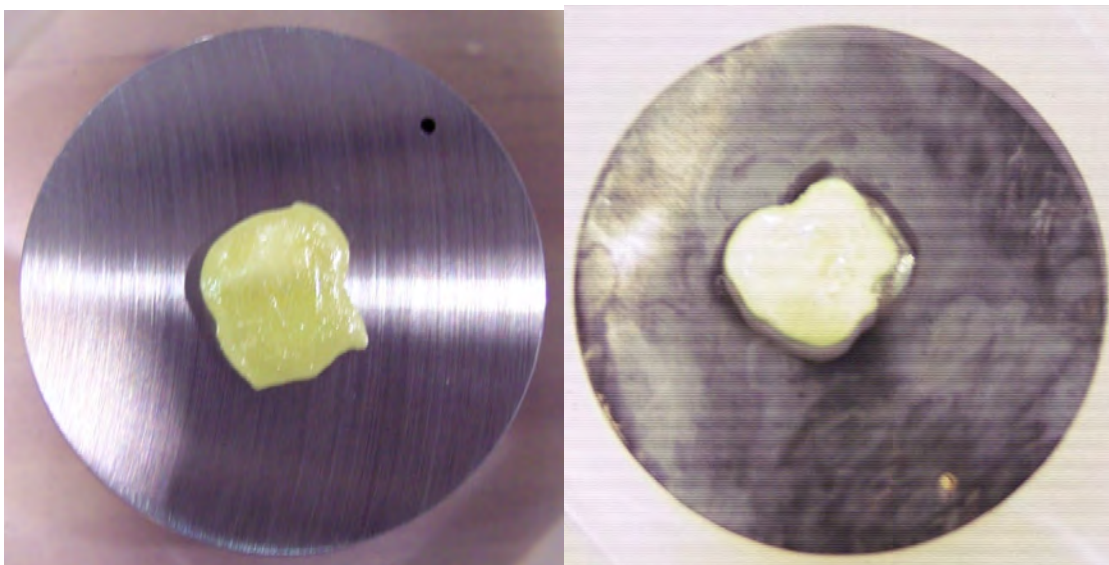


Figure 134. Corrosion specimen before and after 1 day exposure to sulfur at 25°C, 0.175 M NaCl.

The SEM image of a specimen surface that has been in direct contact with elemental sulfur for one day at 25°C, 0.175 M NaCl is shown in Figure 135. It is observed that most film generation occurred in close proximity to the periphery of the sulfur pellet. A further enlargement of the small area on the sulfur edge shows a clearly concentrated film formation. Corrosion products were then removed by Clarke's solution. Figure 136 shows the IFM data of the specimen surface after films were removed. The surface profile indicates that there is no significant depth difference along the whole specimen surface. Therefore, the general corrosion rate is calculated based on the area of the whole specimen surface. The corrosion rate under 0.175 M NaCl condition is around 0.26 mm/yr, which is not a significant difference from the salt free condition corrosion rate.

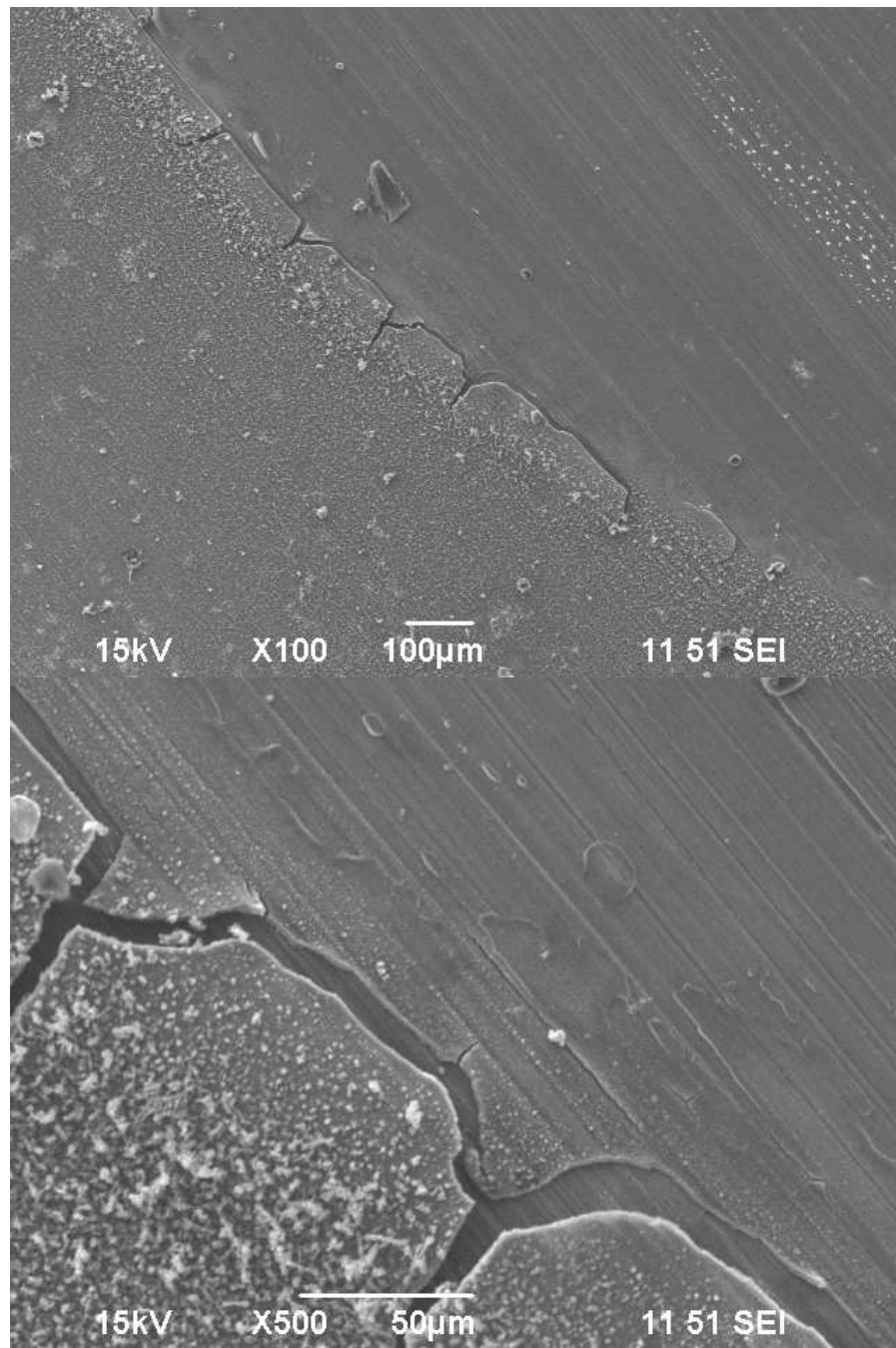


Figure 135. SEM image of specimen surface after 1 day exposure to sulfur at 25°C, 0.175 M NaCl.

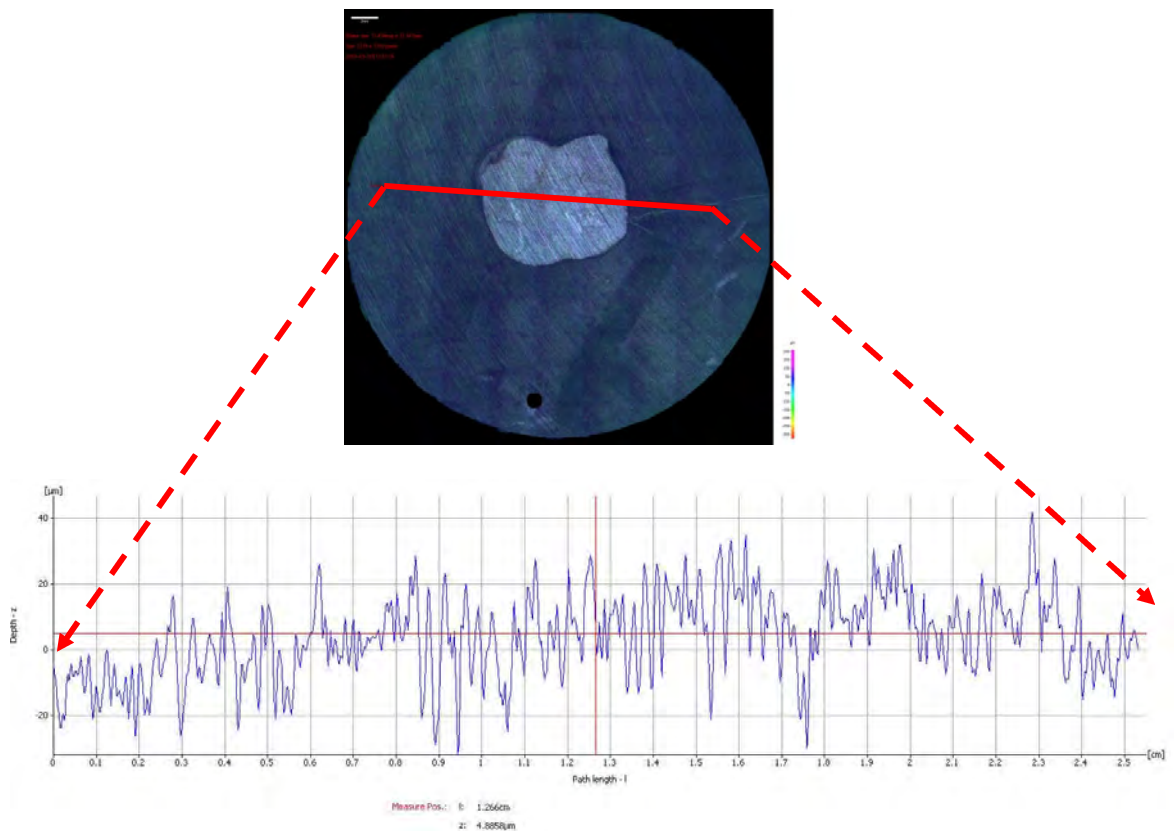


Figure 136. IFM data for corrosion specimen for 1 day at 25°C, 0.175 M NaCl, without film, appearance of the surface and surface profile.

5.5.2.2.5.3 Experiments with 0.175 M Sodium Perchlorate, 25°C

The test solution was changed to 0.175 M sodium perchlorate in the new experiment at 25°C. Figure 137 shows the specimen surface before and after corrosion. Similar to the results at 0.175 M sodium solution, even the specimen surface which was not covered by sulfur was blackened. Further surface analysis was performed by conducting SEM scan on the specimen surface. The results are shown in Figure 138. From the SEM image, it is observed that more film generation occurred at the edge of the elemental sulfur. The film morphology is the same as the result observed at the 0.175 M

sodium chloride condition. This suggests that chloride may not be the key factor which caused the significant difference of the film formation between salt free and high salt concentration conditions. IFM picture of the specimen surface after film removal is shown in Figure 139. Similar to the results of 0.175 M sodium chloride, no significant depth difference along the specimen surface was observed. Therefore, the general corrosion rate is calculated based on the area of whole specimen surface. The rate is around 0.3 mm/yr.

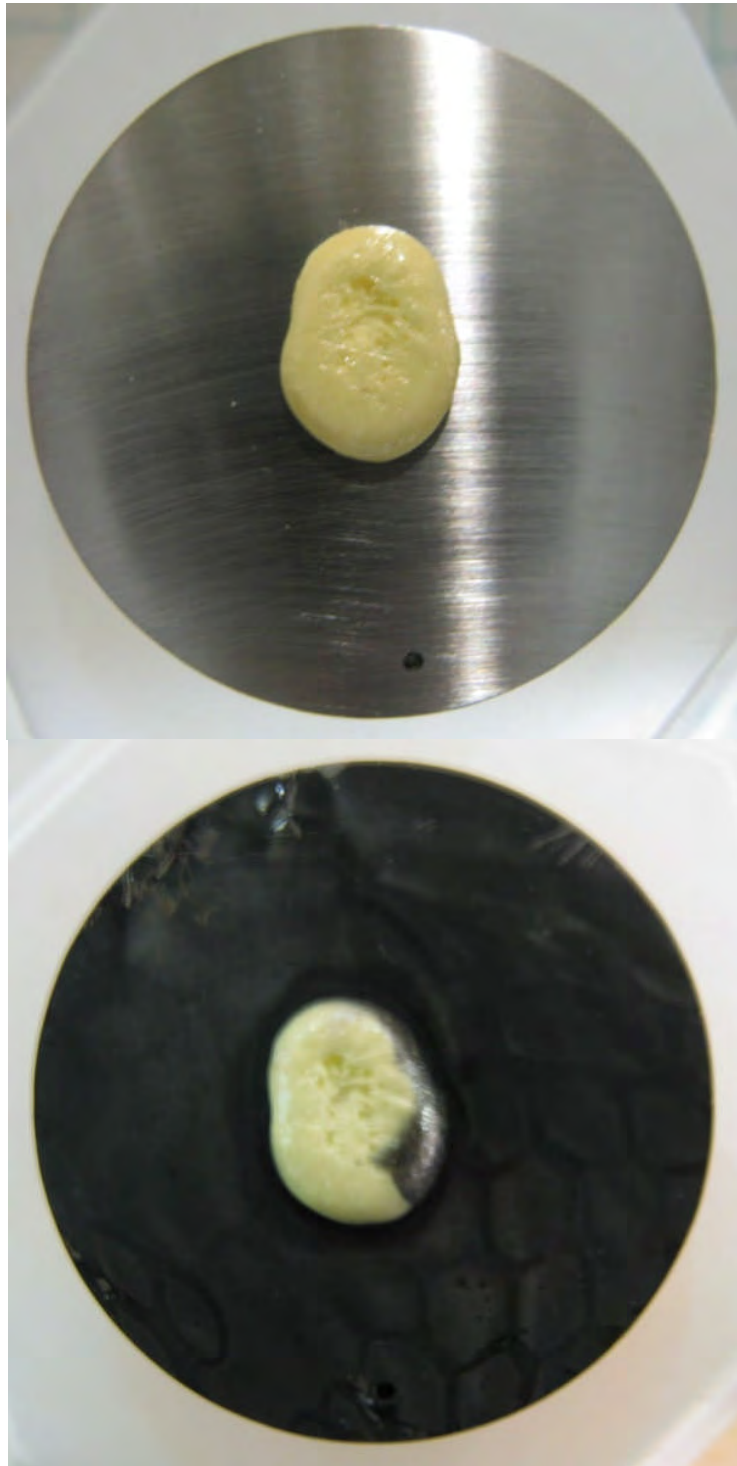


Figure 137. Corrosion specimen before and after 1 day exposure to sulfur at 25°C, 0.175 M NaClO₄.

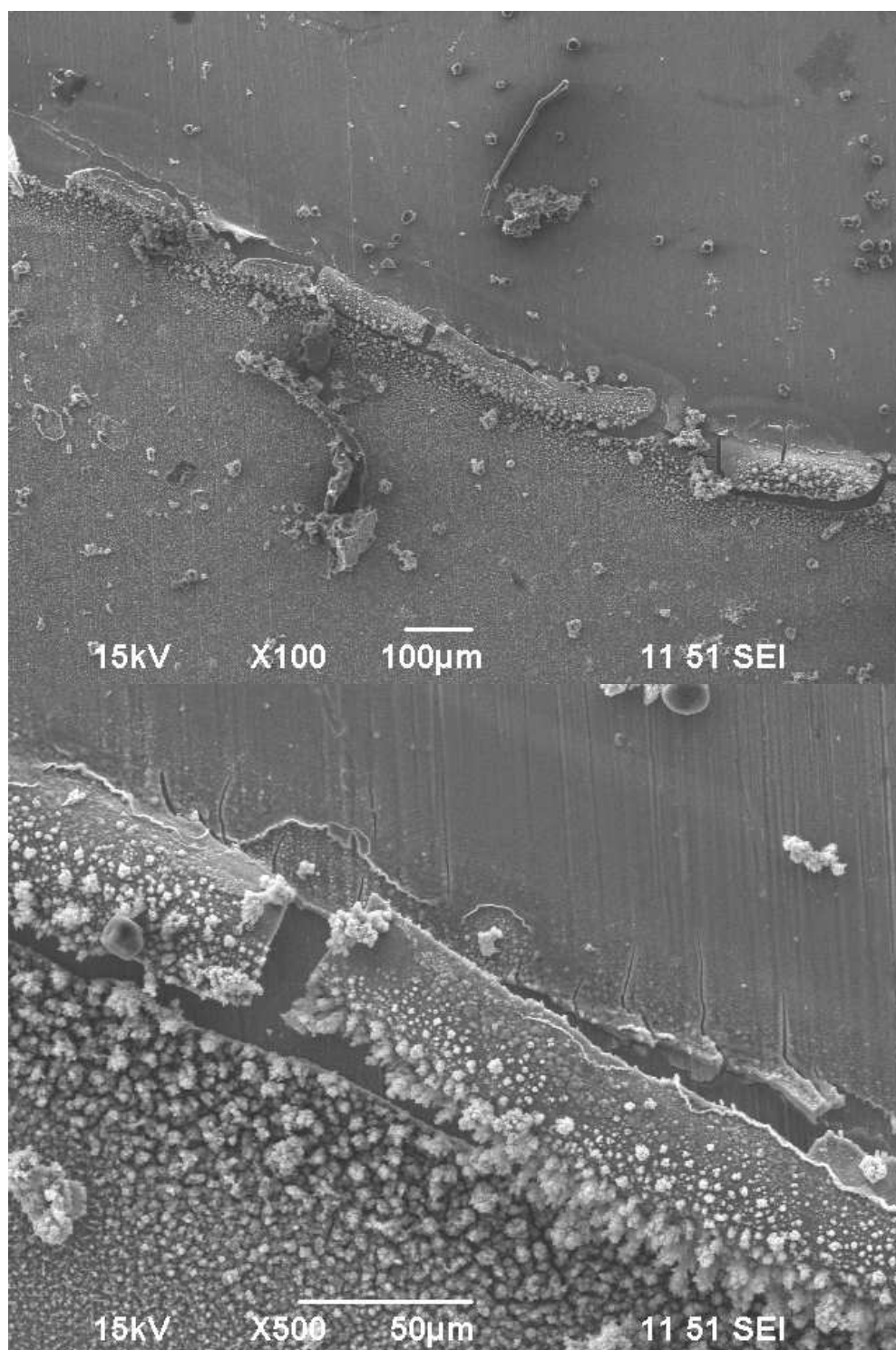


Figure 138. SEM image of specimen surface after 1 day exposure to sulfur at 25°C, 0.175 M NaClO₄.

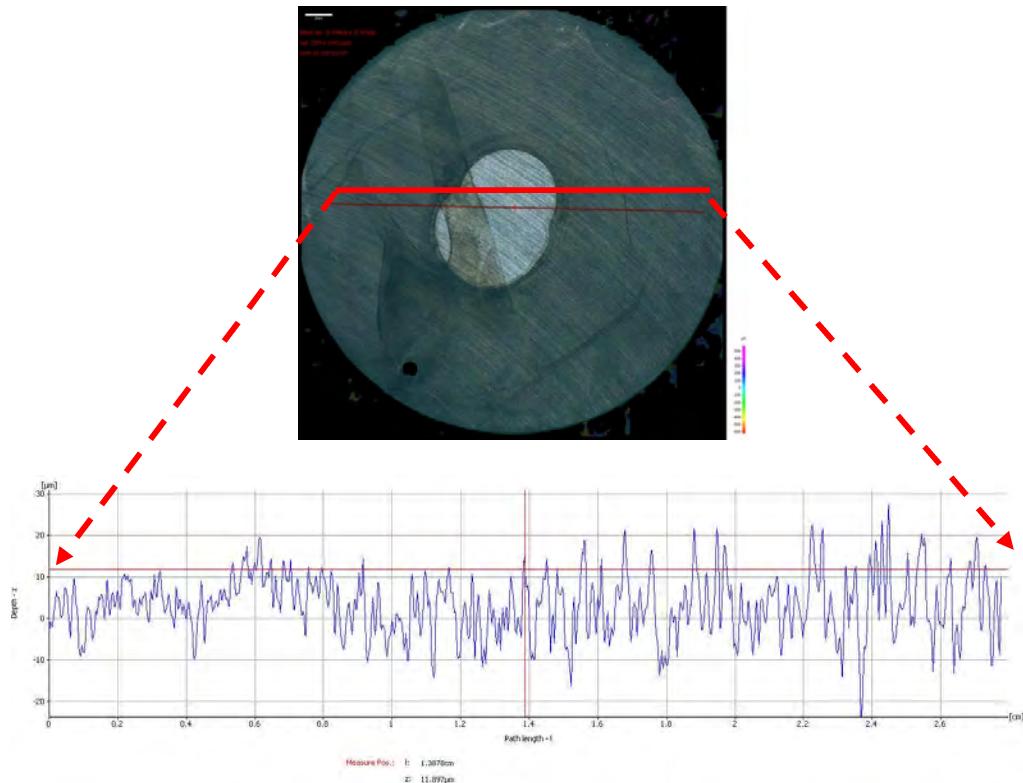


Figure 139. IFM data for corrosion specimen for 1 day at 25°C, 0.175 M NaClO₄, without film, appearance of the surface and surface profile.

A similar series of experiments was conducted at 80°C. However, the salt concentration was increased to 1.5 M. According to the experimental results of previous tests, at high NaCl concentration conditions, corrosion rates were significantly aggregated. The purpose of increasing the salt concentration is to find out if the similar corrosion behavior can be observed at high concentration of sodium perchlorate conditions.

5.5.2.2.5.4 Experiments with deionized Water, 80°C

The specimen surfaces before and after corrosion at 80°C, in salt free condition are shown in Figure 140. It is clear seen that at high temperature, the whole specimen

surface was blackened even at salt free conditions. Based on the previous experiment, it can be explained by the sulfur hydrolysis theory. However, from the SEM image of the specimen surface, it is seen that most film generations still occurs in the area which has direct contact with elemental sulfur. The difference between the result at 80°C and 25°C, salt free condition, is that a thin layer of iron sulfide film (bottom side picture in Figure 141) formed on the surface which is not covered by elemental sulfur at 80°C instead of 25°C.

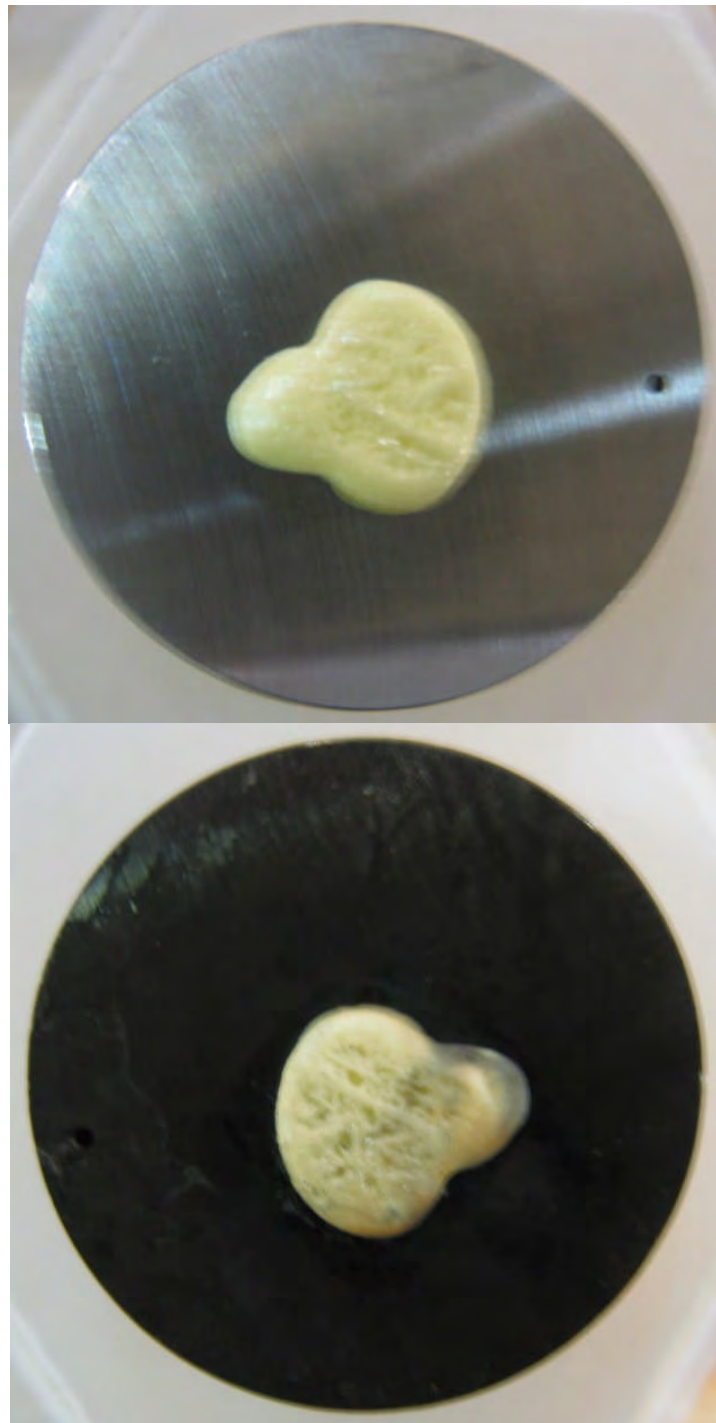


Figure 140. Corrosion specimen before and after 1 day exposure to sulfur at 80°C, salt free condition.

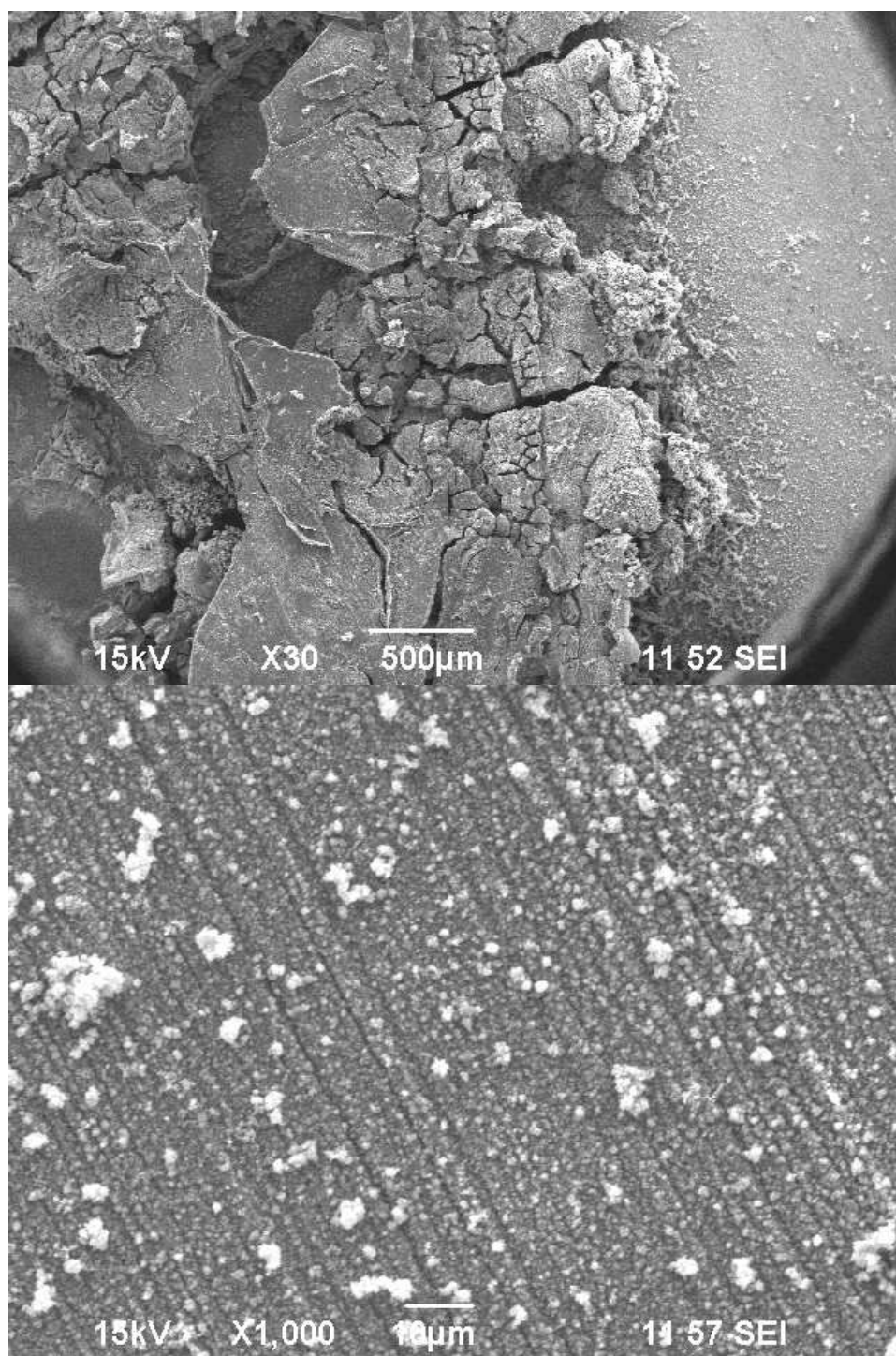


Figure 141. SEM image of specimen surface after 1 day exposure to sulfur at 80°C, salt free condition.

5.5.2.2.5.5 Experiment with 1.5 M Sodium Chloride, 80°C

A test solution of 1.5 M NaCl was used in the next experiment. Figure 142 shows the specimen surface before and after exposure to elemental sulfur for 1 day. The entire specimen surface was significantly blackened. The SEM image of the same specimen is shown in Figure 143. Similar to the result at low NaCl condition, a thicker film formed in close proximity to the periphery of the sulfur pellet. IFM data of the specimen surface after film removal is shown in Figure 144. From the surface profile analysis, it is clearly seen that corrosion occurred on the entire specimen surface; corrosion severity specimen was fairly uniform. Therefore, the general corrosion rate is calculated based on the area of the entire specimen surface and was calculated to be 2.1 mm/yr.



Figure 142. Corrosion specimen before and after 1 day exposure to sulfur at 80°C, 1.5 M NaCl.

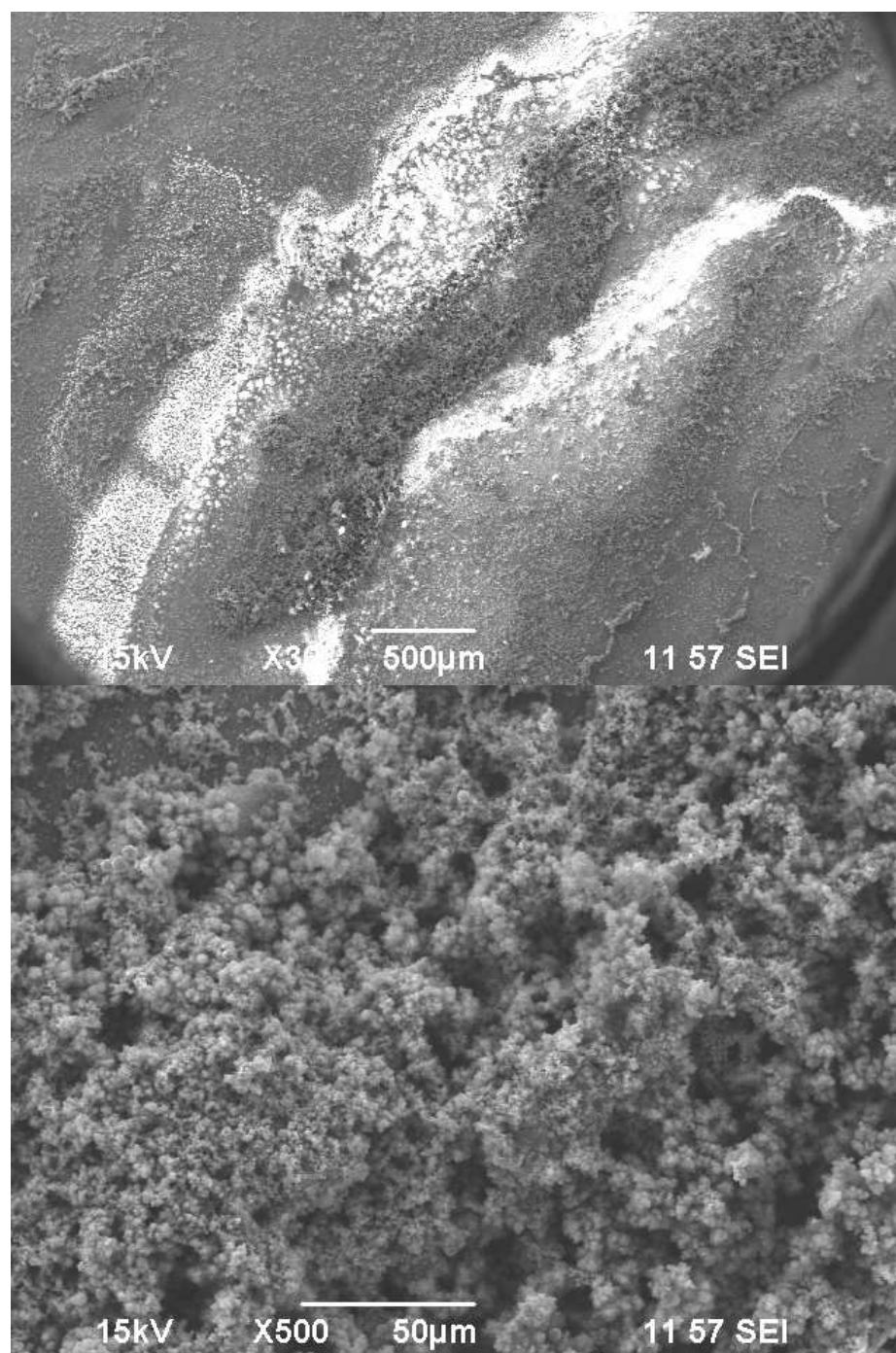


Figure 143. SEM image of specimen surface after 1 day exposure to sulfur at 80°C, 1.5 M NaCl.

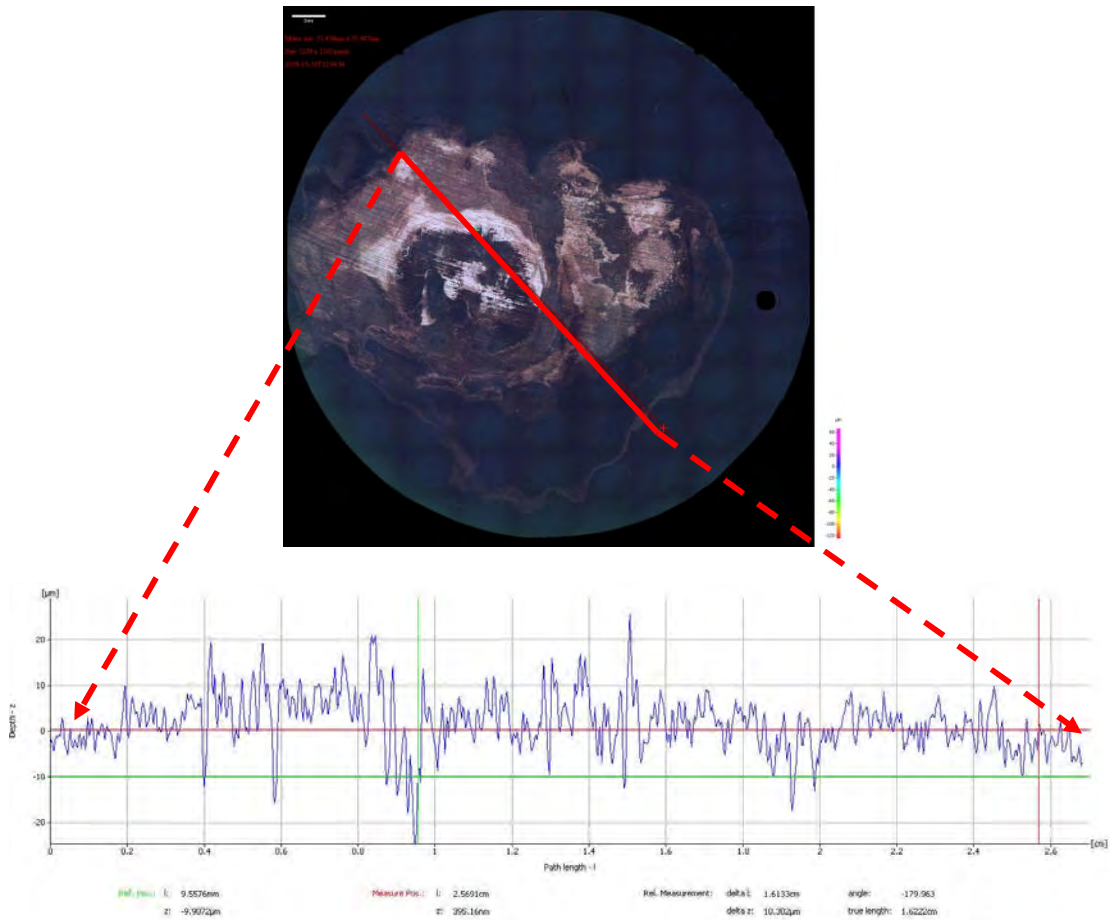


Figure 144. IFM data for corrosion specimen for 1 day at 25°C, 1.5 M NaCl, without film, appearance of the surface and surface profile.

5.5.2.2.5.6 1.5 M Experiment with 1.5 M Sodium Perchlorate, 80°C

The sulfur/iron corrosion experiment was also performed at 80°C, 1.5 M sodium perchlorate (NaClO_4) condition. Figure 145 shows the specimen surface before and after corrosion. A black iron sulfide film formed on the entire specimen surface after 1 day exposure to elemental sulfur, which is the same as in 1.5 M sodium chloride for the same conditions. SEM images of the specimen surface shown in Figure 146 further reveal the

corrosion product morphology. Iron sulfide films formed on both sulfur covered and uncovered surface regions. The high magnification image of the area close to the sulfur edge shows an extra buildup of iron sulfide around the edge of the sulfur droplet. This suggests that something interesting happened in this area that warrants further study. Figure 147 shows the IFM data of the specimen surface. From the surface analysis, corrosion locations appear to be uniform. However, severe localized corrosion occurred on the sulfur edge and sulfur covered area. The uniform corrosion rate is calculated to be 2.4 mm/yr based on the area of the entire specimen surface.

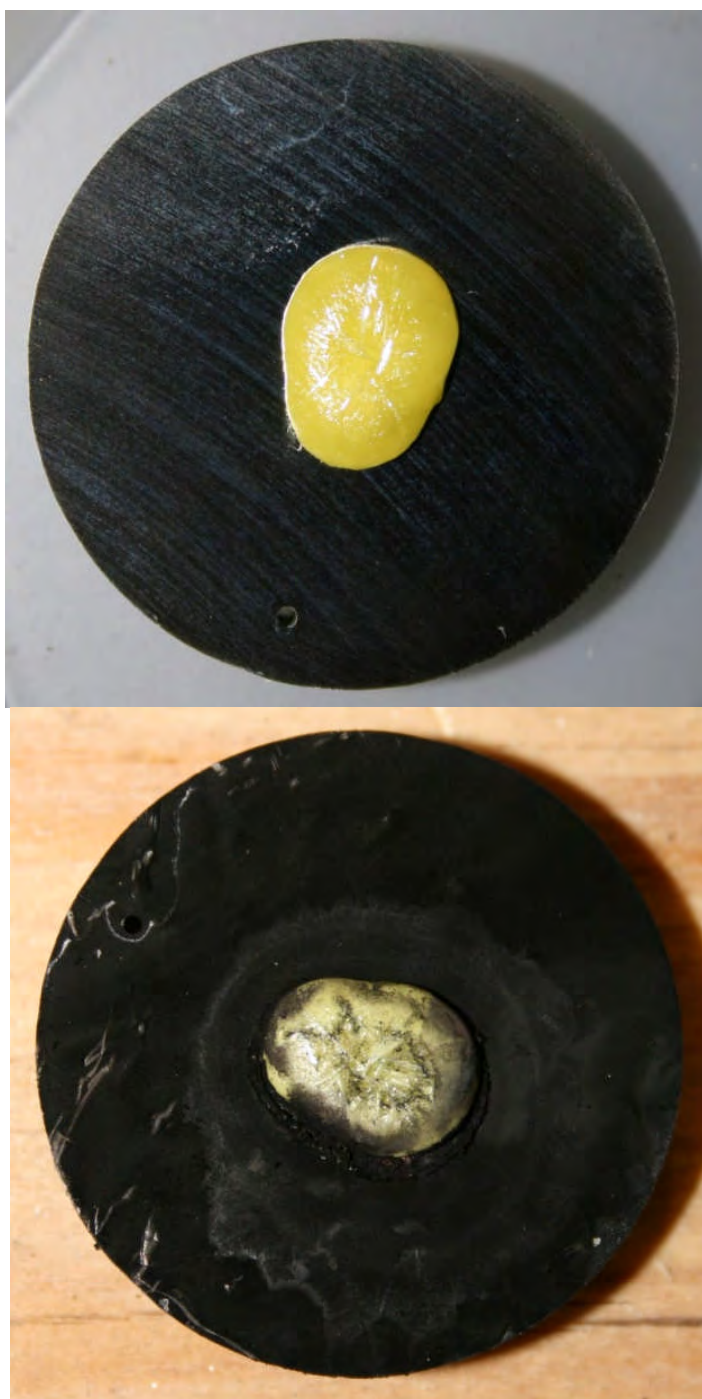


Figure 145. Corrosion specimen before and after 1 day exposure to sulfur at 80°C, 1.5 M NaClO₄.

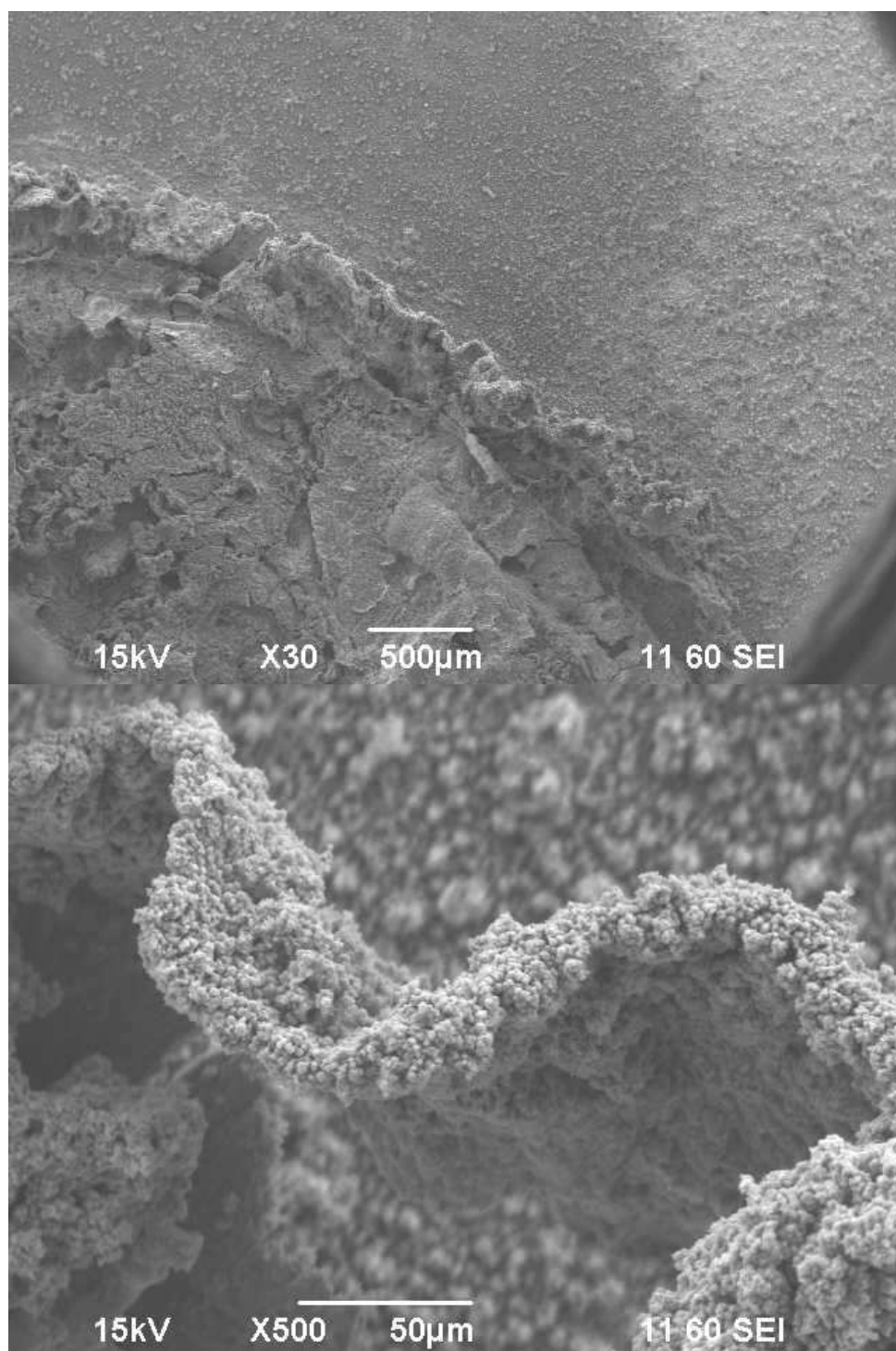


Figure 146. SEM image of specimen surface after 1 day exposure to sulfur at 80°C, 1.5 M NaClO₄.

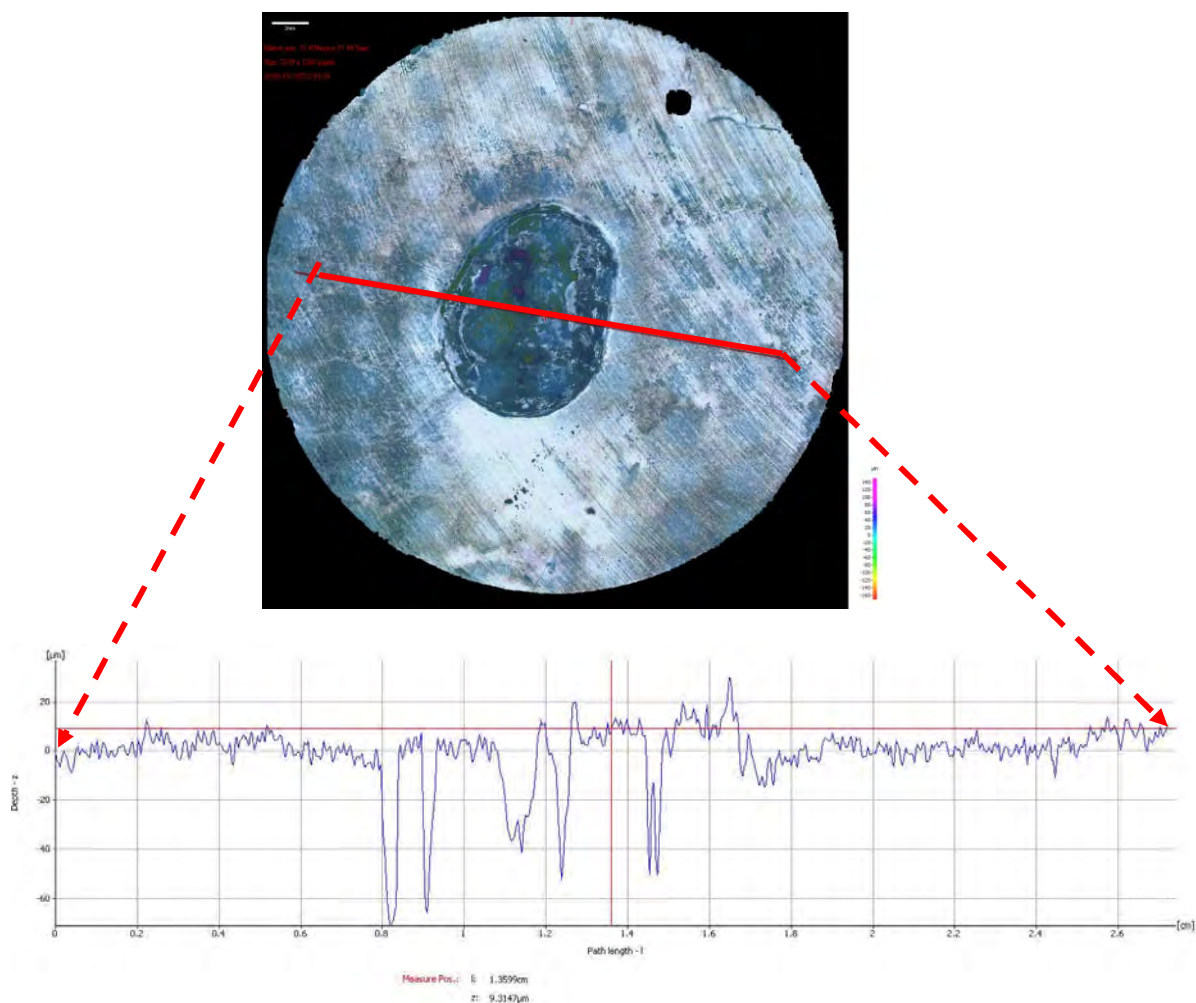


Figure 147. IFM data for corrosion specimen for 1 day at 25°C, 1.5 M NaClO₄, without film, appearance of the surface and surface profile.

A comparison of the experimental results at two different conditions, sodium chloride and sodium perchlorate solutions, was made. The above surface analysis shows that the corrosion products formed at both conditions have similar morphology, most film formation occurs in close proximity to the periphery of the sulfur pellet. Figure 148 shows the comparison of the general corrosion rate at two different salt conditions. The results show no significant difference of corrosion rates (general or localized) between

sodium chloride and sodium perchlorate. This indicates that solution conductivity might be one of the key factors in elemental sulfur corrosion instead of only the chloride ion.

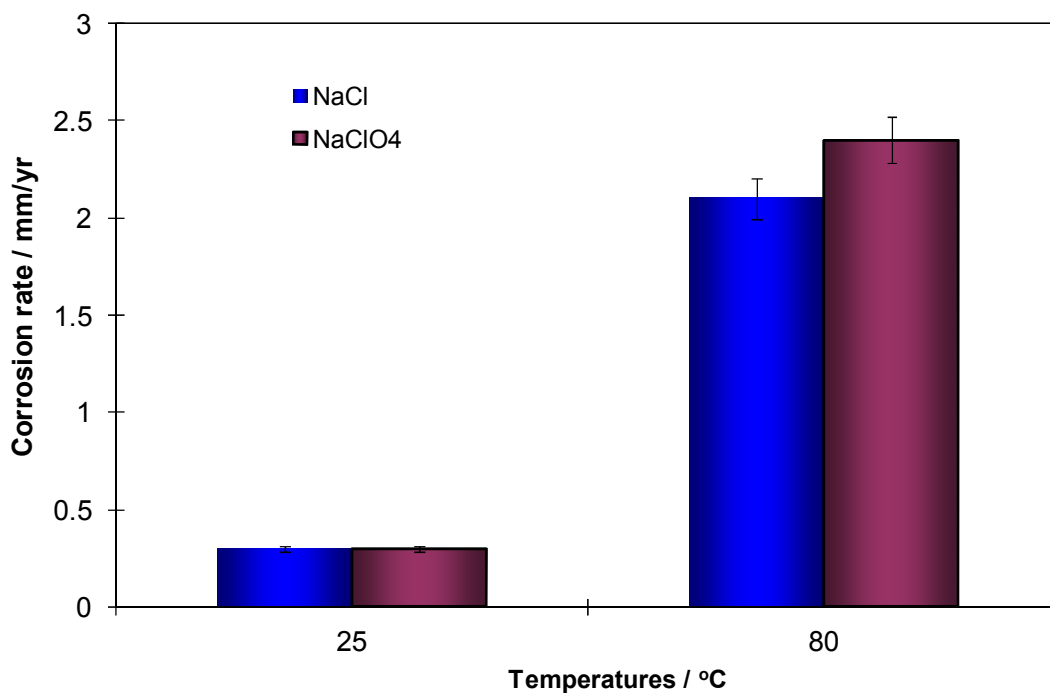


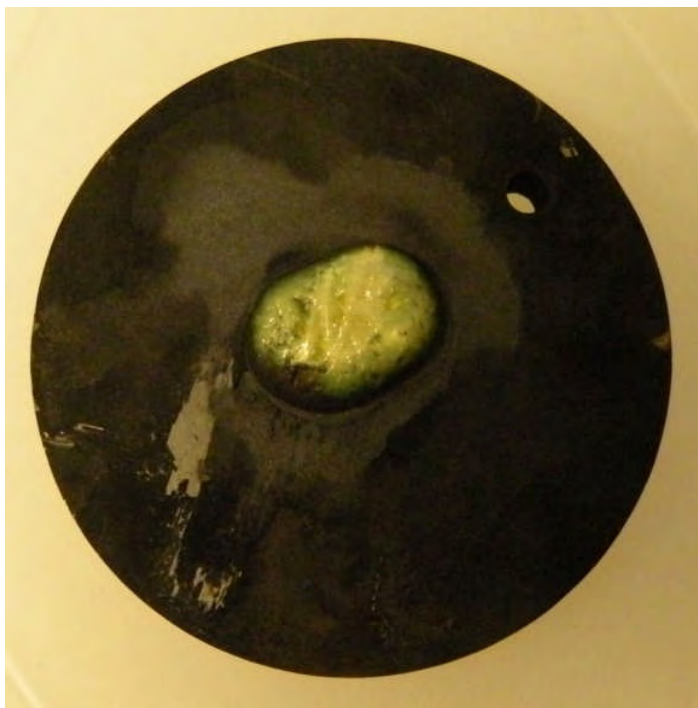
Figure 148. Comparisons of general corrosion rate of two different salt conditions at 25°C and 80°C.

5.5.2.2.5.7 0.5 M Experiments with 0.5 M NaSO₄, 0.5 M CaCl₂ and 1.5 M KCl at 25°C

From the results of previous experimental results, addition of salt was found to accelerate elemental sulfur corrosion. Another significant observation at high salt concentration was that the sulfide film and corrosion attack were spread out across the entire surface of the metal specimen. Unlike the deionized water environment, sulfide films were not only formed on the area which had direct contact with sulfur, but also formed on the surface which was not covered by sulfur. The aggressive chloride ion was

first suspected to be the reason. However, when sodium chloride was changed to sodium perchlorate, the exact same mode of corrosion attack was observed. Therefore, a “chloride ion effect” was basically excluded. However, different ions need to be tested to further confirm this conclusion. In the new experimental sets, sodium sulfate, calcium chloride and potassium chloride electrolytes were used as the test solution. To keep the ionic strength constant, the concentrations used for sodium sulfate, calcium chloride and potassium chloride are 0.5 M, 0.5 M and 1.5 M. By doing this, different ion effects can be clarified. In these experiments, sulfur was directly deposited on the steel surface.

Figure 149 shows the pictures of specimen surface after corrosion under the condition of sodium sulfate, calcium chloride and potassium chloride. The entire specimen surface became black in all three cases. These results are consistent with the results observed in sodium chloride and sodium perchlorate solutions. SEM images (Figure 150) further reveal the film morphologies right on the sulfur edge. The yellow lines represent the sulfur edge and the red arrows point out the area which has direct contact with sulfur. It is clearly seen that more film generation occurs on the area which has no direct contact with sulfur. These phenomena were also consistent with the observation detected in sodium chloride and sodium perchlorate solutions. This again suggests that it is not specifically the chloride ion which affects the increase of corrosion rate as well as the changes in film formation processes. Solution conductivity or ionic strength plays a more important role in elemental sulfur corrosion of mild steel.



a) Sodium sulfate



b) Calcium chloride



c) Potassium chloride

Figure 149. Pictures of specimen surface after corrosion.

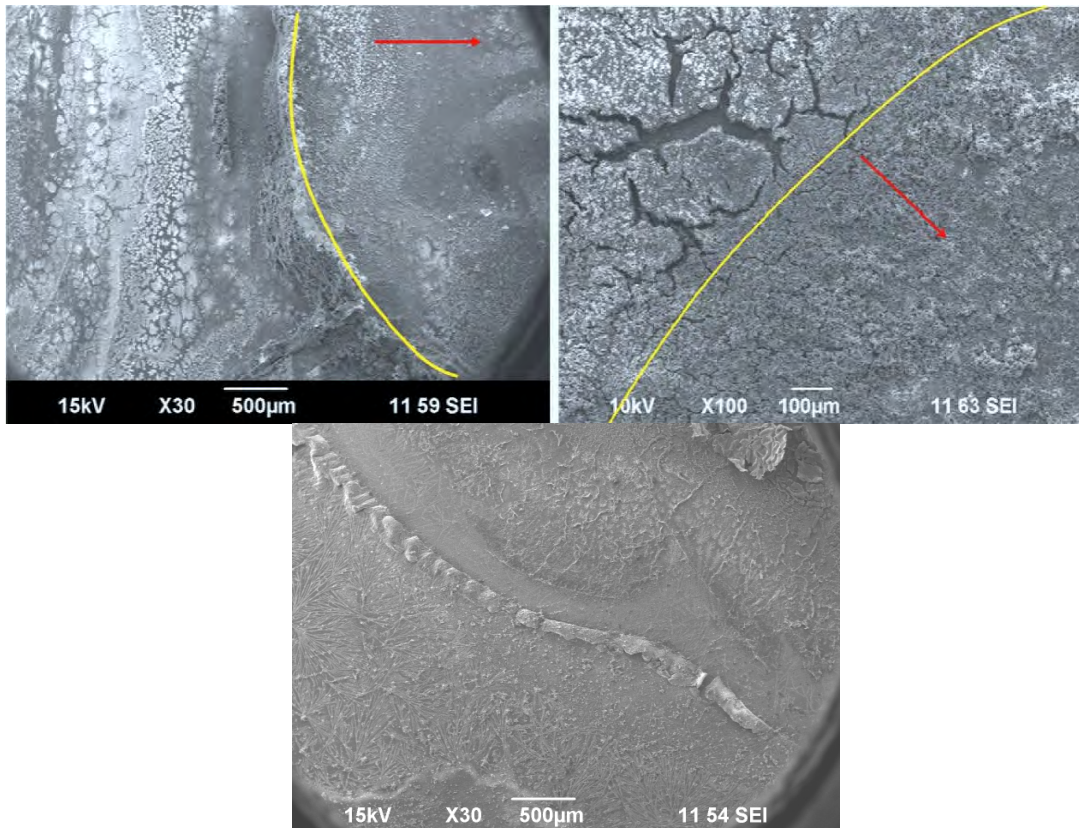
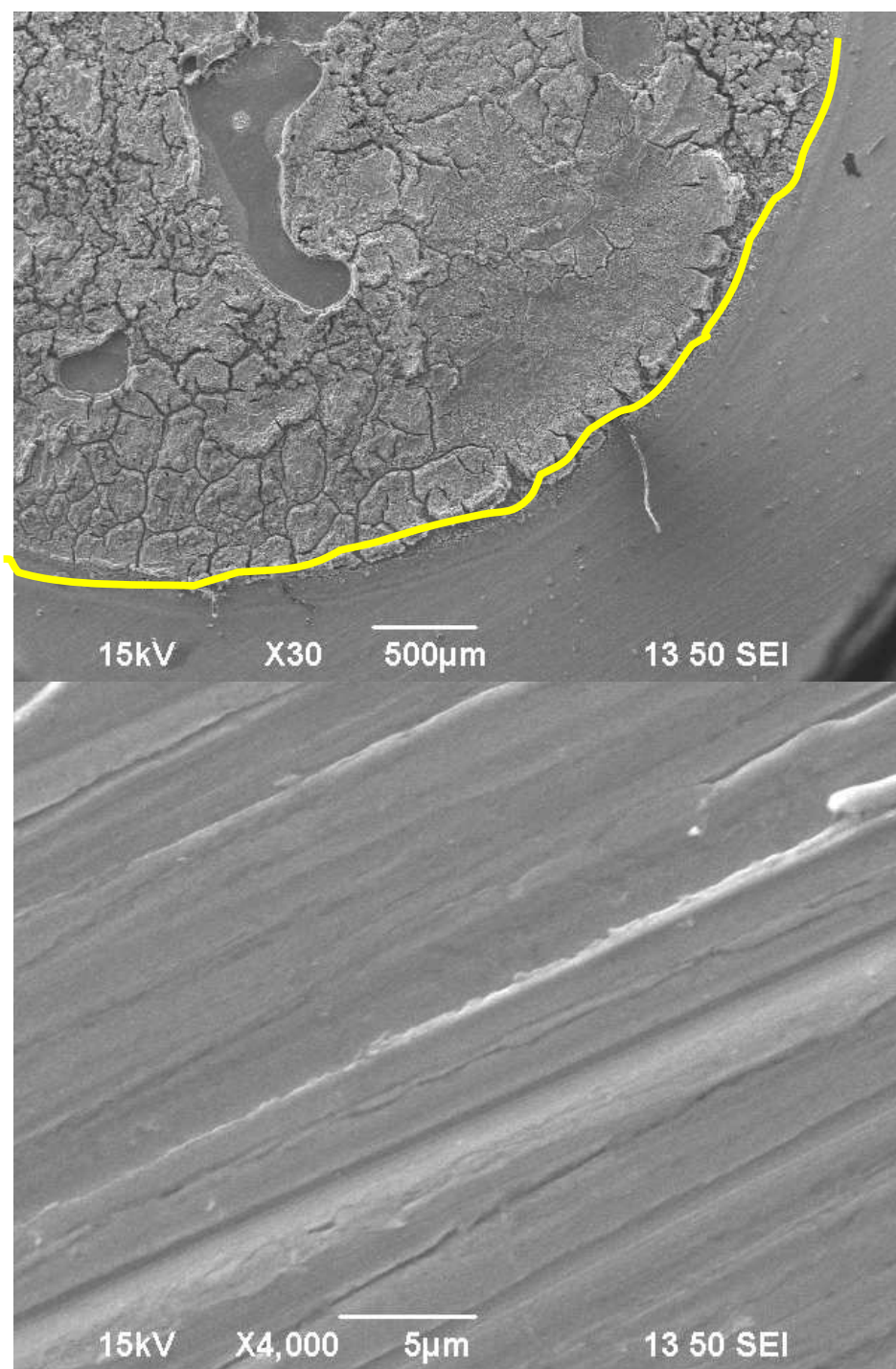


Figure 150. SEM images of specimen surface on the sulfur edge.

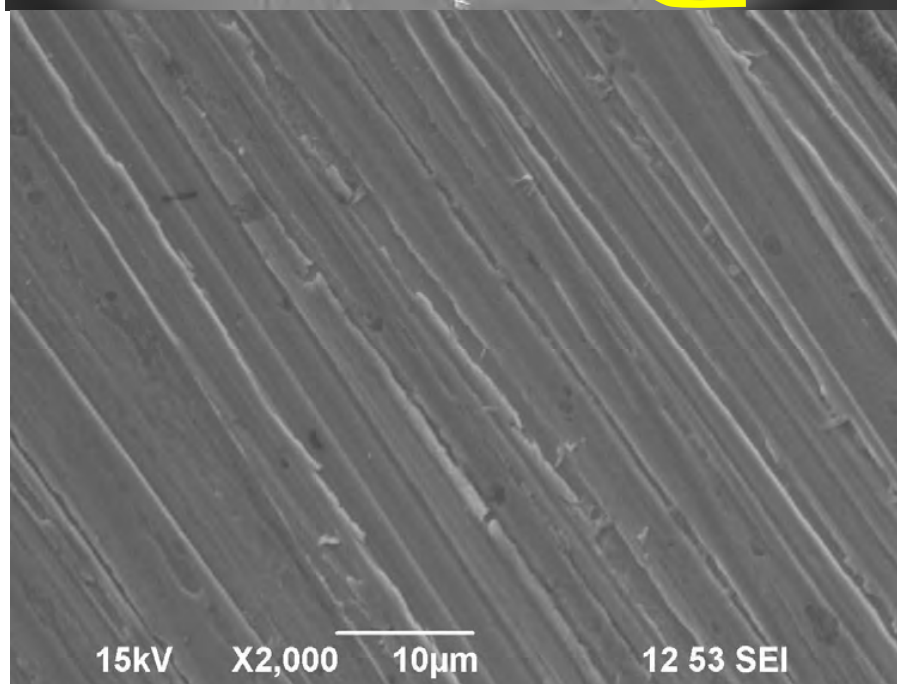
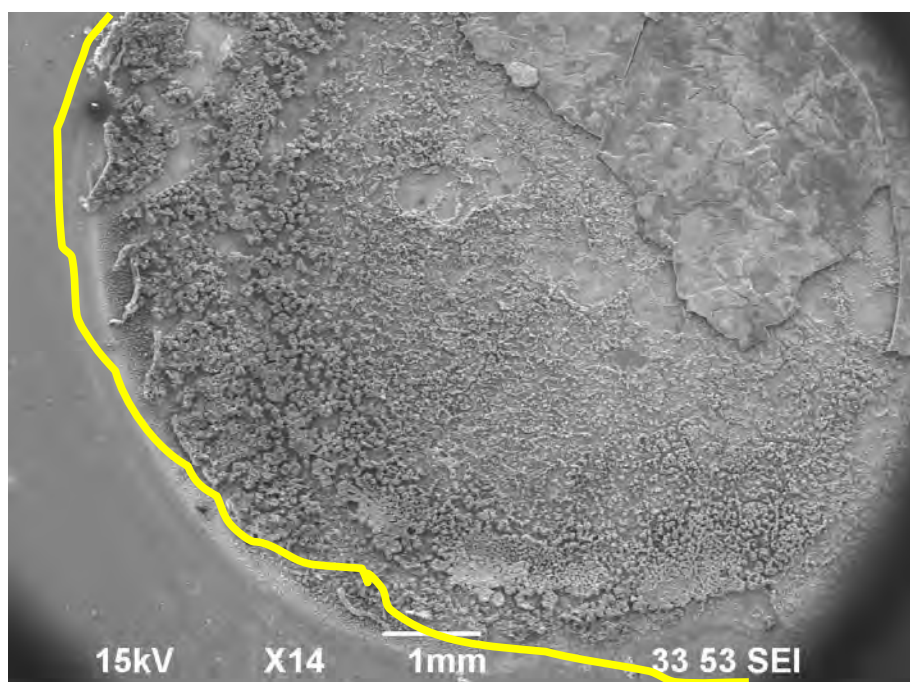
5.5.2.2.6 Sulfur/iron reaction in various pH (4.0, 5.0 and 7.0)

The previous experimental results have shown that addition of salt could expand the corrosion to the area where sulfur has no direct contact with steel. Therefore, to look at the pH effects on the sole sulfur/iron reaction, the experiments were conducted in deionized water purged with nitrogen at 25°C. Three different pH values, 4.0, 5.0 and 7.0, were tested. The pH was controlled during the experiments by adding deoxygenated hydrochloric acid solution. The test duration was 24 hours. After each experiment, the specimen surface was examined by SEM and EDX and the corrosion rate was measured by weight loss.

Figure 151 shows the SEM images of specimen surface at different pH values. The upper three images represent the area which is direct underneath the sulfur droplet. The yellow lines represent the sulfur edges. It has been observed that a significant amount of iron sulfide film was generated direct under the sulfur droplet in each of the three cases. Film formation has no difference between different pH values. The other three images reveal the specimen surface which was not covered by sulfur. Polish marks still remain on the steel surface at pH 7.0, which suggests that acid corrosion was negligible. At pH 5.0, indications of acid corrosion started to appear on the steel surface (b. in Figure 151). At pH 4.0, acid corrosion seems to be more aggravated (c. in Figure 151). From the SEM images, it appears that the change of pH only affected the area which has no direct contact with elemental sulfur. This can be further confirmed by comparing the corrosion rate at different pH values.



a) pH 7.0



b) pH 6.0

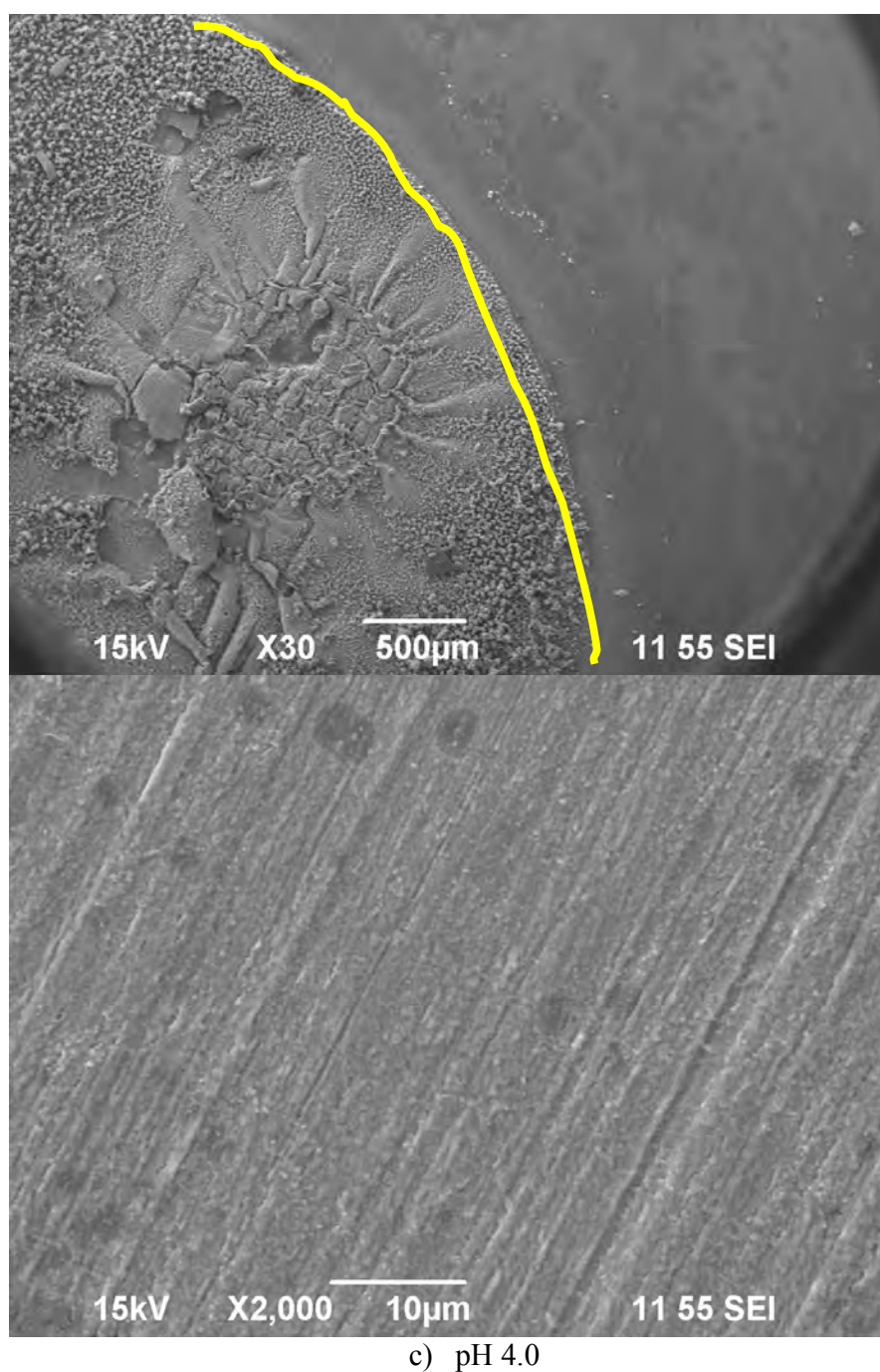


Figure 151. pH effect on film formation underneath (upper pictures) and outside the sulfur droplet (25°C, N₂ purged).

To quantify the pH effect on the sulfur/iron reaction (under the sulfur droplet), the homogeneous pH effect (the area which has no contact with sulfur) has to be eliminated. The weight loss of the uncovered area can be calculated using known corrosion rates at defined pH values. This can then be subtracted from the total weight loss to calculate the corrosion rate just underneath the sulfur droplet. Figure 152 shows the corrosion rates (underneath the sulfur droplet) at the different pH values. The first column represents the corrosion rate calculated based on the total weight loss. It appears that pH has certain effects on the sulfur/iron reaction rate. However, this is the wrong way to calculate the corrosion rate. If the homogeneous pH effect is excluded, it is clearly seen that pH has no significant effect on sulfur/iron reaction rate (shown in the second column).

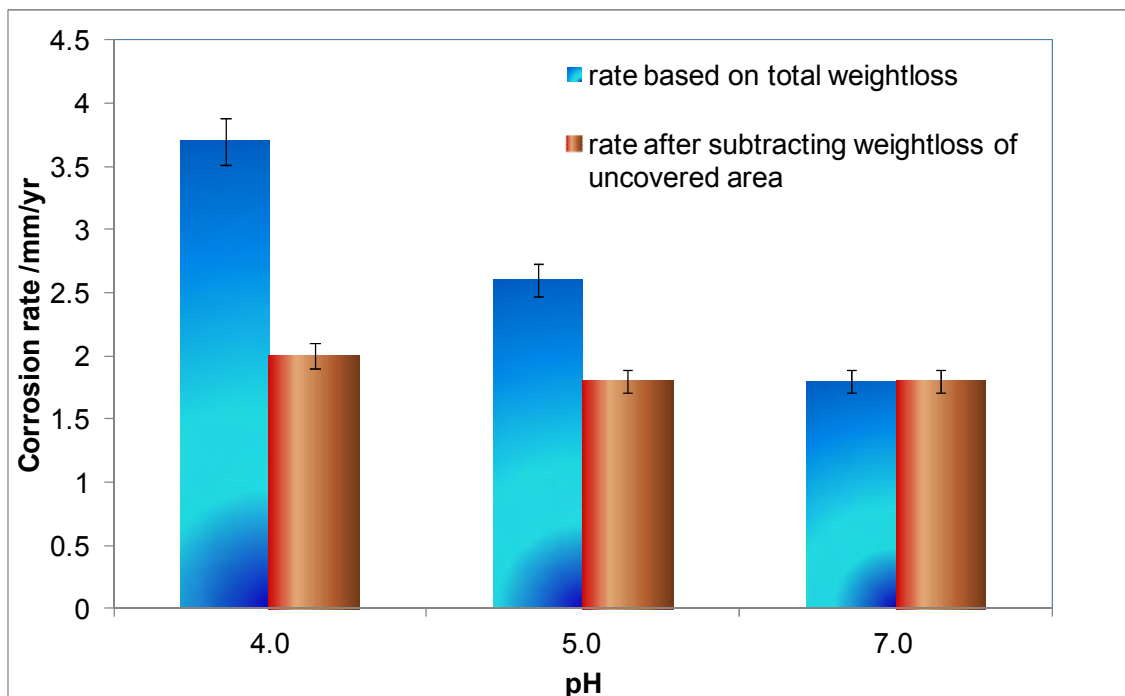
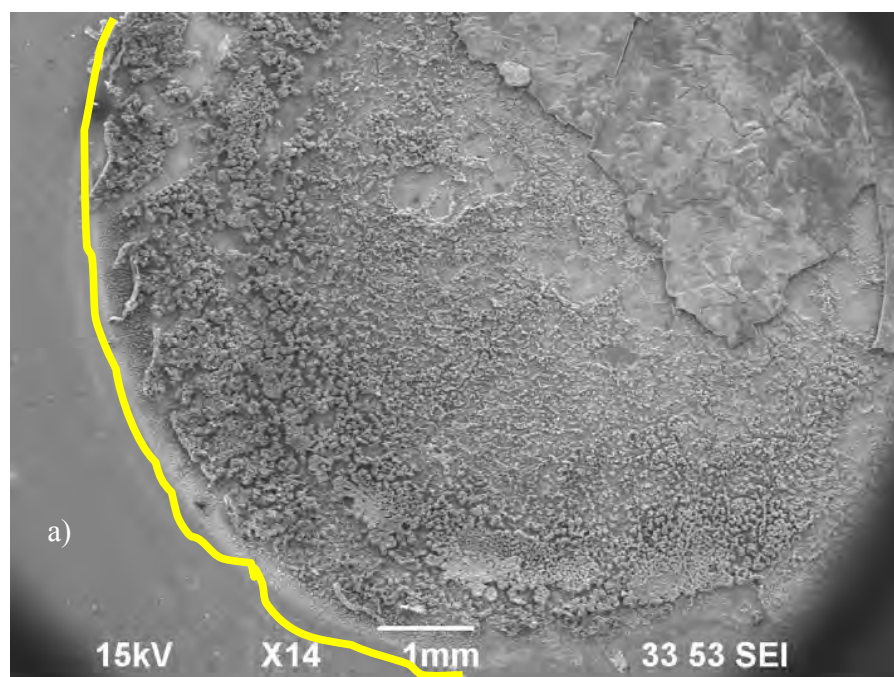
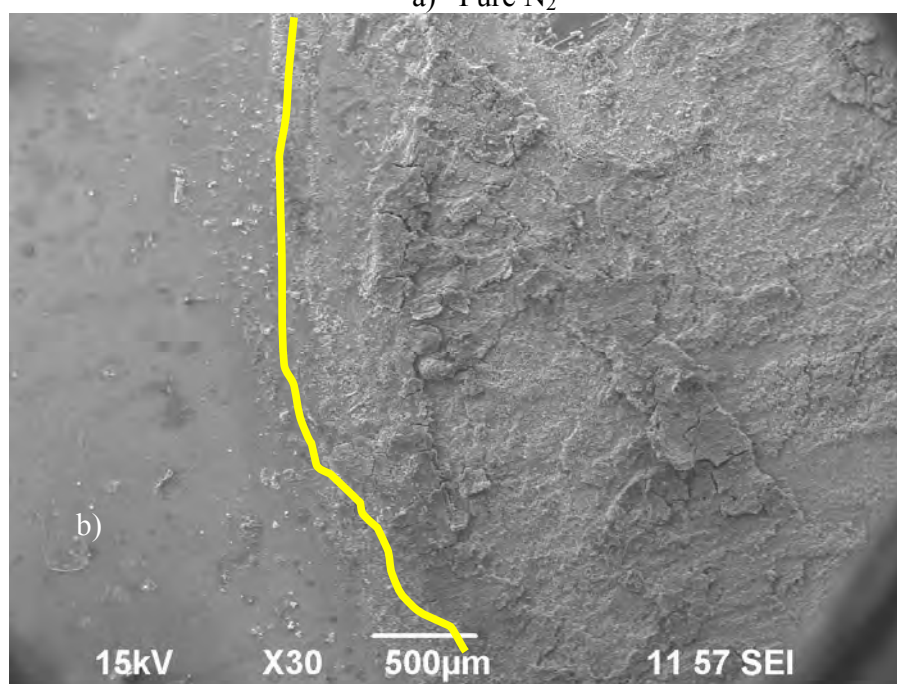


Figure 152. pH effect on sulfur/iron reaction rate(25°C, N₂ purged).

5.5.2.2.7 Sulfur/iron reaction in various gas systems (pure N₂, pure CO₂, N₂ plus 100 ppm H₂S and CO₂ plus 100 ppm H₂S)

To clarify the effect of dissolved gas, elemental sulfur corrosion was investigated in four different aqueous environments, purged with: pure N₂, pure CO₂, nitrogen plus 100 ppm H₂S and CO₂ plus 100 ppm H₂S. The SEM images of specimen surfaces for the different cases are shown in Figure 153. It can be seen there is no significant difference of the film formation in each case. Most of the film generation occurred in the sulfur covered area. Figure 154 shows the SEM image of sulfur uncovered surface for pure N₂ and CO₂ conditions. In pure CO₂ condition (picture on the right), acid corrosion is much more severe compared with the pure nitrogen condition. Representative SEM/EDX data for the specimen surface that has no direct contact with elemental sulfur under the conditions of N₂ plus 100 ppm H₂S and CO₂ plus 100 ppm H₂S are shown in Figure 155. EDX results confirm that iron sulfide films were generated on the specimen surface in both cases. The difference is that more films were formed in the N₂/H₂S system. From the SEM/EDX data, it appears that CO₂ and H₂S effects on elemental sulfur corrosion are most likely just on the sulfur uncovered area. Quantitative analysis of the corrosion rates was conducted to clarify this hypothesis.

a) Pure N₂b) Pure CO₂

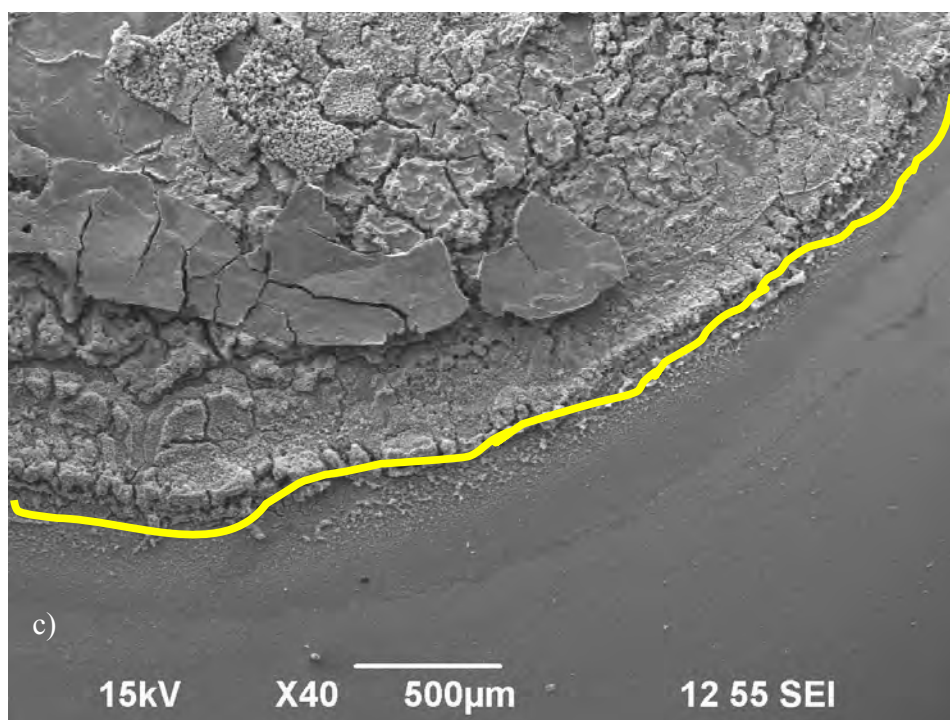
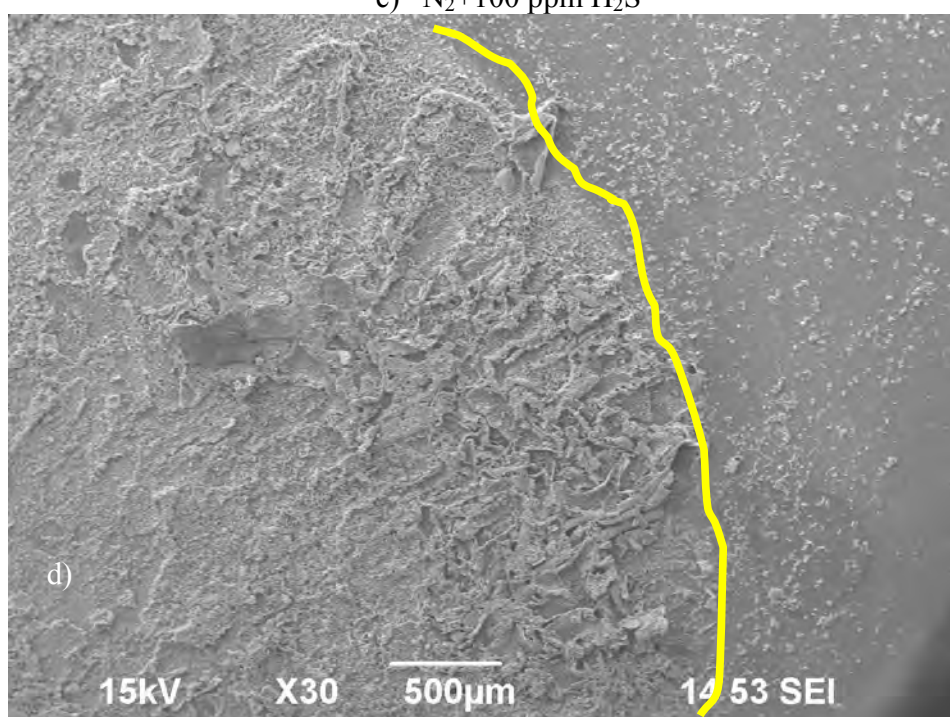
c) N₂+100 ppm H₂Sd) CO₂+100ppm H₂S

Figure 153. Surface morphology underneath the sulfur droplet at different systems (a) pure N₂, b) pure CO₂, c) N₂+100 ppm H₂S, d) CO₂+100 ppm H₂S).

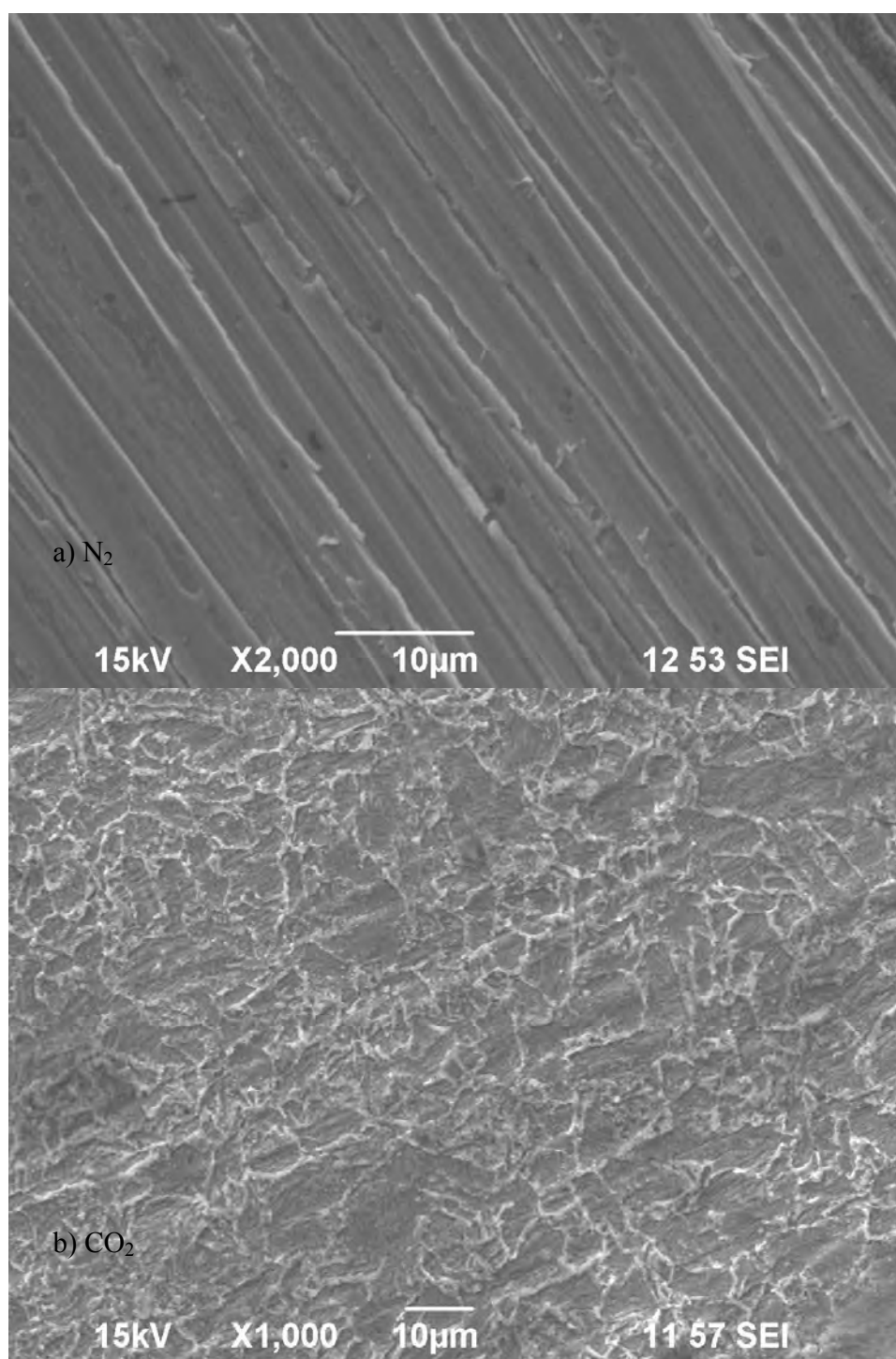
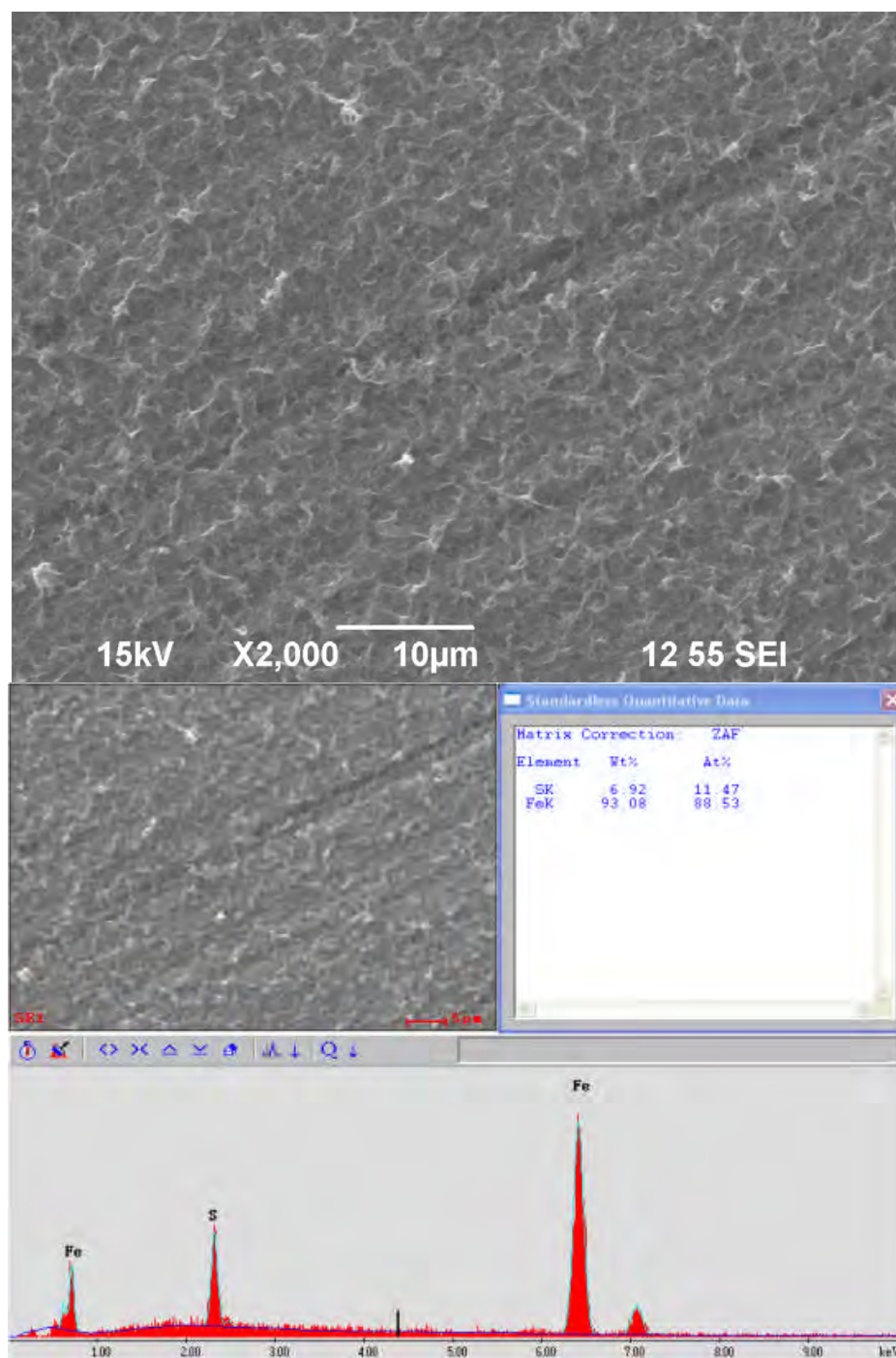


Figure 154. Surface morphology outside the sulfur droplet at different systems (pure N₂ and pure CO₂).

a) N₂+100 ppm H₂S



b) CO₂+100 ppm H₂S

Figure 155. Surface morphology outside the sulfur droplet at different systems (N₂+100 ppm H₂S, and CO₂+100 ppm H₂S).

Corrosion rate underneath the sulfur droplet was calculated based on the method described in last section. The results are shown in Figure 156. The corrosion rate for the pure CO₂ condition is slightly higher than the one in the pure N₂ system, remaining of the same order of magnitude. This suggests that the addition of CO₂ does not appear to have a significant effect on elemental sulfur corrosion. However, interestingly, the addition of 100 ppm H₂S significantly decreased the corrosion rate underneath the sulfur droplet in both N₂ and CO₂ systems. The reason why is difficult to find based on current experimental results.

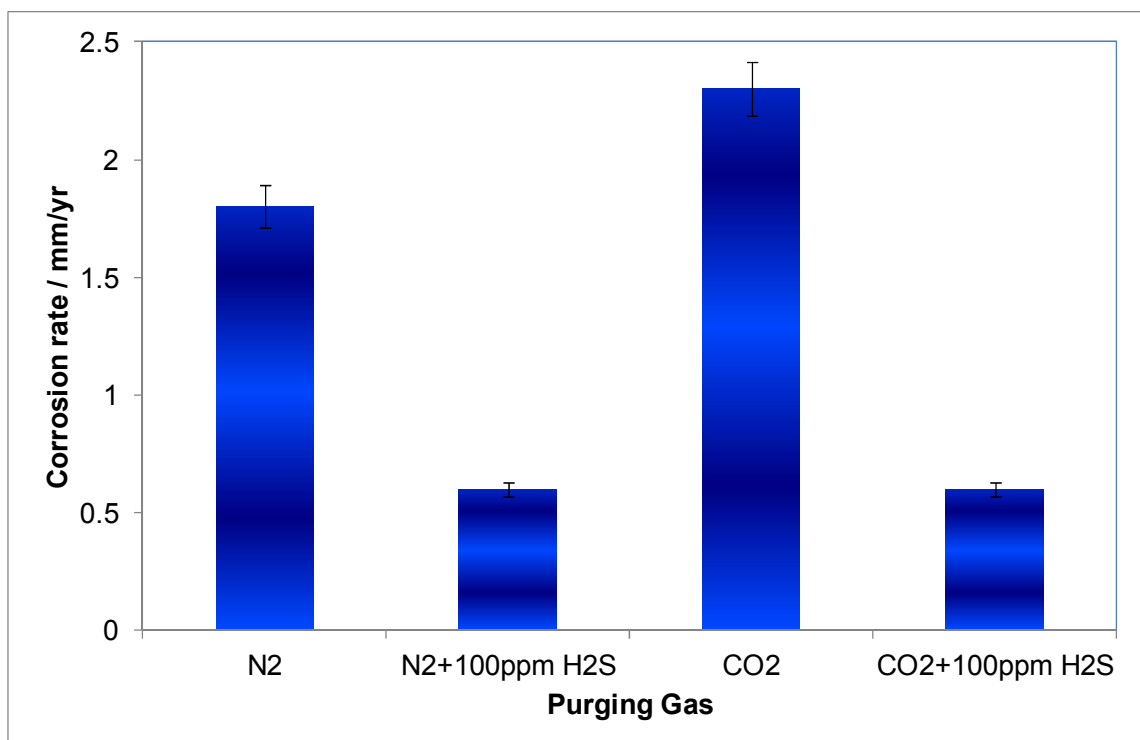


Figure 156. Corrosion rate underneath the sulfur droplet at different systems.

5.5.3 Proposed mechanism of elemental sulfur corrosion of mild steel

Many experiments have been performed to elucidate the elemental sulfur corrosion mechanism. From all the experimental results, it appears that the sulfur hydrolysis reaction does occur according to the following reaction equation:



However, the reaction rate is extremely slow especially at the temperatures that oil and gas industry is interested in. Therefore, sulfur hydrolysis reaction is not the dominant mechanism during elemental sulfur corrosion process.

The elemental sulfur corrosion rate is controlled by the direct sulfur/iron reaction. In salt free condition representing low solution conductivity, the corrosion product, iron sulfide is mainly formed underneath the sulfur particle as shown in Figure 157.

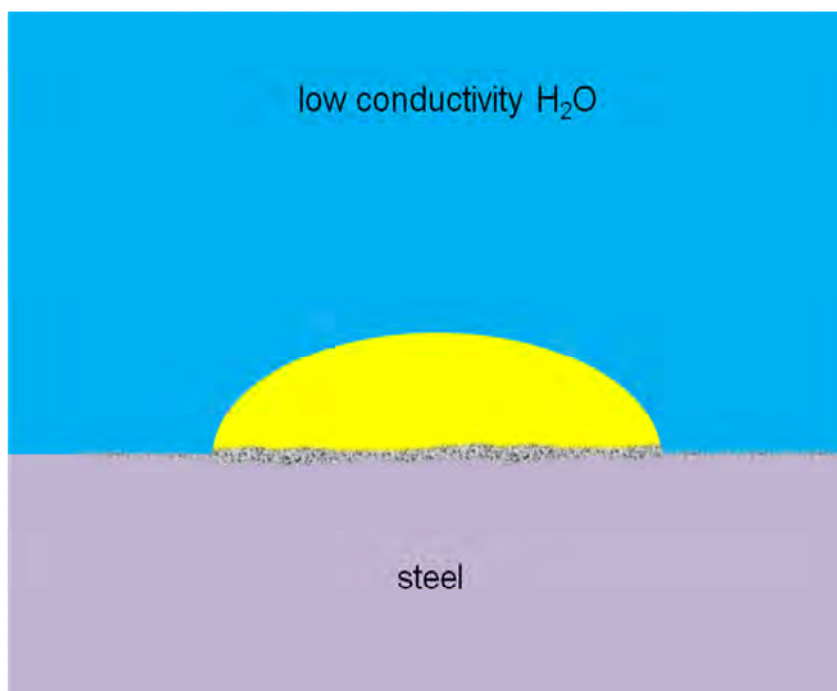
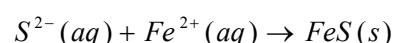
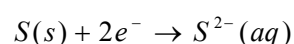
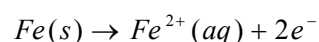


Figure 157. Simulation of elemental sulfur attack in low conductivity conditions.

Initially, after sulfur deposits on the steel surface and is surrounded with water, a thin layer of iron sulfide layer is formed at the interface between the sulfur and steel. This can occur by either reaction between steel and H_2S , generated by the sulfur hydrolysis reaction, or direct electrochemical reaction between sulfur and steel. Iron loses two electrons and releases ferrous ion into the solution. The two electrons are consumed by sulfur, which is then reduced to sulfide ions. Iron sulfide is then formed by the reaction between ferrous ion and sulfide ion.



After the first layer of iron sulfide is formed, thanks to its electrical conductivity, it acts as a transferring medium for electrons from iron to sulfur. As the electrolyte must remain electrically neutral, this requires the same number of equivalents of cations and anions in the solution, to move to accommodate the flowing current¹⁰⁶.

Due to the low solution conductivity in the solution, the ions tend to move via the shortest pathway to close the electrical circuit generated by the electrochemical reaction. Consequently, more corrosion occurs directly underneath the sulfur droplet than elsewhere.

In high salt concentration solution which gives high solution conductivity, most corrosion attack occurs in close proximity to the periphery of the sulfur pellet as shown in Figure 158. This is quite different from what has been observed in salt free conditions.

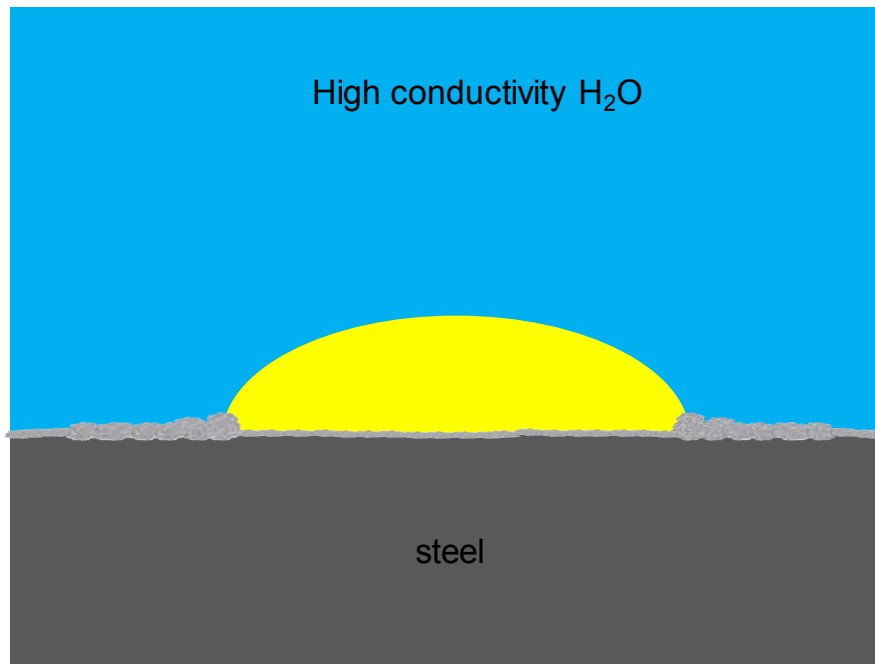


Figure 158. Simulation of elemental sulfur attack in high conductivity conditions.

The different morphology of the corrosion attack is believed to be due to the high solution conductivity surrounding the sulfur droplet. At the beginning, the reaction still starts to occur at the interface of the sulfur and steel surface. With the progressive generation of iron sulfide layer, the conductivity of solution underneath the sulfur droplet is decreased. This is because the mobility of ions is decreased, caused by the formation of mass transfer barrier – the layered iron sulfide. However, the solution outside the sulfur droplet still remain at high conductivity, which makes the least resistance path for the ions to be to the outside the sulfur droplet. Consequently, it is easier for sulfide ion and ferrous ion to transfer through the space outside the sulfur droplet which results in the corrosion current spreading out. As the distance is increased, the magnitude of the ionic current decreases. This is why most severe corrosion attacks occurred in the area

proximate to the sulfur droplet edge. Overall high solution conductivity helps the ionic transfer and also spreads the area of interaction, which results in an overall increase of corrosion rate, under the condition of high salt concentration.

5.5.4 Electrochemical modeling

According to the experimental results of elemental sulfur corrosion, it appears that the solution conductivity plays an important role in the corrosion process. The increase of solution conductivity not only increases the overall corrosion rate but also changes the location of corrosion attack. A hypothesis has been made to explain the corrosion phenomena observed during the test. An electrochemical model based on electrochemical transport theory is built to verify the hypothesis.

5.5.4.1 Foundation of the electrochemical transport model¹⁰⁶

Based on the experimental results, the elemental sulfur corrosion process is dominated by the electrochemical reactions (anodic reaction: iron dissolution and cathodic reaction: sulfur reduction). Cathodic and anodic reactions are separated by the iron sulfide layer. The electrochemical system in elemental sulfur corrosion is schematically illustrated in Figure 159. The governing equation for modeling this electrochemical system is proposed in the following paragraphs.

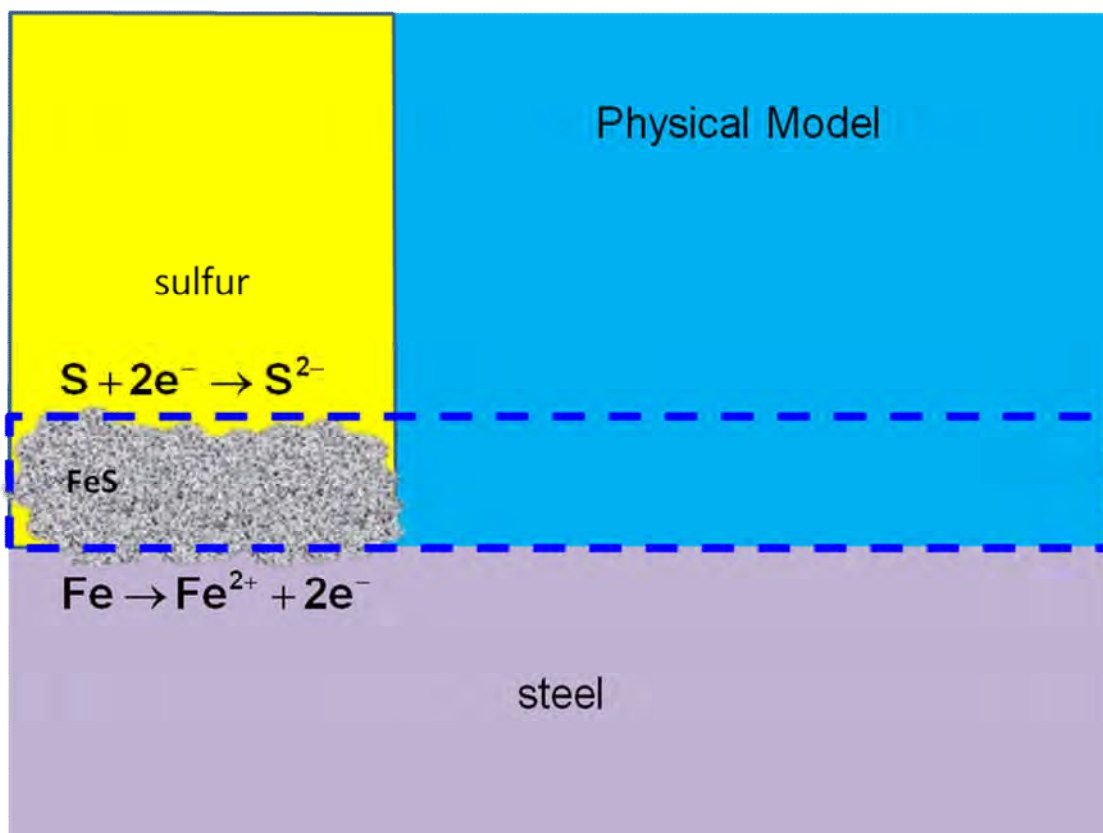


Figure 159. Schematic of the modeled electrochemical system in elemental sulfur corrosion.

In an electrochemical system, the current in the solution is the net flux of charged species:

$$i = \sum_i z_i F N_i$$

Where N_i is the flux density of species i , z_i is the charge number of the species and F is the Faraday constant. The flux density in the solution includes three parts consecutively caused by migration, diffusion and convection.

The flux caused by migration is given by:

$$N_{i,migration} = -z_i u_i F c_i \nabla \Phi$$

where u_i is the mobility of species, c_i is the concentration of species and Φ is the potential in solution.

The flux density due to diffusion is given by:

$$N_{i,diffusion} = -D_i \nabla c_i$$

where D_i is the diffusion coefficient of species i in the solution.

The flux density of a species generated by convection is given by:

$$N_{i,convection} = -c_i v$$

where v is the velocity of the bulk solution.

Therefore, the net flux density in an electrochemical system is given by the combination of three components:

$$N_i = -z_i u_i F c_i \nabla \Phi + -D_i \nabla c_i + -c_i v$$

The conservation of mass law leads to a differential mass conservation equation:

$$\frac{\partial c_i}{\partial t} = -\nabla N_i + R_i$$

In an electrochemical system, the chemical reactions are usually limited to the electrode surface, therefore, the bulk reaction term R_i is zero.

Since the electrochemical reactions are always heterogeneous and occurring at the electrode surface, the bulk solution is electrically neutral:

$$\sum_i z_i c_i = 0$$

If the concentration gradients in the solution are ignored, then the current in the solution can be simplified to:

$$i = -k \nabla \Phi$$

where k is the solution conductivity and is given by:

$$\kappa = F^2 \sum_i z_i^2 \mu_i c_i$$

Finally, for steady state, this yields the classic Laplace's equation for the potential distribution in the solution:

$$\kappa \nabla^2 \Phi = 0$$

This equation is the basis of the calculations presented below.

5.5.4.2 Mathematic model

The governing equation used in the model, which is the classic Laplace's equation, has been derived in the previous section. The mathematical/numerical part of the model is described in this section.

Figure 160 shows the half of the cross-section of the sulfur/iron corrosion system. The black rectangle underneath the droplet represents the iron sulfide layer. The computation domain used in this model is outlined by the blue rectangular line.

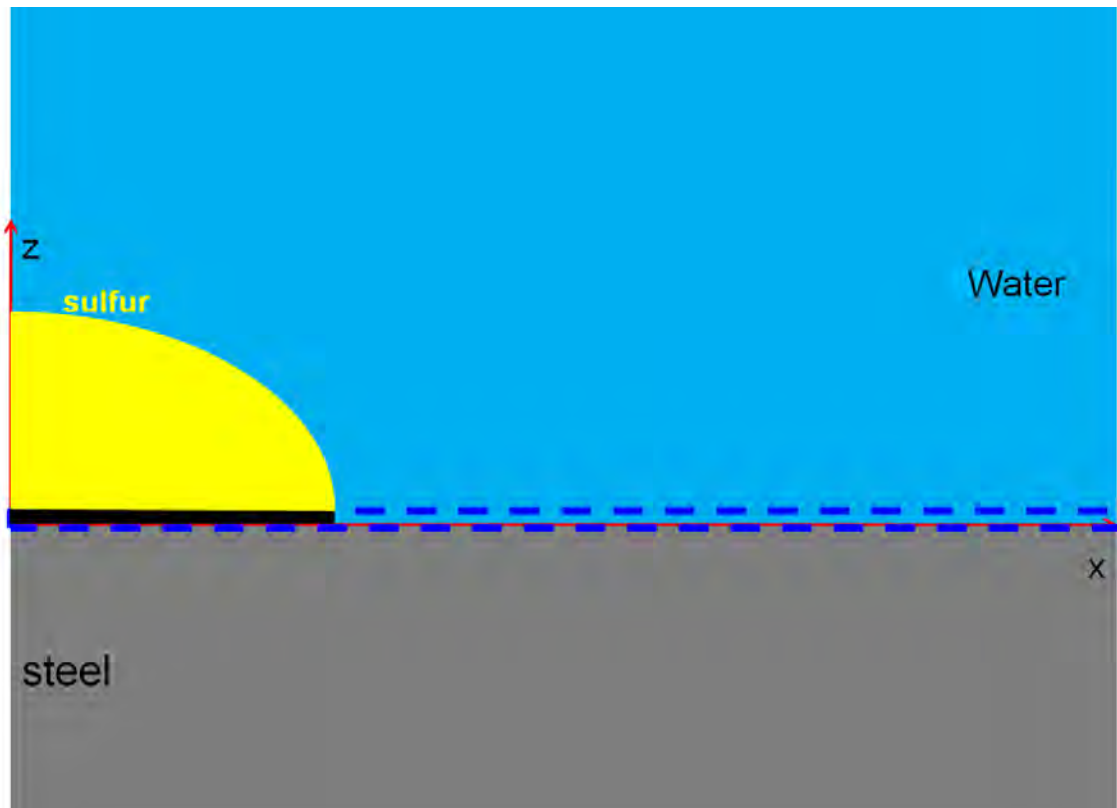


Figure 160. Elemental sulfur corrosion system used in the model.

Figure 161 shows the computational domain alone (not to scale). The model assumes that the cathodic reaction and anodic reaction are not occurring on the same area of the surface, iron oxidation is happening on the bottom (steel) surface and sulfur reduction occurs on the portion of the top surface underneath the droplet. An iron sulfide layer generated underneath the sulfur droplet physically separates but electrically connects the anodic and cathodic areas,

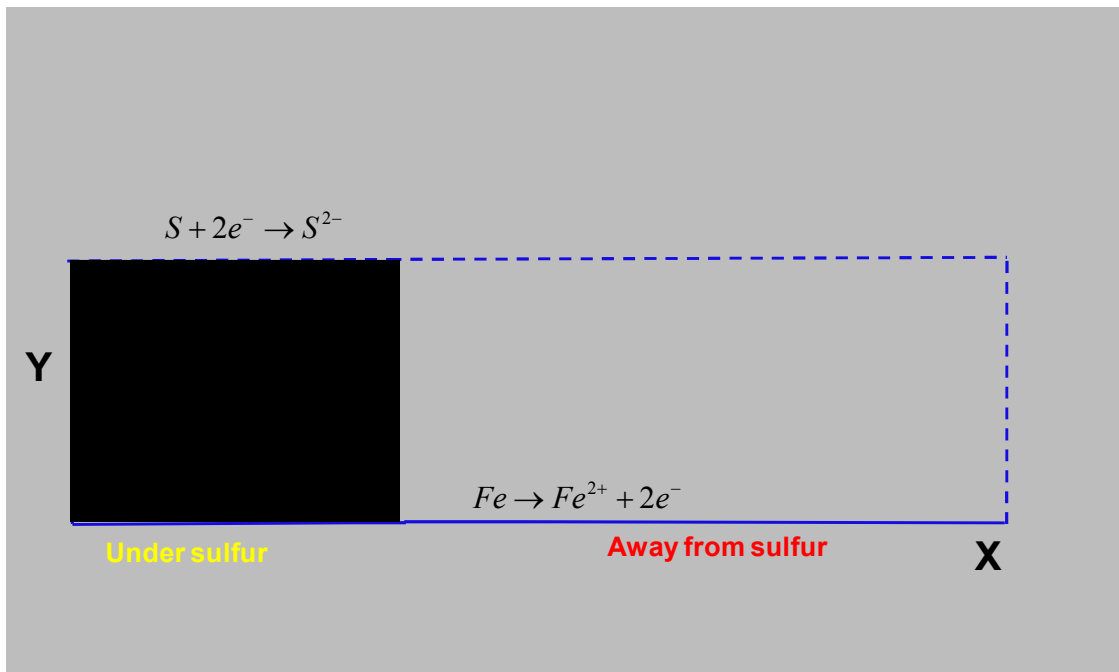


Figure 161. Computational domain of the model.

In this model, the potential and current distribution in between the sulfur and steel surfaces are simulated. The specific governing equation used for this work is listed below:

$$\kappa_x \frac{\partial^2 \Phi}{\partial^2 x} + \kappa_y \frac{\partial^2 \Phi}{\partial^2 y} = 0$$

Where κ_x and κ_y consecutively represent the solution conductivity in x and y directions.

The boundary conditions are listed below,

For west boundary condition, $\frac{\partial \Phi}{\partial x} = 0$, due to symmetry.

For east boundary condition, $\frac{\partial \Phi}{\partial x} = 0$, due to zero current flow.

For south boundary condition, $i_a = -\kappa \frac{\partial \Phi}{\partial y} = -i_{0_Fe} \times 10^{\frac{\Phi - E_{rev_Fe}}{\beta_{Fe}}}$ due to electrochemical reaction.

For north boundary condition, if $x < \text{radius of sulfur droplet}$, $i_c = -\kappa \frac{\partial \Phi}{\partial y} = i_{0_S} \times 10^{\frac{E_{rev_S} - \Phi}{\beta_S}}$, due to electrochemical reaction; if $x > \text{radius of sulfur droplet}$, $\frac{\partial \Phi}{\partial y} = 0$, due to zero current flow.

The data for direct sulfur reduction was not found in the open literature. Therefore the model aims at a qualitative simulation, and the data for sulfur reduction are arbitrarily selected based on similar reduction reaction kinetics. The solution of the Laplace equation is achieved by using the AC/DC module of Comsol Multiphysics[®] software. As the solution conductivity plays a key role in elemental sulfur corrosion hypothesis presented above, this effect was simulated in this model to verify the mechanism proposed in the previous section. Figure 162 shows the actual computational domain used in the model. The radius of the sulfur and the steel specimen are 5 mm and 15 mm respectively. The thickness of the iron sulfide layer generated between sulfur and steel surface is set to 200 μm .

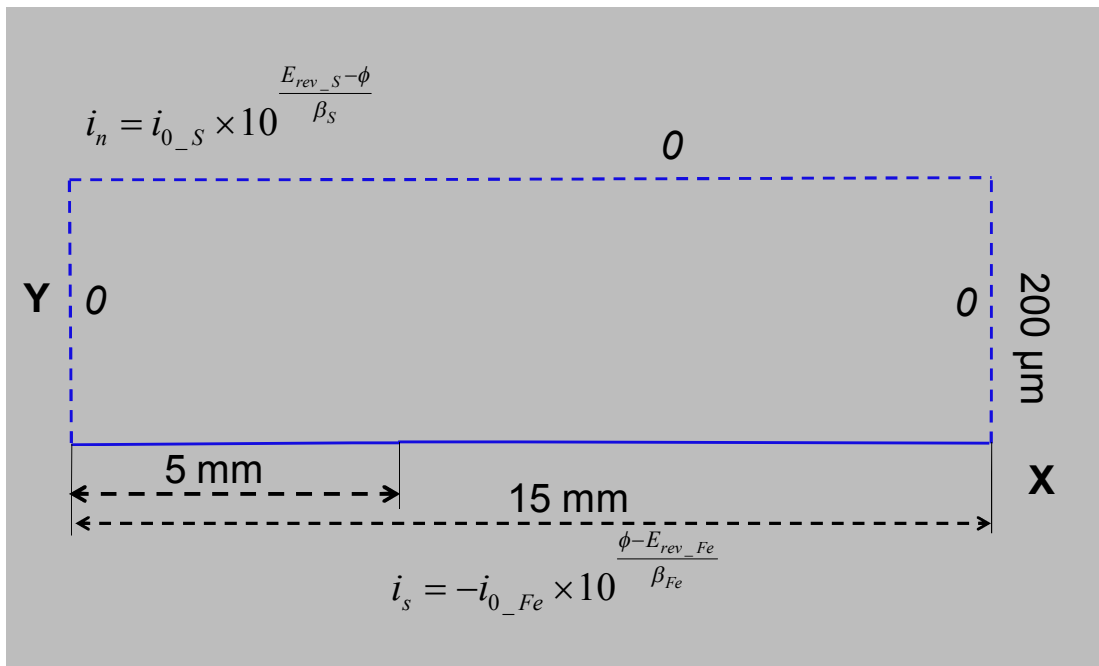


Figure 162. Computational domain used in Comsol Multiphysics[®] software.

The corrosion mechanism for elemental sulfur corrosion proposed above assumed that high solution conductivity can facilitate the corrosion reactions. It was also assumed that formation of the iron sulfide layer may significantly reduce the solution conductivity underneath the sulfur droplet. These assumptions were used to explain the corrosion behavior observed in the high salt concentration solution: less corrosion attack underneath sulfur, most of the corrosion attacks on the steel surface in close proximity to sulfur, and less corrosion attack far away from sulfur. The following simulations by the model illustrated the corrosion behavior with time in the high salt concentration solution.

In the first simulation, the solution conductivity is uniformly distributed in the solution. The conductivity was set high as 13.4 S/m, which was measured in 10 wt.% NaCl solution. This represents the initial stage of corrosion under the condition of high

solution conductivity. Figure 163 shows the potential and current distribution in the whole computational domain. The colors represent the potential distribution, and the unit is Volt. The black lines represent the current (density) streamlines in the solution. The label “x” represents the distance from the sulfur droplet center along the steel surface in m. The label “y” represents the distance from the sulfur droplet center in the direction that is perpendicular to the steel surface. The unit is m as well. It appears that the current is uniformly distributed underneath the sulfur droplet ($x < 0.005$ m) and a small portion of the current from the sulfur edge goes through the solution and beyond the sulfur droplet ($x > 0.005$ m). The current density distribution along the steel surface representing the corrosion rates along the steel surface is shown in Figure 164. It is clearly seen that the current density on the steel surface underneath the sulfur droplet is much higher than the current on the rest of the steel surface. This indicates that the most of corrosion attack occurs on the sulfur covered surface at the beginning of the process. Corrosion rate is high at the beginning due to the high solution conductivity. However, iron sulfide forms on the steel surface which reduced the solution conductivity underneath the sulfur droplet.

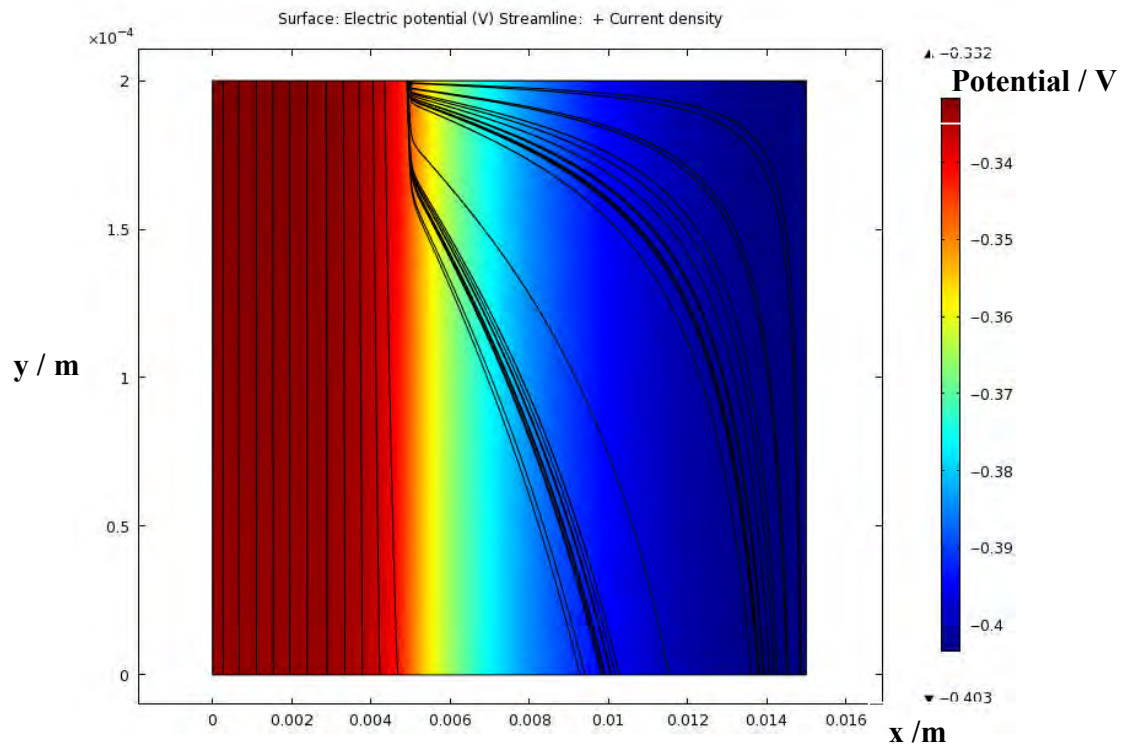


Figure 163. 2D Potential and current distribution – simulation 1.

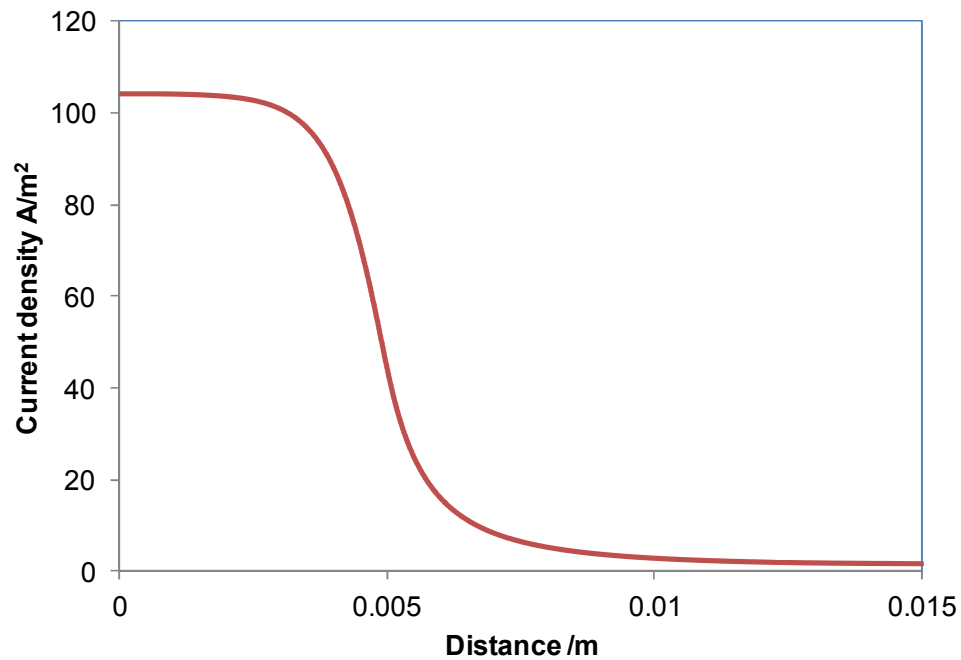


Figure 164. Current distribution along the steel surface – simulation 1.

Due to the formation of iron sulfide, in the second simulation, the solution conductivity underneath the sulfur droplet in the x direction was reduced 100 times lower to 0.134 S/m. The solution conductivity of the rest of solution in both x and y direction remains 13.4 S/m. This simulates the decrease of solution conductivity underneath sulfur due to the growth of the iron sulfide, which was previously hypothesized. The potential and current distributions are shown in Figure 165. Clearly, the current underneath the sulfur droplet starts to flow out to the sulfur uncovered area. This should lead to a decrease of current density on the sulfur covered steel surface and an increase of current density on the sulfur edge. The current density distribution along the steel surface is shown in Figure 166. The current density on the sulfur covered steel surface is still high but does decrease with a decrease of solution conductivity in this area. The significant

increase of current density right on the sulfur edge is due to the sudden change of the solution conductivity in this area.

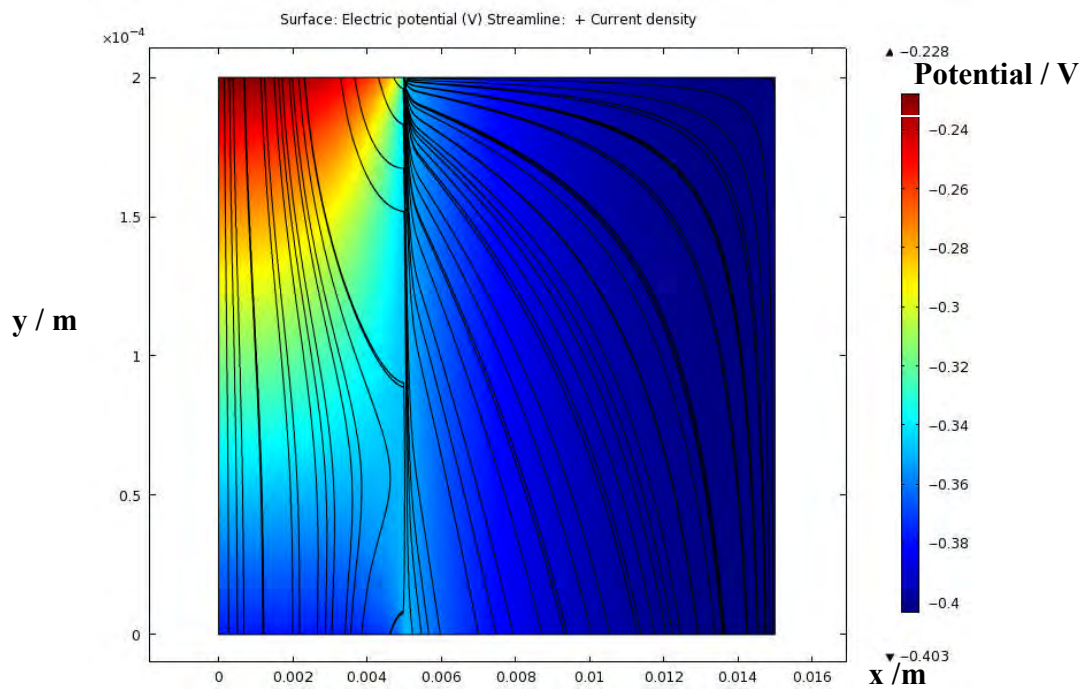


Figure 165. 2D Potential and current distribution – simulation 2.

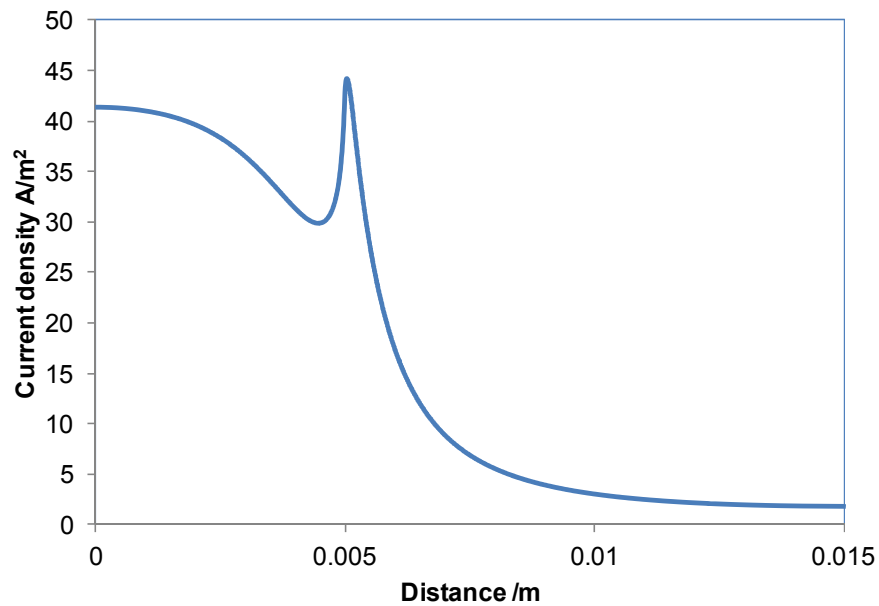


Figure 166. Current distribution along the steel surface – simulation 2.

As hypothesized before, the conductivity of solution underneath the sulfur droplet keeps decreasing as more iron sulfide layer forms with time. Therefore, in the third simulation, the solution conductivity under sulfur was set to 0.00134S/m. The corrosion current within the sulfur droplet further flows out even more (Figure 167). This results in a further decrease of the current density on the sulfur covered steel surface accompanying a further increase of current density on the sulfur edge. The results showing current density along the steel surface, in Figure 168 agree rather well with experimental observation, at least qualitatively.

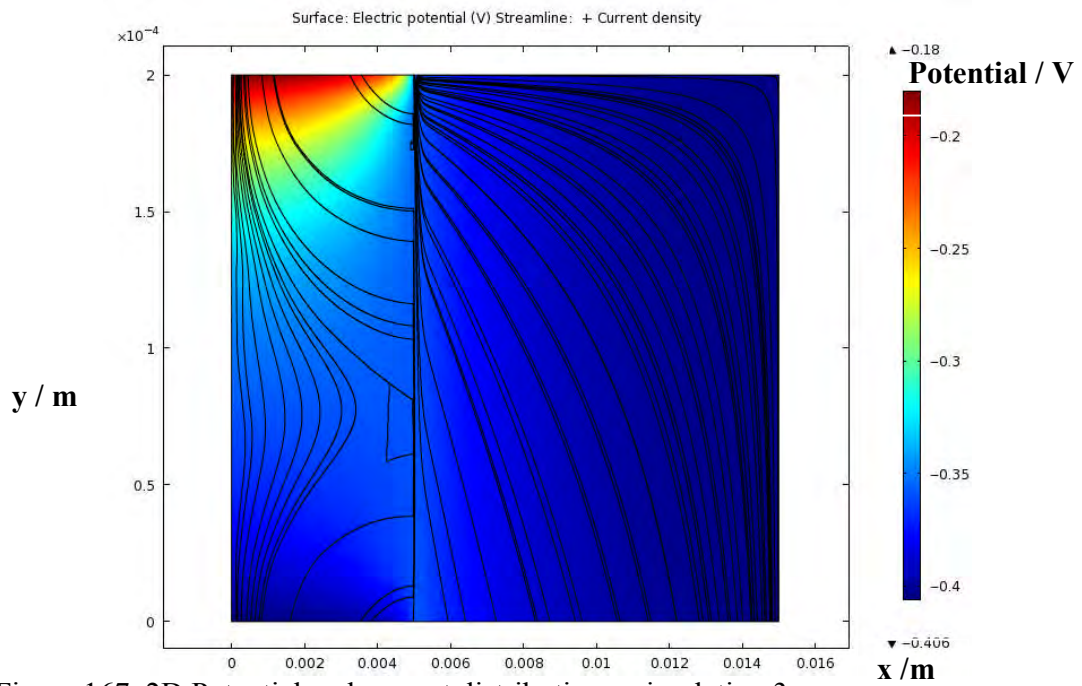


Figure 167. 2D Potential and current distribution – simulation 3.

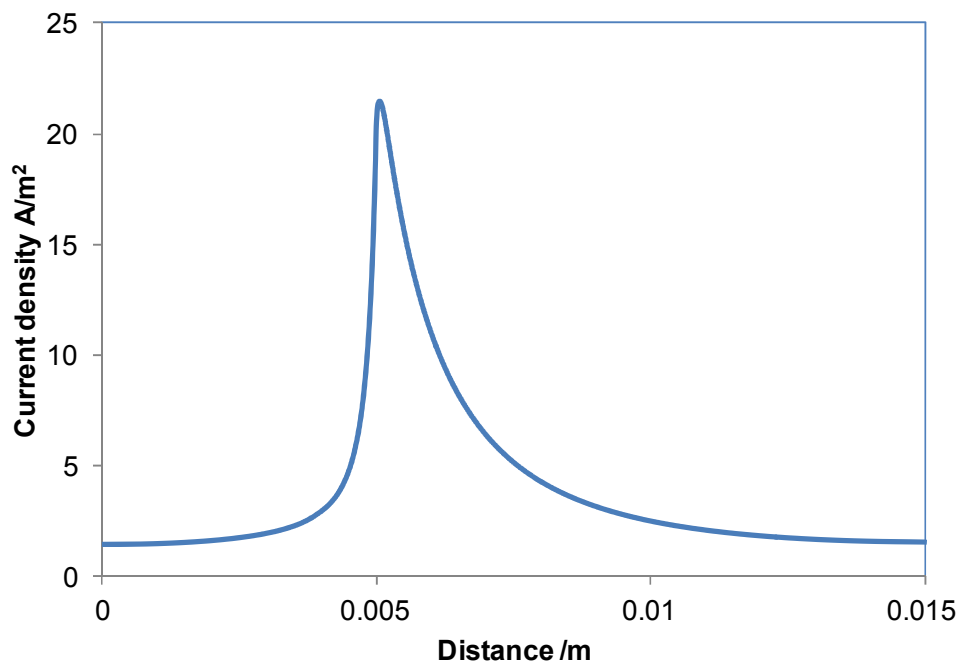


Figure 168. Current distribution along the steel surface – simulation 3.

The solution conductivity underneath sulfur was further decreased to 0.0000055 S/m, which is the conductivity of deionized water. This was assumed to be what occurs in the final stage of elemental sulfur corrosion: enough iron sulfide formation reducing the solution conductivity significantly. Figure 169 illustrates the potential and current distribution in the whole computational domain. As can be seen, under this condition, even more current flows through the solution outside of the sulfur droplet. Barely any current passes through the solution underneath the sulfur droplet. This suggests the steel surface underneath the sulfur undergoes a negligible corrosion attack at this stage. The current distribution along the steel surface is shown in Figure 170. As expected, the highest current density, which means highest corrosion rate, appears on the steel surface in close proximity to the sulfur droplet. This suggests the most severe corrosion attack occurs in this area. The current density gradually decreases along the steel surface away from the sulfur droplet. This was seen in the experiments presented above.

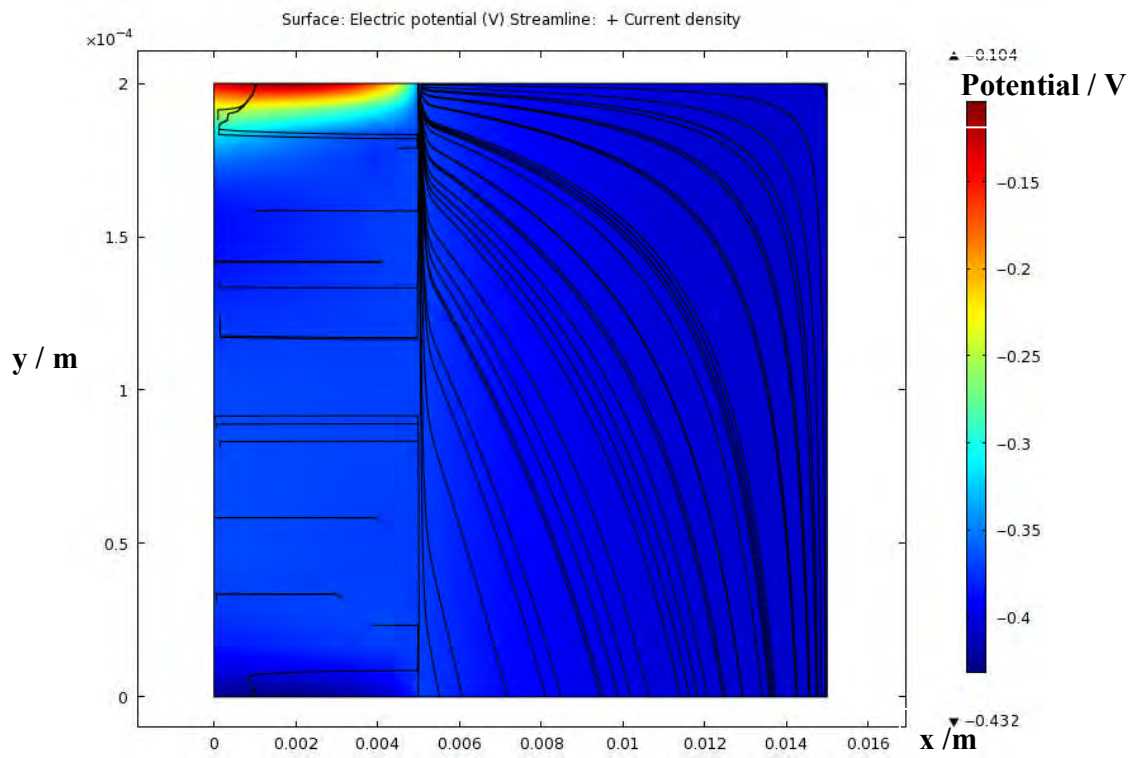


Figure 169. 2D Potential and current distribution – simulation 4.

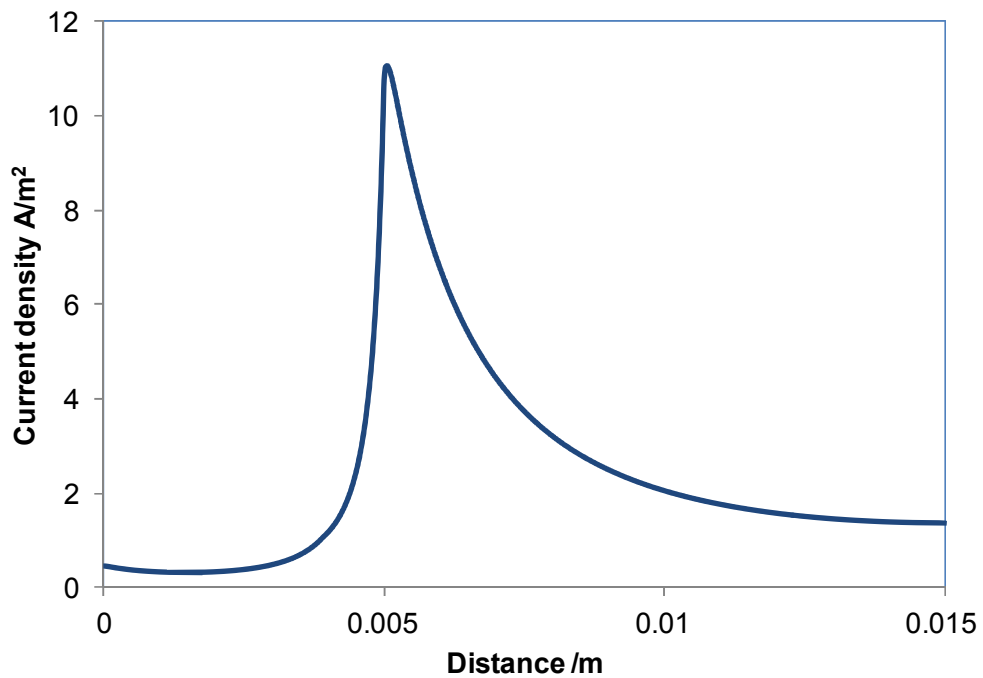


Figure 170. Current distribution along the steel surface – simulation 4.

The model simulations described above qualitatively illustrate the effects of solution conductivity on the potential and current distribution in the solution. From the experimental results, it has been shown that when iron sulfide layers are formed on the steel surface underneath the sulfur droplet, this leads to a decrease of solution conductivity in the sulfur covered steel area. When sulfur is surrounded by the solution with high conductivity (high salt concentration), most of the corrosion attack occurs on the steel surface in close proximity to the periphery of the sulfur pellet. This phenomenon has been hypothesized to be due to the significant difference of solution conductivity between the sulfur covered and uncovered area. The ions which carry the corrosion current tend to transfer more easily through the solution with high conductivity. This

leads to the different corrosion severity along the steel surface: low corrosion rate underneath the sulfur droplet, high corrosion rate in close proximity to the sulfur droplet. The model simulation results successfully verified the proposed mechanism. It qualitatively predicted the corrosion phenomena observed in the experiments. However, more work needs to be done to achieve a precisely quantitative prediction of elemental sulfur corrosion. Many of the electrochemical data needed to build the quantitative model are not readily available and need to be determined in dedicated experiments.

CHAPTER 6 CONCLUSIONS AND FUTURE WORK

6.1 Conclusions

The mechanisms of localized corrosion of mild steel in sour environments were investigated in this project. The experimental results show that no direct evidence was found to prove that chloride is able to initiate localized corrosion in sour environments (at both low and high H₂S concentration).

The mechanism of carbon steel corrosion in the presence of elemental sulfur was also studied in this project. The following conclusions can be drawn from the experimental results:

1. A sulfur hydrolysis reaction does occur, but does not appear to be the dominant mechanism in elemental sulfur corrosion.
2. A direct, solid-state reaction between sulfur and iron is less likely to underpin the main corrosion mechanism of elemental sulfur corrosion.
3. An electrochemical reaction between sulfur and iron (iron oxidative dissolution and sulfur reduction) is more likely to be the controlling mechanism of elemental sulfur corrosion.
4. Electrical connection and physical proximity between sulfur and steel are critical for elemental sulfur corrosion.
5. CO₂ partial pressure, electrolyte type and pH appear to have no significant effect on elemental sulfur corrosion.

6. Salts have a large influence of sulfur corrosion of mild steel but it is the solution conductivity rather than the presence of chloride ions, or any other specific ions that plays an important role in elemental sulfur corrosion.
7. A qualitative model has been built to explain the elemental corrosion phenomena observed in the experiments.

6.2 Future work

Numerous experiments have been conducted to investigate the localized corrosion in sour systems. Questions were proposed at the beginning of this research and they have been partially answered by the work that has been done. However, there are still lingering questions related to this topic that should be addressed. The following recommendations could be taken into consideration for future work:

1. Study the chloride ion effect on localized corrosion in CO₂/H₂S mixed systems, at higher temperatures and in longer test durations.
2. Perform more experiments of elemental sulfur corrosion at various H₂S concentrations.
3. Vary the surface ratio of elemental sulfur and steel specimen surface.
4. Determine a method to electrochemically measure the elemental sulfur corrosion.
5. Quantitatively model the elemental sulfur corrosion phenomena.

REFERENCES

1. C. de Waard and D. E. Milliams, "Carbonic Acid Corrosion of Steel", *Corrosion*, Vol. 31, No. 8, 1975, pp. 177-182.
2. C. de Waard and D. E. Milliams, "Predictive Model for CO₂ Corrosion Engineering in Wet Natural Gas Pipelines", *Corrosion/91*, Paper no. 577, NACE International, Houston, Texas, 1991.
3. C. de Waard and U. Lotz, "Prediction of CO₂ Corrosion of Carbon Steel," *Corrosion/93*, Paper no. 69, NACE International, Houston, Texas, 1993.
4. C. de Waard, U. Lotz and A. Dugstad "Influence of Liquid Flow Velocity on CO₂ Corrosion: A Semi-Empirical Model". *Corrosion/95*, Paper no. 128, NACE International, Houston, Texas, 1995.
5. L. D. S. Gray, B. G. Anderson, M. J. Danysh and P. R. Tremaine, "Mechanisms of Carbon Steel Corrosion in Brines Containing Dissolved Carbon Dioxide at pH 4", *Corrosion/89*, Paper no. 464, NACE International, Houston, Texas, 1989.
6. L. D. S. Gray, B. G. Anderson, M. J. Danysh and P. R. Tremaine, "Effect of pH and Temperature on the Mechanisms of Carbon Steel Corrosion by Aqueous Carbon Dioxide", *Corrosion/90*, Paper no. 40, NACE International, Houston, Texas, 1990.
7. S. Nestic, J. Postlethwaite and S. Olsen "An Electrochemical Model for Prediction of Corrosion of Mild Steel in Aqueous Carbon Dioxide Solutions", *Corrosion*, Vol. 52, 2003, pp. 280-294.
8. K. Videm and A. Dugstad, "Corrosion of Mild Steel in an Aqueous Carbon Dioxide Environment. Part 1: Solution Effects", *Material Performance*, Vol. 28, 1989, pp. 63-67.
9. K. Videm and A. Dugstad, "Corrosion of Mild Steel in an Aqueous Carbon Dioxide Environment. Part 2: Scale Formation", *Material Performance*, Vol. 28, 1989, pp. 46-50.
10. K. Videm and A. M. Koren, "Corrosion, Passivity and Pitting of Carbon Steel in Aqueous Solutions of HCO₃⁻, CO₂ and Cl⁻", *Corrosion/92*, Paper no. 12, NACE International, Houston, Texas, 1992.
11. K. Videm, "Fundamental Studies Aimed at Improving Models for Prediction of CO₂ Corrosion of Carbon Steels", *Progress in the Understanding and Prevention of Corrosion*, Vol. 1, Barcelona, Spain, 1993, pp. 504-512.

12. M. H. Achour, J. Kolts, A. H. Johannes and G. Liu, "Mechanistic Modeling of Pit Propagation in CO₂ Environment under High Turbulence Effects", Corrosion/93, Paper no. 87, NACE International, Houston, Texas, 1993.
13. Z. Xia, K. C. Chou and Z. Szklarska-Smialowska, "Pitting Corrosion of Carbon Steel in CO₂-Containing NaCl Brine", Corrosion, Vol. 45, No. 8, 1989, pp. 636-642.
14. J. L. Crolet, "Which CO₂ Corrosion, Hence Which Prediction? in Predicting CO₂ Corrosion in the Oil and Gas Industry", London: The Institute of Materials, 1994, pp. 1-26.
15. R. Nyborg and A. Dugstad, "Mesa Corrosion Attack in Carbon Steel and 0.5% Chromium Steel", Corrosion/98, Paper no. 29, NACE International, Houston, Texas, 1998.
16. A. Dugstad, "Mechanism of Protective Film Formation during CO₂ Corrosion of Carbon Steel", Corrosion/98, Paper no. 31, NACE International, Houston, Texas, 1998.
17. R. Nyborg, "Initiation and Growth of Mesa Corrosion Attack during CO₂ Corrosion of Carbon Steel", Corrosion/98, Paper no. 48, NACE International, Houston, Texas, 1998.
18. R. Nyborg and A. Dugstad, "Understanding and Prediction of Mesa Corrosion", Corrosion /2003, Paper no. 642, NACE International, Houston, Texas, 2003.
19. Technical Document, "Recommended Practice for Mitigation of Internal Corrosion in Sour Gas Gathering Systems", Canadian Association of Petroleum Producers. January, 2003.
20. T. W. Hamby, "Development of High Pressure Sour Gas Technology", Journal of Petroleum Technology, Vol. 33, No. 05, 1981, pp. 792-798.
21. D. F. Ho-Chung-Qui and A. I. Williamson, "Corrosion Experiences and Inhibition Practices in Wet Sour Gas Gathering Systems", Corrosion/87, Paper no. 46, NACE International, Houston, Texas, 1987.
22. A. K. Tiller, "Electrochemical Aspects of Microbial Corrosion: An Overview", Microbial Corrosion, Mar. 1983, pp. 56-65.
23. S. C. Dexter, "Localized Biological Corrosion and Biological Effects", Metals Handbook, Vol. 13, 9th ed., 1987.

24. M. Nemati and G. Voordouw, "Identification and Characterization of Sulfate-reducing Bacteria Involved in Microbially Influenced Corrosion in Oil Fields", NACE/2000, Paper no. 00126, NACE International, Houston, Texas, 2000.
25. D. Alazard, A. Alejandra Padilla-Viveros and S. Miguel Garcia Ochoa, "Electrochemical Behavior of Localized Corrosion in Steel, by Sulfate-reducing Bacteria under Oligotrophic Conditions", NACE/2004, Paper no. 04583, NACE International, Houston, Texas, 2004.
26. J. S. Lee, R. I. Ray, E. J. Lemieux, A. U. Falster and B. J. Little, "An Evaluation of Carbon Steel Corrosion under Stagnant Seawater Conditions", *Biofouling*, Vol. 20, 2004, pp. 237-247.
27. J. S. Smith and J. D. A. Miller, "Nature of Sulphides and Their Corrosive Effect on Ferrous Metals: A Review". *British Corrosion Journal*, Vol. 10, No. 3, 1975, pp. 136-143.
28. F. Farelas, "Thin Channel Flow Cell Study: Mechanical Removal and Chemical Dissolution of FeCO_3 Scale on Carbon Steels", Institute for Corrosion and Multiphase Technology Boardmeeting report, November 2008.
29. L. Corbari, M. A. Cambon-Bonavita, G. J. Long, F. Grandjean, M. Zbinden, F. Gaill and P. Comp`ere, "Iron Oxide Deposits Associated with the Ectosymbiotic Bacteria in the Hydrothermal Vent Shrimp *Rimicaris Exoculata*", *Biogeosciences*, Vol. 5, 2008, pp. 1295–1310.
30. J. Goldstein, D. E. Newbury, D. C. Joy, C. E. Lyman, P. Echlin, E. Lifshin and L. Sawyer, *Scanning Electron Microscopy and X-Ray Microanalysis*. Springer. 3rd edition, 2003.
31. H. Fang, "Corrosion of Mild Steel in the Presence of Sulfur", Institute for Corrosion and Multiphase Technology Boardmeeting report, March 2007.
32. L. Skrtic, "Hydrogen Sulfide, Oil and Gas, and People's Health", M.S. Thesis, University of California, Berkeley, 2006.
33. C. James and D. Lewis, "Hydrogen Sulfide: Evaluation of Current California Air Quality Standards with Respect to Protection of Children". Air Toxicology and Epidemiology Section, California Office of Environmental Health Hazard Assessment (OEHHA). September 1, 2000.
34. P. M. Davis, N. I. Dowling, R. A. Marriott and T. Owens, ASRL Course: Sulfur Deposition and Other Aspects of the Chemistry and Technology of Sour Gas Production, Albert Sulphur Research LTD. Sulfur Deposition Symposium, 2009.

35. M. K. Cottle, and T. L. Guidotti, "Process Chemicals in the Oil and Gas Industry: Potential Occupational Hazards." *Toxicology and Industrial Health*. 6: (1) 41-56, 1990.
36. S. Dubyk and S. Mustafa. "Trip Report: H₂S Survey", March 18-22, 2002, New Mexico Environment Department, Air Quality Bureau.
37. D. C. Fuller and A. J. Suruda, "Occupationally Related Hydrogen Sulfide Deaths in the United States from 1984 to 1994." *Journal of Occupational and Environmental Medicine*. Vol. 42, No. 9, 2000, pp. 939-942.
38. M. Nordsveen, S. Nestic, R. Nyborg and A. Stangeland, "A Mechanistic Model for Carbon Dioxide Corrosion of Mild Steel in the Presence of Protective Iron Carbonate Films – Part 1: Theory and Verification", *Corrosion*, Vol. 59, 2003, pp. 443-457.
39. R. F. Weiss, "The Solubility of Nitrogen, Oxygen and Argon in Water and Seawater", *Deep Sea Research*, Vol. 17, 1970, pp. 721-735.
40. B. E. Roberts, "Vapor Liquid Equilibrium Calculations for Dilute Aqueous Solutions of CO₂, H₂S, NH₃ and NaOH to 300°C", *The Canadian Journal of Chemical Engineering*, Vol. 63, 1985, pp. 294-300.
41. J. Carroll and A. E. Mather, "The Solubility of Hydrogen Sulfide in Water from 0 to 90°C and Pressures to 1 MPa", *Geochimica et Cosmochimica Acta.*, Vol. 53, 1989, pp. 1163-1170.
42. O. M. Suleimenov and R. E. Krupp, "Solubility of Hydrogen Sulfide in Pure Water and in NaCl Solutions, from 20 to 320°C and at Saturation Pressures", *Geochimica et Cosmochimica Acta*, Vol. 58, 1994, pp. 2433-2444.
43. O. M. Suleimenov and T. M. Seward, "A Spectrophotometric Study of Hydrogen Sulfide Ionization in Aqueous Solutions to 350°C", *Geochimica et Cosmochimica Acta*, Vol. 61, 1997, pp. 5187-5198.
44. P. A. A. Douabul and J. P. Riley, "The Solubility of Gases in Distilled Water and Seawater – V. Hydrogen Sulphide", *Deep Sea Research*, Vol. 26, No. 3, 1979, pp. 259-268.
45. H. A. Flaschka, A. J. Barnard, Jr. and P. E. Starrock, *Quantitative Analytical Chemistry*, 2nd ed., Willard Grant Press, Boston, MA, 1980.
46. D. A. Day and A. L. Underwood, *Quantitative Analysis*, 6th ed., Prentice-Hall, Englewood Cliffs, NJ, 1991.

47. T. Almgren, D. Dyrssen, B. Elgquist and O. Johansson, "Dissociation of Hydrogen Sulphide in Seawater and Comparison of Ph Scales", *Marine Chemistry*, Vol. 4, No. 31976, pp. 289-297.
48. H. L. Loy and D. M. Himmelblau, "The First Ionization Constant of Hydrogen Sulfide in Water", *J. Phys. Chem.*, Vol. 65, 1961, pp. 264-267.
49. A. Ringborn, "Solubility of Sulfides", Report to Anal. Sect. of IUPAC, 1953.
50. Y. S. Su, K. L. Cheng and Y. C. Jean, "Amplified Potentiometric Determination of pK00, pK0, pK1, and pK2 of Hydrogen Sulfides with Ag₂S ISE", *Talanta*, Vol. 44, 1997, pp. 1757-1763.
51. E. H. Swift and E. A. Butler, *Quantitative Measurements and Chemical Equilibrium*, W. H. Freeman & Co Ltd; 1st ed., 1972.
52. R. C. Weast, *Handbook of Physics and Chemistry*, 72nd ed., CRC Press, Boca Raton, FL, 1991.
53. A. J. Ellis and R. M. Golding, "Spectrophotometric Determination of Acid Dissociation Constant of Hydrogen Sulfide", *Journal of Chemical Society*, 1959, pp. 127-130.
54. D. C. Harris, *Quantitative Chemical Analysis*, 4th ed., Freeman, New York, 1995.
55. D. W. Shoesmith, P. Taylor, M. G. Bailey, and D. G. Owen, "The Formation of Ferrous Monosulfide Polymorphs during the Corrosion of Iron by Aqueous Hydrogen Sulfide at 21°C", *Journal of the Electrochemical Society*, Vol. 125, 1980, pp. 1007-1015.
56. D. W. Shoesmith, "Formation, Transformation and Dissolution of Phases Formed on Surfaces", Lash Miller Award Address, Electrochemical Society Meeting, Ottawa, Nov. 27, 1981.
57. W. Sun and S. Nescic, "A Mechanistic Model of H₂S Corrosion of Mild Steel", *Corrosion/2007*, Paper no. 07665. NACE International, Houston, Texas, 2007.
58. S. N. Smith, "A Proposed Mechanism for Corrosion in Slightly Sour Oil and Gas Production," *International Corrosion Congress*, Houston, Texas, 1993.
59. A. G. Wikjord, T. E. Rummery, F. E. Doern and D. G. Owen, "Corrosion and Deposition during the Exposure of Carbon Steel to Hydrogen Sulphide-Water Solutions," *Corrosion Science*, Vol. 20, 1980, pp. 651-671.

60. R. A. Berner, "Thermodynamic Stability of Sedimentary Iron Sulfides", *American Journal of Science*, Vol. 265, 1967, pp. 773-785.
61. A. D. Wadsley, in 'Non-stoichiometric Compounds', ed. L. Mandelcorn, 1964 (London: Academic Press)
62. R. G. Arnold and L. E. Reichen, "Measurement of the Metal Content of Naturally Occurring, Metal-Deficient, Hexagonal Pyrrhotite by an X-ray Spacing Method" *American Mineralogist*, Vol. 47, 1962, pp. 105-112
63. R. C. Erd, H. T. Evans and D. H. Richter, "Smythite, A New Iron Sulfide, and Associated Pyrrhotite from Indiana", *American Mineralogist*, Vol. 42, 1957, pp. 309-333.
64. J. A. Morice, L. V. C. Rees and D. T. Richard, "Mössbauer Studies of Iron Sulphides", *Journal of Inorganic and Nuclear Chemistry*, Vol. 31, 1969, pp. 3797-3802.
65. B. J. Skinner, R. C. Erd and F. S. Grimaldi, "Greigite, the Thio-spinel of Iron; A New Mineral", *American Mineralogist*, Vol. 49, 1964, pp. 543-555.
66. J. W. Wallace, R. V. Reddy and D. V. Pugh, "Sour Service Pit Growth Predictions of Carbon Steel Using Extreme Value Statistics", NACE/2007, Paper no. 07657, NACE International, Houston, Texas, 2007.
67. R. V. Reddy, J. L. Nelson and J. L. Pacheco, "Accurate Corrosion Prediction through an Integrated Approach", International Petroleum Technology Conference Paper no. 10675, Doha, Qatar, 2005.
68. W. Sun, D. V. Pugh, S. N. Smith, S. Ling, J. L. Pacheco and R. J. Franco, "A Parametric Study of Sour Corrosion of Carbon Steel", NACE/2010, Paper no. 10278, NACE International, Houston, Texas, 2010.
69. J. Kvarekval, A. Dugstad and M. Seiersten, "Localized Corrosion on Carbon Steel in Sour Glycolic Solutions", NACE/2010, Paper no. 10277, NACE International, Houston, Texas, 2010.
70. P. R. Roberge and V. S. Sastri, "Laboratory and Field Evaluation of Organic Corrosion Inhibitors in Sour Media", *Corrosion Science*, Vol. 35, No. 5-8, 1993, pp. 1503-1513.

71. B. Brown, D. Young and S. Nestic, "Localized Corrosion in an H₂S/CO₂ Environment", Paper no. 2704, 17th International Corrosion Congress, Las Vegas, NV, October 6-10, 2008.
72. O. E. Olorunniwo, B. I. Imasogie and A. A. Afonja, "Evaluation of Pipeline Corrosion in Sour-gas Environment", *Anti-Corrosion Methods and Materials*, Vol. 54, No. 6, 2007, pp. 346 – 353.
73. J. Kvarekval, "Morphology of Localised Corrosion Attacks in Sour Environments", NACE/2007, Paper no. 07659, NACE International, Houston, Texas, 2007.
74. H. Wang, and J. Wylde, "Corrosion Inhibitor Development for Slight Sour Environment with Oxygen Intrusion Issue", NACE/2010, Paper no. 10275, NACE International, Houston, Texas, 2010.
75. J. Crolet, and M. Bonis, "Algorithm of the Protectiveness of Corrosion Layers 1 – Protectiveness Mechanisms and CO₂ Corrosion Prediction", NACE/2010, Paper no. 10363, NACE International, Houston, Texas, 2010.
76. M. Bonis, "Weight Loss Corrosion with H₂S: from Facts to Leading Parameters and Mechanisms", NACE/2009, Paper no. 09564, NACE International, Houston, Texas, 2009.
77. T. Haruna, "Initiation and Propagation of Stress Corrosion Cracks for Type 3041 Stainless Steel in Chloride Solutions Containing Thiosulfate", *Corrosion Science*, Vol. 39, No. 10-11, 1997, pp. 1935-1947.
78. O. Raquet, M. Hélie and G. Santarini, "Initiation and Propagation of Stress Corrosion Cracking of Type 304L Austenitic Stainless Steel in Hot Aqueous Chloride Solution", *Corrosion*, Vol. 52, No. 8, 1996, pp. 697.
79. T. Laitinen, "Localized Corrosion of Stainless Steel in Chloride, Sulfate and Thiosulfate Containing Environments", *Corrosion Science*, Vol. 42, No. 3, 2000, pp. 421-441.
80. S. Lee, J. Ahn, D. Kim, S. Hong and K. Lee, "Influence of Chloride and Bromide Anions on Localized Corrosion of 15%Cr Ferritic Stainless Steel", *Materials Science and Engineering A*, Vol. 434, No. 1-2, 2006, pp. 155-159.
81. S. Moussa, "The Photo-Inhibition of Localized Corrosion of 304 Stainless Steel in Sodium Chloride Environment", *Corrosion Science* Vol. 43, No. 11, 2001, pp. 2037-2047.

82. A. I. Almarshad and D. Jamal, "Electrochemical Investigations of Pitting Corrosion Behaviour of Type UNS S31603 Stainless Steel in Thiosulfate-Chloride Environment", *Journal of Applied Electrochemistry*, 2004, Vol. 34, No. 1, pp. 67-70.
83. H. Fang, B. Brown and S. Nestic, "Effects of Sodium Chloride Concentration on Mild Steel Corrosion in Slightly Sour Environment", *Corrosion*, Vol. 67, No. 1, 2011, pp. 1-12.
84. J. Han, "Galvanic Mechanism of Localized Corrosion for Mild Steel in Carbon Dioxide Environments", Ph.D Dissertation, Ohio University, 2009.
85. D. W. Davis and R. A. Detro, "Fire and Brimstone The History of Melting Louisiana's Sulphur", Louisiana Geological Survey, Baton Rouge, Louisiana 1992.
86. G. Schmitt, "Effects of Elemental Sulfur on Corrosion in Sour Gas Systems", *Corrosion*, Vol. 47, 1991, pp. 285-309.
87. B. Meyer. ed., *Elemental Sulfur. Chemistry and Physics*, New York, NY: Wiley Interscience. 1965.
88. N. N. Greenwood and A. Earnshaw, *Chemistry of the Elements* (2nd ed.), Oxford: Butterworth-Heinemann, 1997.
89. M. G. Voronkov, N. S. Vyazankin, E. N. Deryagina, A. S. Nakhmanovich and V. A. Usov, "Reaction of Sulfur with Organic Compounds", ed. J.S. Pizey, New York, NY: Consultants Bureau, 1987, pp. 18-19.
90. S. A. Al-Mutairi, A. I. Abdulhadi and I. M. Al-Taie, "Sour Gas Dehydration System: Corrosivity and Selection in the Presence of Elemental Sulfur", *Corrosion/2003*, Paper no. 07397, NACE International, Houston, Texas, 2007.
91. P. J. Boden and S. B. Maldonado-Zagal, "Hydrolysis of Elemental Sulfur in Water and its Effects on the Corrosion of Mild Steel", *British Corrosion Journal*, Vol. 17, No. 3, 1982, pp. 116-202.
92. D. D. MacDonald, B. Roberts and J. B. Hyne, "The Corrosion of Carbon Steel by Wet Elemental Sulphur", *Corrosion Science*, Vol. 18, No. 5, 1978, pp. 411-425.
93. N. I. Dowling, P. D. Clark and J. B. Hyne, "Understanding and Mitigation Corrosion during Handling and Transportation of Elemental Sulfur", *Alberta Sulfur Research Center Quarterly Bulletin*, Vol. XXXIII, No. 1 April-June 1996, pp. 15-28.

94. N. I. Dowling, "Corrosion of Materials Used in Storage and Handling of Solid Elemental Sulphur", Proceeding of the International Symposium on Materials Performance: Sulphur and Energy, 31st Annual Conference of Metallurgists of CIM, Edmonton, 1992, pp. 103-115.
95. M. R. Gregg, J. Slofstra, D. Thill and W. Sudds, "Corrosion Experiences and Inhibition Practices Managing Wet Sour Salty Gas Pipeline Environments Contaminated with Elemental sulfur Deposits", Corrosion/2003, Paper no. 03174, NACE International, Houston, Texas, 2003.
96. J. A. Dougherty, "Corrosion Inhibition of Wet, Sour Gas Lines Carrying Elemental Sulfur". Corrosion/92, Paper no. 12, NACE International, Houston, Texas, 1992.
97. J. A. Dougherty, "Factors Effecting H₂S and H₂S/CO₂ Attack on Carbon Steels under Deep Hot Well Conditions", Corrosion/88, Paper no. 190, NACE International, Houston, Texas, 1988.
98. J. A. Dougherty and B. A. Alink, "Corrosion Inhibition of Mild Steel in Natural Gas Systems Containing Elemental Sulfur, H₂S and CO₂". 7th European Symposium - on Corrosion inhibitors (7SEIC) Ann. Univ. Ferrara, N.S. Sez. (Suppl.9): pp. 1299, 1990.
99. J. A. Dougherty, B. A. Alink, D. Ho Chung Qui and K. van Geider, "Corrosion Inhibition of Super Sour (90+% H₂S) Gas Production", Corrosion/94, Paper no. 29, NACE International, Houston, Texas, 1994.
100. M. C. Place, "Corrosion Inhibition for Severely Corrosive Gas Wells", Corrosion/90, Paper no. 226, NACE International, Houston, Texas, 1990.
101. J. Lerbscher, D. Thill, G. McDonald and D. Ohri, "Management of Wells That Co-produce Elemental Sulfur", NACE Northwest Regional Conference, Calgary, Canada, Paper no. 1, 1999.
102. S. Boursiquot, M. Mullet, M. Abdelmoula, J. M. Génin and J. J. Ehrhardt, "The Dry Oxidation of Tetragonal FeS_{1-x} Makinawite", Physics and Chemistry of Minerals, Vol. 28, No. 9, 2001, pp. 600-611.
103. L. G. Benning, R. T. Wilkin and H. L. Barnes, "Reaction Pathways in the Fe-S System below 100°C", Chemical Geology, Vol.167, 2000, pp. 25-51.
104. D. Rickard and G. W. Luther III, "Chemistry of Iron Sulfides", Chemical Reviews, Vol. 107, No. 2, 2007, pp. 514-562.

105. K. J. Kennelley, S. N. Smith and T. A. Ramanarayanan, "Effect of Elemental Sulfur on the Performance of Nitrogen-Based Oilfield Corrosion Inhibitors", *Material Performance*, Vol. 29. No. 2, 1990, pp. 48-52.
106. J. Newman and K. E. Thomas-Alyea, *Electrochemical System*, 3rd ed., Wiley-Interscience, 2004.



Thesis and Dissertation Services